University Of Bergen

PhD Thesis

Monitoring and Measurements with the ATLAS Inner Detector and Search for Supersymmetry using ATLAS data

Author:
Konstantinos A. Kastanas

Supervisor:
Prof. Anna Lipniacka
Dr. Heidi Sandaker
Dr. Pippa Wells

October 13, 2014

Abstract

This thesis was completed in the ATLAS experiment at the Large Hadron Collider at CERN. The work presented here spans from detector monitoring to the early collision physics and finally to the analysis of 7 TeV collisions data in search for New Physics. Three main topics are presented in the thesis. The first one is the monitoring and data quality of the ATLAS Inner Detector. The measurements of charged particle spectra in p-p collisions with energies of 900 GeV, 2.36 TeV and 7 TeV are shown in Paper I attached in the thesis and the cross-check that was carried out on the analysis 7 TeV dataset is presented. A search for Supersymmetric events in the 7 TeV data is presented and the results are summarised in Paper II attached in the thesis.

Acknowledgements

First of all I want to thank my supervisors Anna Lipniacka, Heidi Sandaker and Pippa Wells. You have been very helpful during the course of this PhD and above all patient. My biggest thanks for everything I have learnt from you over the years.

Thanks to all of my coworkers in the Inner Detector and the Data Quality groups. In particular I would like to thank Gaetano Barone and Per Johansson for working with me on the monitoring even long after they needed to. My thanks to Steve McMahon, Saverio D'Auria and Dave Robinson for their input and useful discussions. And of course all the great people I met in the 007 office at CERN, it was a pleasure sharing an office with you all.

Thanks to the Bergen group for giving me a good environment to work in. I am grateful to Wolfgang Liebig and Therese Sjursen in particular for reading this thesis and providing valuable input. I also want to thank Ørjan for being good company over skype during the days and nights of finalising the SUSY analysis.

Many thanks to Prafula Behera and Remi Zaidan, who introduced me to Minimum Bias physics. It was great working with you and I learned a lot.

I would like to mention Kostas, Christos, Eleni, Thodoros and Fanouria; some of the nicest people one could hope to meet, it would not have been the same without you there. And a big thanks to Kostas for his philosophical advice, even if I did not always follow it.

Many thanks to Øystein and Therese for being around this entire process. You have always made things interesting and kept me going. My friends outside of physics, particularly Nina, Sebastian, Fedon and Filippas; thank you for being there for me even though you were far away and for often giving me the perspective I needed.

My family, whether in Iceland, Athens or Chalkidona, I am grateful for your constant support and enouragement. Last but not least my deepest gratitude to Alicia for her support and love, this would not have been possible without you. This PhD has to a large extent defined our life so far, now it is time for new adventures.

Contents

Chapter 1

Introduction

The Large Hadron Collider (LHC) is a state of the art proton-proton collider built at CERN. It has a 27 km circumference and is designed to reach Center of Mass (CoM) energies of 14 TeV. This is the highest energy ever achieved in a collider, and by analysing the output of its collisions the physics at these high energies can be studied. To this end there are four major experiments at the LHC, built to record the particles produced in collision at the LHC. These experiments are ATLAS, ALICE, CMS and LHCb; I participated in the ATLAS experiment.

The physics investigated covers many different areas. The most important goal for the ATLAS experiment was to find the Higgs particle, the discovery of the Higgs particle was indeed announced by both ATLAS and CMS on July 4th 2012. In addition, searching for physics beyond the Standard Model (SM), such as Supersymmetry, is an important topic. The detector is also suited for doing more refined measurements of SM properties, taking advantage of the very high event output of the LHC, as well as probing SM physics at the higher energy of the LHC.

I had the privilege of doing my PhD during the time when the first LHC run took place, starting in 2009 and ending in 2013. This allowed me to participate in the detector commissioning for collisions, the start of the run, as well as the gradual improvements in the understanding of the detector and the machine.

During the entire run I worked on the Inner Detector Global monitoring, a monitoring package responsible for assessing the status and performance of the ATLAS Inner Detector as a whole. Throughout this I worked closely with the ATLAS Inner Detector and Data Quality communities, which was greatly aided by being stationed at CERN as a Technical PhD Fellow. In the years 2009-2014 I was responsible for the Inner Detector Global Monitoring package as well as day-to-day operations; assessing the quality of data as well as maintaining the system for running the monitoring package during data-taking.

I got the opportunity to participate in the 7 TeV minimum bias analysis in 2010. This analysis produced the first 7 TeV minimum bias result for ATLAS and combined them with the results from the analysis of the 900 GeV and 2.36 TeV data collected in the first months of operation in 2009. In this paper I was responsible for the cross-check analysis performed on the 7 TeV dataset, leading to the same distributions as those published. This was very interesting as it was the first chance to see how the work on monitoring comes into play in a physics analysis and getting a better understanding of the impact of tracking on physics analyses. The work on this is published in Paper I included in the thesis, entitled "Charged-particle multiplicities in pp interactions measured with the ATLAS detector at the LHC".

Paper II, entitled "Search for supersymmetry in events with large missing transverse momentum, jets, and at least one tau lepton in 7 TeV proton-proton collision data with the ATLAS detector", presents a search for Supersymmetric events in the 7 TeV data collected in 2011 with tau leptons as a signature. Supersymmetry is an extension of the Standard Model that predicts a relatively light Higgs boson and solves the so called hierarchy problem, stabilizing the Higgs boson mass. There are also good Dark Matter candidates among supersymmetric particles. In many supersymmetric models a partner of the tau lepton, the stau, is the so called Next to Lightest Supersymmeric Particle (NLSP). This leads to tau lepton signatures in the detector. My role in Paper II was to develop methods to estimate backgrounds from W and top production. In addition, I have been responsible for large parts of the developement of the framework used for the analysis. The framework relies on so called "skims and slims", to produce subsets of interests from the ATLAS data with preselected information which is important for the analysis. I have continued my active analysis support also for the analysis based on 8 TeV data from 2012, which resulted in a conference note [1] and a paper [2].

I got the opportunity to present results on behalf of ATLAS, including my work, on two occasions, once at the *2nd International Workshop on Multiple Partonic Interactions at the LHC* in Glasgow with a talk titled "Minimum bias measurements at ATLAS" and in the *First Large Hadron Collider Physics Conference* in Barcelona with a talk titled "Inclusive searches for squarks and gluinos with the ATLAS detector".

Chapter 2

LHC and ATLAS

The work presented in this thesis has been performed at the ATLAS detector situated at the Large Hadron Collider (LHC), both presented in this chapter. This chapter discusses the relevant accelerator parameters as well as ATLAS detector technologies, operation, data taking and reconstruction of physics objects and quantities used in the analysis. This forms the background needed for the work presented in the following chapters. All ATLAS information in this chapter is based on the ATLAS detector reference paper [3], unless otherwise stated.

2.1 LHC

The LHC [4] is a new collider built at CERN. It is a proton-proton collider nominally operating at a 14 TeV CoM energy. It is built within the old Large Electron Positron Collider (LEP) tunnel and has a 27 km circumference, see figure 2.1. The entire collider is operated with superconducting magnets, which are cooled down to 1.9 K to keep the dipoles superconducting and providing the necessary 8.3 T field to bend the protons.

The accelerator has four interaction points, where collisions take place. There are the four main experiments of the LHC, ATLAS (Point 1), ALICE (Point 2), CMS (Point 5) and LHCb (Point 8).

Luminosity is a very important collider parameter, allowing us to calculate expected event rates given a process cross-section. It can be approximated as

$$L = \frac{f \times N^2}{4\pi\sigma_x\sigma_y} \tag{2.1}$$

where f is the rotation frequency of particles in the beam, N is the number of particles and σ_x and σ_y are the spread of the beam in the directions orthogonal to the beam. Nominally the LHC could be filled with 2808 bunches

with a 25 ns bunch spacing between them, each containing 1.1×10^{11} protons, to reach a design luminosity of $10 \times 10^{34}\,\mathrm{cm}^{-2}\,\mathrm{s}^{-1}$. The resulting interaction rate at the detectors is about one billion collisions per second, putting a heavy strain on the detector readout and trigger systems. As the luminosity is very high and the bunch spacing is tight there is more than one interaction in each bunch crossing. These additional additional interactions are referred to as pileup. At such high luminosity and tight bunch spacing pileup becomes a significant problem.

The results presented in this thesis use data collected during the years 2011-2012. During this time the LHC underwent commissioning towards increasingly higher CoM energies and luminosity. The CoM energy was 7 TeV and 8 TeV in 2011 and 2012 respectively, with 1368 bunches at 50 ns spacing. The integrated luminosity and average number of interactions per bunch crossing for the 2011 and 2012 runs can be found in figure 2.2.

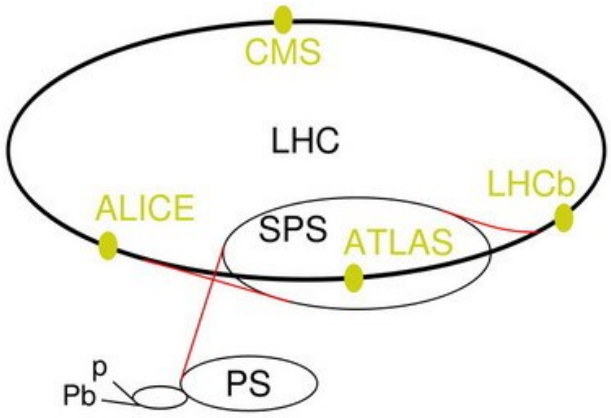

Figure 2.1: Overview of the LHC accelerator chain. The proton beam enters the LHC from the SPS with an energy of 450 GeV, with collisions happening at four interaction points around the ring, one for each of the main experiments; ATLAS, ALICE, CMS and LHCb. The interaction point where ATLAS is located is referred to as Point-1.

2.2 ATLAS

The ATLAS detector is a general purpose detector, situated in one of the four LHC interaction points, as indicated in figure 2.1. The detector is built with a broad physics programme in mind, ranging from searches for the Higgs boson and physics beyond the Standard Model to top physics and precision Standard Model measurements. It is a 44 m long and 25 m tall detector, built with three primary components: the Inner Detector (ID), the calorimeters

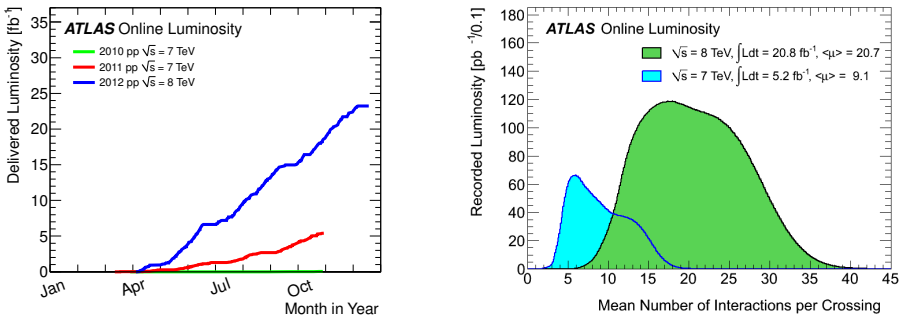

Figure 2.2: Total integrated luminosity delivered by the LHC as a function of time as measured by ATLAS (left) and average number of interactions per bunch crossing, weighted by luminosity (right) for the 2011 and 2012 runs.

and the Muon Spectrometer; the overall structure of the detector is shown in figure 2.3. All of these components are built for providing excellent hermiticity as well as giving reliable measurements of particle properties under the conditions of the LHC. These include very high event rates, large event multiplicities and a high radiation environment.

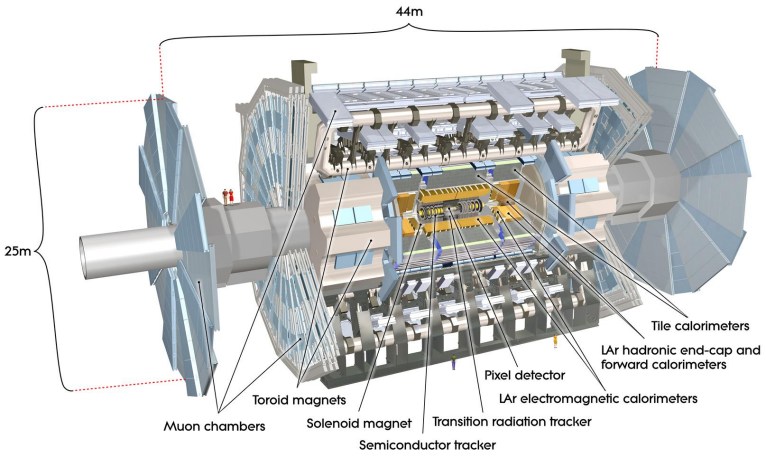

Figure 2.3: Overview of the ATLAS detector. Shown are the main detectors of ATLAS and the magnet system [5].

2.2.1 Coordinate system

The ATLAS coordinate system is oriented such that the x-axis points towards the center of the LHC ring and the y-axis points upwards. Thus the z-axis is along the beam pipe, pointing counter-clockwise. The azimuthal

angle ϕ is defined as $\phi = \arctan(y/x)$ and the polar angle, θ between the particle and the z-axis. Pseudorapidity is commonly used instead of θ, defined as $\eta = -\ln\tan\theta/2$. The transverse momentum of a particle is defined as $p_{\mathrm{T}} = \sqrt{p_{\mathrm{x}}^2 + p_{\mathrm{y}}^2}$. Angular distances between objects, denoted ΔR, are defined as: $\Delta R = \sqrt{\Delta\eta^2 + \Delta\phi^2}$

2.3 Inner Detector

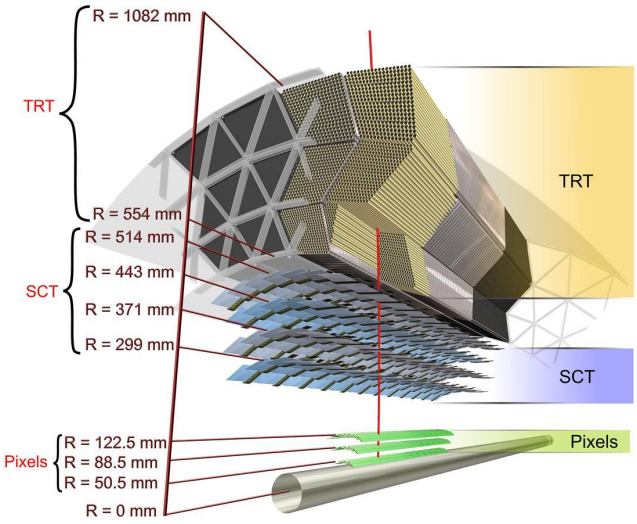

Figure 2.4: The ATLAS inner detector, showing a cutaway view of the barrel and end-caps. The Pixel detector is closest to the beampipe, followed by the SCT and the TRT. The dimensions of the entire ID are shown for perspective [5].

The ID is a tracking detector, comprised of three sub-detectors. These are two silicon detectors, the Pixel and the SemiConductor Tracker (SCT) and a straw tube detector, the Transition Radiation Tracker (TRT). An overview of the detector layout can be found in figure 2.4.

A solenoid magnet provides a 2 T magnetic field with the field aligned with the beampipe bending the tracks of charged particles in the x-y plane allowing for momentum measurements in the tracker, see figure 2.5.

An evaporative cooling system, using C_3F_8 as coolant, is used to keep the Pixel and SCT detectors at a $-7\,^{\circ}\mathrm{C}$ temperature. This ensures that the detector performance stays high even after irradiation. The TRT operates

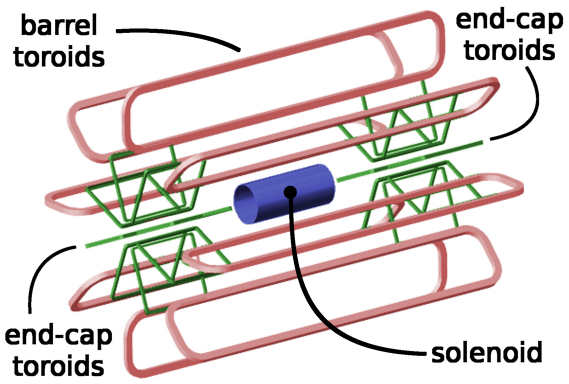

Figure 2.5: Overview of the ATLAS magnet systems, showing the solenoid, which provides the magnetic field to the ID and the toroid magnets providing magnetic field in the MS volume [6].

at room temperature, therefore heating pads are placed at the SCT-TRT boundary.

Pixel

The Pixel detector consists of three concentric cylindrical layers in the barrel and three disks for the endcap on each side with a total 1744 modules in the whole detector. The barrel and end-cap modules are identical, with nominal Pixel size of $50 \times 400\,\mu m^2$ and a sensor thickness of 250 µm. Each sensor has 46 080 independently read-out channels, resulting in more than 80 million readout channels for the whole detector. The Pixel sensors are built using an oxygenated n-type bulk material. One side is n^+ implanted where the sensors are placed. The detector is operated with a 150 V depletion voltage applied to the sensors. As charged particles traverse the sensor they produce electron-hole pairs that are then collected and read out as electric signal by the electronics. The accuracy of the detector is 10 µm in the R-ϕ plane and 115 µm in the z direction (R in the endcap). The innermost layer of the Pixel detector is referred to as the b-layer and is very important for vertexing.

Semiconductor Tracker

The SCT is a silicon microstrip detector. It consists of four double sided concentric layers in the barrel and nine single-sided endcap disks on each side, with 15912 modules in total and more than six million readout channels. The sensors are made using a single sided p-in-n design with each sensor consisting of 768 strips with 12 cm length and 80 µm strip pitch. As charged particles traverse the detector they create electron-hole pairs that are collected and read out by the electronics. The strips are aligned along the z-axis in the

barrel and radially in the end-caps. In order to provide position information along the sensor strip direction the two modules in each layer have a stereo angle of 40 µrad, resulting in 580 µm accuracy along the strips. The detector is operated at 150 V bias voltage.

Transition Radiation Tracker

The TRT is a straw tube detector, placed outside the SCT. The detector is constructed from 4 mm diameter straw tubes with each tube made of two 35 µm layers, containing a gas mixture of 70% Xe, 27% CO_2 and 3% O_2. The straws are 144 cm long in the barrel. In order to cope with the high track multiplicities they are split in two sides, each side read out separately; this means there is no measurement of the z coordinate. In the end-caps the straws are arranged radially and are 39 cm long. As charged particles traverse the straws they create electron-ion pairs, that drift to the cathode and anode respectively. The detector records the position of charged passing particles by measuring the drift time of the electrons to the anode. The spatial accuracy for the drift radius is 130 µm. A distinction is made between low threshold minimum ionising particle hits and high threshold transition radiation hits. This is used to provide separation between pions and electrons. The TRT provides coverage for $|\eta| < 1.1$ in the barrel and $1.0 < |\eta| < 2.0$ in the end-cap. The total number of readout channels of the whole detector is 350 000.

The TRT provides an large number of additional hits from each straw, typically 36 per track. This significantly improves the transverse momentum resolution, by extending the lever arm for the measurement, while also enhancing the electron/pion separation via its coating that produces transition radiation for high p_T electrons.

2.4 Calorimeters

The ATLAS calorimetry system is built from five different sub-detectors, split into electromagnetic and hadronic calorimetry. Electromagnetic calorimetry is done using liquid argon as active material and lead as absorber. Behind the electromagnetic calorimeters are the hadronic calorimeters. In the barrel this is done by the tile calorimeter and in the end-caps by the Hadronic Endcap Calorimeter (HEC). At high pseudorapidities the Forward Calorimeter (fCal) provides both electromagnetic and hadronic calorimetry. In the barrel the cryostat houses the Liquid Argon Calorimeter (LAr) while in the end-caps the LAr, HEC and fCal share a common cryostat. An overview of the calorimetry system can be found in figure 2.6 and it is described as follows:

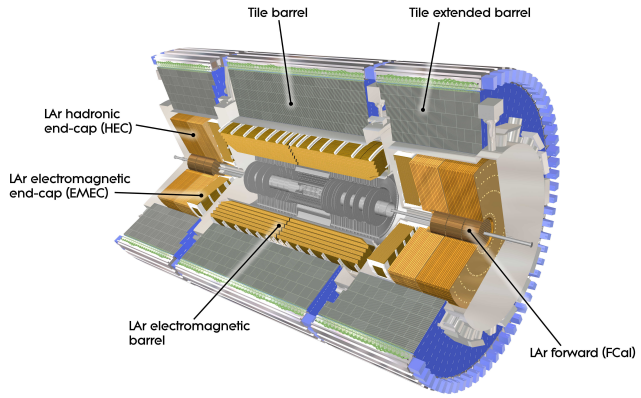

Figure 2.6: Overview of the ATLAS calorimeters [5].

Electromagnetic calorimetry

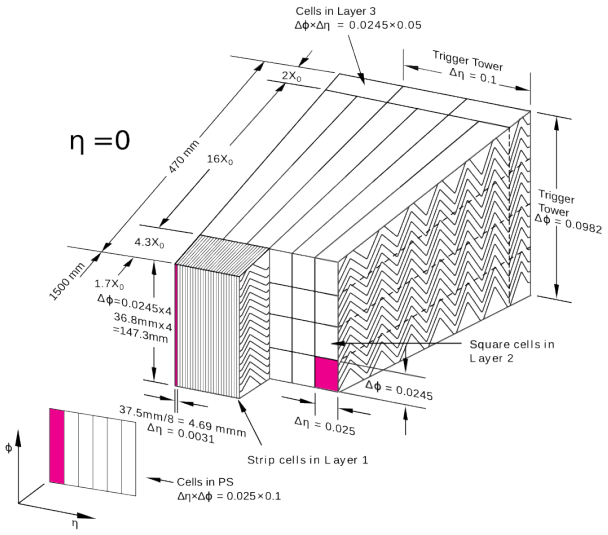

Figure 2.7: Structure of the ATLAS electromagnetic calorimeter, showing the accordion shape of the detector as well as the different layers and their granularity [5].

The ATLAS electromagnetic calorimeter is a sampling calorimeter using lead absorbers and liquid argon as the active material. A schematic view of the calorimeter can be seen in figure 2.7. The calorimeter is built using an accordion structure covering the $|\eta| < 2.5$ region in the barrel and $2.5 < |\eta| < 3.2$ in the end-caps. The detectors are segmented in three (two) regions in depth in the barrel (end-cap) with varying granularity in η. The first

layer is very finely segmented in η in order to provide accurate direction determination. Starting from the innermost, each layer provides 4.3, 16 and 2 radiation lengths respectively. The accordion ridges run along ϕ (R) in the barrel (end-cap). Between the absorbing layers there is an electrode mesh, consisting of three copper layers, the first and third layer at 2 kV potential and the second layer is used to read out the signal. This results in a 450 ns charge collection time. The energy resolution of the calorimeter can be parametrised as:

$$\frac{\sigma(E)}{E} = \frac{\mathrm{a}}{\sqrt{E\ (\mathrm{GeV})}} \oplus \mathrm{b} \tag{2.2}$$

where the stochastic term is $a = 10\% \cdot \sqrt{\mathrm{GeV}}$ and the constant term is $b = 0.17\%$.

Hadronic calorimetry

The hadronic calorimeter of ATLAS sits outside the LAr calorimeter and is used to provide measurement of energy for hadronically interacting particles that will punch through the LAr calorimeter. It is built from iron absorber tiles and plastic scintillator tiles covering the $|\eta| < 1.7$ region. The tiles are arranged azimuthally.

The detector is split into three layers. The layers are segmented into areas of $\Delta\phi \times \Delta\eta = 0.1 \times 0.1$ in the first two layers and $\Delta\phi \times \Delta\eta = 0.1 \times 0.2$ in the third layer. On average the active detector spans 8 interaction lengths.

As hadrons transverse the detector they interact with the iron tiles, initiating showers. As the resulting shower goes through the scintillating tiles ultraviolet light is emitted, which is collected at the edge of each scintillating tile through wavelength shifting fibers connected to PhotoMultiplier Tubes (PMTs) at the outer surface of the detector. The collected light is converted into electric signal and read out.

The relative resolution of the Tile calorimeter can be parametrised as in eq. 2.2 with parameters $\mathrm{a} = (56.4 \pm 0.4)\% \cdot \sqrt{\mathrm{GeV}}$ and $\mathrm{b} = (5.5 \pm 0.1)\%$.

In the end-caps, the HEC is used, which is a liquid argon calorimeter with copper plates as the absorber material, covering the $1.5 < |\eta| < 3.2$ region. The detector is built from two wheels with the innermost having 24 layers and the outer 16 layers. The absorbing copper layers are flat and a nominal voltage of 1.8 kV is applied between the absorbers and the electrodes.

Forward Calorimeters

In the forward region ($3.1 < |\eta| < 4.9$) the fCal is used to provide calorimetry for both electromagnetically and hadronically interacting particles. The detector uses liquid argon as the active material. It is further segmented into

three regions in depth, the one closest to the interaction point using copper as the absorber and specialising for electromagnetic calorimetry, with the next two using tungsten absorbers and meant to provide hadronic calorimetry and limit punch through to the muon systems.

Calorimeter calibration

The calorimeter response is different depending on the type of particle traversing it. In ATLAS two different calibration schemes are used:

Electro-Magnetic Energy Scale (EMES) is a calibration based on the calorimeter response to electrons and photons. This calibration was performed using test beam data. It is the baseline calibration applied to calorimeter clusters.

Jet Energy Scale (JES) is a calibration appropriate for Quantum Chromodynamics (QCD) jets. It is applied as a correction to the EMES calibration.

2.5 Muon spectrometer

The muon spectrometer makes up the largest part of the detector and is composed of four detector systems with two different purposes:

- Precision measurements
  - Monitored Drift Tubes (MDT) ($|\eta| < 2.7$)
  - Cathode Strip Chambers (CSC) ($2.0 < |\eta| < 2.7$, in the innermost layer)
- Triggering
  - Resistive Plate Chambers (RPC) ($|\eta| < 1.05$)
  - Thin Gap Chambers (TGC) ($1.05 < |\eta| < 2.4$)

MDTs are used for precision measurements throughout most of the detector, providing coverage for $|\eta| < 2.7$. These are 30 mm diameter drift tubes, filled with a 93%/7%Ar/CO_2 mixture under 3 bar pressure. At the center of the tube is a 50 µm thick tungsten-rhenium wire at a 3080 V potential difference compared to the tubes. The passage of muons triggers ionisation of the gas mixture and the readout of the resulting electrons at the wire.

CSCs are used for the innermost muon wheel, covering $2.0 < |\eta| < 2.7$, as they have very good granularity and timing resolution. The detector is a multi wire proportional chamber, with wires running in the radial direction at a 1900 V potential. Cathode strips run both parallel and perpendicular to the wires. Based on the charge collected at each strip it is possible to pinpoint the position of the track in both dimensions.

RPCs are built using electrode plates only, and no wires, with a 2 mm gap. A 4.9 kV mm^{-1} electric field leads to electron avalanches as muons pass between the plates.

TGCs are multi wire proportional chambers. Their defining feature is that the distance between the wires is larger than between the wire and the cathode. They have excellent timing resolution for the detector.

RPCs and TGCs are used for providing input to the Level one (L1) trigger, owing to their high readout speed, as well as additional hits for muon tracking.

An air-core superconducting toroid magnet provides magnetic field in the muon spectrometer volume, as indicated in figure 2.5. The magnet system consists of eight toroid coils in the barrel and two magnets in the endcaps built of eight coils, see figure 2.8. The coils in each endcap are housed inside a common cryostat. Due to the low number of coils building up the field there is considerable variation in the magnetic field, with values between 2 to 4 T m.

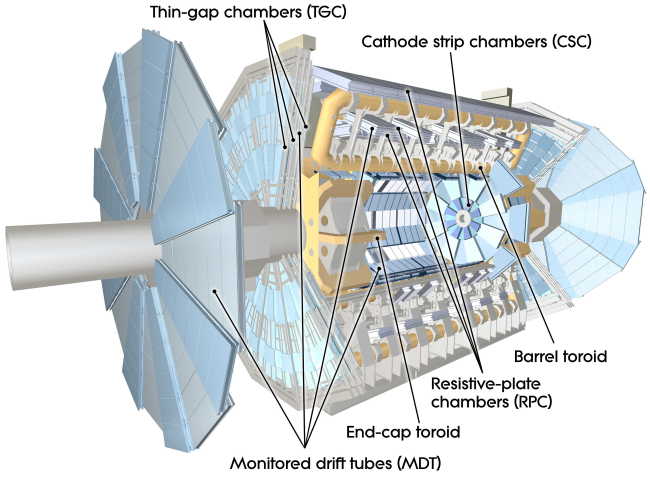

Figure 2.8: Overview of the ATLAS Muon Spectrometer. Shown are the MDTs and CSCs as well as the TGCs and RPCs. The barrel toroid magnets are also visible as are the end-cap magnets [5].

2.6 Reconstruction

Reconstruction is the process of going from the raw detector output to objects which are closer to the particles that were produced in the collision. In the ID and the MS the hits are combined to form tracks, recording the passage of charged particles. In the calorimeters, nearby energy deposits are combined to form clusters, representing possibly related energy deposits. From this point, they can be further combined to produce composite objects.

Tracks are the object of interest both in chapter 2 and 3 that follow. For the analysis presented in chapter 4 taus and jets are the main focus, as well as $E_{\mathrm{T}}^{\mathrm{miss}}$, which is very important in the characterisation of Supersymmetry (SUSY) events.

Below follows a brief summary of the physics objects reconstructed in ATLAS with focus on the most important ones for the work presented in the following chapters.

Tracks

Tracks are reconstructed particle trajectories using data from the ID and the muon spectrometer (for muon tracking). The following track parametrisation is used in ATLAS (see section 2.2.1 for coordinate system summary):

d_0 The transverse distance of the particle to a reference at the point of closest approach.

z_0 The longitudinal distance of the particle to a reference at the point of closest approach.

η The η direction of the particle.

ϕ_0 The ϕ direction of the particle.

p_{T} The transverse momentum of the particle.

Primary tracks, those originating from p-p interactions, are found using the so-called "inside-out" track reconstruction. This is the principal step in the track reconstruction and is seeded by hits in the Pixel and SCT. The track seeds are constructed by finding three hits in the Pixel and/or SCT that are compatible with a charged particle trajectory. These seeds are then propagated outwards through the Pixel and SCT detector using a Kalman filter to find compatible hits and update the track parameters at each layer of the detector. At this stage any ambiguities in the hit association to tracks are resolved and following this the track candidates are propagated to the TRT. Finally, the tracks are scored, in order to select the candidates that correspond most likely to primary charged particles. This procedure is done for tracks with momenta down to a certain minimal pT threshold. This

threshold is typically set at 500 MeV but can go down to as little as 100 MeV for minimum bias event reconstruction.

.

For handling secondary charged particles, an additional tracking mode is in place using TRT hits as seeds to construct TRT-only tracks, these are then propagated inwards towards the interaction point adding extra Pixel and SCT hits to the track [7].

Finally, tracks are also built with Pixel hits alone. This is done in the very forward region, where Pixel alone provides coverage. These tracks are combined with muon hits to produce forward muons.

During the hit collection phase the tracking is aware of disabled modules in the detector, such that if a disabled module is passed by a track, the resulting missing hit is treated like a properly associated hit in the requirements applied during event reconstruction and physics analyses. On the other hand, active modules that did not add a hit to the trajectory count against the track hypothesis, and only a limited number of such occurrences is allowed per track. This allows the tracking to handle the large hit multiplicities in the detector, where fake tracks can easily arise from combinatorics. The exact quality requirements for a successful track fit and suppression of fakes depend on the luminosity, becoming tighter as the luminosity increases [8].

Vertexing and Beamspot

Vertex reconstruction uses primary tracks to determine the location of interaction and decay vertices in the event. This is made more difficult in the high-pile-up LHC environment, requiring many separated vertices to be found. For the LHC runs in 2011 and 2012 the mean number of interactions per bunch crossing (μ) was 9.1 and 20.7 respectively and the distribution of μ can be seen in figure 2.2.

Vertex reconstruction uses an iterative χ^2 fit of tracks to a common vertex. The z_0 parameter of the tracks is used to produce seeds, by combining nearby tracks, and then tracks are added and scored according to their contribution to the χ^2. Tracks that are more than $7\,\sigma$ away are taken out and used to seed a new vertex candidate.

The beamspot is reconstructed by taking the vertices found during reconstruction and fitting an ellipsoid to contain them. The determination is done every ten Luminosity Blocks (LBs), letting the software track changes in beamspot position. When available, the beamspot is used as a three dimensional constraint on the vertex parameters. The procedure terminates when no more seeds are available [8].

Jets

Jets are reconstructed using the anti-k_T algorithm [9] where the distance parameter is set to 0.4. The calorimeter inputs to the jet reconstruction are topological calorimeter clusters. Energy determination is done in two different ways. One scheme relies on cluster energy being evaluated with the EMES calibration with the JES correction factor applied [10] while the other method relies on a direct calibration of the cluster energy using a local calibration scheme. This correction factor is meant to correct for the different calorimeter response to hadrons compared to the electron beams that the EMES calibration is based on.

B-tagging Jets originating from b-quark hadronisation can be distinguished from jets originating from other quarks. This is due to the relatively long lifetime of b-hadrons. To identify these jets a secondary vertex is reconstructed from the charged tracks belonging to the jet.

In order to provide b-tagging, special algorithms are used. In use in ATLAS are `IP3D` [11] which relies on the impact parameter of the tracks to identify b-jets. `SV0` [11] uses secondary vertex information to identify such decays. `JetCombNN` [12] does more sophisticated identification, exploiting the topology of the decays in the b-jet. Finally, the `MV1` [11] algorithm uses the output of all the above algorithms and combines them using a neural network, to produce one combined output from all of these, and thus achieving the highest discrimination power.

Taus

Tau leptons, due to their larger mass, can decay into a large variety of states. In all decays there is a tau-neutrino, an odd number of charged particles and possibly neutral mesons are produced. Classified by the type of the charged particles, the possible decay modes include decays through electrons or muons as well as hadronic decay modes. The goal of tau reconstruction is to be able to correctly reconstruct and identify hadronically decaying taus, since it is very hard to distinguish taus decaying through leptonic modes from primary electrons or muons.

The main challenge of identifying hadronic tau decays is that they are very similar to QCD jets. Hadronic decay modes include charged and neutral hadrons, primarily pions. The decay modes are split by the number of charged particles, most commonly one or three, referred to as one- and three-prong decays respectively. These charged hadrons are detected in the tracking and as hadronic energy. The neutral pions in the decay are seen as electromagnetic energy, as they promptly decay into photons. An example of a hadronic tau decay is shown in figure 2.9. The neutrino produced in tau decays escapes detection, which means that some information about the

four-momentum of the original tau is lost. The combined four momentum of the hadronic decay products of the tau is referred to as the visible tau momentum ($p_{\mathrm{T}}^{\mathrm{vis}}$).

Hadronic tau reconstruction in ATLAS is seeded by jets coming from jet reconstruction, anti-$\mathrm{k_T}$ jets with radius $R = 0.4$ which satisfy the requirements $|\eta \leq 2.5|$, to be within the acceptance of the ID, and $|p_{\mathrm{T}}| > 10\,\mathrm{GeV}$. During tau reconstruction this region is further split into the core ($R < 0.2$) and the isolation annulus ($0.2 < R < 0.4$). As the decay products of taus are more collimated than QCD jets these two regions are used to differentiate hadronic tau decays from jets. These regions can be seen schematically in figure 2.9. Additionally, each of these jets is associated to a vertex where the tau is most likely to originate from.

The tau four-momentum is determined at this stage. First, the barycenter of the clusters that form the seed jet is calculated; the four-momentum of all clusters within $\Delta R < 0.2$ of this barycenter are then summed to form the tau four-momentum. The energy of the clusters in this last step is calibrated using the so-called Tau Energy Scale (TES) calibration schema, reflecting the particular mixture of electromagnetic and hadronic energy found in tau decays.

Once the tau four-momentum has been determined, tracks can be associated to the tau candidate. Tracks falling within the core cone are associated provided they satisfy the following criteria:

- $p_{\mathrm{T}} \geq 1\,\mathrm{GeV}$
- At least two Pixel hits
- At least seven Pixel and SCT hits
- $|d_0| \leq 1.0\,\mathrm{mm}$
- $|z_0 \sin\theta| \leq 1.2\,\mathrm{mm}$,

where the last two criteria are defined with the tau vertex as reference point. Tracks inside the isolation annulus are not associated to the tau candidate but are still used for producing discriminating variables for identification.

In order to identify taus, a number of variables are used to discriminate between taus and other objects (e.g. jets, electrons or muons). One important distinction comes from the number of tracks associated with the tau and three variables use this information during identification:

- Track radius, the p_{T} weighted angular distance of associated tracks and tracks in the isolation annulus to the tau axis ($\mathrm{R_{track}}$)
- Invariant mass of associated tracks, if more than one ($\mathrm{m_{tracks}}$)

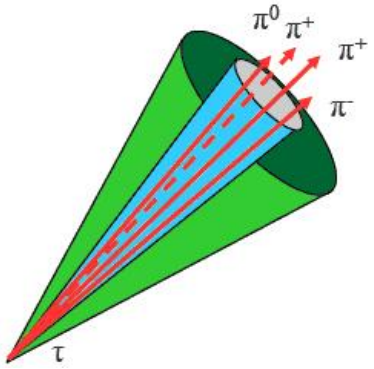

Figure 2.9: An example of a hadronic tau decay. The region within the inner cone is called the core and between the two cones is called the isolation annulus.

- Fraction of total transverse momentum carried by the leading associated track (f_{track})

In addition to the lower track multiplicities of tau decays compared to jets, the energy deposits of taus are also more focused, compared to the larger spread of QCD jets. This gives rise to a second set of discrimination variables:

- Maximum ΔR (ΔR_{max}) between clusters
- Fraction of total energy carried by clusters in the core (f_{core})
- Number of tracks in isolation annulus ($N_{trk}^{0.2<R<0.4}$)

Finally, taus have a non-negligible lifetime of $(2.906 \pm 0.010) \times 10^{-13}$s [13], the following variables that depend on the flight distance are used to characterise tau candidates:

- Leading associated track Impact Parameter (IP) significance ($S_{leadtrack}$)
- Transverse flight path significance (S_T^{flight})

These are combined using multivariate techniques to produce the final discriminant. Three different identification discriminants are used; these are used for rejection of fakes originating from jets (the biggest contribution), electrons and muons (including electrons and muons originating from leptonic tau decays). Three selection types are provided, each presenting a different compromise of efficiency versus purity for the identified taus. These are referred to as the loose, medium and tight selections, each having progressively higher purity at the expense of lowered efficiency [14].

The analysis presented in chapter 4 uses the Boosted Desicion Tree (BDT) based method for identification. The following selection is applied:

- BDT based jet rejection (Tight selection)
- BDT based electron rejection (Tight selection)
- Muon veto

Missing E_{T}

The $E_{\mathrm{T}}^{\mathrm{miss}}$ observable is the momentum imbalance of the event in the transverse plane. It is reconstructed from calorimeter clusters and reconstructed muons.

In order to provide as accurate an energy measurement as possible the energy of each cluster is evaluated depending on the kind of physics object it is associated with, if any. When an association is possible the energy scaling of the appropriate object type is used. The full $E_{\mathrm{T}}^{\mathrm{miss}}$ is built from the following components [15]:

- Jets are taken into account and the JES is used to calibrate the energy of the associated clusters.
- Electrons are accounted for and the EMES is used for energy calibration.
- Taus are not given special treatment in the $E_{\mathrm{T}}^{\mathrm{miss}}$ calculation, their clusters are therefore treated as jets or electrons depending on how they are reconstructed.
- Muons are added in using muons reconstructed in the muon spectrometer alone. The reason for this is that the clusters of deposited energy in the calorimeters are already taken into account in the $E_{\mathrm{T}}^{\mathrm{miss}}$ reconstruction. Using standalone muons ensures that these are not double counted due to energy corrections.
- Calorimeter energy deposits around an identified muon are also added to account for the remaining muon momentum. In this case calorimeter cells are directly used to build up this contribution instead of clusters.
- The soft energy term covers all calorimeter clusters not otherwise associated with an object. They get added to the $E_{\mathrm{T}}^{\mathrm{miss}}$, with the EMES energy calibration.

Useful discrimination variables

A few variables are of particular importance in the work presented further, these are:

- The transverse mass, m_{T}, is defined between a lepton in the event and the $E_{\mathrm{T}}^{\mathrm{miss}}$:

$$m_{\mathrm{T}} = \sqrt{2(|E_{\mathrm{T}}^{\mathrm{miss}}||p_{\mathrm{T}}^{\tau}| - \vec{E}_{\mathrm{T}}^{\mathrm{miss}} \cdot \vec{p}_{\mathrm{T}}^{\tau})}$$

- The effective mass, m_{eff} is the scalar sum of the $E_{\mathrm{T}}^{\mathrm{miss}}$ and the transverse momenta of all jets and taus in the event

$$m_{\mathrm{eff}} = \sum_i p_{\mathrm{T}}^{\tau} + \sum_j p_{\mathrm{T}}^{\mathrm{jet}} + E_{\mathrm{T}}^{\mathrm{miss}}$$

- $\mathrm{H_T}$ is calculated as the scalar sum of the transverse momenta of selected jets and taus in the event

$$H_{\mathrm{T}} = \sum_i p_{\mathrm{T}}^{\tau} + \sum_j p_{\mathrm{T}}^{\mathrm{jet}}$$

These variables are useful for characterising events and are used particularly to discriminate between signal and background.

2.7 Trigger and DAQ

The trigger system is responsible for selecting events that are of interest for the physics programme of ATLAS. The computing time required to process those events and storage space to record them put stringent limits on the amount of events that can be stored offline for analysis. Additionally, while the event data is retrieved by the readout electronics there is dead time for the detector, no events can be recorded. Therefore it is important to select the most interesting events for readout. All the above issues are addressed by the trigger system.

The trigger system consists of three stages, each successively producing a more refined event selection with a lower output rate.

As collisions occur in the LHC the output of each detector is kept in memory on board the detector elements. This information is buffered there until a decision is received from the L1 trigger that the event should be read out. The L1 trigger uses information from the muon detectors to identify high p_{T} muons and calorimeter information to identify jets, electrons/photons, taus and events with large $E_{\mathrm{T}}^{\mathrm{miss}}$ or total transverse energy. In order to keep processing time within the small 2.5 µs latency window of the L1 trigger, reduced granularity information is used at the L1 stage. Furthermore, the calorimetry trigger is implemented in hardware in its entirety. After L1 selection the event rate is reduced down to 75 kHz. Events passing the L1 trigger are passed to the High Level Trigger (HLT).

The HLT is composed of two stages, the Level two (L2) trigger and the Event Filter (EF). Both use algorithms similar to those implemented in offline reconstruction and provide a more refined event selection, that further reduces the event rate.

The L2 trigger works on Regions Of Interest (ROI), defined by the features identified by the L1 trigger. Now the full granularity detector data in this region as well as ID data are used, allowing for more refined reconstruction of the objects of interest. The L2 further pushes down the event rate to about 3.5 kHz.

Finally, in the EF the entire detector data is used at full granularity, producing the final decision on whether the event should be kept. Events selected at this stage are recorded for offline processing. The final event rate is about 200 kHz which is the maximum rate that can be handled by the offline computing resources. The overall structure of the triggering system of ATLAS can be seen in figure 2.10.

The events that are recorded in ATLAS are then split into streams. These streams classify events into sets with common characteristics. The streams typically used in data analysis are:

`JetTauEtmiss` which contains events passing triggers involving jets, taus or $E_{\mathrm{T}}^{\mathrm{miss}}$.

`Egamma` which contains events passing triggers involving electrons or photons.

`Muons` which contains events passing triggers involving muons.

`Express` which contains a mix of triggers intended for fast processing for the purposes of calibration and monitoring.

While the majority of events are only classified into one stream, it is possible for an event to satisfy the trigger requirements of more than one of the above categories, these streams are not exclusive. Additional streams are available for use in performance studies or more specialised analyses.

For the minimum bias study presented in chapter 3 the Minimum Bias Trigger Scintillator (MBTS) trigger is used (`L1_MBTS_1`), which requires at least one hit in one side of the scintillators. A looser trigger is used for tracking studies in the analysis, which triggers randomly on a filled bunch in the LHC.

For the SUSY analysis presented in chapter 4 the triggers used rely on jets and $E_{\mathrm{T}}^{\mathrm{miss}}$. The objects are selected in such a way that the analysis is limited to the trigger plateau. This is the region where the efficiency of the trigger is close to 100%. The cuts placed are on the primary jet p_{T} and the $E_{\mathrm{T}}^{\mathrm{miss}}$, at 130 GeV and 150 GeV respectively.

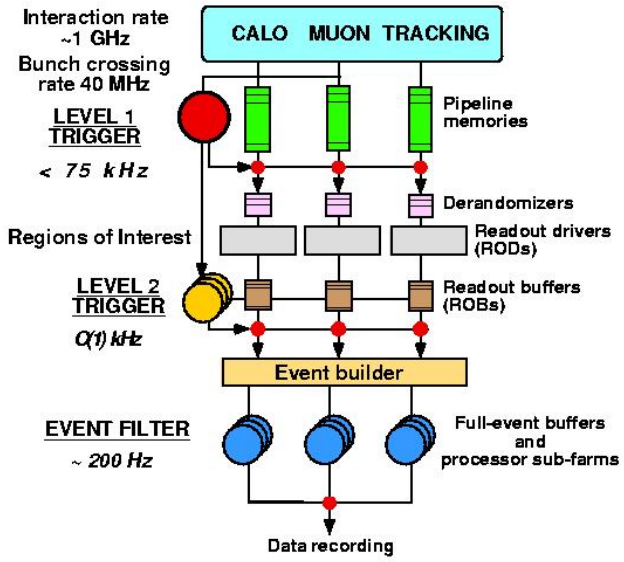

Figure 2.10: Overview of the ATLAS trigger system. Shown are the three trigger levels as well as the typical output rate. An overview of the readout system components at each level is also shown.

2.8 Offline processing

Events that are selected from the trigger are read out from the Data AQuisition (DAQ) system and are streamed to Tier-0 for storage and processing. The Tier-0 center is located at CERN and provides the computing capacity to promptly reconstruct the events coming out of ATLAS and the other LHC experiments. Data taking in ATLAS is done in intervals known as LBs. These represent periods of stable running conditions from both the machine and the detector. During stable conditions a LB was switched every two minutes in the 2012 run.

The output of the offline processing is the Event Summary Data (ESD) format, which is the base format used for data analysis. These files contain the objects used in physics analysis. A second format, Analysis Object Data (AOD), is used as well, which contains the same information as the ESD but with fewer details, making for a smaller and more manageable set of information for physics analyses. These formats can be read in `ATHENA`. It is also common to convert these formats into flat `ROOT` [16] ntuples that can be used for `ROOT` based analyses, these are commonly referred to as D3PDs in ATLAS.

Chapter 3

ID Monitoring

In this chapter the ATLAS Inner Detector Global Monitoring is presented. It is a software package used to produce information to assess the Inner Detector performance and flag potential problems during data taking. The package is designed to provide a global overview of the performance of the three ID detectors combined and act as a middle ground between the ID sub-detectors and reconstructed objects that rely on tracking.

The overall structure of the monitoring and related processes can be seen in figure 3.1. These cover the production of the monitoring histograms as well as preparing the output used by the shifters to evaluate Data Quality (DQ).

The package runs after reconstruction, providing prompt feedback based on the data reconstructed. It is primarily used during data taking, including cosmic ray, p-p and p-Pb collisions. It is also used during reprocessing campaigns when all data taken is processed with a new release.

3.1 Software

All ATLAS monitoring packages based on `ATHENA` are implemented as a collection of `ATHENA` tools tied together by a manager. The packages are implemented in `C++` and the monitoring tools and manager are implemented as classes. The common ATLAS base classes for these are found in the `ManagedMonitoringBase` `ATHENA` package, which provides a consistent interface for all monitoring packages. The manager is responsible for setting up the monitoring tools and calling them for each event. The tools in turn initialise all histograms that are produced and retrieve the event and condition information needed to fill them. The base class for the monitoring tools defines methods for initialisation during the beginning of a run or LB, filling histograms as well as performing any necessary processing at the end of a run or LB. An overview of the structure of the ID global monitoring package in term of classes and their inheritance structure can be found in figure 3.2. The package consists of the following tools:

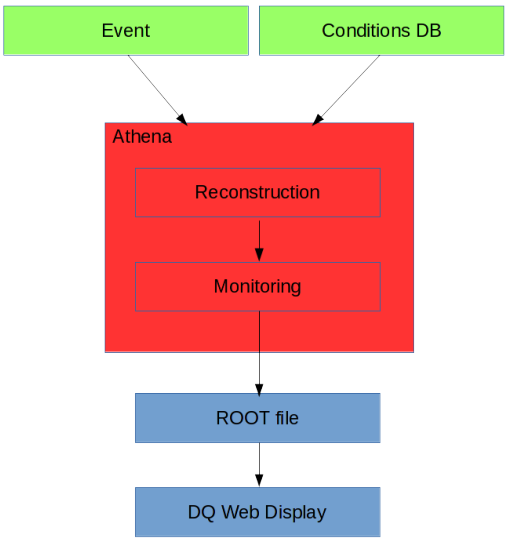

Figure 3.1: Functional diagram for the offline monitoring. Shown in green are the inputs, which are the event as well the detector conditions. In red is `ATHENA` which provides the framework for running reconstruction as well as monitoring. Finally, in blue, the output of the monitoring in `ROOT` format as well as the DQ Web Display which produces the web pages used by the DQ shifters.

InDetGlobalHitsMonTool is responsible for retrieving the number of hits that make up each track and the number of dead modules traversed by the tracks. It can also check the distribution of holes on each track, which represents the number of detector elements crossed by the track without an associated measurement. This runs in the online environment to promptly spot issues but is disabled in offline running to reduce CPU time. These distributions are produced also as a function of the η-ϕ parameters of the track, to localise problems in the detector.

InDetGlobalTrackMonTool which produces distributions of the track parameters as well as the total number of tracks in each event. These distributions are produced for a number of track selections fulfilling different criteria in order to diagnose specific potential issues.

As there was much common code in the two tools described above, they were merged during the 2012 run in order to reduce CPU time and memory used by the monitoring.

InDetGlobalSynchMonTool checks the synchronisation of ID Read Out Drivers (RODs) as well as the number of hits and tracks in the event as a function of Bunch Crossing IDentification (BCID). The BCID is the identification number given to each bunch in the accelerator. These checks were particularly useful during commissioning.

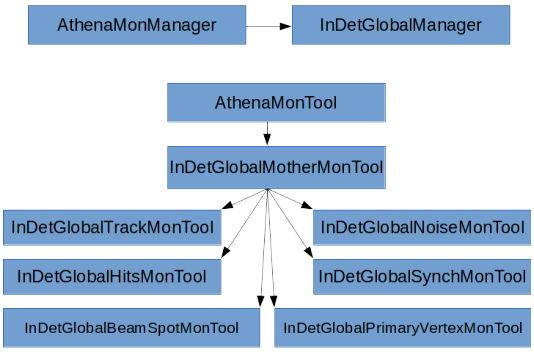

Figure 3.2: The inheritance diagram of the `ATHENA` tools used in the ID global monitoring. The tools inherit from a common base class, derived from the `ManagedMonitoringBase` package, which provides the basic monitoring interfaces. The last row of tools provide basic monitoring of beamspot and primary vertexing which were contributed to ID Global monitoring.

InDetGlobalNoiseMonTool checks the noise occupancy of the detectors and any correlation between them. The noise occupancy determination is very simple, using a direct subtraction of hits associated to tracks from the total detector occupancy. While this strategy works well in the low detector occupancies during cosmic ray data taking and low-pileup p-p collision runs, which it was designed for, it cannot cope with the occupancies seen in high luminosity LHC runs, deferring to the more advanced noise occupancy monitoring of the sub-detectors.

InDetGlobalPixelMonTool monitors the performance of the tracking with Pixels in mind. Information specific to the Pixel detector is shown for all hits on track in the Pixels.

InDetGlobalPrimaryVertexMonTool Monitors the performance of the primary vertexing in ATLAS. It provides basic information about the spatial distribution of primary vertices, track composition and the quality of fit.

These tools run for each event processed by `ATHENA`. During data taking these tools run in the end of event reconstruction, giving the monitoring access to both the raw detector data as well as to all reconstructed quantities that go into the ESD. It is also possible to produce the monitoring output from ESD files directly.

The package is primarily used in two different settings, during data taking at Point 1 as well as offline reconstruction at Tier-0.

3.1.1 Online monitoring

Within the Point 1 environment the monitoring runs on dedicated machines which sample events in real time, directly from the trigger. The purpose of the online monitoring is to provide feedback to the detector and data quality shifters about detector conditions and give an early alert for potential problems. The overall structure of the online monitoring and related processes can be seen in figure 3.3.

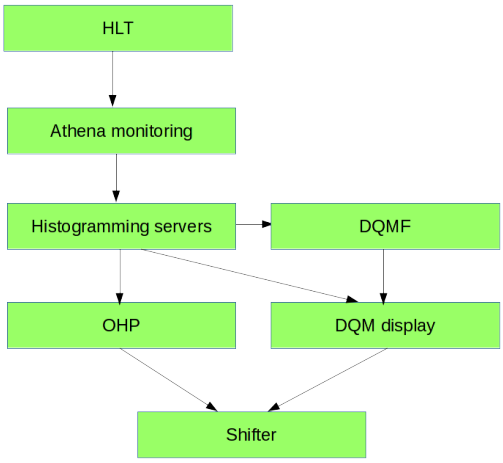

Figure 3.3: An overview of the components of the online monitoring in Point 1 for the ID. The entire reconstruction and monitoring runs alongside the ATLAS trigger and DAQ software during regular runs with the `OHP` (Online Histogram Presenter) and `DQMD` (Data Quality Monitoring Display) tools used by the shifter to view the output.

The monitoring runs within dedicated `ATHENA` jobs, which do full reconstruction of ID data. During the 2012 run this was done in jobs which provided output for all the ID detectors. The histograms produced by the ID monitoring are checked by the ID shifter.

Two machines were used for this purpose, each with eight cores and 24 Gb RAM, running eight reconstruction processes in parallel. The total number of jobs was limited by CPU and network utilisation. The reconstruction only runs the ID reconstruction and tracking. The sampled events come from the `express`, `JetTauEtmiss` and `Egamma` streams. An additional set of jobs is used to provide monitoring of the detector's noise occupancy; this is best done with empty events, sampled from the so-called ID monitoring stream, which outputs these empty events at a fixed rate. Finally, a dedicated job is used to produce detailed output of the current status of the Pixel detector, producing output for each individual module.

For the physics stream monitoring there is a dedicated gatherer application that merges the histograms from each job to provide the final histograms

displayed to the shifter, with the total gathered statistics.

The shifter gets information from the monitoring through two applications, `OHP` [17] and `DQMD` [18]. The `OHP` application produces customised views of the monitoring histograms, giving an easy overview to the shifter and gathering related histograms together. The `DQMD` application displays histograms and the result of automatic tests that are run on the histograms.

The online rate for running `ATHENA` reconstruction and monitoring is about 1 Hz per process on the monitoring machines, giving a total of 8 Hz sampling rate for the physics stream monitoring jobs. The total rate was limited by the processing power of the machines and network usage. This results in a restriction in the statistics that are available. For noise occupancy monitoring the event processing speed is much higher, since reconstructing empty events is much faster.

3.1.2 Offline monitoring

During offline processing the monitoring runs after reconstructing the RAW detector information to produce ESDs or after reconstruction of ESDs to AODs [19]. In contrast to the online mode all gathered events are available at this stage. The monitoring output of the offline monitoring is the authoritative view on DQ as it provides a full view of the run.

Offline reconstruction monitoring is done in two passes. The first pass, where only the `express` stream is processed and the bulk pass where all streams are processed. The first pass starts immediately after data taking and the results are used for initial data quality assessment and to check for changes in detector conditions and calibration, which is done in the so-called calibration loop. Following the calibration loop the bulk processing starts.

The most important part of the calibration loop for the ID global monitoring is the beamspot determination [20], which determines the extent of the luminous region where collisions happen. After the beamspot position has been determined, it is used in the bulk processing as a de-facto measurement in track reconstruction, ensuring that all tracks have their origin in the luminous region.

In the bulk processing the ID global monitoring is run on the `express` stream as well as the `JetTauEtmiss` physics stream, chosen due to the large number of events therein with high track multiplicity. The monitoring runs on one physics stream only in order to limit the use of computer resources at Tier-0.

At the end of processing the output of the monitoring is assessed by DQ shifters to ensure there are no problematic data to be used by physics analyses. Any such problematic issues are then recorded in a dedicated database. Each issue is stored in the form of a “defect” along with the associated time duration, in terms of LBs [21], and details to describe what was observed.

The defects themselves are prespecified problematic conditions. These describe specific problems for data quality, e.g. regions with low tracking efficiency or a bug in software affecting reconstruction. A defect can be set as intolerable or tolerable, which determines if a LB with a given defect is suitable to be used by physics analyses.

3.2 Monitored quantities

The ID global monitoring checks quantities related to the tracking in the ID. This is complementary to the ID alignment monitoring, which monitors the efficiency and tracking residuals, and the ID performance monitoring, which checks for the reconstruction and properties of some basic resonances, using ID and muon tracks.

The track collection monitored is the complete collection of primary tracks, i.e. tracks reconstructed by the inside-out Pixel and SCT seeded tracking, see section 2.6. A $p_{\mathrm{T}} > 0.5\,\mathrm{GeV}$ selection is made, to only keep tracks that traverse the whole ID detector. In addition, during 2012, Pixel tracklets were reconstructed in the high-η region where only Pixels provide coverage, to be combined with muon spectrometer hits to form muon tracks in the high η regions.

3.2.1 Hits on Track

The number of hits associated to each reconstructed track are monitored for all primary ID tracks. Examples of such distributions are shown in figure 3.4, showing the number of hits in each subdetector for all ID tracks. This is also broken down by the η and ϕ parameters of the track to allow potentially problematic regions to be localised.

The number of hits are checked as a function of η-ϕ as well as an average over the primary tracking regions in η, covering the barrel, end-caps and the transition region between the two. This provides a good check of the hits in the various regions. Examples of these distributions are shown in figure 3.5, showing the $\eta - \phi$ distribution of hits and dead modules for the Pixel and SCT detectors. If a detector is suffering from inefficiencies or the number of disabled modules aligning goes up this would be visible in these plots.

Additionally, hitmaps are produced in the x-y and z-r coordinate frames, see figure 3.6. These show the accumulated number of hits associated to a track in the detector and is a useful tool for visual inspection of the run. These make it possible to check that combined track reconstruction worked during cosmic runs or to see if any parts of the detector are not working properly. While useful in the early stages of the first LHC run, producing these plots is quite demanding on computing resources, so these plots were disabled to conserve CPU time and memory.

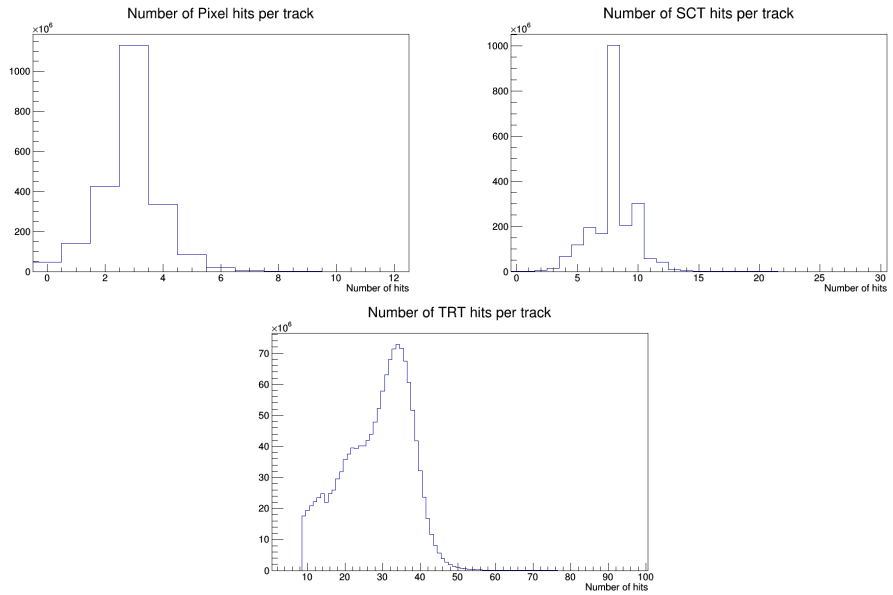

Figure 3.4: Number of hits per track in each subdetector. Disabled modules a track passes by are counted as hits.

These distributions do not provide specific information on the nature of problems but can be useful in spotting potentially problematic regions. The primary purpose is to spot generally problems and possibly assist other combined performance groups in identifying and understanding problems. One example of this is shown in the bottom left plot of figure 3.5, where in the upper left corner a disabled SCT endcap quadrant is visible (disabled due to a dead cooling loop, in 2012). In figure 3.6, where hits from TRT only tracks are shown, it can be seen that part of the detector hits are not being associated with tracks, around $\phi_0 = 0$. As there was no drop in occupancy in the TRT around that region the tracking was investigated and a problem was found in associating hits to the track in that region due to ϕ_0 not wrapping around at $\phi_0 = 0$.

Within the online environment the number of Pixel and SCT modules that are either in error or are disabled are also tracked in bins of η and ϕ to identify potential regions where problematic modules align. These maps are updated at the start of each LB in order to minimize the time needed to access the conditions DataBase (DB); this should not cause problems as conditions are stable during a LB. Examples of such plots are shown in figure 3.7. These plots allow us to check whether disabled modules or modules in error have an effect on tracking during the run. These checks are important since as the run progresses modules can go into an error state. This is especially true in high luminosity collisions where the rate of data and the

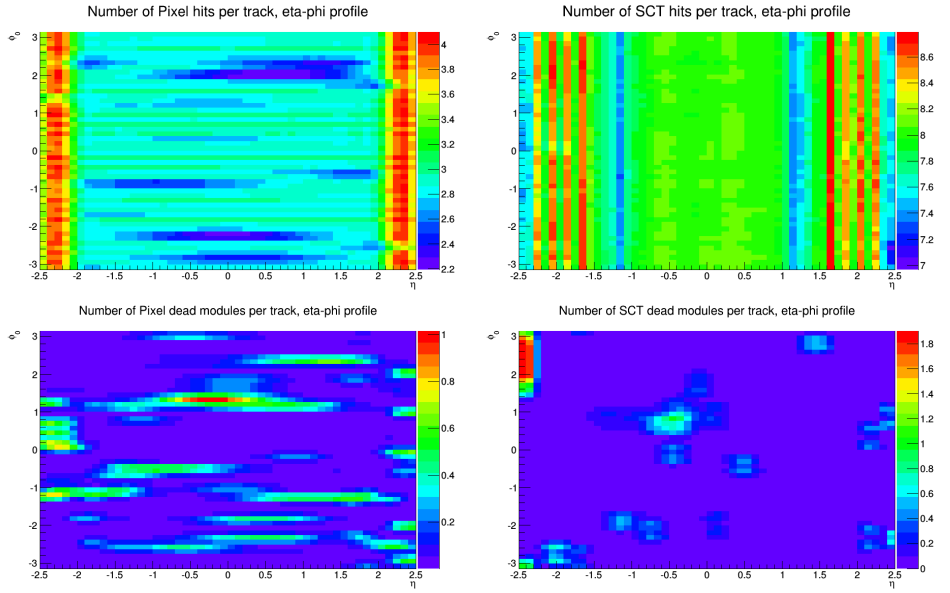

Figure 3.5: The distribution of the number of hits per track in η and ϕ. Shown here is the number of Pixel hits (top left) and SCT hits (top right). Also shown is the average number of dead Pixel (bottom left) and SCT (bottom right) modules traversed by each track. As an example a quarter disk of dead SCT modules can be seen in the top left corner in the bottom right plot. The average number of hits depends on the η of the track, with variations due to modules with errors or low efficiency. The filled entries in the disabled module plots correspond to disabled modules in the Pixel and SCT, with different sizes due to the positioning of each module.

effect of radiation on the electronics can cause problems in the electronics. This leads to modules slowly being disabled, but with no geometric correlation, save for the fact that the innermost layers of the ID are more affected. It is important to note that this check does not rely on the tracking at all; rather, it makes assumptions about the tracks, that they are straight and originate at the center of the detector, with a set longitudinal spread around the interaction point, Δz_0. With a correctly set parameter this can give a good approximation of the effects on the tracking, at least for high-p_{T} tracks. While this was only available online during the 2012 run, the monitoring has been updated since then to produce these plots also in offline monitoring in a similar manner.

The number of holes in the track are also monitored, that is to say active modules in the detector that did not produce a hit, but where the extrapolated track assumes a hit should be in place. A limited number of such holes are allowed in each track fit, else the fit can fail.

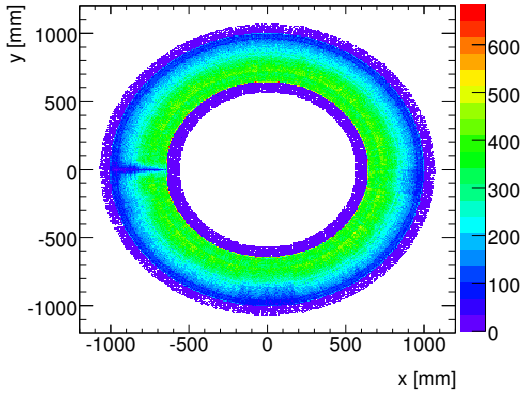

Figure 3.6: The x and y coordinates of hits associated to a track in the ID. Shown is an example of TRT only hits for a collisions run with a problem where TRT hits at $\phi = \pm\pi$ are not associated to a track, due to a bug in track reconstruction where ϕ is not wrapped around $\pm\pi$.

3.2.2 Track distributions

The track parameter distributions are also checked, in particular the η-ϕ distribution of the tracks to spot possible defects due to detector effects; this is done with various sets of cuts. The quality criteria are fairly loose, focusing on each detector in turn. This allows to see if a given detector causes problems to the tracking. Examples of these distributions are shown in figure 3.8, top. Of note is the b-layer which is explicitly checked to ensure there are no inefficient regions, see figure 3.9. This is of particular importance as several algorithms for physics object reconstruction explicitly assume that the b-layer is working at full efficiency.

These distributions are also produced as fractional displays of the total number of tracks showing the fraction of tracks satisfying each selection criterion, allowing to easily spot any deficiencies relative to the expected number of tracks.

In addition, for the forward Pixel tracklets the distribution of η-ϕ is checked separately, shown as example in figure 3.10.

The number of hits in each subdetector as well as the total number of tracks as a function of BCID is also displayed, which is useful for looking at the response of each detector when there are beams, shown in figure 3.11. This allows for a very low level check of the detector response to the colliding bunches, and is useful when there is a smaller number of colliding bunches in the machine, in the earlier parts of the run and during commissioning.

Additionally, graphs of the total number of tracks as a function of LB which is used to check for the stability of the number of tracks in time. The average number of tracks per event is also shown as a function of LB.

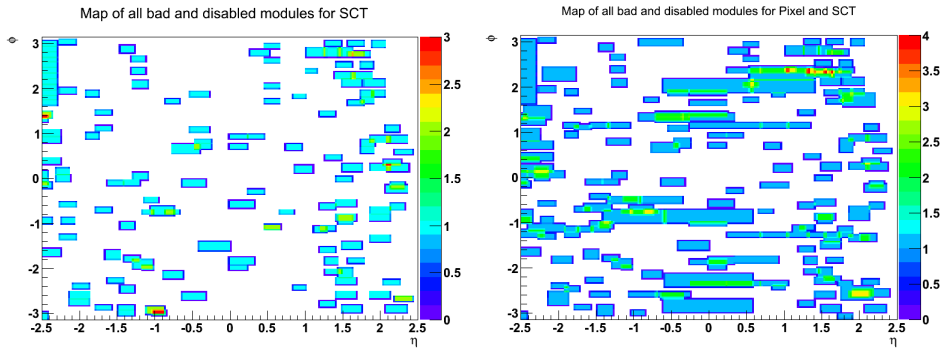

Figure 3.7: Number of modules in error or disabled along a straight track. The x- and y-axis show the ϕ and η parameters of the tracks and the value of each bin the number of problematic modules traversed. On the left is a plot of disabled SCT modules and on the right the number of modules in error and disabled modules for Pixel and SCT combined. Disabled modules are seen as rectangular regions, the size varying due to the different angular size of modules. The borders around the regions are due to modules covering only a fraction of the bin area. The information comes directly from the Conditions DB.

These plots are shown for illustration in figure 3.12. This has two prominent features, one being that the plot itself follows the decreasing luminosity envelope for the run as well as having kinks due to changes in the trigger menu during the run.

3.2.3 Synchronisation

A number of plots is also produced to check the synchronisation of RODs in the ID. This is an error condition when one of the RODs goes busy. This can have large effects on the tracking in certain conditions as the data from these RODs will be lost; these plots detect whether the run contains such conditions. An example of such a plot can be seen in figure 3.13. During online running this information is also automatically checked by the DAQ software, but these plots provide an offline record.

3.2.4 Granularity in time

Within the `ATHENA` monitoring framework the default setting is to produce all the above distributions using data from the entire run, but it is also possible to make the distributions from limited time intervals. This is very important since detector problems commonly affect only parts of the run, either because they are temporary or fixed. The lowest possible interval for such distributions is 10 LBs intervals, which corresponds to at most ten minutes of data-taking. It is possible that this interval is smaller, since

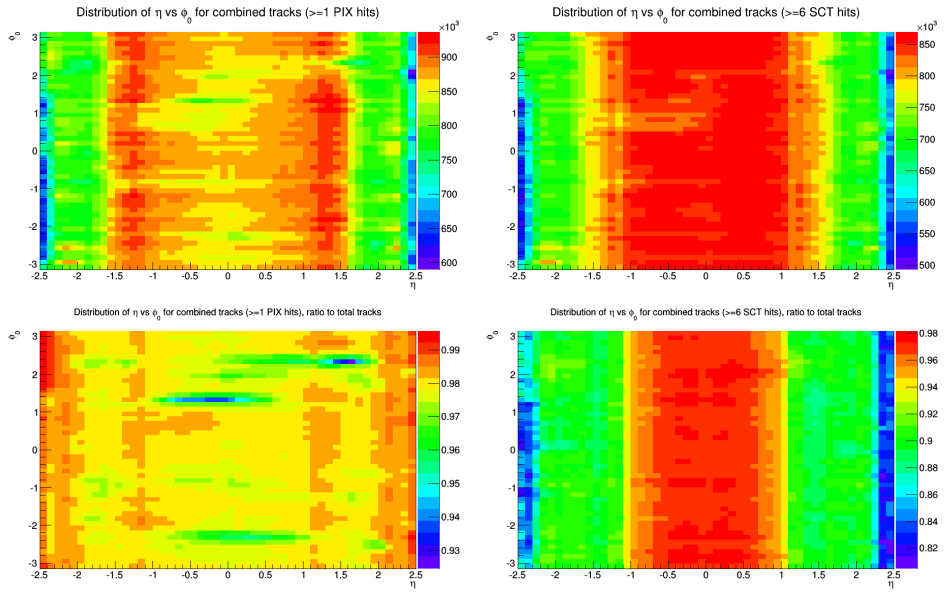

Figure 3.8: The distribution of tracks in η and ϕ. Shown here is the selection of at least one Pixel hit (left) and at least six SCT hits (right). At the top is the number of tracks passing these criteria and at the bottom the ratio of these tracks to the total number in each bin.

LBs switch when detector conditions change. It is also possible to produce distributions per LB, but this is avoided, due to the heavy impact on the size of the monitoring output as well as the limited statistics available in a single LB.

During online running a different approach is used, where histograms are built from data of the last ten LBs. This is a compromise between getting the statistics needed to get enough information about the detector condition and not losing out the current conditions due to the high number of previously accumulated events. This is a specially developed class that wraps the histogram classes and allows to make such histograms for arbitrary LB ranges, at the cost of higher memory usage and an extra delay at the beginning of each LB as the histogram is rebuilt from the buffers.

This splitting into different LB ranges is done for the tracking η-ϕ distributions as well as the number of hits per track. The data quality framework only provides 10 LB granularity, smaller intervals would result in very large storage requirements. However, the number of LBs rejected is usually reduced using feedback from the subdetectors where the extent of the problem in time can be identified.

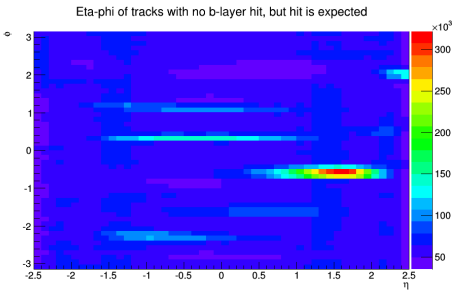

Figure 3.9: Number of tracks with a missing b-layer hit, when a hit is expected. If a module is disabled it does not show up. As a b-layer hit is a requirement for many algorithms used to reconstruct physics objects, this in an important check.

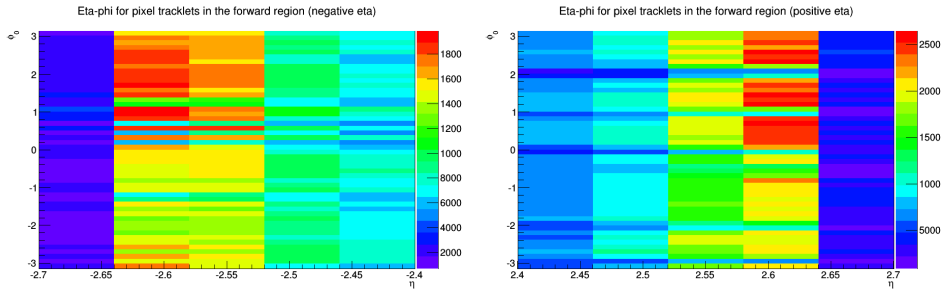

Figure 3.10: Distribution of forward Pixel tracks in η and ϕ, in the end cap side A on the left and end cap side C on the right.

3.3 Data Quality

The following defects are defined for the ID global monitoring, with further details given in the rest of the chapter:

ID_NOTRACKS **INTOLERABLE**
Significant loss of tracking coverage throughout or in a region of the ID.

ID_OUTOFTIMETRACKS **INTOLERABLE**
Fake tracks formed by out-of-time pileup hits in the SCT.

ID_TRACKBUG **INTOLERABLE**
Problem in the tracking caused by a software bug.

ID_VERTEXBUG **INTOLERABLE**
Problem in the vertexing caused by a software bug.

ID_BLAYER_EFFICIENCY **INTOLERABLE**
Tracking affected by low efficiency in the Pixel b-layer

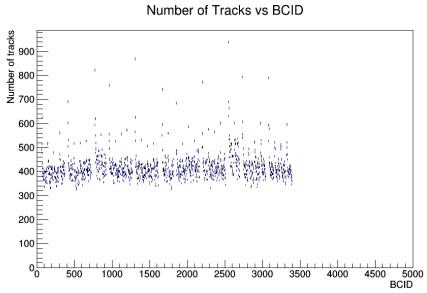

Figure 3.11: The average number of tracks per event by BCID number. This plot includes events from the entire run. These plots are also available showing the number of hits in each subdetector.

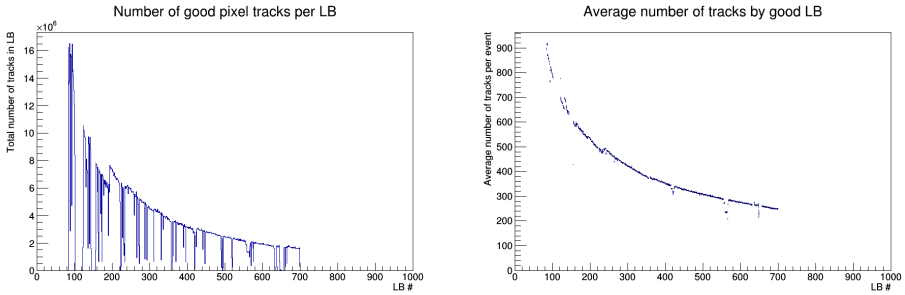

Figure 3.12: The figure on the left shows the number of tracks in each event satisfying various criteria by LB. The figure on the right shows the average number of tracks per event split by LB. The luminosity profile of the run can be seen in these plots as well as jumps arising from changing trigger conditions. Gaps arise due to times when the detector is busy and not taking data.

ID_PIXEL_TRACKCOVERAGE TOLERABLE
Small loss of tracking efficiency due to modules in the Pixel.

ID_SCT_TRACKCOVERAGE TOLERABLE
Small loss of tracking efficiency due to modules in the SCT.

ID_TRT_TRACKCOVERAGE TOLERABLE
Small loss of tracking efficiency due to modules in the TRT.

The defects in bold are those that are set as intolerable, meaning that LBs where these defects are set are not used in physics analyses. The other defects are there for book keeping and tracking abnormalities in the data that might prove to be a problem later on.

The combined output of the DQ assessment is the so-called Good Run List (GRL). This is a selection of LBs that are suitable for use by physics analyses, i.e. not containing any intolerable defects. As analyses can have

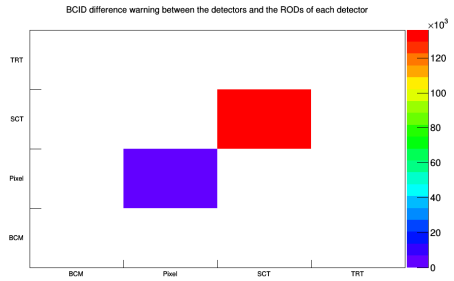

Figure 3.13: Synchronisation between the RODs in each detector. Each ROD in detector has a counter of which BCID it is looking at. Under certain conditions it is possible that a ROD fails to update this counter and therefore not in the same state as the rest, this is referred to as a desynchronisation. Each entry denotes desynchronisation in one event. Diagonal entries mean one of the the detector RODs is not synchronised with the rest, while off-diagonal entries mean that the RODs of two detectors are desynchronised, the figure showing desynchronisation of Pixel and SCT RODs.

different requirements from the detectors and physics objects it is possible to construct specific GRLs for each physics. In the 2010 and 2011 runs there were many GRLs produced, while in the 2012 run the different GRLs were collapsed into a common physics GRL.

The GRL is specific to each processing of the same data, as different kinds of defects can be expected to be fixed after a reprocessing of the data. After each reprocessing a new evaluation of the data is done in order to check for improvements or catch possible regressions.

In addition to the GRLs used by physics analyses a "tight" GRL is also defined, where even smaller defects are also excluded. This is done to provide a possible way for analyses to check if they are affected by smaller issues in DQ that were not foreseen to have an effect. Defects such as smaller differences in track coverage are found in this GRL, e.g. LBs marked with the ID_PIXEL_TRACKCOVERAGE detect are excluded from the tight GRL.

ROD busy issues

The cabling from the detector modules to the RODs is different between the ID subdetectors. This means that the effect of a problematic ROD on the tracking can vary depending on which detector it corresponds to.

For the Pixel detector the modules belonging to each ROD all belong to the same layer. A loss of one ROD will result in a number of tracks with a missing hit, but only in one layer. At the same time this also means that a possible loss of a b-layer ROD can cause significant disturbance by compromising accurate vertexing for the affected tracks.

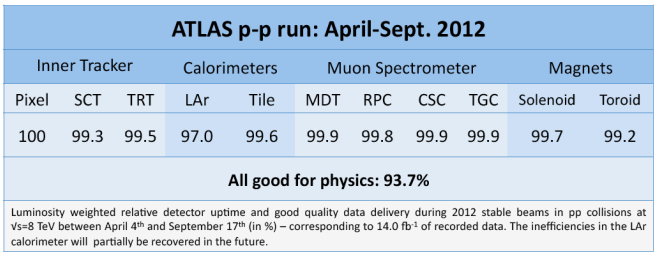

Figure 3.14: A summary of the performance of the ATLAS detector DQ throughout the 2012 LHC run. Shown is the percentage of integrated luminosity excluded from the GRL due to problems spotted by the DQ process of each subdetector.

In the SCT barrel the RODs are arranged in a radial layout, meaning that each ROD covers the same η-ϕ region across all the layers in the barrel. The result of this is that a ROD busy results in many modules along the track path being disabled. While the tracking can handle disabled modules along a track, the tracking will fail when such a high number of disabled modules is present.

Disabled modules

Typically, modules that are disabled will have little effect on the tracking, as the tracking algorithms take this into account. In cases where many such modules align however this can be problematic as the tracking needs a certain number of hits to be able to perform.

To establish this issue the η-ϕ map of tracks is used. In cases where such alignments take place it is possible to get a situation where tracks cannot be reconstructed at all, either due to track seeding being unable to construct seeds or the track fit failing due to a large number of disabled modules. This is identified as a region in η-ϕ where there is a significant deficiency of tracks compared to other regions. This is recorded as the `ID_NOTRACKS` defect.

In most cases however, the disabled modules are picked up by the tracking as dead modules without this having an effect on the number of reconstructed tracks. In this case the effects, if any, on the tracking are minor, as this is a design consideration for the tracking algorithms. In cases where this amounts to more than 10% of tracks missing this is recorded as the `ID_PIXEL_TRACKCOVERAGE`, `ID_SCT_TRACKCOVERAGE` and `ID_TRT_TRACKCOVERAGE` defects; depending on which subsystem is responsible for the performance degradation.

One important aspect of this is the need to be able to decide during data-taking in P1 whether detector conditions can cause a problem and therefore the run should be stopped to fix problems in the run. This function will be served by the disabled and error module maps.

B-layer issues

Issues arising in the Pixel b-layer have strong implications for the reconstruction and identification of many physics objects. Many algorithms rely on the presence of b-layer hits, when one is expected, to reject fake objects. This is particularly true for the b-tagging and electron identification. The primary responsibility for assessing the impact of such effects on DQ lies with dedicated groups and monitoring tools for each reconstruction object.

However, it is possible that inefficiencies in the b-layer to overlap with other inefficiencies in the sub-detector causing problem to the tracking. This is checked by comparing the $\eta - \phi$ distributions of tracks to the $\eta - \phi$ distribution of tracks lacking b-layer hits, to see if regions of problematic b-layer modules are potentially causing losses in the tracking.

A more severe issue is whether there are losses due to inefficient b-layer modules that are not masked (potentially leading to efficiency loss in other CP groups). A b-layer hit is required in order to reject possible fake objects. This was unfortunately not spotted in the 2012 run, but steps have been taken to cover such cases.

Software issues

Defects related to software issues are also taken out in the GRL, though these can be corrected in reprocessings. These issues are rooted in bugs in the vertexing and tracking and can cause large scale problems for physics analysis. However only a small fraction of the data collected are affected by such issues. These issues are tracked using the `ID_TRACKBUG` or `ID_VERTEXBUG`.

Beamspot issues

Defects related to beamspot determination are also taken out from the GRL as they have a significant effect on the reconstruction of other physics objects. This is mostly affecting LBs where there is a smaller number of vertices due to low luminosity or large movements in the beamspot due to Van de Meer scans for example. Typically such data is not suitable for physics analysis and therefore excluded.

Calibration and timing

Additionally, there are cases where the calibration of TRT is problematic, meaning that no hits get associated to the track.

For earlier runs when the bunch spacing was first reduced to 50 ns the hits in the detector can also come from earlier bunch crossings. The results in reconstructed tracks that are fake, forming from hits that do not belong to the same collision. Such occurrences are tracked using the `ID_OUTOFTIMETRACKS` defect. The issue itself is fixed by tightening the timing selection for hits

used in track reconstruction. As this issue can be fixed by changing the settings of track reconstruction this issue is fixed after a reprocessing.

3.3.1 Performance during the 2011 and 2010 runs

The amount of data lost during 2012 due to problems spotted by the ID monitoring is summarised in table 3.14. The primary reason for lost data is the SCT RODs going busy which result in certain LB where tracking is severely affected in certain regions. These losses occur in the barrel where due to the detector readout geometry a ROD corresponds to a roughly rectangular sector in η-ϕ coordinates across all layers of the SCT.

A summary of data that was rejected from the GRL due to defects related to the tracking can be found in table 3.1 showing the percentage of luminosity lost in each data period for the 2011 and 2012 p-p collision runs as well as the 2011 Pb-Pb run and 2013 p-Pb run.

3.4 Conclusions and outlook

The monitoring ran successfully throughout the first LHC run and was able to spot problems as they arose and monitoring the development of others. It was important both during the start of running, with focus on detector performance and feedback, as well as during the later part of the run, moving focus to combined performance effects.

It provides an interface between the ID detectors and the Combined Performance (CP) groups as well as combined performance during the early stages of the LHC run.

In online monitoring the main limiting factor for discovering problems in the tracking was the statistics collected, as the monitoring samples only a fraction of recorded events. Additionally, a larger number of machines is foreseen to be used in the next run, as well as improvements in the tracking CPU time use should improve on the monitoring rate.

Additionally, the monitoring needs to have as up-to-date information on the detector conditions as possible. To this end a solution was found by sourcing the information about module status and errors directly from `ATHENA` which limits the statistics needed since we are not relying on reconstructed tracks. This is in the form of the η-ϕ disabled and error module maps.

With respect to DQ the ID monitoring package was part of the DQ assessment for the ID. This meant the weekly review of the runs as well as assessment after data reprocessing campaigns. This means both initial assessment of collected data, re-assessment of the bulk processing and follow-up of potential problems.

Preparations for the start of the LHC Run-II in 2015 have started, with the ID monitoring already fully integrated and ready for data taking in

Year	Period	Good data [%]	Year	Period	Good data [%]
	A	98.4			
	B	98.1		B	95.4
	C	92.0			
	D	98.6		D	99.4
	E	96.4		E	100.0
2012			**2011**	F	98.7
8 TeV	G	99.1	**7 TeV**	G	99.1
	H	99.5		H	98.4
	I	97.9		I	99.9
	J	97.1		J	100.0
				K	99.8
	L	96.9		L	95.8
				M	98.4
Overall		**98.1**	**Overall**		**97.5**
	A1	100.0		N	98.5
	A2	99.0			
	A3	97.8			
2013	A4	96.0	**2011**		
p-Pb	B1	100.0	**Pb-Pb**		
	B2	100.0			
	B3	78.3			
	B4	98.9			
Overall		**98.0**	**Overall**		**98.5**

Table 3.1: Summary of data lost due to defects in the data ralated to tracking and the ID detectors in the 7 TeV run and 8 TeV run. Missing entries correspond to periods in each year that do not contain physics data and therefore not taken into account for DQ assessment.

the next run as well as cosmic data taking during detector commissioning. Testing as part of the ATLAS readiness milestones has also begun. This includes updates to the new version of the software packages for the new ATLAS release and updates to take into account the experiences of the past year.

Chapter 4

Minimum bias physics

Minimum bias physics deals with soft QCD events that result from the dominant part of the proton-proton cross-section. These events have very high cross-section but cannot be described by perturbative QCD. These soft interactions are of four different kinds; elastic, single diffractive, double diffractive and inelastic. The total cross-section, σ_{mb} is the sum of these contributions:

$$\sigma_{\text{mb}} = \sigma_{\text{elastic}} + \sigma_{\text{sd}} + \sigma_{\text{dd}} + \sigma_{\text{inelastic}} \tag{4.1}$$

The elastic cross-section covers processes where the protons do not break up in their interaction. The diffractive components cover processes where either one (single) or both (double) protons are scattered into a low-mass state. The defining characteristic of the diffractive component is a large separation between the resulting outgoing particles, particularly in η. Finally, the inelastic component contains events where both protons break up and interactions between coloured particles take place. For the diffractive and elastic components a large number of events are not recorded as they fall outside the acceptance of the detector, in order to correct for this model-dependent assumptions about the kinematics of these events are needed.

This is the total cross-section, but for the measurement in an experiment these cross-sections must also include a correction for the acceptance of the detector itself, since at least some particles must be present in the event to be able to trigger the detector. As, by definition, the minimum bias events are those that trigger the detector and are recorded the events are defined with respect to the detector recording them.

The ATLAS minimum bias analysis [22] relies on particle level observables alone and making no attempt to remove any of these components, resulting in a mixture of these different contributions within the sample. At the same time a large fraction of the diffractive components is not seen in the detector as no observable particles are produced. As the distributions are not corrected for these effects the resulting distributions can be reproduced

by theorists using the efficiencies of the trigger and tracking as inputs. New tunes of MC software can then be compared against the distributions of the analysis.

This results in the most useful information for tuning MC and as input to theory, but is not as useful for making comparisons to other experiments which produce distributions with full corrections for the missing components.

The observables from minimum bias analyses carry large importance in the field of MC tuning. In addition, minimum bias events are very similar to pileup events in the high luminosity LHC conditions. For this reason understanding such events is important for all other ATLAS analyses. Due to the soft nature of these QCD events is also not possible to describe them by perturbation theory, requiring phenomenological approximations which are parametrised in the Monte Carlo (MC) generators. Measurements of the properties of such events are therefore important for producing the best possible tuning of these free parameters at the LHC energy scale.

The distributions considered in this analysis are the track multiplicity

$$\frac{1}{N_{\mathrm{ev}}} \cdot \frac{dN_{\mathrm{ev}}}{dnch},$$

the track p_{T} spectrum

$$\frac{1}{N_{\mathrm{ev}}} \cdot \frac{1}{2\pi p_{\mathrm{T}}} \cdot \frac{d^2 N_{\mathrm{ch}}}{d\eta dp_{\mathrm{T}}},$$

the track eta distribution

$$\frac{1}{N_{\mathrm{ev}}} \cdot \frac{dN_{\mathrm{ev}}}{d\eta}$$

and the mean p_{T} of tracks in each event versus the track multiplicity ($< p_{\mathrm{T}} >$ vs n_{ch}). N_{ev} refers to the total number of events accepted by the analysis and n_{ch} is the number of charged particles in each event. Only primary charged particles are considered, i.e. particles originating from the primary vertex.

4.1 Cross check analysis

For the minimum bias analysis a full cross check analysis was done alongside the main analysis. Here we refer to the nominal analysis as Analysis-I and the cross-check as Analysis-II. The cross-check analysis uses the same inputs as the main analysis but is done with independently developed code and procedures. The goal is to check the validity of the selection, corrections and systematic error determination for the most inclusive phase space considered in the paper, see section 4.1.1 for the definition.

The data considered in the analysis consists of six early 7 TeV runs[1]. In addition to this run selection additional selection criteria are used to ensure the good quality of data used in the analysis:

[1] 152166, 152214, 152221, 152345, 152409, 152441, 152508

- Good DQ for all ID detectors and successful beamspot determination
- `L1_MBTS_1` trigger fired
- At least one vertex with at least two **selected** tracks, see section 4.1.1.
- Pileup suppression, no additional primary vertices with four or more tracks.

The `L1_MBTS_1` trigger uses the MBTS, two plastic scintillator end-caps placed on each side of the LAr barrel, see section 2.4. It requires at least one hit on either side of the detector. This gives minimal requirements on the activity in the detector for selected events. The other selections ensure that an interaction took place in the event and suppress events with substantial pileup vertex contributions. The number of events accepted after each of these selections is shown in table 4.1.

4.1.1 Phase space

The primary phase space of the analysis, namely the $n_{\text{sel}} \geq 2$, $p_{\text{T}} \geq 100\,\text{MeV}$ and $|\eta| \leq 2.5$ phase space was fully cross checked. The following track selection criteria apply, where the selection used in the primary phase space is highlighted:

- $p_{\text{T}} > 100\,\text{MeV}$
- b-layer hit, if active sensor crossed
- At least one hit in the Pixel detector
- At least **2**, 4, 6 SCT hits for the $p_{\text{T}} >$ **100**, 200 and 300 MeV phase spaces respectively
- $|d_0| < 1.5\,\text{mm}$
- $|z_0 \sin\theta| < 1.5\,\text{mm}$
- χ^2 fit probability > 0.01 for tracks with $p_{\text{T}} > 10\,\text{GeV}$

These cuts ensure that primary tracks are selected, rejecting secondary tracks and fake tracks arising from random hit combinatorics. The p_{T} requirement splits the analysis into multiple phase spaces, the cross-check analysis is applied to the most inclusive phase-space, $p_{\text{T}} > 100\,\text{MeV}$. The last cut is done in order to reject tracks with spurious transverse momentum measurement, an effect of the large extrapolation distance between the Pixel and SCT endcaps. The number of tracks selected after these criteria is denoted n_{sel}. For certain studies an alternative selection is used, including all the above criteria except the requirements on d_0 and z_0. Instead, the transverse

distance of the track to the beamspot at the point of closest approach is used and the selection is $|d_0^{\mathrm{BS}}| < 1.8\,\mathrm{mm}$. The number of tracks passing this set of requirements is referred to as $n_{\mathrm{sel}}^{\mathrm{BS}}$. The uncorrected distributions for η, p_{T} and n_{ch}, after this selection are shown in figure 4.1, which are in perfect agreement between the two analyses. The number of tracks kept after these selections can be found in table 4.1.

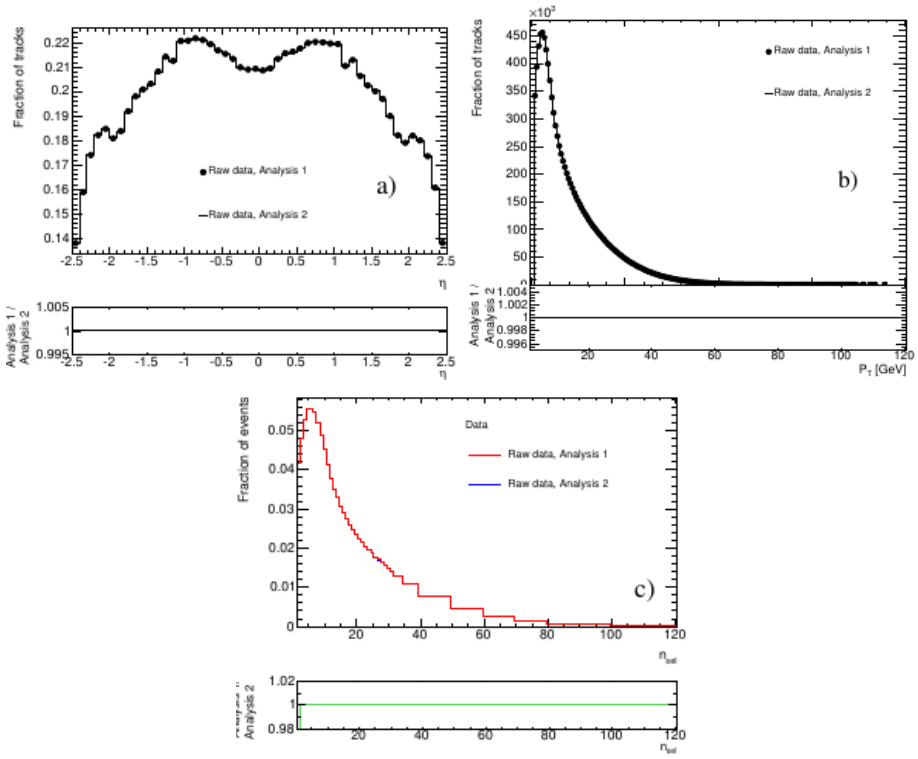

Figure 4.1: The raw distributions of η (a), p_{T} (b) and n_{ch} (c). At this level the two analyses are in perfect agreement.

4.2 Corrections to particle level

At this stage the tracks are selected and the distributions can be made. However, these are not the "true" distributions, rather they are convoluted with detector efficiency and detector effects on observables. These uncorrected distributions are referred to as raw or track level distributions. The distributions after correcting for detector effects are referred to as particle level distributions. Such deconvolution is very important to allow comparison with generator outputs and results from other experiments.

	Run number						
Selection	**152166**	**152214**	**152221**	**152345**	**152409**	**152441**	**152508**
Total events	675766	344531	1487570	1421215	5589888	4902686	1096648
Data quality	514612	250450	1442202	1088865	4733210	4484642	334055
Trigger	437273	212751	1242202	958609	4171423	3978804	295432
Vertexing	389466	188873	1122051	862073	3736987	3576501	264862
Track selection	386669	187438	1113639	855910	3708987	3550540	262889
Total tracks	17508795	8465356	50360637	38830614	168141336	160908202	11902114
Selected tracks	8072503	3899575	23218783	17870135	77243070	74023616	5481758

Table 4.1: The number of events selected after each selection step as well as the number of selected tracks. The numbers are broken down by run number. The same number of events and tracks are accepted by both Analysis-I and Analysis-II.

The corrections applied per-event can be calculated as:

$$w_{\text{ev}}(n_{\text{BS}}^{\text{sel}}) = \frac{1}{\epsilon^{\text{vertexing}}(n_{\text{BS}}^{\text{sel}}) \cdot \epsilon^{\text{trigger}}(n_{\text{BS}}^{\text{sel}})} \tag{4.2}$$

The terms in the denominator account for inefficiencies in the trigger ($\epsilon^{\text{trigger}}$) and vertexing ($\epsilon^{\text{vertexing}}$). These are taken from studies done for the analysis and are used in both Analysis-I and Analysis-II.

The trigger efficiency is determined using a control trigger, which is a random filled bunch trigger at L1, see section 2.7, and a requirement of four hits in the Pixel and SCT detectors. This provides a looser sample with which to gauge the trigger efficiency.

The vertexing efficiency is measured by looking at the ratio of triggered events with a vertex to the total number of triggered events. For this to work it is important to remove the contribution of beam background events, which would skew the efficiency calculation. Additionally, in the case of $n_{\text{sel}}^{\text{BS}} = 2$ an additional correction is applied based on Δz_0^{BS}, the longitudinal separation of the track perigees. The distribution used for the correction is shown in figure 4.2.

Trigger and vertexing corrections are applied as an event wide weight, and the efficiencies are plotted in figure 4.3 as a function of the number of selected tracks.

The tracking efficiency correction is applied per track as a function of p_{T} and η, as shown in figure 4.4. The weight applied for each track can be expressed as:

$$w_{\text{trk}}(p_{\text{T}}, \eta) = \frac{(1 - f^{\text{nonpri}}(p_{\text{T}}))(1 - f^{\text{okr}}(p_{\text{T}}, \eta))}{\epsilon^{\text{tracking}}(p_{\text{T}}, \eta)} \tag{4.3}$$

The factors in the numerator correct for contamination from non-primary tracks (f^{nonpri}) and tracks that are outside the kinematic range of the analysis (f^{okr}), while in the denominator is the tracking efficiency ($\epsilon^{\text{tracking}}$).

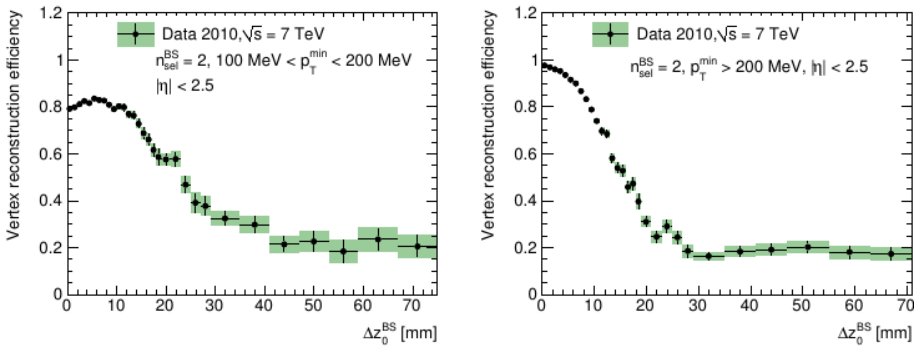

Figure 4.2: The vertex reconstruction efficiency as a function of Δz_0^{BS} for events with $n_{\mathrm{sel}}^{\mathrm{BS}} = 2$. Two cases are considered based on the lowest track p_{T} in the event; events with $p_{\mathrm{T}}^{\mathrm{min}} \leq 200\,\mathrm{MeV}$ (left) and $p_{\mathrm{T}}^{\mathrm{min}} > 200\,\mathrm{MeV}$ (right).

The tracking efficiency is estimated from MC, by checking the reconstruction efficiency of charged particles in bins of p_{T} and η. As the tracking efficiency is determined using MC, excellent agreement between the data and MC simulation is needed to obtain valid results. Some examples of the level of agreement can be found in figures 4.5 and 4.6, showing the high degree of accuracy of the MC simulation across the full pseudorapidity and transverse momentum range considered in the analysis. The procedure for matching reconstructed tracks to truth tracks is to give a match if the true and reconstructed tracks are found within $\Delta R < 0.15$ and the two share at least one Pixel hit. For the tracking efficiency the dependence on two different estimates of the material distribution uncertainty is also shown in figure 4.4. The tracking efficiency correction accounts also for non-primary tracks as well as tracks falling outside the kinematic range of the analysis.

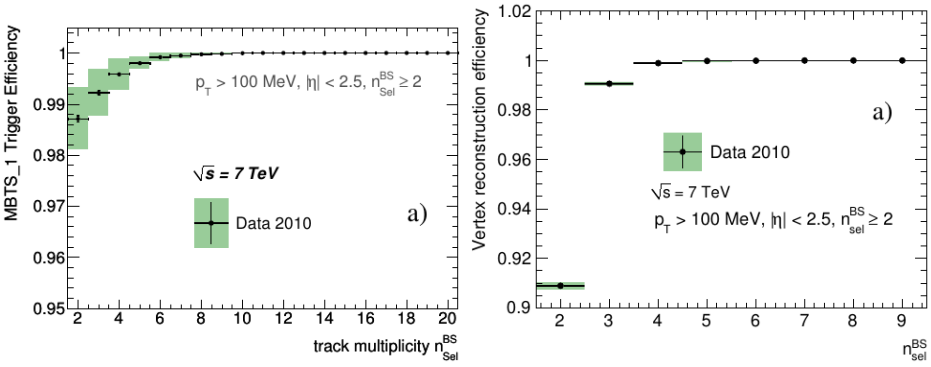

Figure 4.3: A plot of the trigger (left) and vertexing (right) efficiency as a function of the number of selected tracks ($n_{\mathrm{sel}}^{\mathrm{BS}}$). This efficiency is used in both analysis-I and analysis-II as an input for the trigger and vertexing corrections.

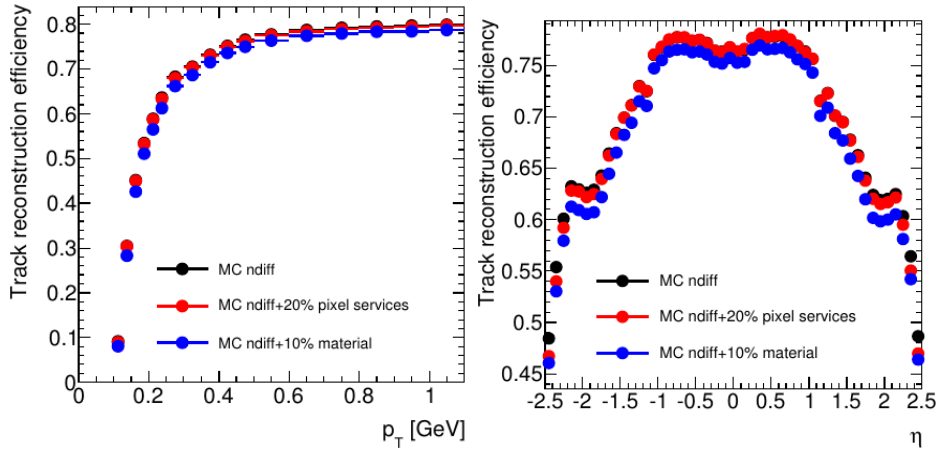

Figure 4.4: A plot of the tracking efficiency as a function of p_{T} (left) and η (right). Additionally, the effect of two material uncertainties are shown for comparison to the nominal distribution, a 10% increase in the material budget and a 20% increase in the Pixel service budget.

4.3 Bayesian unfolding

All the correction procedures used so far rely on weights. In this sense only the relative weights of each bin in the histogram are altered and migration from one bin to another is not handled. In the final step of the correction an unfolding procedure is used, where such bin migrations are properly taken into account. The procedure used in the paper is the so-called Iterative Bayesian Unfolding [23].

The starting point of the procedure is the migration matrix, which describes the probability of a given observed state to be produced from each true state. Using this matrix as a starting point together with Bayes' theorem, it is possible to produce an unfolding matrix, which can revert the observed distribution back to particle level. As this is a Bayesian method, there is a prior involved, in the form of a best guess of the true distribution of the data.

In order to get past this unwanted dependence on a prior, the procedure is modified to be iterative. With each iteration the effects of the choice of prior become less important. The iterations repeat until some termination condition is met, typically a test on the amount of change due to the unfolding. In the case of this analysis the chosen test was that the χ^2 difference between the distributions produced by successive unfolding iterations should be smaller than the number of bins in the unfolding.

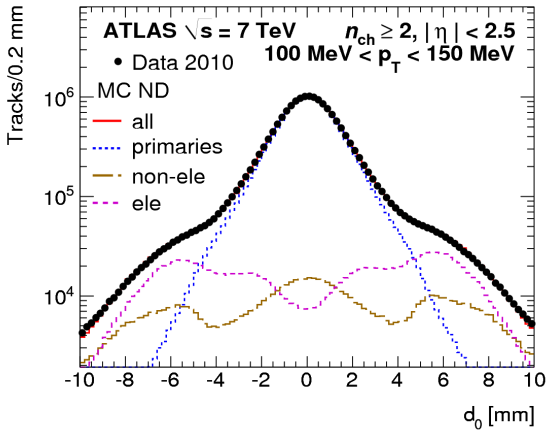

Figure 4.5: A view of the track d_0 distribution, along with the contributions from different sources, taken from MC. The contributions are split up into primary particles (dashed blue) and non-primary particles, electrons (brown dashed) and non-electrons (pink dashed). Excellent agreement between the data and MC simulation is found as well as good understanding of the components of the distribution.

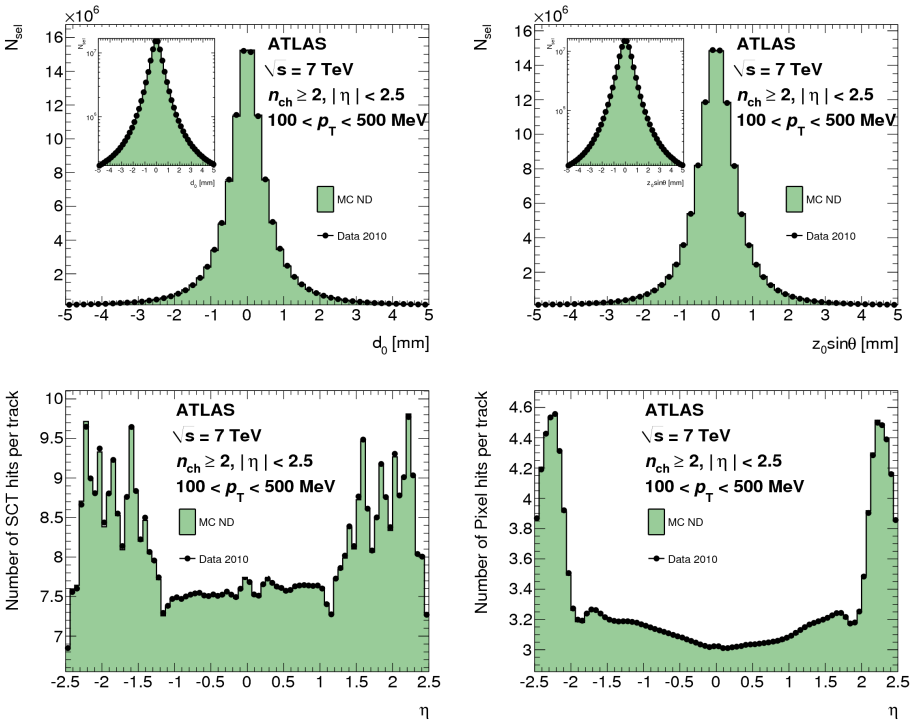

Figure 4.6: Comparison of the data and MC for d_0, z_0 and the number of Pixel and SCT hits; showing very good agreement between data and MC.

4.3.1 n_{ch} unfolding

The unfolding procedure is applied to the n_{ch} spectrum to account for migration between different n_{ch} bins due to the tracking efficiency. This allows to correctly take into account tracks that were missed in reconstruction. The migration matrix is populated by minimum bias MC samples. An efficiency correction is applied to the n_{ch} distribution at the end of the unfolding procedure to account for the fact that events with $n_{\mathrm{sel}} < 2$ fall outside the analysis phase space and therefore cannot be accounted for by the unfolding procedure. This correction,$w_{0/1\mathrm{bin}}$, is the probability of losing all or all-but-one tracks in the event due to tracking inefficiency.

$$w_{0/1\mathrm{bin}} = \frac{1}{1-(1-\epsilon_{\mathrm{trk}})^{n_{\mathrm{sel}}} - n_{\mathrm{sel}}\epsilon_{\mathrm{trk}}(1-\epsilon_{\mathrm{trk}})^{n_{\mathrm{sel}}-1}} \tag{4.4}$$

4.3.2 Transverse momentum unfolding

For the transverse momentum of the tracks a Bayesian unfolding procedure was used, correcting the momentum of the tracks back to particle-level. The procedure uses the migration matrix to migrate entries from their respective bins to the particle-level spectrum. The matrix is populated by minimum bias MC samples as well as single particle MC samples with high p_{T} particles, in order to populate the high-p_{T} bins. The migration matrix used in the procedure is the same that is used by Analysis-I for the final result, though the determination of the matrix is also cross-checked. See figure 4.7 for a visualisation of the matrix contents.

An initial "guess" of the spectrum is neededd and for this the spectrum from a minimum bias `Pythia` MC sample is used. In order to preserve the total number of tracks after unfolding the distribution each column of the unfolding matrix is normalised before the unfolding step.

In order to assess the effect of the prior distribution and correct for any bias this may introduce, the unfolding procedure is repeated with a flat prior distribution. This check results in a 2% uncertainty.

4.4 Cross check results

A comparison of the n_{ch}, p_{T}, η and $< p_{\mathrm{T}} >$ distributions coming from Analysis-II and Analysis-I is shown in figures 4.8. Good agreement is found between the two analyses, with agreement within 0.001% level for the n_{ch} distribution and better than 0.5% across most bins in the other distributions. In all distributions the unfolding procedure was also explicitly checked and found to be in agreement between the two analyses. This level of agreement was found to be satisfactory to rule out any possible issues in the analysis and the complex correction procedures used.

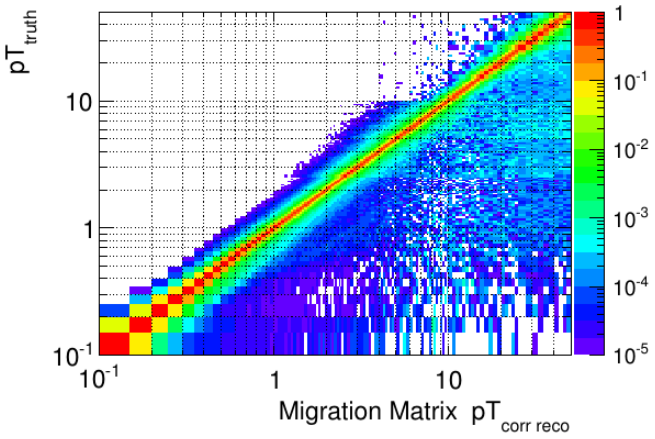

Figure 4.7: A plot of the migration matrix used for the iterative unfolding of the p_{T} spectrum. The reconstructed p_{T} after all corrections is plotted on the x-axis and the true p_{T} on the y-axis.

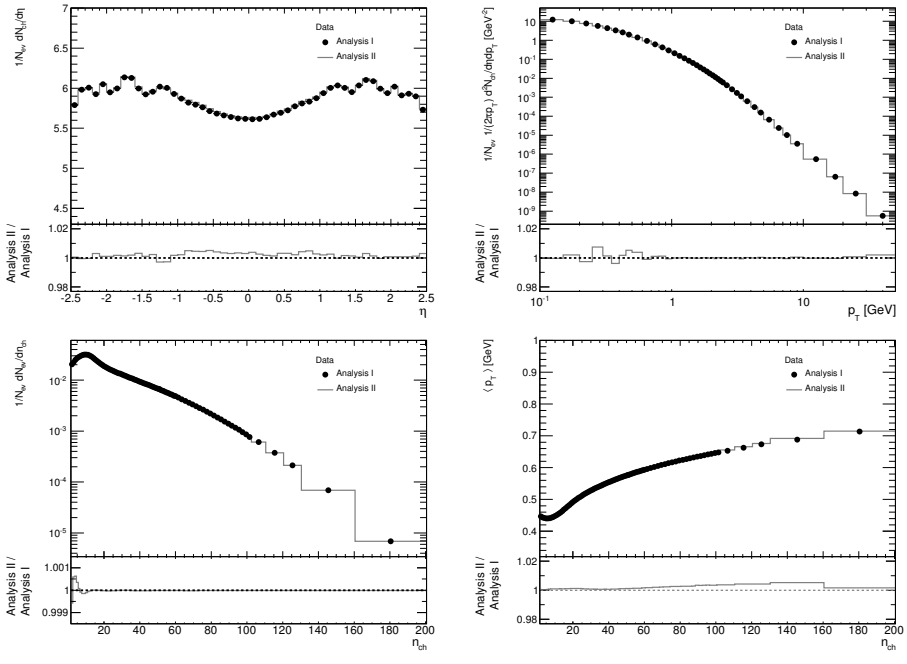

Figure 4.8: Comparison of the distributions produced by Analysis-I and Analysis-II, with a ratio of the two in the lower part. Good agreement is found between the two analyses, in all cases disagreements are below 0.5%.

4.5 Systematic uncertainties

The effect of the dominant systematic uncertainties is also checked in Analysis-II. The estimated systematic uncertainties for Analysis-I and Analysis-II are plotted in figure 4.9 and the good agreement between the two is shown.

4.5.1 Systematic Uncertainties on the n_{ch} distribution

The systematic uncertainties checked on the n_{ch} distribution are the tracking efficiency and detector material uncertainty. Both systematic uncertainties are taken as inputs from dedicated tracking studies and used directly. The exact same distributions are also used by the primary analysis. The systematic uncertainties evaluation is done using a toy MC to remove tracks from the distribution to simulate the tracking efficiency when systematic effects are taken into account. The resulting distribution from this procedure is then put through the unfolding to produce a new distribution, the difference to the nominal distribution is taken as a systematic uncertainty. For the total number of events N_{ev} the same systematic uncertainties are checked, but the only contribution comes from events that might leave the analysis phase space due to systematic variations. The total effect on N_{ev} is at 0.3%.

4.5.2 p_{T} systematic uncertainties

For the p_{T} distribution, the effect of the mis-measurement of track p_{T} is checked. This applies to tracks with $p_{\mathrm{T}} \geq 10\,\mathrm{GeV}$. The estimation is performed by scaling the number of mis-measured tracks in MC to match the number found in data, which is known to be higher. The resulting distribution is then put through the unfolding procedure and the difference found to the nominal distribution is evaluated as a systematic uncertainty. The results are found to be compatible between the two analyses.

Additionally, the effect of the p_{T} resolution systematic is evaluated by introducing a Gaussian smearing to the track p_{T} in MC and taking this modified distribution through the unfolding procedure. Any differences to the final distribution are taken as a systematic uncertainty.

For the two unfolding procedures there is an additional systematic uncertainty related to the amount of non-closure observed, i.e. the disagreement between the true MC spectrum and the unfolded result of the observed p_{T} spectrum. The difference is used as a systematic uncertainty. One possible cause of the observed non-closure is that the unfolding of n_{ch} and p_{T} distributions is done separately, not taking into account correlations between the two.

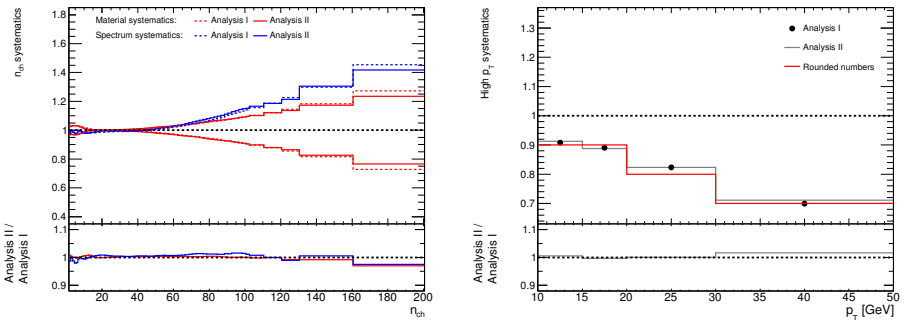

Figure 4.9: Comparison of the systematic uncertainties as estimated by Analysis-I and Analysis-II. Shown are the track multiplicity systematic uncertainties (left) and track p_{T} systematic uncertainties (right). The errors in the two analyses agree to better than 5%.

4.6 Results

Based on the results of the analysis a new tune was produced for `Pythia` 6, named the AMBTS1 tune [24]. This is a best fit of the `Pythia` 6 soft QCD parameters to the ATLAS data. The final results of the analysis can be found in figure 4.10, showing the distributions as well as a comparison to various generators and tunes, to check how they perform. In particular the AMBTS1 tune is also shown.

4.7 Minimum bias energy evolution

At the time of the minimum bias analysis the LHC had runs at CoM energies of 900 GeV, 2.36 TeV and 7 TeV. By analysing data at each of these energies it is possible to determine the evolution of Minimum Bias physics as a function of CoM energy. The evolution of the track multiplicity per unit η is shown in figure 4.11 for the central region, $\eta = 0$. The ATLAS AMBT1 tune is successful in describing the looser $p_{\mathrm{T}} > 500\,\mathrm{MeV}$ phase spaces, but cannot adequately describe the evolution for the most inclusive $p_{\mathrm{T}} > 100\,\mathrm{MeV}$ phase space. The looser phase spaces are adequately described by most considered tunes, though Phojet [25] and the `Pythia` 6 DW tune perform considerably worse, as shown in figure 4.11.

4.8 Conclusions

For the primary phase-space of the 7 TeV minimum bias analysis a full cross-check of the analysis procedure was carried out, showing very good agreement with the results produced by the primary analysis. This covered both the in-

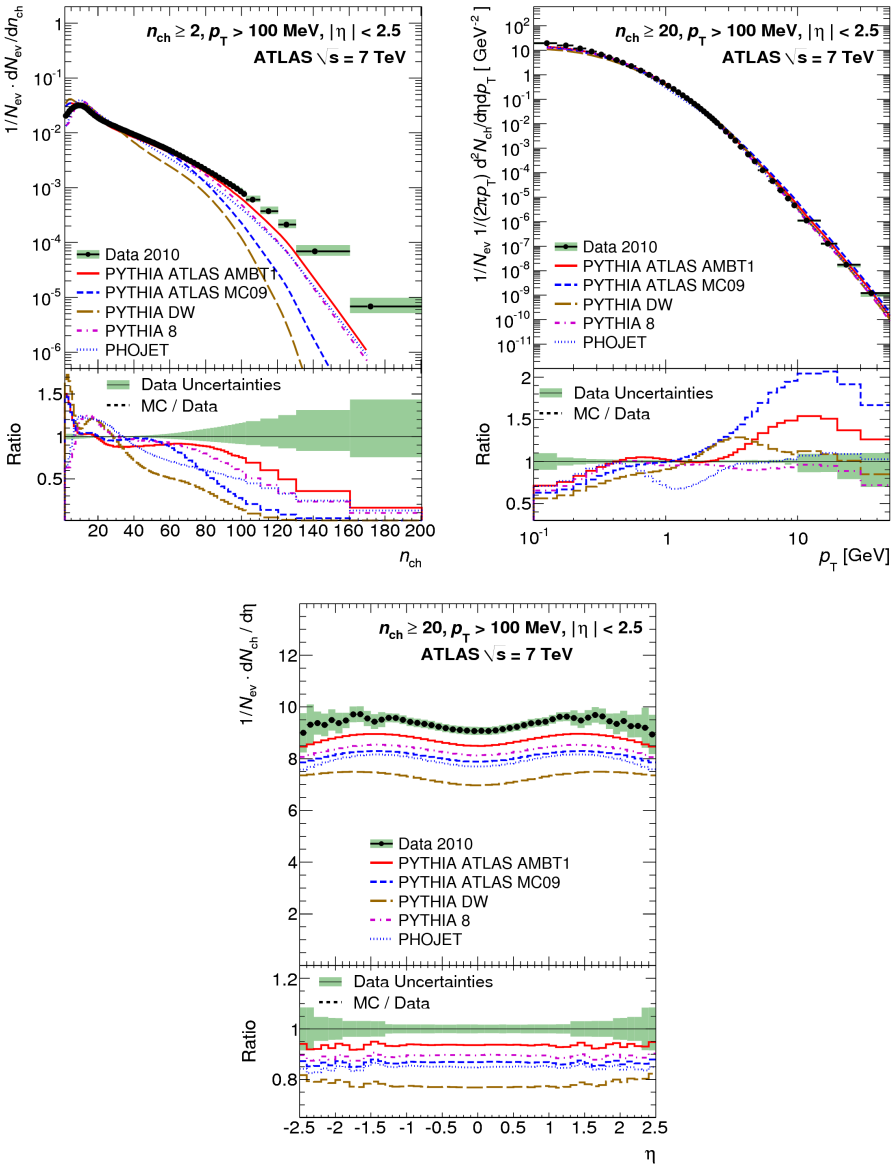

Figure 4.10: The final distributions produced by the analysis at particle level. Shown are the distributions along with the total error on the distribution. For comparison, also shown are the distributions that are predicted by various generators and generator tunes.

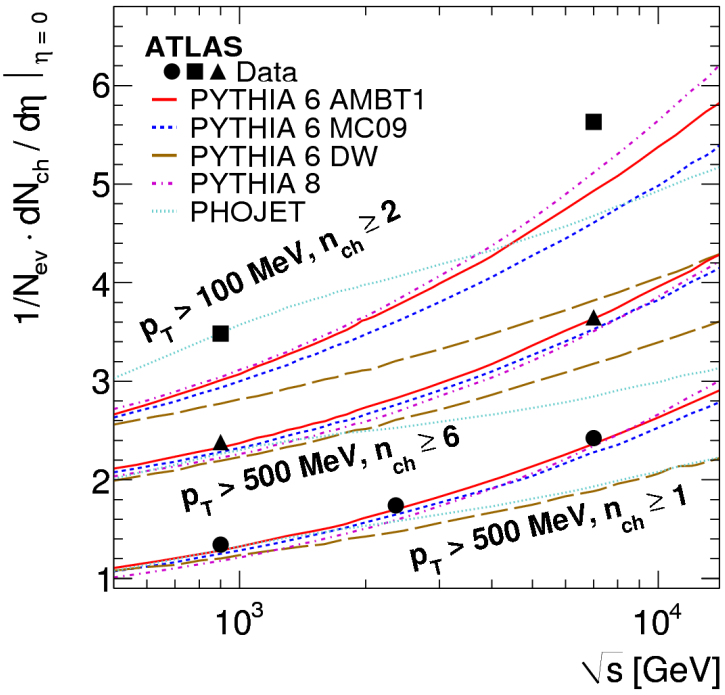

Figure 4.11: Evolution of the average number of tracks per unit pseudorapidity across different CoM energies. Shown here is the distribution at $\eta = 0$ for different phase spaces. Results from different generators and tunes are shown for comparison.

put and basic selection as well as corrections and determination of systematic uncertainties.

Chapter 5

Supersymmetry

5.1 Motivation

SUSY is an additional symmetry imposed on top of the SM, which helps avoid various problems present in the model [26]. It provides a solution to the hierarchy problem [27], the problem of Dark Matter (DM) in certain models [28, 29] as well as a way for the gauge couplings to unite [30]. The theory also features rich phenomenology at the center of mass energy of the LHC.

Due to these attractive features of the theory there is a large effort to find evidence in support of SUSY or to exclude parts of its parameter space using LHC data. One such ATLAS analysis is presented here. In many SUSY models taus are of particular interest as a signature. At the energy scale of the LHC, the production of taus can be significantly boosted with respect to the lighter lepton generations. Analyses targeting final states with taus provide an opportunity to look into such parts of the parameter space specifically. The tau based analysis presented here is interpreted in the context of the Gauge Mediated Symmetry Breaking (GMSB) model in particular, where such regions of parameter space are present.

5.2 SUSY models

The minimal model of SUSY with the most general parametrisation of symmetry breaking is the Minimal Supersymmetric Standard Model (MSSM). The model is minimal in the sense that there is only one set of superpartners for the SM particles. While SUSY in itself does only add few parameters to the SM, the symmetry breaking mechanism is not constrained. Including all possible breaking mechanisms in the model leads to 120 free parameters, making it unwieldy for experimental studies and phenomenology. To create more manageable models the symmetry breaking is constrained to one mechanism and some assumptions are made about the physics at the symmetry

Table 5.1: The parameters ranges of the GMSB grid studied in the analysis.

Parameter	Λ	$\tan\beta$	M_{mess}	N_5	c_{grav}	$\text{sgn}\,\mu$
Value	10 - 80 GeV	2 - 50	250 GeV	3	1	+

breaking scale, e.g. assumptions about the masses of sparticles.

One such model, investigated in the context of this analysis, is the GMSB model [31, 32, 33, 34, 35, 36]. The choice of symmetry breaking mechanism, as implied by the name, is gauge mediation and the Lightest Supersymmetric Particle (LSP) in this model is the gravitino ($\tilde{\text{G}}$). In gauge mediation it is assumed that symmetry breaking occurs in a hidden sector, i.e. through particles not interacting with the SM particles, and the symmetry breaking is communicated to the MSSM sparticles via gauge interactions at loop level. The parameter space consists of six free parameters:

M_{mess}: the mass of the messenger field that mediates symmetry breaking,

Λ: the effective scale at which symmetry breaking occurs,

N_5: the number of SU(5) multiplets involved in symmetry breaking,

c_{grav}: the coupling to gravity, which influences the mass of the gravitino,

$\tan\beta$: the ratio between the Vacuum Expectation Values (VEVs) of the two Higgs doublets and

$\text{sgn}\,\mu$: the sign of the Higgsino mass parameter, μ.

The first four of these parameters deal with the symmetry breaking mechanism and the last two are for the Higgs sector. The parameter Λ gives the overall mass scale of sparticles. The N_5 parameter affects the masses of the sparticles, with gauginos scaling linearly and scalars scaling as $\sqrt{N_5}$. Of particular importance is the $\tan\beta$ parameter, influencing which sparticle is the Next-to-Lightest Supersymmetric Particle (NLSP). Three NLSPs are possible in the parameter space looked at by the analysis; the lighter stau, the right-handed sleptons or all three being degenerate in mass. In the last case they all effectively act as NLSP; this is referred to as the coNLSP region. As it looks at final states with taus, this analysis is most sensitive in the stau region. A further region is present, for low Λ, where the lightest neutralino is the NLSP; however this region is already excluded by OPAL [37].

The parameter ranges for the GMSB grid used in this study are motivated by a study of the ATLAS discovery potential for the GMSB model [38] and can be found in table 5.1.

The splitting of masses between the up and down type quarks is driven by the $\tan\beta$ parameter, regardless of the specific model discussed. This

splitting is driven by electroweak symmetry breaking and is often called the "hyperfine" splitting. At large values of $\tan\beta$ the lightest stau mass is significantly pushed down. In the case of third generation squarks and sleptons the left- and right-handed helicity states are mixed, with larger values of $\tan\beta$ leading to stronger mixing between them. A typical mass spectrum of supersymmetric particles is shown in figure 5.2.

A very common symmetry added in addition to SUSY is R-parity. This is an additional discrete symmetry, conceptually similar to parity, that is even for SM particles and odd for SUSY particles. This results in sparticles always being produced in pairs, as well as requiring that a sparticle always decays to other sparticles and possibly SM particles. This symmetry, while ad-hoc, has the very important consequence of preventing proton decay from SUSY processes, as well as making the LSP a dark matter candidate, as it is stable.

5.3 Production And Decay Modes

In models where R-parity is conserved sparticles must be produced in pairs. At the LHC the dominant mode is expected to be the so-called strong production, where pairs of gluinos or squarks are produced, due to the strong couplings of the colliding partons. An example of such a process is shown in figure 5.1. Weak production modes, direct production of neutralinos or sleptons, are also present though with lower cross-sections.

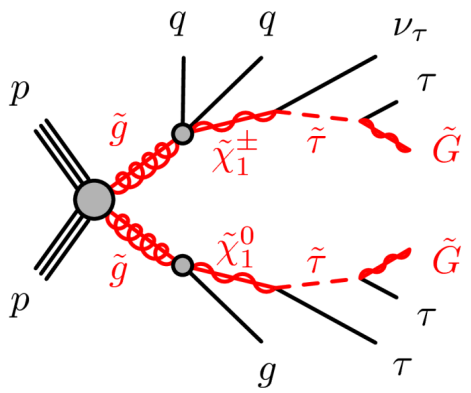

Figure 5.1: An example cascade decay chain in the GMSB model, with strongly produced sparticles and taus in the final state. The chain ends with a decay to gravitino.

The gluinos can only decay into squarks and do so via strong couplings. If kinematically allowed, the preferred decay mode for squarks is via gluino, otherwise they decay via weak couplings into neutralinos or charginos. All

of these decay modes result in the production of jets. The large mass difference between the strongly interacting sparticles and the weakly interacting gauginos and neutralinos means these jets have high energy, see figure 5.2.

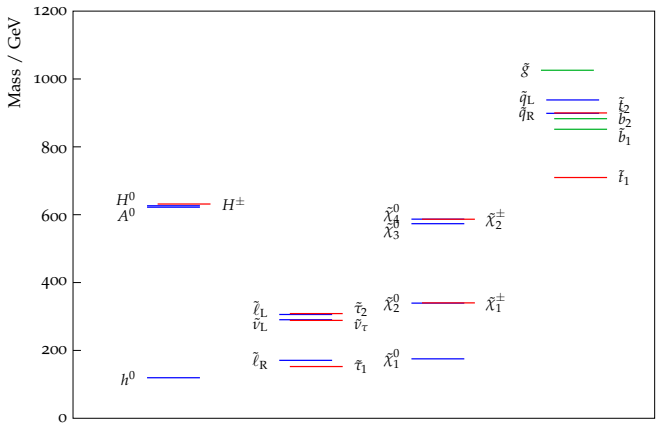

Figure 5.2: The sparticle spectrum of an example GMSB model used, $\Lambda = 50\,\text{GeV}$, $\tan\beta = 20$ and other parameters at $M_{\text{mess}} = 250\,\text{GeV}$, $N_5 = 3$, $c_{\text{grav}} = 1$, $\text{sgn}\,\mu = +$. In columns from left to right; Higgses, sleptons, gauginos and squarks/gluinos. Plots produced using the `PySLHA` [39] python package. The gravitino mass is of the order of eV and is not shown on the plot.

Charginos and neutralinos decay weakly into sleptons or lighter neutralinos until the LSP is reached. The decays of the sleptons typically take place via decay into neutralinos where such decays are kinematically allowed. In this part of the decay chain the production of leptons and gauge bosons is possible, depending on the sparticle mass hierarchy of the model.

Finally, since the LSP of GMSB models is the gravitino, all decays to the LSP happen through gravitational coupling. As this is far smaller than the SM couplings all branching ratios for decay to LSP are small, except for the NLSP where no other decay channels are open.

5.4 Monte Carlo Samples

The MC samples used in the analysis were produced centrally by the ATLAS collaboration. They form a set of all backgrounds that are expected to contribute in the Signal Region (SR).

Top

For top production both $t\bar{t}$ and single top production processes are considered. All primary samples are generated by the `MC@NLO` [40] generator with `HERWIG` [41] showers, except for the t-channel single top production where

the AcerMC [42] generator is used with Pythia [43] showers. The alternative generator for the t-channel is due to problems with unphysical jets from the HERWIG showers. A summary of the samples used can be found in table A.1.

An alternative set of samples generated with AcerMC is used to evaluate generator effects on the background estimate.

W + jets and Z + jets

For W + jets and Z + jets the samples used cover decays into leptons with a separate sample for decay into each lepton flavour. Additionally, the samples are split based on the number of additional associated partons produced, covering all cases from no partons to up to six partons. The samples are produced using Alpgen [44] to generate the process and Jimmy [45] for showering.

A summary of all the samples used can be found in table A.2 for W + jets and table A.3 for Z + jets.

Finally, contributions from Drell-Yan processes are also evaluated using the samples shown in table A.6, also procuced using Alpgen and Jimmy, and as their contribution is relatively small it is estimated directly from MC.

QCD

QCD samples are produced through the Pythia generator. The details of these samples can be found in table A.5. The samples are broken down by the energy range of the produced jets. $E_{\mathrm{T}}^{\mathrm{miss}}$ in such events is due to instrumental effects in jet reconstruction.

Dibosons

One final contribution that is checked is the contribution from diboson production. This contribution is taken as is from simulated data and is produced using the MC@NLO generator. The details of the samples used can be found in table A.4.

Signal samples

The signal samples used can be found in table A.7 and cover a grid in the GMSB parameter space spanned by the parameters $\tan\beta$ and Λ. A model grid refers to a set of model points where each point corresponds to a certain set of parameter values. A separate sample is produced for each model point. The values of the parameters used in the grid can be found in table 5.1. The sparticle mass spectra are produced using ISAJET [46] while the events themselves are produced using the HERWIG generator. The sample for each point in the grid contains 10k events.

5.5 Analysis channels

The analysis presented here is one of four channels in a common analysis. This analysis looks at final states with exactly one tau, high p_{T} jets and high $E_{\mathrm{T}}^{\mathrm{miss}}$ (referred to as the "one-tau" analysis. One further analysis channel looks at final states with two taus, high p_{T} jets and high $E_{\mathrm{T}}^{\mathrm{miss}}$ ("two-tau"). Finally, two analysis channels look at states with a tau and a muon ("tau + muon") or a tau and an electron ("tau + electron"). The result of these four channels are combined in the end to produce one common result for the entire analysis. What follows is the description of the procedures and results from the one-tau channel as well as the final statistical combination with the other three channels.

5.6 Event selection

The analysis uses the full 4.7 fb^{-1} 7 TeV CoM dataset from 2011. Events with sparticle production are characterized by a high $E_{\mathrm{T}}^{\mathrm{miss}}$, originating from the undetected heavy LSP, and associated high-p_{T} jets. The analysis therefore uses data from the `JetTauEtMiss` stream, which contains events triggered by $E_{\mathrm{T}}^{\mathrm{miss}}$, jet and tau signatures.

Trigger selection on 2011 collision data

The trigger chain `EF_j75_a4tc_EFFS_xe45_loose_noMu` is required to have fired for data taking periods B2–I (i.e. run numbers $\leq$ 186493), recording events with at least one jet above 75 GeV and $E_{\mathrm{T}}^{\mathrm{miss}}$ above 45 GeV. For periods J–M the $E_{\mathrm{T}}^{\mathrm{miss}}$ threshold has been raised to 55 GeV, represented by the trigger chain `EF_j75_a4tc_EFFS_xe55_noMu`. In both cases these were unprescaled triggers with the lowest available p_{T} and $E_{\mathrm{T}}^{\mathrm{miss}}$ thresholds. An explanation of these triggers can be found in section 2.7. The trigger requirement is only applied to data.

One of the background estimation techniques, the correction of the rate of the Z + jets background events, studies identified Z decays to muons, and for that purpose uses the muon stream with the trigger `EF_mu15_mu10_EFFS` for periods B2–I, and `EF_mu15_mu10_EFFS_medium` thereafter.

Baseline event selection

The analysis baseline event selection is to select only events which are suitable for the analysis. This means passing trigger requirements, data quality requirements and a selection of the physics objects required by the analysis. The physics objects referred to here are defined in section 2.6. The baseline event selection involves the following steps in the order given:

- A preselection of data from the GRL rejects p–p collision data with problematic detector conditions, in the way described in section 3.3. It ensures that only well reconstructed physics objects enter the analysis.

- For certain events the LAr calorimeter reports an error condition. Such error conditions act on single events only and do not compromise the whole LB or run. The luminosity calculation accounts for these and about 0.28% of the total integrated luminosity is lost after this selection.

- Select events with a primary vertex with at least four associated tracks. This ensures that a hard process took place in the event.

- While the trigger requirements apply only to data, kinematic selections are imposed to jet p_{T} and $E_{\mathrm{T}}^{\mathrm{miss}}$ in both data and MC events. At least two jets must be selected, one with $p_{\mathrm{T}} > 130\,\mathrm{GeV}$ and a second with $p_{\mathrm{T}} > 30\,\mathrm{GeV}$, as well as $E_{\mathrm{T}}^{\mathrm{miss}} > 130\,\mathrm{GeV}$. This selection means only events in the trigger plateau region are selected, where the trigger efficiency is close to 100%, see figure 5.3. For data taking periods L–M the last selection is raised to $E_{\mathrm{T}}^{\mathrm{miss}} > 150\,\mathrm{GeV}$.

- A veto for events containing muons or electrons is applied.

- Finally, events pass the selection if a tau-lepton is reconstructed with $p_{\mathrm{T}} > 20\,\mathrm{GeV}$ and being identified as a tau, using the "tight" jet rejection requirements and "tight" electron rejection requirements [14]. The presence of additional "loose" tau candidates disqualifies the event from selection.

- A veto of events where "bad" jets are found after overlap removal. These are jets which originate from beam background or detector effects and jets which have mismeasured energy. Additionally, events where jets or taus received large corrections due to the LAr hole treatment are rejected. The procedure is described in detail in [47].

The rejection of events with an additional tau candidate or events that contain muon or electron candidates ensures that the one-tau analysis channel is orthogonal to the two tau and tau plus muon/electron channels, making it possible to statistically combine the results of all four channels in a straightforward manner.

Background rejection and signal selection

After the events pass the trigger and baseline event selection, the following additional selections are applied to reject as much of the background as possible, while preserving the signal:

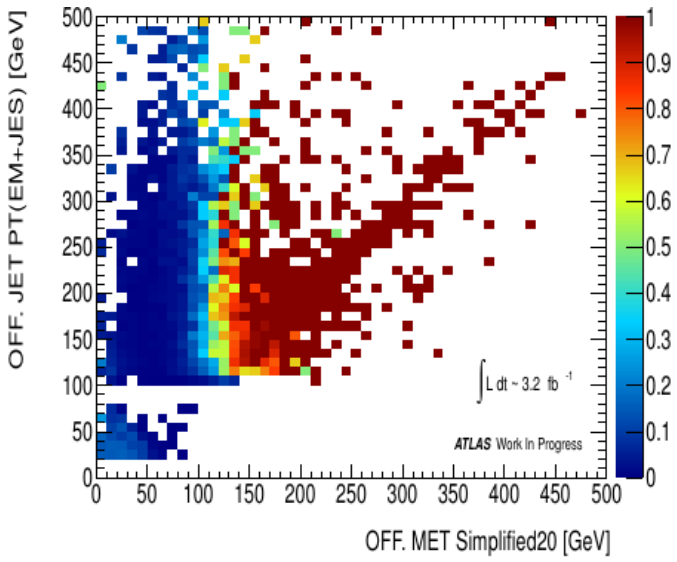

Figure 5.3: The efficiency of the trigger for the 2011 run as a function of $E_{\mathrm{T}}^{\mathrm{miss}}$ versus jet p_{T}. Of note is the plateau region, where the trigger efficiency becomes uniform; this trigger achieves almost 100% efficiency there.

- $\Delta\phi_{\mathrm{min}} > 0.3$,
- $E_{\mathrm{T}}^{\mathrm{miss}}/m_{\mathrm{eff}} > 0.3$,
- $m_{\mathrm{T}} > 110\,\mathrm{GeV}$,
- $H_{\mathrm{T}} > 775\,\mathrm{GeV}$.

These variables are introduced in section 2.6 and define the used SR in which the SUSY signal looked at is enhanced compared to background. This region is kept blind (i.e. the data in this region are not looked at) until the background estimation is finalised. This is done to avoid biasing the selection by looking at the data, which are subject to statistical fluctuations. This makes the background estimation even more crucial, as there is no comparison between data and MC in the SR until the final results are ready to be produced.

The first two selections are designed to reject QCD background. The m_{T} selection is designed to remove backgrounds containing a W boson decaying to a tau and a neutrino, which is the dominant non-QCD background in this analysis. The H_{T} selection is designed to suppress the remaining backgrounds, primarily W + jets, top, $Z \to \nu\nu$ and dibosons.

The H_{T} selection value is chosen by optimising the expected exclusion limit in the GMSB grid. This is done by varying the value of the H_{T} cut and calculating the expected limit on the model cross section for the GMSB

points with cross section $0.05\,\text{pb} < \sigma < 0.5\,\text{pb}$. Model points with cross sections in this range are close to the expected exclusion reach. The GMSB points used for the optimisation are listed in table 5.2. Figure 5.4 shows the optimisation results, yielding an optimal selection of $H_\text{T} > 775\,\text{GeV}$.

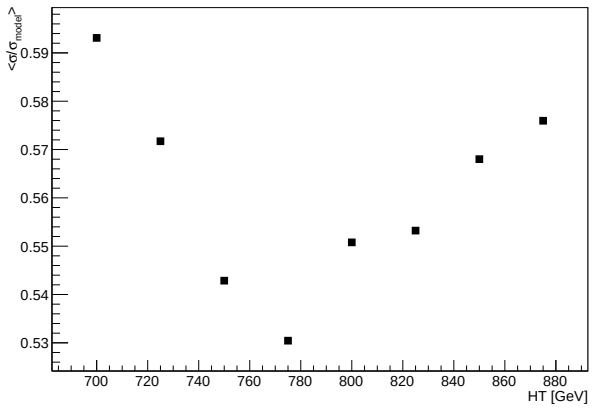

Figure 5.4: Optimisation of the H_T selection to define the signal region of the one-tau analysis. The y-axis shows the cross section which can be excluded at 95% CL_s relative to the cross section of the tested GMSB models, averaged over all models listed in table 5.2.

5.7 Control regions

In order to minimise the effect of uncertainties on the background estimation the number of events in each of the dominant background contributions is normalised to data. To do this Control Regions (CRs) are defined where each background component is enhanced. The techniques used to normalise each background source are outlined in section 5.8.

5.7.1 W + jets and top

The CRs for the W + jets and top backgrounds are defined by the baseline selection requirements, see section 5.6, and an additional selection on $m_\text{T} < 80\,\text{GeV}$, to keep only taus coming from W decays. Separation between top and W + jets is achieved via b-tagging. Events with b-tagged jets form the top CR and all others the W + jets CR. This criterion is effective in classifying these two contributions as shown in figure 5.6.

As the kinematics and simulation of fake taus is different from true taus (fake taus are typically misidentified jets) a second set of CRs is used to get Scale Factors (SFs) for processes involving fake taus. The region with

Sample	Λ [TeV]	$\tan\beta$	σ [pb]	Sample	Λ [TeV]	$\tan\beta$	σ [pb]
137934	40	2	0.39	142573	45	25	0.22
137935	40	5	0.42	142574	45	30	0.22
137936	40	10	0.43	142575	45	35	0.23
137937	40	15	0.43	142576	45	40	0.26
137938	40	20	0.44	137944	50	2	0.09
137939	40	25	0.44	137945	50	5	0.11
137940	40	30	0.45	137946	50	10	0.11
137941	40	36	0.48	137947	50	15	0.11
142568	45	2	0.18	137948	50	20	0.11
142569	45	5	0.21	137949	50	30	0.12
142570	45	10	0.21	137950	50	40	0.13
142571	45	15	0.21	137951	50	50	0.25
142572	45	20	0.22	137959	60	50	0.06

Table 5.2: GMSB points that are included in the optimisation of the H_{T} selection for the one-tau analysis.

$80\,\mathrm{GeV} < m_{\mathrm{T}} < 110\,\mathrm{GeV}$ is used. An additional selection on $H_{\mathrm{T}} < 775\,\mathrm{GeV}$ is made to ensure separation with the SR.

These CRs are summarised in figure 5.5, showing the separation between them and the SR.

5.7.2 Z + jets

In the case of the Z + jets estimation the SF is derived using $Z \to \mu\mu$ processes as well as data using di-muon triggers to normalise the MC to data. In defining this region a requirement is placed for two muons which have invariant mass within the Z mass window $66\,\mathrm{GeV} < M(\mu^+, \mu^-) < 116\,\mathrm{GeV}$. These muons are required to pass the baseline SUSY muon identification criteria.

5.8 Background estimation

The two primary backgrounds for this study are the W + jets and top production. These form a big contribution both because of their high cross-section but also due to the decay of Ws into neutrinos, giving a real $E_{\mathrm{T}}^{\mathrm{miss}}$ contribution.

The Z + jets background is also important in the study, particularly the decays $Z \to \nu\nu$ + jets, where one of the jets is misidentified as a tau and the neutrinos provide the $E_{\mathrm{T}}^{\mathrm{miss}}$ signature. This background contribution is estimated in the Z + jet CR

Multijet processes do not contribute much in the SR but need to be

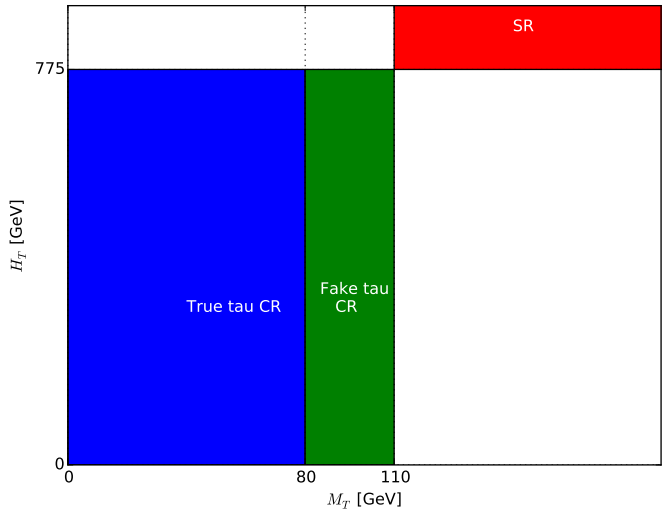

Figure 5.5: Plot of the defined CRs and SR for the analysis in the m_{T} and H_{T} space. A m_{T} selection splits the regions into true and fake tau dominated, while a H_{T} selection separates them from the SR. The CRs can be further split into W and top dominated, based on the b-tagged jet multiplicity in the event.

estimated as the uncertainty on the contamination is very large if MC is used alone. Diboson production and Drell-Yan processes are also considered, though of lesser importance in the final signal region.

5.8.1 Top background with a true tau estimate

In the case of the top background with true taus, the background estimation is done through a template fit. The variable used to split between the top and the W backgrounds is the number of b-tagged jets in the event, which is larger in the case of top, due to the $t \to W^{\pm}, b^{\mp}$. Templates of the number of b-tagged jets are produced from MC for top processes ($t\bar{t}$ and single top production) and a combined template for the other backgrounds using events from the true tau CR. Figure 5.6 shows plots of the templates used. These templates are then fitted to the b-tagged jet multiplicity from data events in the true tau CR. The fit results in a fraction of data events accounted for by each template, the resulting fit is shown in figure 5.7. The total number of events in the CR is then constrained by the data and the data/MC fraction gives the total number of events from top, from which a SF can be computed to correct the MC estimate for top. the fraction to all other events is not used further.

From the fit a SF of

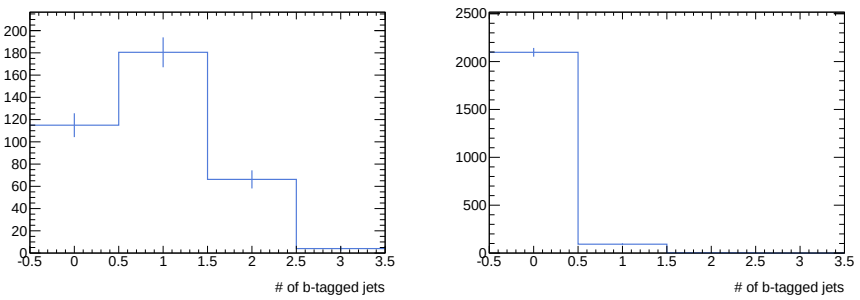

Figure 5.6: The multiplicity of b-tagged jets for samples with top production (right) and for all other contributions (left) in the top/W CR.

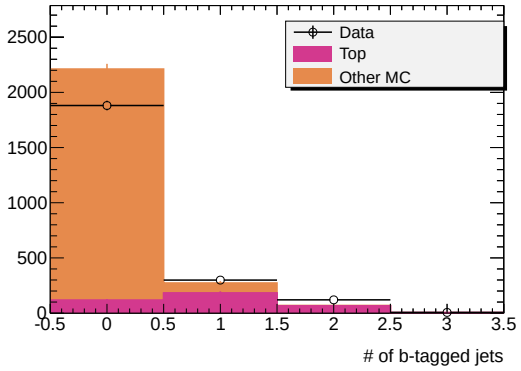

Figure 5.7: The multiplicity of b-tagged jets in data along with the final fit of the contributions from top and other sources.

Region	Scale Factor ($\omega_{\text{top}}^{\text{true}}$)
$\lvert\eta\rvert < 0.8$	1.46 ± 0.08
$0.8 < \lvert\eta\rvert < 1.6$	1.35 ± 0.13
$1.6 < \lvert\eta\rvert$	1.60 ± 0.25

Table 5.3: The true tau top SF obtained for the different regions in η.

$$\omega_{\text{top}}^{\text{true}} = 1.39 \pm 0.08^{\text{stat.}}\ {}^{+0.06}_{-0.08}\ ^{\text{syst.}}$$

is found.

To cross-check the stability of the method the process is repeated also using different slices of η and computing the SF in each slice. The results of this check are shown in table 5.3 and good agreement is found, within statistical uncertainties.

5.8.2 W + jets background with a true tau estimate

The W + jets background estimation uses the asymmetry in the charge of Ws produced in LHC. This asymmerty arises due to the p-p collisions in the LHC. As the colliding protons consist of two up and one anti-down valence quarks the production of W^+ through an up and anti-down quark interaction is more likely than W^- through down and anti-up; as in the former case one of the quarks can be a valence quark. This particular effect is only visible for W production. The production of top quarks is mainly in pairs, thus no such effect is present. This means that it is possible to estimate the W content in data by measuring this charge asymmetry. The final SF is determined by finding the value which results in identical asymmetry in data and MC.

First the ratio of positive to negative taus, r_{MC}, needs to be etracted in the W true tau CR from W + jets and WZ MC. These MC samples are used as these are the ones that contribute to this measurement. Additional contributions can come from single top production but this is a much smaller effect. With this ratio and the number of positively and negatively charged W candidate events from data, D^+ and D^- respectively, the number of true Ws can be estimated as:

$$N_W = N_W^+ + N_W^- = \frac{r_{\text{MC}} + 1}{r_{\text{MC}} - 1}\left(D^+ - D^-\right) \quad . \tag{5.1}$$

Contributions due to fake taus are naturally suppressed, since fake taus do not have a particular preference towards a certain charge, meaning that they cancel out once the subtraction is carried out.

The value of r_{MC} seen in W + jets and WZ MC events in the W/top CR is:

$$r_{\mathrm{MC}} = 2.15 \pm 0.05 \quad ,$$

In the same CR from data:

$$D^{+} - D^{-} = 502.$$

These result in a SF for the true W contribution of:

$$\omega_{\mathrm{W}}^{\mathrm{true}} = 0.75 \pm 0.04^{\mathrm{stat}} \pm 0.03^{\mathrm{syst}} \quad .$$

5.8.3 Combined top and W estimation

For these two backgrounds a combined method is also considered, relying on the information about true and fake taus of the background categories in the two CRs. The SFs for true and fake taus are kept separate since these come from different sources (fake taus are typically misidentified jets), meaning that any possible mismodelling of the two in MC can be different. This results in four input variables and four variables to estimate the scale factors required to make the MC estimates match the data in the two CRs. This method of estimation is commonly referred to as the "matrix method".

$$\begin{pmatrix} N_{\mathrm{W,true}}^{\mathrm{WT1}} & N_{\mathrm{W,fake}}^{\mathrm{WT1}} & N_{\mathrm{top,true}}^{\mathrm{WT1}} & N_{\mathrm{top,fake}}^{\mathrm{WT1}} \\ N_{\mathrm{W,true}}^{\mathrm{WT2}} & N_{\mathrm{W,fake}}^{\mathrm{WT2}} & N_{\mathrm{top,true}}^{\mathrm{WT2}} & N_{\mathrm{top,fake}}^{\mathrm{WT2}} \\ N_{\mathrm{W,true}}^{\mathrm{WT3}} & N_{\mathrm{W,fake}}^{\mathrm{WT3}} & N_{\mathrm{top,true}}^{\mathrm{WT3}} & N_{\mathrm{top,fake}}^{\mathrm{WT3}} \\ N_{\mathrm{W,true}}^{\mathrm{WT4}} & N_{\mathrm{W,fake}}^{\mathrm{WT4}} & N_{\mathrm{top,true}}^{\mathrm{WT4}} & N_{\mathrm{top,fake}}^{\mathrm{WT4}} \end{pmatrix} \begin{pmatrix} \omega_{W}^{\mathrm{true}} \\ \omega_{W}^{\mathrm{fake}} \\ \omega_{\mathrm{top}}^{\mathrm{true}} \\ \omega_{\mathrm{top}}^{\mathrm{fake}} \end{pmatrix} = \begin{pmatrix} N_{\mathrm{data}}^{\mathrm{WT1}} - N_{\mathrm{Oth.MC}}^{\mathrm{WT1}} \\ N_{\mathrm{data}}^{\mathrm{WT2}} - N_{\mathrm{Oth.MC}}^{\mathrm{WT2}} \\ N_{\mathrm{data}}^{\mathrm{WT3}} - N_{\mathrm{Oth.MC}}^{\mathrm{WT3}} \\ N_{\mathrm{data}}^{\mathrm{WT4}} - N_{\mathrm{Oth.MC}}^{\mathrm{WT4}} \end{pmatrix} .$$

In order to correct for other contributions all MC samples that are not contributing to the estimated quantities are subtracted from MC. Where applicable SFs are applied to the MC estimates.

This allows us to estimate the vector $\vec{\omega}$, which contains the SFs for each CR with true and fake taus, by inverting the matrix.

$$\begin{pmatrix} \omega_{W}^{\mathrm{true}} \\ \omega_{W}^{\mathrm{fake}} \\ \omega_{\mathrm{top}}^{\mathrm{true}} \\ \omega_{\mathrm{top}}^{\mathrm{fake}} \end{pmatrix} = \begin{pmatrix} 0.91 \pm 0.03^{\mathrm{stat}} + 0.05^{\mathrm{syst}} \\ 0.32 \pm 0.28^{\mathrm{stat}} + 0.17^{\mathrm{syst}} \\ 1.32 \pm 0.10^{\mathrm{stat}} + 0.13^{\mathrm{syst}} \\ 1.92 \pm 0.41^{\mathrm{stat}} + 0.22^{\mathrm{syst}} \end{pmatrix} \quad . \tag{5.2}$$

This method provides a cross-check of the true tau W and top SF. In the case of the top the two results are in agreement within statistical uncertainties. As this is not the case for the true tau W the difference between

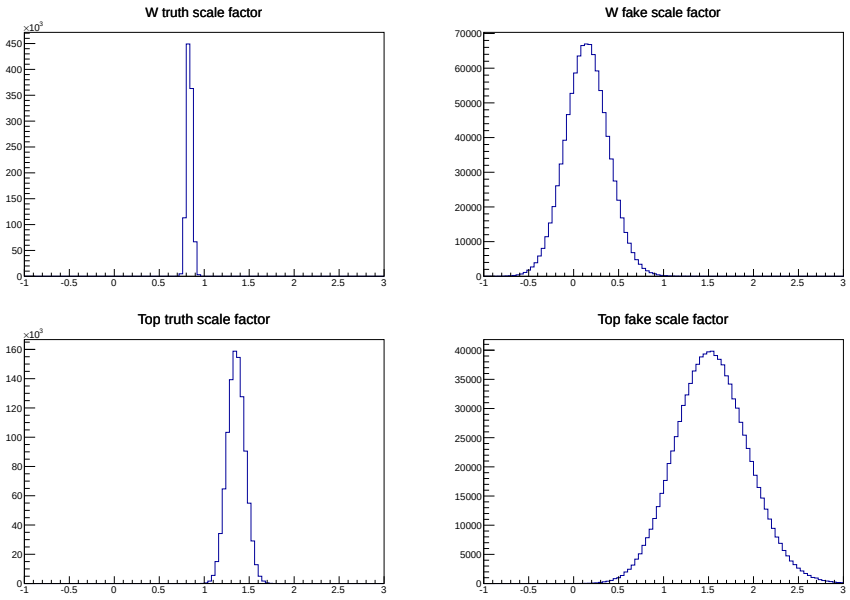

Figure 5.8: The scale factors obtained via the matrix method for the W + jets and top true and fake tau contributions. The distributions are obtained using toy MCs.

the two SFs is taken as an additional systematic uncertainty. For the fake tau SFs this is the only determination done. The error in the number of events in each region is also taken into account using toy MC. The output distributions where these uncertainties are taken into acount are shown in figure 5.8.

5.8.4 Z + jets

The presence of Z + jets as one of the backgrounds in the SR is also estimated from a data-driven technique. First it is studied that the main contribution of Z + jets to the signal region actually comes from events where the Z decays to a pair of neutrinos and contributes fully to the observed $E_{\mathrm{T}}^{\mathrm{miss}}$. However, $\mathrm{Z} \to \nu\nu$ decays can not be studied directly with high purity. Also, while Z + jets production with the Z boson decaying to ee or $\mu\mu$ has been measured by ATLAS, this analysis operates in a more extreme kinematic regime compared to the ATLAS results, so these can not be directly applied either. The Z + jets contribution is therefore estimated from the data by measuring the data/MC ratio from $\mathrm{Z} \to \mu\mu$ decays in a dedicated CR and scaling the number of all Z + jets events from MC in the SR with that factor.

$$Z_{\nu\nu}^{\mathrm{Data,SR}} = Z_{\nu\nu}^{\mathrm{MC,SR}} \frac{Z_{\mu^+\mu^-}^{\mathrm{Data,CR}}}{Z_{\mu^+\mu^-}^{\mathrm{MC,CR}}} \,. \tag{5.3}$$

Sensitivity to $Z \to \nu\nu$ decays is emulated by using a modified $E_T^{miss}*$ in the analysis where the transverse momenta of muons from the Z decay are made part of the missing energy vector:

$$E_T^{miss}* = \left|\left(\vec{E}_T^{miss} + \vec{p}_\mu + \vec{p}_\mu\right)_T\right| \tag{5.4}$$

For simplicity, in this analysis only the $\mu^+\mu^-$ channel is considered. The baseline event selection of section 5.6 is substantially altered to obtain a high statistics $Z+$jets control sample.

The selection starts from the `Muon` stream instead of `JetTauEtMiss` and requires the trigger: `EF_mu15_mu10_EFFS` for data taking periods B2–I and `EF_mu15_mu10_EFFS_medium` for periods J–M. After GRL and vertex requirements it selects only events with two opposite signed isolated muons with $|\eta| < 2.4$, $p_T > 20\,\text{GeV}$ and with invariant mass within the range $66\,\text{GeV} < M(\mu^+,\mu^-) < 116\,\text{GeV}$. To make the CR signal-like at least 2 jets are required with $p_T(\text{jet}_1) > 130\,\text{GeV}$ and $p_T(\text{jet}_2) > 30\,\text{GeV}$ and a high "missing" transverse energy $E_T^{miss}* > 130\,\text{GeV}$ (150 GeV for data taking periods L–M, to account for the different trigger plateau requirements). Figure 5.9 shows the data and MC contributions to the CR as function of the dimuon invariant mass for two different muon p_T selections. The MC predicts a very high Z purity but overestimates the number of events in the $Z+$jets control sample. A SF of 0.81 ± 0.01 is derived from these studies.

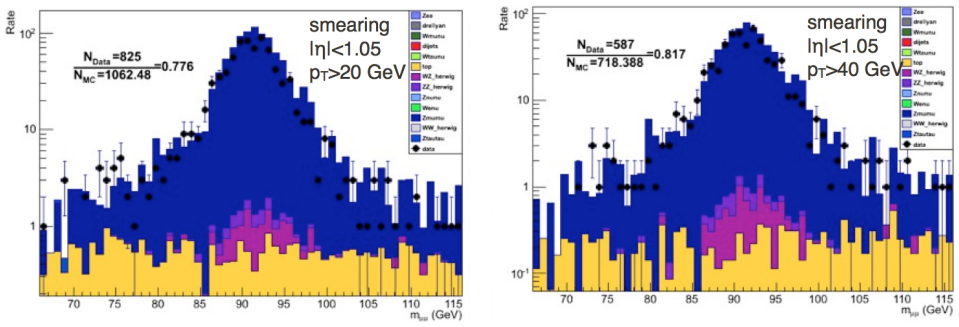

Figure 5.9: Di-muon invariant mass distribution for events from the $Z+$jets CR. The difference in numbers of event between data and MC gives rise to a scale factor. The right distribution tests the agreement for a more stringent requirement on the Z decay muons of $p_T > 40\,\text{GeV}$.

5.8.5 QCD estimation

The method used for QCD estimation is the so-called ABCD method, which allows a data-driven estimate of a background rate. Events are selected by a pair of cuts in a plane of two uncorrelated variables, such that both of the selections enhance the signal-to-background ratio.

Scaling	One-tau	Two-Tau	Tau + Muon	Tau + Electron
$\omega^{\mathrm{W}}_{\mathrm{true}}$	0.75 ± 0.04	0.74 ± 0.02	-	-
$\omega^{\mathrm{t}}_{\mathrm{true}}$	1.39 ± 0.08	1.17 ± 0.03	-	-
$\omega^{\mathrm{Z}}_{\mathrm{true}}$	0.81 ± 0.01	0.96 ± 0.38	-	-
$\omega^{\mathrm{W}}_{\mathrm{fake}}$	0.32 ± 0.28	0.65 ± 0.32	0.58 ± 0.02	0.61 ± 0.01
$\omega^{\mathrm{t}}_{\mathrm{fake}}$	1.92 ± 0.41	0.89 ± 0.23	0.84 ± 0.16	0.84 ± 0.14

Table 5.4: Comparison of the scale factors for W + jets, Z + jets and top background contributions derived by the different analyses.

	Extra Loose τ	Nominal τ
$\Delta\phi_{\mathrm{min}} < 0.3$	Control region A	Control region B
$\Delta\phi_{\mathrm{min}} > 0.3$	Control region C	Signal region D

Table 5.5: Definitions of QCD regions used in the ABCD method for the one-tau analysis.

The two variables used here are the tau identification tightness and $\Delta\phi_{\mathrm{min}}$ so that an event sample with high QCD contamination is separated into four regions, these are shown in table 5.5. Figure 5.10 shows a scatterplot of the tau BDT score against $\Delta\phi_{\mathrm{min}}$ for QCD MC after the m_{T}^{τ} selection, but skipping the QCD suppressing selection and final H_{T} selection. In this definition the regions A, B and C are QCD enriched with small signal contamination. Using the number of events in these regions it is possible to estimate the number of QCD events in region D. The tau identification becomes a background discriminator variable by adding an "extra loose tau" working point to the already defined nominal tau definition from section 2.6. An extra loose tau candidate has the nominal tau ID selection with the exception of the BDT identification; if the event features several such taus,

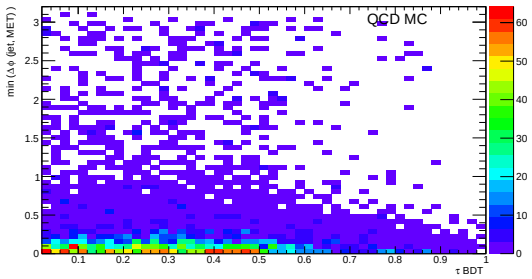

Figure 5.10: Plot of the variables used to define the ABCD regions and before the final H_{T} selection in the one-tau analysis for QCD MC. The two variables should be independent of each other in order for the ABCD method to work.

one of them is picked at random. An extra loose tau candidate is only picked as long as it does not overlap with the two leading jets in the event. These extra loose tau candidates are then used in place of the nominal taus in the event selection. The sample is split into events where an extra loose tau is identified but would not pass the nominal tau definition and events passing only the tighter nominal tau identification. The variable $\Delta\phi_{\text{min}}$, is sensitive to events where $E_{\text{T}}^{\text{miss}}$ originates largely from a single mis-measured jet instead of a real undetected particle.

Event selection for the ABCD method

The baseline event selection from section 5.6 is applied. To improve the statistical power of the method the $E_{\text{T}}^{\text{miss}}/m_{\text{eff}}$ selection and the final selection on H_{T} is not applied. An additional selection on $E_{\text{T}}^{\text{miss}}/m_{\text{eff}} < 0.3$ is made for region C, in order to reduce the non-QCD contamination, making the method less affected by uncertainties in non-QCD SFs.

A significant contamination from non-QCD events is observed in all CRs except for region A, as shown in figure 5.11.

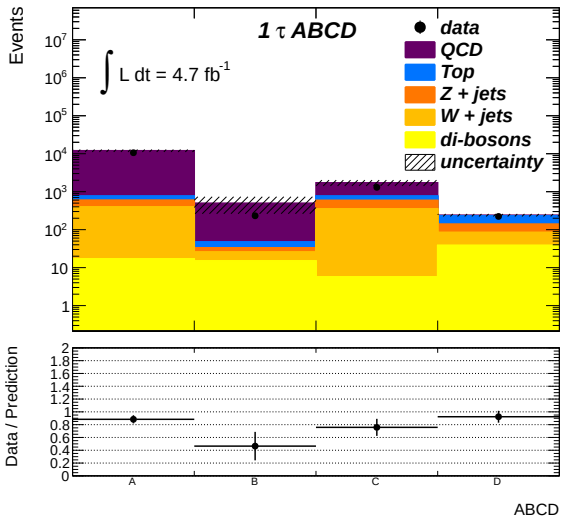

Figure 5.11: Summary of background composition in the four samples defined by extra loose/nominal tau ID and the $\Delta\phi_{\text{min}}$ selection for the ABCD method.

Figures 5.12 and 5.13 show the H_{T} and $E_{\text{T}}^{\text{miss}}/m_{\text{eff}}$ distributions in regions A-C.

Separating backgrounds inside the ABCD method

Other non-QCD backgrounds contribute to the observed number of events in the CRs A–C region, this effect needs to be corrected. Two methods are studied for this correction, labelled *subtraction method* and *likelihood method*. Details of these methods are presented in what follows.

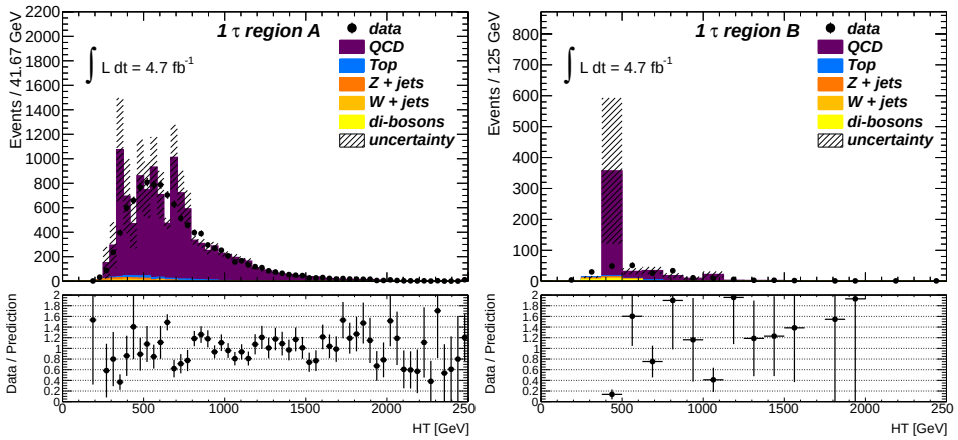

(a) A

(b) B

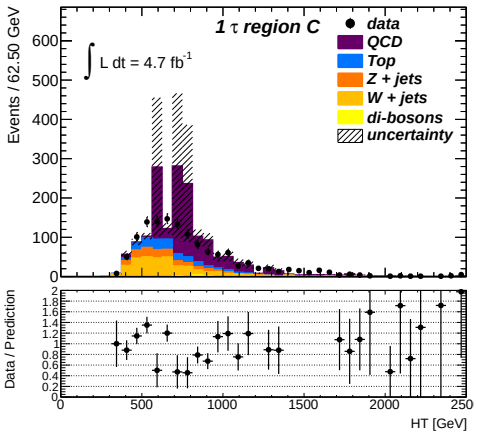

(c) C

Figure 5.12: m_{eff} distributions in regions A, B and C for the one-tau analysis, showing good agreement between data and MC, in the areas where it is possible to compare. Certain bins have large statistical unertainties due to the high weight of the events contributing to them.

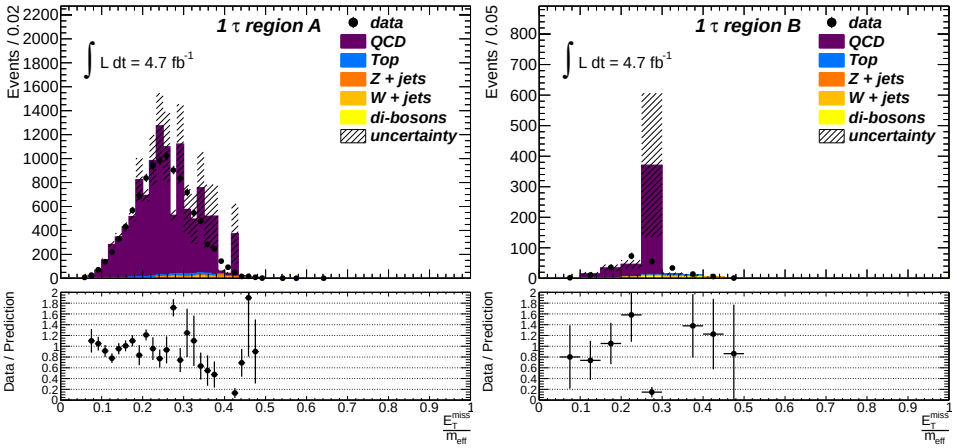

(a) A

(b) B

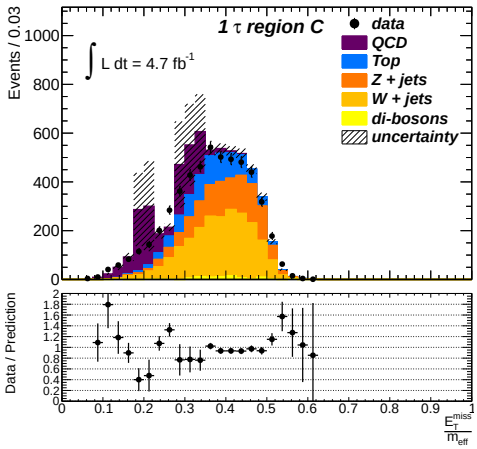

(c) C. No selection applied on $E_{\mathrm{T}}^{\mathrm{miss}}/m_{\mathrm{eff}}$

Figure 5.13: $E_{\mathrm{T}}^{\mathrm{miss}}/m_{\mathrm{eff}}$ distributions in regions A, B and C for the one-tau analysis, showing good agreement between data and MC, in the areas where it is possible to compare. Certain bins have large statistical unertainties due to the high weight of the events contributing to them.

- The *subtraction method* is a simple subtraction of the non-QCD MC from the data in the regions A–C, using the scale factors obtained for the top and vector boson backgrounds from the data-driven methods in the following sections. Scale factors for true and fake non-QCD contributions are dependent on the tau ID. The influence of the uncertainty of the SFs on the method is estimated by scaling the extra loose tau region and not applying the SFs to this region, and adding the difference of the results as an additional systematic uncertainty of the method.

- The other way incorporates the non-QCD background by additional terms in a *likelihood function method*. This way is more robust if the amount of background to be subtracted is comparable to the number of events observed in one or more of the regions.

Subtraction method as part of background treatment in the ABCD method

The subtraction

$$N_{\mathrm{A,B,C}}^{\mathrm{QCD}^*} = N_{\mathrm{A,B,C}}^{\mathrm{data}} - N_{\mathrm{A,B,C}}^{\mathrm{non-QCD}} \tag{5.5}$$

allows the number of QCD events in the signal region D, for $E_{\mathrm{T}}^{\mathrm{miss}}/m_{\mathrm{eff}} < 0.3$, to be estimated by

$$N_{\mathrm{D}}^{\mathrm{QCD}^*} = \frac{N_{\mathrm{B}}^{\mathrm{QCD}^*}}{N_{\mathrm{A}}^{\mathrm{QCD}^*}} N_{\mathrm{C}}^{\mathrm{QCD}^*} \tag{5.6}$$

To get the number of estimated QCD events in the signal region used in the real event selection this number has to be scaled by the ratio of events with $E_{\mathrm{T}}^{\mathrm{miss}}/m_{\mathrm{eff}} < 0.3$ and the final selection on H_{T} and $E_{\mathrm{T}}^{\mathrm{miss}}/m_{\mathrm{eff}} > 0.3$. This ratio may be taken from the QCD-dominated region A, provided that these variables are independent of tau ID and $\Delta\phi_{\mathrm{min}}$. This yields $N_{\mathrm{D}}^{\mathrm{QCD}^*} = 9.9 \pm 1.0^{\mathrm{stat}}$ and in the final signal region $N_{\mathrm{D,\ E_T^{miss}/m_{eff}>0.3\ \&\ H_T>775\,GeV}}^{\mathrm{QCD}^*} = N_{\mathrm{SR}}^{\mathrm{QCD}^*} = 0.13 \pm 0.03^{\mathrm{stat}}$ when the W, Z and top background scale factors are not yet applied to the regions A and C (extra loose tau). This result is consistent with the ratios from the other QCD-enriched regions, the statistically limited regions B (only one event passes $E_{\mathrm{T}}^{\mathrm{miss}}/m_{\mathrm{eff}} > 0.3$) and C. It is also consistent with result obtained when varying the tau definition, by using BDT "loose" taus as well as an even looser tau definition (tau candidates with basic kinematic selection, and charge $< |3|$ and nTracks $< |6|$ with and without lepton vetoes, here labelled "extra loose").

The final QCD estimate is calculated from the extra loose regions, where non-QCD contributions have been scaled using the SFs obtained in sections 5.8.1-5.8.4. These include the W, Z and top SFs found in table 5.4,

as found by the other background estimation methods in the analysis. This yields $N_{\mathrm{SR}}^{\mathrm{QCD}^*} = 0.17 \pm 0.04^{\mathrm{stat}}$. The difference between the two numbers are taken as an additional systematic uncertainty on the method. Figure 5.14 shows the numbers of estimated QCD events in the SR from this method for different values of QCD reducing selections on $\Delta\phi_{\mathrm{min}}$ and $E_{\mathrm{T}}^{\mathrm{miss}}/m_{\mathrm{eff}}$.

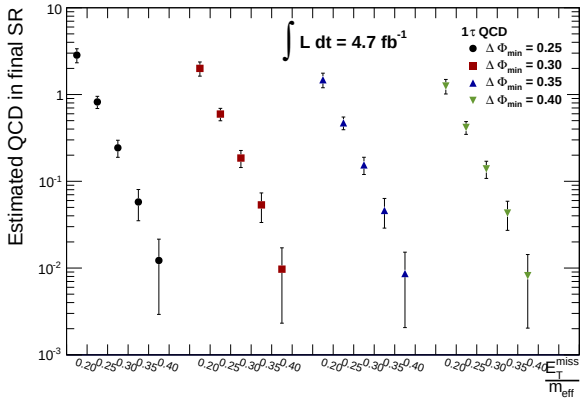

Figure 5.14: Shows number of QCD events estimated from the ABCD subtraction method in the final SR for different selection values on $\Delta\phi_{\mathrm{min}}$ and $E_{\mathrm{T}}^{\mathrm{miss}}/m_{\mathrm{eff}}$.

Likelihood method as part of background treatment in the ABCD method

The background correction via likelihood function works as follows: the predicted rates for the non-QCD background components are denoted here by $\mu_{\mathrm{D;A,B,C}}^{\mathrm{nQCD}}$ and are taken from MC with appropriate SFs applied, given in table 5.4 (no scaling of extra loose taus). A possible signal contribution in region D is denoted by μ. The signal leakage into the other regions is expressed in terms of $\mu_{\mathrm{A,B,C}}$ and a signal acceptance factor into this region taken from MC in a sample GMSB signal. Then there is the "unknown" QCD background which is completely data driven. Denoting the component in the search region D as μ^{QCD}, we describe the ABCD-relation between the other three components with two additional nuisance parameters τ_B and τ_C. The estimated rates in the 4 regions are thus described by:

$$
\begin{aligned}
\mu_A &= \mu_{\mathrm{A}} + \mu_A^{\mathrm{nQCD}} + \mu^{\mathrm{QCD}}\tau_B\tau_C \\
\mu_B &= \mu_{\mathrm{B}} + \mu_B^{\mathrm{nQCD}} + \mu^{\mathrm{QCD}}\tau_B \\
\mu_C &= \mu_{\mathrm{C}} + \mu_C^{\mathrm{nQCD}} + \mu^{\mathrm{QCD}}\tau_C \\
\mu_D &= \mu + \mu_D^{\mathrm{nQCD}} + \mu^{\mathrm{QCD}}
\end{aligned}
$$

The likelihood function is the product of the four likelihoods for the counting experiments in the four regions:

$$L(n_A, n_B, n_C, n_D|\mu, \theta_\mu) = \prod_{\mathrm{i=A,B,C,D}} \frac{e^{-\mu_\mathrm{i}} \mu_i^{\mathrm{n_i}}}{n_i!}$$

The maximum likelihood fit to data yields $\mu^{\mathrm{QCD}} = 9.9 \pm 1.0$. This yields an estimate of 0.13 ± 0.03 events in the region with $E_\mathrm{T}^\mathrm{miss}/m_\mathrm{eff} > 0.3$ and $H_\mathrm{T} > 775\,\mathrm{GeV}$ using the ratio of events in region A as for the subtraction method and no scaling of the extra loose tau region. This is the same result as the one obtained from the subtraction approach, which shows that the simple treatment (by subtraction) has already been robust.

5.9 Events in SR after selection

The number of events after each selection, as outlined in section 5.6, for the SM backgrounds is shown in table 5.7, where the SFs obtained in section 5.8 have been applied. For comparison between MC and data the total sum of the MC output is compared to data at each step in the cutflow, shown in table 5.6.

After cut	SM	Data
τ (no overlap 2 τ)	3656 ± 256	3751
$\Delta\phi_\mathrm{min} > 0.3$	3028 ± 120	3370
$E_\mathrm{T}^\mathrm{miss}/m_\mathrm{eff} > 0.3$	2441 ± 99	2673
$m_\mathrm{T}^\tau > 110\,\mathrm{GeV}$	178 ± 22	184
$H_\mathrm{T} > 775\,\mathrm{GeV}$	1.31 ± 0.37	4

Table 5.6: Cut-flow for the kinematic selections defining the SR of the one-tau analysis after the baseline selection. Shown errors are statistical only. The sum of all Standard Model background processes is compared to the data. The value of 1.31 ± 0.37 expected events is composed of the predicted events from the corrected top quark, W + jets and Z + jets MC and the events for QCD background estimated from the data.

After cut	Top	W + jets	Z + jets	Di-boson	QCD	Drell-Yan
1 τ (no overlap 2 τ)	890 ± 55	2045 ± 114	243 ± 15	9.0 ± 1.0	456 ± 222	4.1 ± 1.2
$\Delta\phi_\mathrm{min} > 0.3$	834 ± 50	1951 ± 107	205 ± 14	7.8 ± 0.9	28 ± 10	2.2 ± 0.9
$E_\mathrm{T}^\mathrm{miss}/m_\mathrm{eff} > 0.3$	680 ± 41	1593 ± 89	157 ± 13	5.8 ± 0.6	3.7 ± 3.6	1.5 ± 0.8
$m_\mathrm{T}^\tau > 110\,\mathrm{GeV}$	90 ± 14	34 ± 15	52 ± 8	1.5 ± 0.3	< 3.5	< 0.36
$H_\mathrm{T} > 775\,\mathrm{GeV}$	0.61 ± 0.25	0.30 ± 0.16	0.22 ± 0.22	< 0.05	0.17 ± 0.04	< 0.36

Table 5.7: Number of events after each step in the kinematic selection defining the SR of the one-tau analysis after the baseline event selection. All numbers are from MC with scale factors applied to top, W + jets and Z + jets except for the final estimate of QCD events, which is from section 5.8.5. The uncertainties are statistical only.

5.10 Systematic uncertainties

Systematic uncertainties play an important effect on the results of the analysis as they influence the estimated number of events in the SR. In this section a description of the sources of uncertainties and their treatment is presented and the effect they have on the result of the analysis can be found in table 5.8.

Each of the following uncertainty sources affects the properties of physics objects used in the analysis or the weight given to individual events. For each of these uncertainty sources the relevant MC objects are modified, e.g. the energy of jets lowered to account for uncertainty in the energy scale, and then the analysis repeats with these new objects. This also includes the SF determination as well as the full selection. The difference of this estimate to the nominal one is taken as the effect of the systematic.

5.10.1 Tau systematic uncertainties

The systematic uncertainties considered for taus in the analysis are the tau energy scale [48] and the tau identification efficiency. These systematic uncertainties are dependent on the p_{T} of the tau as well as the η range in which it is located. They also depend on the identification used. The evaluation of these systematic uncertainties was done by the ATLAS tau working group centrally for all analyses.

5.10.2 b-tagging systematic uncertainties

Systematic uncertainties due to b-jet identification are also considered, as these affect the uncertainty on the top and $\mathrm{W}+\mathrm{jets}$ SFs. For this uncertainty three components are considered, the uncertainty on the scale factor for b-jets and light jets as well light jet misidentification. A fourth source of uncertainty, the scale factor due to c-quarks was not considered, as it was found to be negligible in comparison.

5.10.3 Jet systematic uncertainties

For jets the systematic uncertainties considered are the uncertainty on the JES, as well as the Jet Energy Resolution (JER) [49]. The JER uncertainty is applied as an additional Gaussian smearing on the jet energy, making the energy resolution in MC match what is observed in data.

5.10.4 $E_{\mathrm{T}}^{\mathrm{miss}}$ systematic uncertainties

As the $E_{\mathrm{T}}^{\mathrm{miss}}$ is a composite quantity, the uncertaintes on all input terms have to be considered, see section 2.6. In the case of this analysis these are terms affecting the soft $E_{\mathrm{T}}^{\mathrm{miss}}$ terms as well as the jets. As with the

jet systematic uncertainties the soft energy systematic uncertainties include the uncertainty on the energy scale as well as the enery resolution. The tau systematic uncertainties need not be considered as they are not used in the $E_{\mathrm{T}}^{\mathrm{miss}}$ determination. When the variation is done the $E_{\mathrm{T}}^{\mathrm{miss}}$ needs to be recalculated taking the updated objects into account.

5.10.5 Other systematic uncertainties

Other uncertainties considered are due to the pileup reweighting procedure, additional uncertainties from generators for top and dibosons as well as from the methods used to estimate the background contributions in the SR. The pileup reweighting uncertainty is evaluated by making a 10% downwards scaling of the spectrum of number of interactions per event (μ). This is a common procedure used in the SUSY WG for the evaluation of this uncertainty and is found to be sufficient to cover the possible error due to the μ uncertainty.

The generator uncertainties studied cover the effect of the MC shape on the extrapolation from the CRs to SR. To study this settings of the generators used are varied; such as the renormalisation and factorisation scales. Due to the many different setting combinations that need to be checked to evaluate generator uncertainties these studies are done on generator level only. The assumption is that the differences seen at generator level will translate correctly to reconstruction level. As such, samples with different generator settings are produced and the effect of each on the final count is evaluated.

The final extra systematic uncertainty is due to the difference in the results on the true tau W SFs determined by the charge subtraction and matrix methods, outlined in 5.8.2 and 5.8.3 respectively. The difference is considered as an additional error on the true tau W SF itself.

5.10.6 Effects of uncertainties on the analysis

A complete summary of the uncertainties from statistics as well as systematic uncertainties can be found in table 5.8. This includes all evaluated uncertainties and their combination, taking into account the correlation between uncertainties where applicable.

5.11 Results

In table 5.9 the number of events passing the SR selection for each of the relevant MC samples as well as all uncertainties can be seen. These numbers are normalised to the luminosity found in the data. The total expected number of events is found to be $1.31 \pm 0.37^{\mathrm{stat}} \pm 0.65^{\mathrm{syst}}$, while 4 events are observed in the data. No statistically significant excess above the standard

Systematic	QCD	W + jets (true)	W + jets (fake)	Top (true)	Top (fake)	Z + jets	di-boson
JER	0.33	<0.002	1.1	-0.06	0.14	0.23	<0.002
JES ⇑	0.16	0.03	1.4	0.02	0.15	0.23	-0.33
JES ⇓	-0.09	-0.22	-0.90	-0.04	-0.10	<0.002	<0.002
TES ⇑	0.03	<0.002	0.07	-0.007	0.13	0.23	<0.002
TES ⇓	0.06	<0.002	0.20	-0.13	-0.10	<0.002	<0.002
Tau ID	0.07	0.06	-0.01	0.06	0.07	0.06	0.07
Pile-up	0.01	<0.002	0.20	-0.02	-0.05	<0.002	<0.002
STES ⇑	0.01	<0.002	<0.002	<0.002	<0.002	<0.002	<0.002
STES ⇓	-0.06	<0.002	<0.002	<0.002	<0.002	<0.002	<0.002
STR ⇑	0.04	<0.002	<0.002	<0.002	<0.002	<0.002	<0.002
STR ⇓	-0.01	<0.002	<0.002	<0.002	<0.002	<0.002	<0.002
Bjet ⇑	-0.02	0.05	0.33	-0.10	-0.08	0.02	<0.002
Bjet ⇓	0.04	-0.05	-0.07	0.09	0.08	-0.02	<0.002
Bjet (L) ⇑	0.01	-0.01	0.01	-0.02	-0.04	-0.004	-0.003
Bjet (L) ⇓	0.01	0.01	-0.06	-0.003	0.04	0.004	0.003
Method	0.50	0.21	—	—	—	—	—
Gen. DiBosons	—	<0.002	<0.002	<0.002	<0.002	0.05	0.04
Gen. $t\bar{t}$	—	—	—	0.15	0.15	—	—
Theory/Extr.	—	0.30	0.27	0.26	0.26	—	—
Total syst.	0.63	0.39	1.65	0.33	0.40	0.57	0.34
Stat.	0.21	0.70	1.13	0.38	0.81	1.0	—

Table 5.8: Overview of all systematic and statistical uncertainties for the one-tau channel. The uncertainties are presented in relative variations of the predicted number of background events. A statistical uncertainty is only listed for the channels which are found to contribute to the signal region.

model expectation is found. For comparison purposes the number of events accepted by the analysis in some selected signal points can be seen in table 5.10. These points are selected as they lie close to the border of expected exclusion limit.

The limits on the parameters of GMSB model are produced using the profile likelihood method [50] and the CL_S criterion [51]. The exclusion reach of this study at the 95% CL over the $\tan\beta$-Λ plane of the GMSB model (see section 5.2) is shown in figure 5.15. Models with $\Lambda < 45\,\text{TeV}$ (corresponding to gluino masses up to about 1000 GeV) for $40 > \tan\beta > 20$ are excluded. For lower values of $\tan\beta$ models with $\Lambda < 35\,\text{TeV}$ (gluino masses up to about 800 GeV) are excluded. As expected the exclusion is strongest for larger values of $\tan\beta$ where the stau is the NLSP. The results after the statistical combination with the two-tau, tau+muon and tau+electron channels, as well as the individual limits of each analysis are shown in figure 5.16. This leads to stronger exclusion of gluino masses up to about 1300 GeV for $40 > \tan\beta > 20$ and progressively worse for lower values, down to 1000 GeV. These results presented the strongest ATLAS limits for the GMSB model at the time of

top	$0.61 \pm 0.35^{\text{stat}} \pm 0.22^{\text{syst}}$
W + jets	$0.128 \pm 0.234^{\text{stat}} \pm 0.20^{\text{syst}}$
Z + jets	$0.22 \pm 0.22^{\text{stat}} \pm 0.13^{\text{syst}}$
QCD	$0.17 \pm 0.04^{\text{stat}} \pm 0.11^{\text{syst}}$
Drell-Yan	< 0.36
Diboson	< 0.05
Total	$1.31 \pm 0.37^{\text{stat}} \pm 0.65^{\text{syst}}$

Table 5.9: Number of expected event in the one-tau analysis SR from all contributing SM processes along with the statistical and systematic uncertainties. This leads to a final estimate of $1.31 \pm 0.37^{\text{stat}} \pm 0.65^{\text{syst}}$.

Λ	$\tan\beta$	Expected events	Stat. uncertainty	Cross section uncertainty	Syst. uncertainty
45	20	5.35	0.11	0.19	0.11
45	40	7.46	0.10	0.19	0.17
50	20	2.36	0.13	0.23	0.11
50	40	3.67	0.11	0.22	0.08
60	20	0.37	0.20	0.25	0.10
60	40	0.81	0.13	0.23	0.13

Table 5.10: Signal prediction and uncertainties in the one-tau analysis for six selected reference points from the GMSB grid around the expected exclusion contour. Uncertainties are relative.

publication.

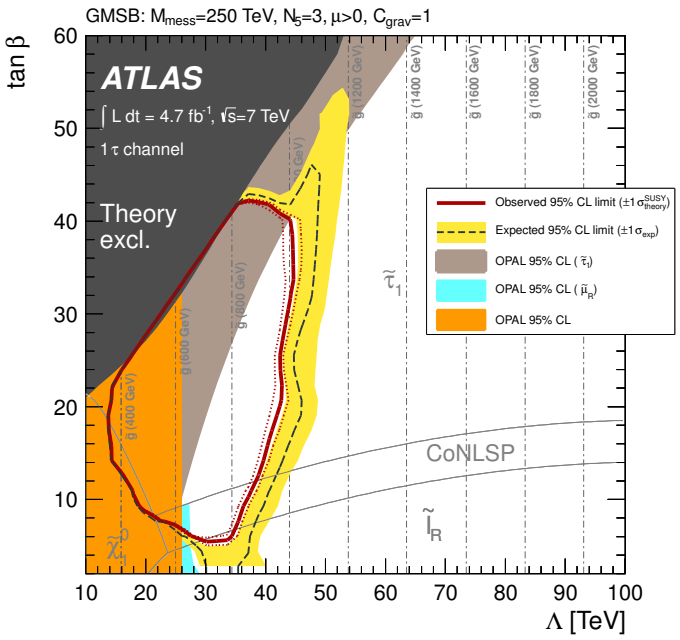

Figure 5.15: Exclusion contour of the one-tau analysis over the $\tan\beta - \Lambda$ parameter plane of the GMSB model. At the top of the plot the fixed parameters are displayed. The dashed vertical lines show the mass of gluinos in the model. The dark area corresponds to the region of parameter space excluded by theory, while the coloured regions correspond to the parameter space excluded by OPAL results.

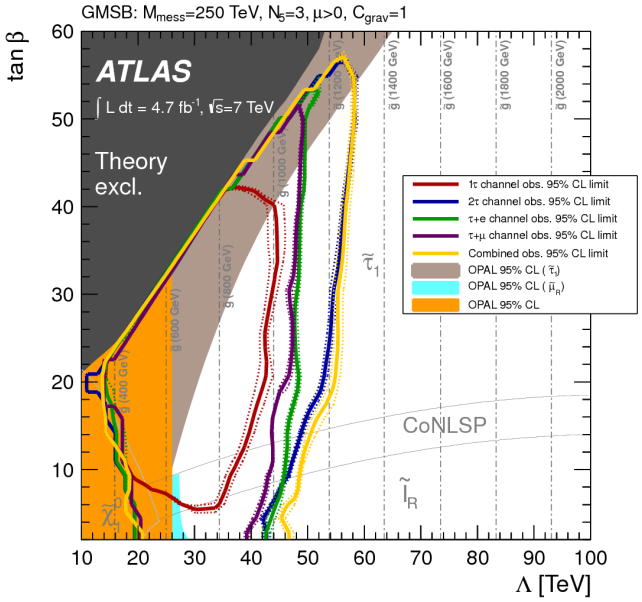

Figure 5.16: Exclusion contour of all channels in the analysis as well as the combined limit. The dashed vertical lines show the mass of gluinos in the model. The dark area corresponds to the region of parameter space excluded by theory, while the coloured regions correspond to the parameter space excluded by OPAL results.

Chapter 6

Conclusions

The work presented in the thesis covers many different levels of results from the ATLAS experiment at the LHC, each of them important to the working of the experiment and its physics goals.

The Inner Detector Global monitoring package was used throughout Run I to spot issues in the detector as they arose. The input from this package was important for checking the performance of the Inner Detector and excluding problematic data from physics analyses. All data in Run I passed through this monitoring and it forms part of the basis for monitoring the ID in Run II, the preparations for which have already started.

The measurements of minimum bias event spectra were crucial in enabling the tuning of MC generators as well as getting a better understanding of the type of event that form the pileup in the detector. These two factors are vital for making searches for new physics possible even under the effects of very high pileup during the increased luminosity at the end of Run I.

Chapter 4 presented a search for Supersymmetry using events with tau leptons performed on the full 2011 dataset, comprising 4.7 fb recorded at 7 TeV CoM energy. No signal above the Standard Model expectation was observed. The result was used to set limits on the GMSB model parameters which translates to lower limits on the sparticle masses. A followup paper was produced presenting the analysis of the full 2012 8 TeV dataset of 20.1 fb. This search included additional interpretations; the mSUGRA, nGM and bRPV models. SUSY is still a hypothetical model after Run I, no experiment has as of yet evidence of Supersymmetry.

As run I has come to its end the focus has shifter towards Run II of the LHC. This will not only bring an increase in CoM energy to 13 TeV, but also an increase in luminosity, with 100 fb^{-1} of data expected. This means a far greater physics reach but also challenges in understanding the detector. Run II is expected to start in Spring 2015.

Appendix A

List of samples considered in the SUSY study

A list of all the samples considered in the study presented, along with their identification number for ATLAS and their cross-section and number of events present in the samples.

Sample ID	Name	Generator	NNLO [pb]	No. of events
105200	$t\bar{t}$ semileptonic (T1)	MCAtNLOJimmy	90.57	14983835
105204	$t\bar{t}$ full hadronic	MCAtNLOJimmy	76.23	1199034
117360	t-channel $t \to e\nu$	AcerMCPythia	6.97	999295
117361	t-channel $t \to \mu\nu$	AcerMCPythia	6.97	999948
117362	t-channel $t \to \tau\nu$	AcerMCPythia	6.97	998995
108343	s-channel $t \to e\nu$	MCAtNLOJimmy	0.50	299948
108344	s-channel $t \to \mu\nu$	MCAtNLOJimmy	0.50	299998
108345	s-channel $t \to \tau\nu$	MCAtNLOJimmy	0.50	299899
108346	single top Wt	MCAtNLOJimmy	15.74	899694

Table A.1: Used $t\bar{t}$ and single t MC samples with their corresponding sample ID, event generator, NLO cross section and number of generated events.

Sample ID	Name	Generator	NNLO [pb]	# events
107680	WenuNp0	AlpgenJimmy	8288.88	3458883
107681	WenuNp1	AlpgenJimmy	1561.14	2499645
107682	WenuNp2	AlpgenJimmy	452.24	3768632
107683	WenuNp3	AlpgenJimmy	121.82	1008947
107684	WenuNp4	AlpgenJimmy	30.71	250000
107685	WenuNp5	AlpgenJimmy	8.36	69999
144022	WenuNp6_pt20	AlpgenJimmy	1.85	145000
144196	WenuNp1_susyfilt	AlpgenJimmy	8.83	180899
144197	WenuNp2_susyfilt	AlpgenJimmy	7.47	134998
144198	WenuNp3_susyfilt	AlpgenJimmy	4.15	139999
144199	WenuNp4_susyfilt	AlpgenJimmy	1.73	75000
107690	WmunuNp0	AlpgenJimmy	8284.22	3462942
107691	WmunuNp1	AlpgenJimmy	1560.55	2498593
107692	WmunuNp2	AlpgenJimmy	451.79	3768737
107693	WmunuNp3	AlpgenJimmy	121.71	1008446
107694	WmunuNp4	AlpgenJimmy	30.74	254950
107695	WmunuNp5	AlpgenJimmy	8.37	70000
144023	WmunuNp6_pt20	AlpgenJimmy	1.85	145000
144200	WmunuNp1_susyfilt	AlpgenJimmy	8.46	171000
144201	WmunuNp2_susyfilt	AlpgenJimmy	7.34	139900
144202	WmunuNp3_susyfilt	AlpgenJimmy	4.09	139899
144203	WmunuNp4_susyfilt	AlpgenJimmy	1.73	70000
107700	WtaunuNp0	AlpgenJimmy	8283.50	3418296
107701	WtaunuNp1	AlpgenJimmy	1559.36	2499194
107702	WtaunuNp2	AlpgenJimmy	451.63	3750986
107703	WtaunuNp3	AlpgenJimmy	121.84	1009946
107704	WtaunuNp4	AlpgenJimmy	30.72	249998
107705	WtaunuNp5	AlpgenJimmy	8.37	65000
144024	WtaunuNp6_pt20	AlpgenJimmy	1.85	150000
144204	WtaunuNp1_susyfilt	AlpgenJimmy	13.08	265000
144205	WtaunuNp2_susyfilt	AlpgenJimmy	11.06	204999
144206	WtaunuNp3_susyfilt	AlpgenJimmy	6.09	209900
144207	WtaunuNp4_susyfilt	AlpgenJimmy	2.52	104999

Table A.2: Used W + jets MC samples with their corresponding sample ID, event generator, LO cross section, and section, k-factor, NNLO cross section and number of generated events. Samples marked "susyfilt" have been produced with a truth level filter requiring one jet of at least 100 GeV p_{T} and at least 100 GeV of missing transverse energy.

Sample ID	Name	Generator	NNLO [pb]	# events
107650	ZeeN0p	AlpgenJimmy	832.61	6618284
107651	ZeeN1p	AlpgenJimmy	167.31	1334897
107652	ZeeN2p	AlpgenJimmy	50.55	2004195
107653	ZeeN3p	AlpgenJimmy	14.00	549949
107654	ZeeN4p	AlpgenJimmy	3.53	149948
107655	ZeeN5p	AlpgenJimmy	0.95	50000
107660	ZmumuN0p	AlpgenJimmy	832.61	6615230
107661	ZmumuN1p	AlpgenJimmy	167.31	1334296
107662	ZmumuN2p	AlpgenJimmy	50.55	1999941
107663	ZmumuN3p	AlpgenJimmy	14.00	549896
107664	ZmumuN4p	AlpgenJimmy	3.53	150000
107665	ZmumuN5p	AlpgenJimmy	0.95	50000
107670	ZtautauN0p	AlpgenJimmy	832.61	10613179
107671	ZtautauN1p	AlpgenJimmy	167.31	3334137
107672	ZtautauN2p	AlpgenJimmy	50.55	1004847
107673	ZtautauN3p	AlpgenJimmy	14.00	509847
107674	ZtautauN4p	AlpgenJimmy	3.53	144999
107675	ZtautauN5p	AlpgenJimmy	0.95	45000
107710	ZnunuNp0	AlpgenJimmy	49.93	54949
107711	ZnunuNp1	AlpgenJimmy	569.09	909848
107712	ZnunuNp2	AlpgenJimmy	247.68	169899
107713	ZnunuNp3	AlpgenJimmy	75.45	144999
107714	ZnunuNp4	AlpgenJimmy	19.55	309899
107715	ZnunuNp5	AlpgenJimmy	5.42	189998

Table A.3: Used Z + jets MC samples with their corresponding sample ID, event generator, LO cross section, k-factor, NNLO cross section, and number of generated events.

Sample ID	Generator	Final state	NLO [pb]	No. of events
105921	McAtNlo_JIMMY	$W^{\pm} \to e\nu e\nu$	0.51	199949
105922	McAtNlo_JIMMY	$W^{\pm} \to e\nu\mu\nu$	0.51	200000
105923	McAtNlo_JIMMY	$W^{\pm} \to e\nu\tau\nu$	0.51	200000
105924	McAtNlo_JIMMY	$W^{\pm} \to \mu\nu\mu\nu$	0.51	199000
105925	McAtNlo_JIMMY	$W^{\pm} \to \mu\nu e\nu$	0.51	199949
105926	McAtNlo_JIMMY	$W^{\pm} \to \mu\nu\tau\nu$	0.51	200000
105927	McAtNlo_JIMMY	$W^{\pm} \to \tau\nu\tau\nu$	0.51	499676
105928	McAtNlo_JIMMY	$W^{\pm} \to \tau\nu e\nu$	0.51	199950
105929	McAtNlo_JIMMY	$W^{\pm} \to \tau\nu\mu\nu$	0.51	200000
105930	McAtNlo_JIMMY	$ZZ \to \ell\ell q\bar{q}$	0.270	25000
105931	McAtNlo_JIMMY	$ZZ \to \ell\ell\ell\ell$	0.026	99999
105932	McAtNlo_JIMMY	$ZZ \to \ell\ell\nu\nu$	0.077	99999
106036	McAtNlo_JIMMY	$ZZ \to 2\ell 2\tau$	1.695	25000
106037	McAtNlo_JIMMY	$ZZ \to 4\tau$	0.164	25000
113192	McAtNlo_JIMMY	$ZZ \to \tau\tau\nu\nu$	0.514	24950
113193	McAtNlo_JIMMY	$ZZ \to \tau\tau q\bar{q}$	0.928	25000
105940	McAtNlo_JIMMY	$W^{+}Z \to \ell\nu q\bar{q}$	0.090	100000
105941	McAtNlo_JIMMY	$W^{+}Z \to \ell\nu\ell\ell$	0.28	100000
105942	McAtNlo_JIMMY	$W^{+}Z \to q\bar{q}'\ell\ell$	0.086	25000
106024	McAtNlo_JIMMY	$W^{+}Z \to \tau\nu\ell\ell$	0.082	25000
106025	McAtNlo_JIMMY	$W^{+}Z \to \ell\nu\tau\tau$	0.043	199950
106026	McAtNlo_JIMMY	$W^{+}Z \to \tau\nu\tau\tau$	0.047	25000
113190	McAtNlo_JIMMY	$W^{+}Z \to q\bar{q}'\tau\tau$	0.045	25000
105970	McAtNlo_JIMMY	$W^{-}Z \to \ell\nu q\bar{q}$	0.0234	200000
105971	McAtNlo_JIMMY	$W^{-}Z \to \ell\nu\ell\ell$	0.0129	25000
105972	McAtNlo_JIMMY	$W^{-}Z \to q\bar{q}'\ell\ell$	0.0065	25000
106027	McAtNlo_JIMMY	$W^{-}Z \to \tau\nu\ell\ell$	0.2568	199949
106028	McAtNlo_JIMMY	$W^{-}Z \to \ell\nu\tau\tau$	0.1397	200000
106029	McAtNlo_JIMMY	$W^{-}Z \to \tau\nu\tau\tau$	0.0386	200000
113191	McAtNlo_JIMMY	$W^{-}Z \to q\bar{q}'\tau\tau$	0.1348	199950

Table A.4: Used diboson MC samples with their corresponding sample ID, event generator, final state, NLO cross section, and number of generated events.

Sample ID	Name	Generator	LO [pb]	No. of events
105009	J0	Pythia	12030000000	999997
105010	J1	Pythia	807266000	999993
105011	J2	Pythia	48048000	999999
105012	J3	Pythia	2192900	999992
105013	J4	Pythia	87701	989992
105014	J5	Pythia	2350.1	999987
105015	J6	Pythia	33.61	999974
105016	J7	Pythia	0.13744	998955
105017	J8	Pythia	0.000006	998948

Table A.5: Used dijet MC samples with their corresponding sample ID, event generator, cross section and number of generated events.

Sample ID	Name	Generator	NNLO [pb]	# events
116250	ZeeNp0Mll10to40	AlpgenJimmy	3798.37	994949
116251	ZeeNp1Mll10to40	AlpgenJimmy	105.58	299998
116252	ZeeNp2Mll10to40	AlpgenJimmy	51.22	999946
116253	ZeeNp3Mll10to40	AlpgenJimmy	10.38	149998
116254	ZeeNp4Mll10to40	AlpgenJimmy	2.30	40000
116255	ZeeNp5Mll10to40	AlpgenJimmy	0.57	10000
116260	ZmumuNp0Mll10to40	AlpgenJimmy	3798.62	999849
116261	ZmumuNp1Mll10to40	AlpgenJimmy	105.42	300000
116262	ZmumuNp2Mll10to40	AlpgenJimmy	51.14	999995
116263	ZmumuNp3Mll10to40	AlpgenJimmy	10.37	150000
116264	ZmumuNp4Mll10to40	AlpgenJimmy	2.33	39999
116265	ZmumuNp5Mll10to40	AlpgenJimmy	0.57	10000
116270	ZtautauNp0Mll10to40	AlpgenJimmy	3798.49	999649
116271	ZtautauNp1Mll10to40	AlpgenJimmy	105.54	299999
116272	ZtautauNp2Mll10to40	AlpgenJimmy	51.33	498899
116273	ZtautauNp3Mll10to40	AlpgenJimmy	10.38	150000
116274	ZtautauNp4Mll10to40	AlpgenJimmy	2.28	39999
116275	ZtautauNp5Mll10to40	AlpgenJimmy	0.57	10000

Table A.6: Used Drell-Yan MC samples with their corresponding sample ID, event generator, LO cross section, k-factor, NNLO cross section and number of generated events.

Sample	Λ [TeV]	$\tan\beta$	σ [pb]
137915	10	2	552.595
137916	10	5	552.996
137917	10	10	552.960
137918	10	15	552.166
137919	10	20	661.116
137920	10	21	659.621
143061	12	21	312.079
143055	15	2	106.275
143056	15	5	109.792
143057	15	10	102.78
143058	15	15	100.390
143059	15	20	99.823
143060	15	23	100.555
137921	20	2	21.666
137922	20	5	22.427
137923	20	10	21.964
137924	20	15	21.795
137925	20	20	21.846
137926	20	27	22.994
137927	30	2	2.212
137928	30	5	2.344
137929	30	10	2.339
137930	30	15	2.337
137931	30	20	2.346
137932	30	30	2.458
137933	30	36	3.207
142558	35	2	0.882
142559	35	5	0.951
142560	35	10	0.956
142561	35	15	0.958
142562	35	20	0.963
142563	35	25	0.974
142564	35	30	1.000
142565	35	35	1.073
142566	35	40	1.546
142567	35	42	2.962
137934	40	2	0.389
137935	40	5	0.427
137936	40	10	0.433
137937	40	15	0.434
137938	40	20	0.436
137939	40	25	0.442
137940	40	30	0.452
137941	40	36	0.484
137942	40	40	0.546
137943	40	46	1.814
142568	45	2	0.184
142569	45	5	0.208
142570	45	10	0.213
142571	45	15	0.214
142572	45	20	0.215
142573	45	25	0.218
142574	45	30	0.223
142575	45	35	0.233
142576	45	40	0.256
142577	45	50	1.327
137944	50	2	0.093
137945	50	5	0.109
137946	50	10	0.112
137947	50	15	0.113
137948	50	20	0.114
137949	50	30	0.118
137950	50	40	0.133
137951	50	50	0.248
137952	60	2	0.028
137953	60	5	0.035
137954	60	10	0.037
137955	60	15	0.038
137956	60	20	0.038
137957	60	30	0.040
137958	60	40	0.044
137959	60	50	0.060
137960	70	2	0.011
137961	70	5	0.014
137962	70	10	0.015
137963	70	15	0.015
137964	70	20	0.016
137965	70	30	0.016
137966	70	40	0.018
137967	70	50	0.022
137968	80	2	0.0046
137969	80	5	0.0063
137970	80	10	0.0070
137971	80	15	0.0072
137972	80	20	0.0073
137973	80	30	0.0076
137974	80	40	0.0084
137975	80	50	0.0101

Table A.7: List of MC samples for SUSY signal. All samples are generated using Herwig++. Four out of six parameters defining the GMSB points are the same for all samples: $M_{\text{mess}} = 250$ TeV, $N_5 = 3$, sign(μ) = +, and C_{grav}. The parameters Λ and $\tan\beta$ are varied as shown in the table.

Appendix B

Event displays from Supersymmetry analysis

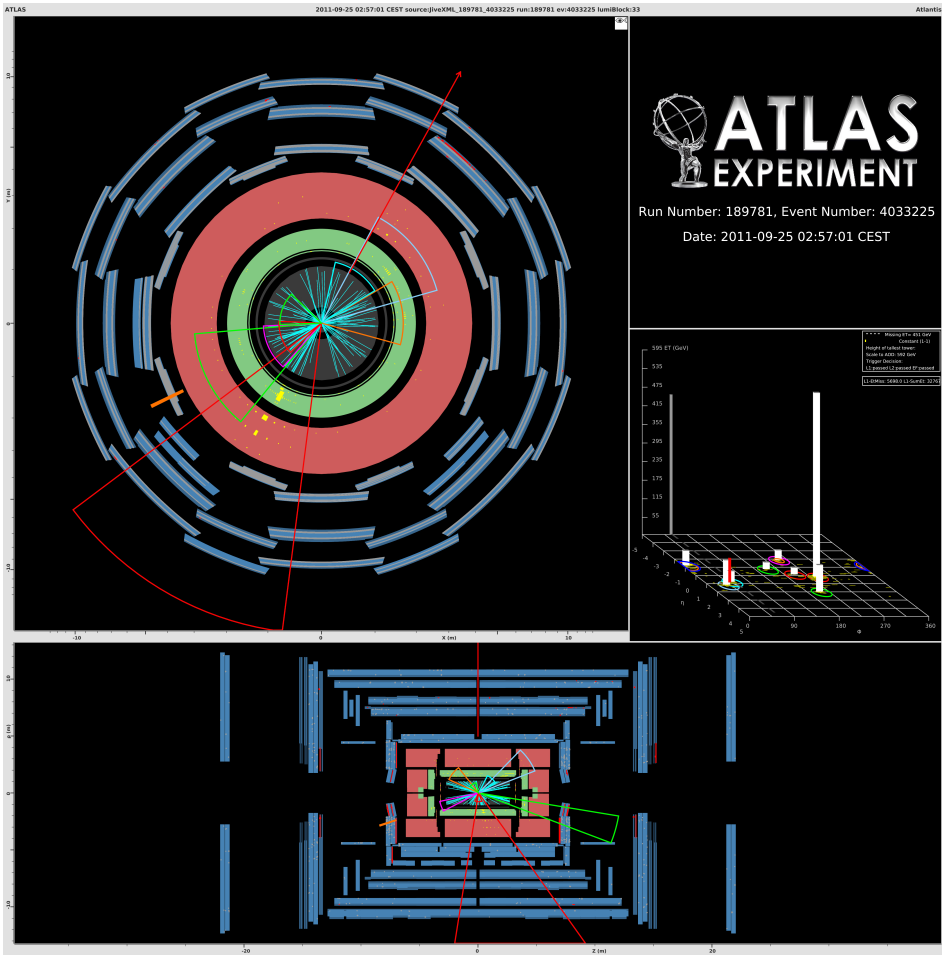

Figure B.1: Event selected in the SR of the supersymmetry with taus analysis. The $p_{mathrmT}$ of the leading and sub-leading jets are 592 GeV (red) and 86 GeV (green) respectively. The selected tau p_{T} is 32 GeV (orange spike in prolongation of jet axis). $E_{\mathrm{T}}^{\mathrm{miss}}$ is 478 GeV (red arrow).

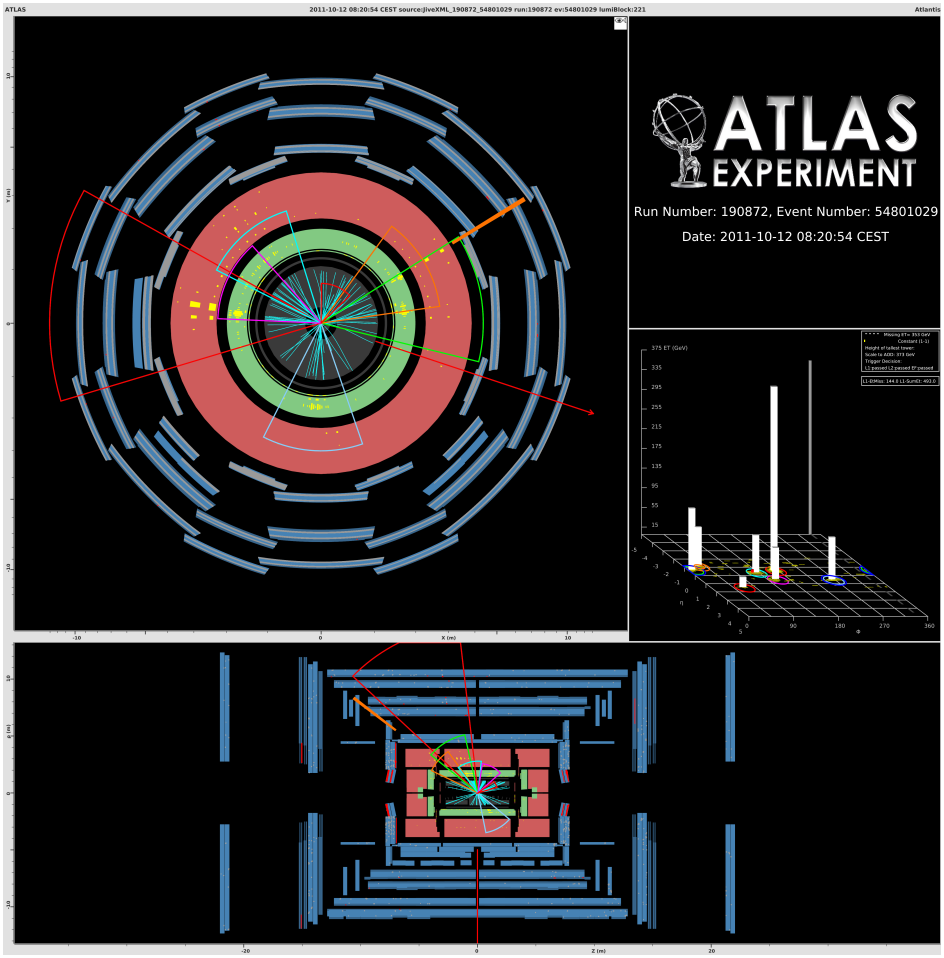

Figure B.2: Event selected in the SR of the supersymmetry with taus analysis. The $p_{mathrmT}$ of the leading and sub-leading jets are 372 GeV (red) and 124 GeV (green) respectively. The selected tau p_{T} is 66 GeV (orange spike in prolongation of jet axis). $E_{\mathrm{T}}^{\mathrm{miss}}$ is 324 GeV (red arrow).

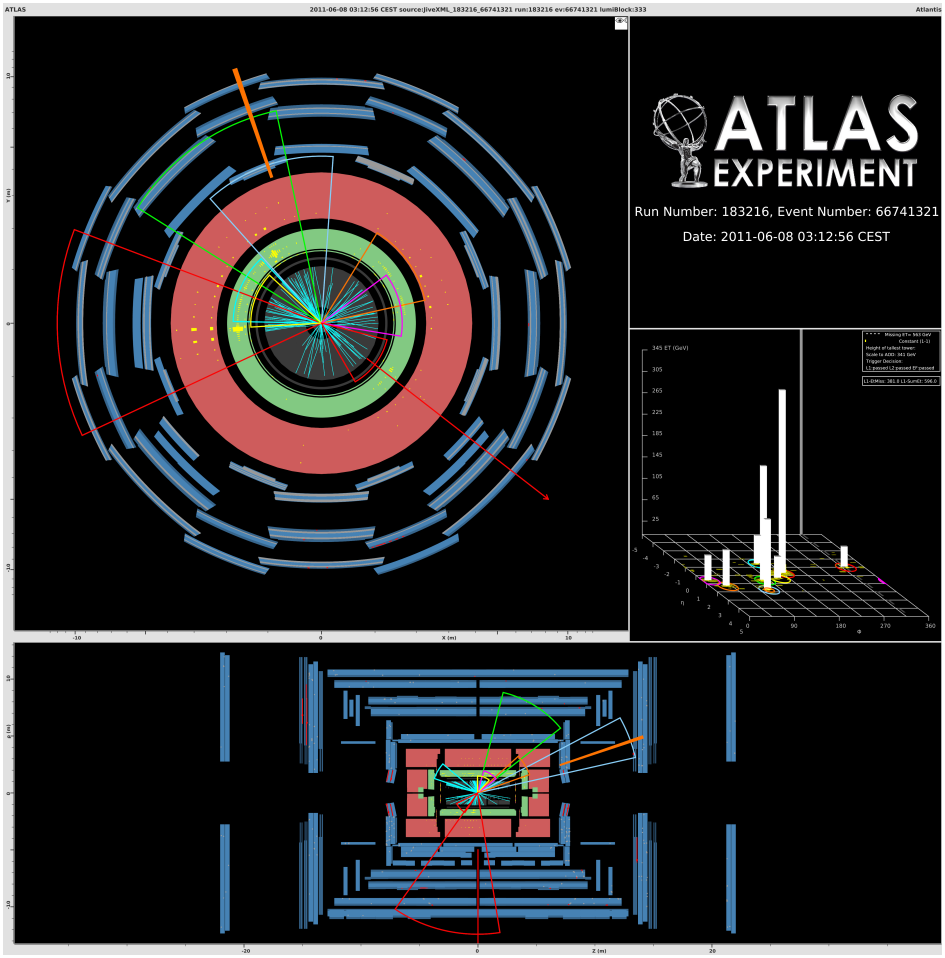

Figure B.3: Event selected in the SR of the supersymmetry with taus analysis. The $p_{mathrmT}$ of the leading and sub-leading jets are 341 GeV (red) and 212 GeV (green) respectively. The selected tau p_{T} is 109 GeV (orange spike in prolongation of jet axis). $E_{\mathrm{T}}^{\mathrm{miss}}$ is 507 GeV (red arrow).

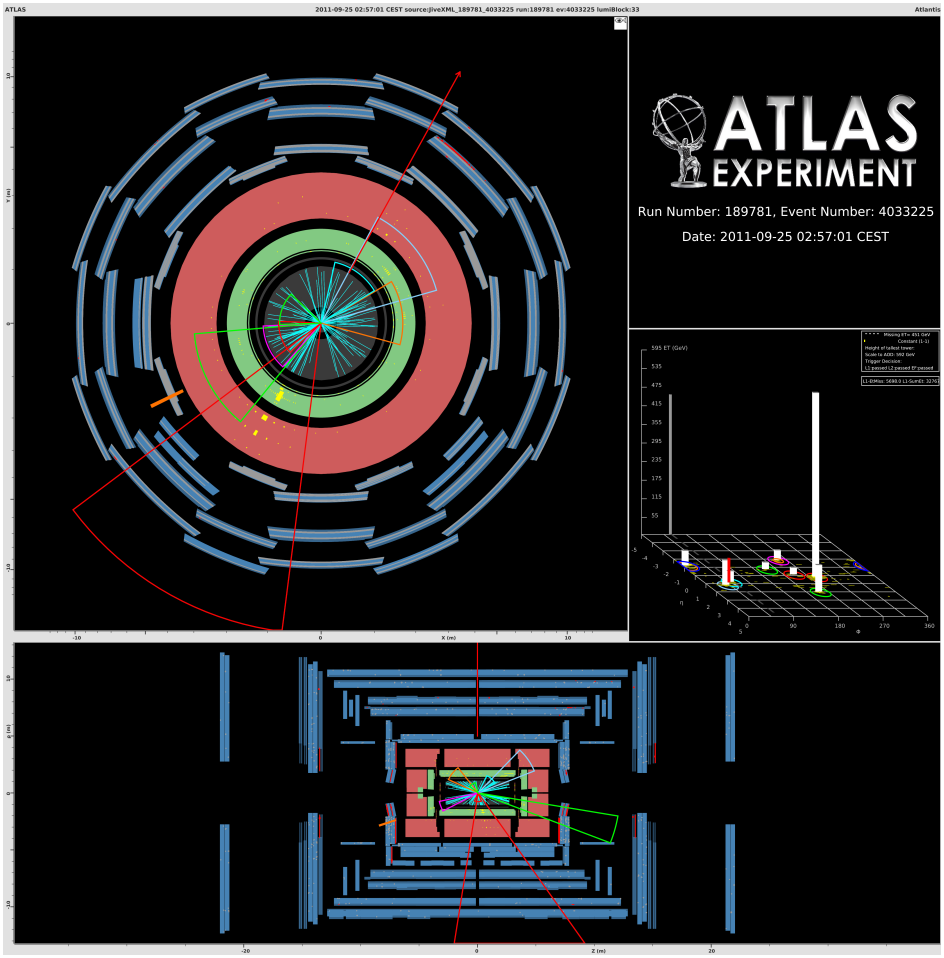

Figure B.4: Event selected in the SR of the supersymmetry with taus analysis. The $p_{mathrmT}$ of the leading and sub-leading jets are 386 GeV (red) and 188 GeV (green) respectively. The selected tau p_{T} is 266 GeV (orange spike in prolongation of jet axis). $E_{\mathrm{T}}^{\mathrm{miss}}$ is 300 GeV (red arrow).

Bibliography

[1] ATLAS Collaboration. Search for Supersymmetry in Events with Large Missing Transverse Momentum, Jets, and at Least One Tau Lepton in 21 fb^{-1} of $\sqrt{s} = 8$ TeV Proton-Proton Collision Data with the ATLAS Detector. Technical Report ATLAS-CONF-2013-026, CERN, Geneva, Mar 2013.

[2] ATLAS Collaboration. Search for supersymmetry in events with large missing transverse momentum, jets, and at least one tau lepton in 20 fb^{-1} of $\sqrt{s} = 8$ tev proton-proton collision data with the atlas detector. *Journal of High Energy Physics*, 2014(9), 2014.

[3] ATLAS Collaboration. The ATLAS Experiment at the CERN Large Hadron Collider. *Journal of Instrumentation*, 3(08):S08003, 2008.

[4] O. S. Brüning et al. *LHC Design Report*. CERN, Geneva, 2004.

[5] Picture courtesy of CERN.

[6] J. J. Goodson. Search for supersymmetry in states with large missing transverse momentum and three leptons including a z-boson. May 2012. Presented 17 Apr 2012.

[7] T. Cornelissen et al. Concepts, Design and Implementation of the ATLAS New Tracking (NEWT). Technical Report ATL-SOFT-PUB-2007-007, CERN, Geneva, Mar 2007.

[8] ATLAS Collaboration. Performance of the ATLAS Inner Detector Track and Vertex Reconstruction in the High Pile-Up LHC Environment. Technical Report ATLAS-CONF-2012-042, CERN, Geneva, Mar 2012.

[9] Gavin P. Salam. Towards Jetography. *European Physical Journal C*, 67:637, 2010. 88 pages, 27 figures, an extended version of lectures given at the CTEQ/MCNET school, Debrecen, Hungary, August 2008.

[10] ATLAS Collaboration. Jet energy measurement with the ATLAS detector in proton-proton collisions at $\sqrt{s} = 7$ TeV. *Eur.Phys.J.*, C73:2304, 2013.

[11] ATLAS Collaboration. Commissioning of the ATLAS high-performance b-tagging algorithms in the 7 TeV collision data. Technical Report ATLAS-CONF-2011-102, CERN, Geneva, Jul 2011.

[12] G. Piacquadio and C. Weiser. A new inclusive secondary vertex algorithm for b-jet tagging in atlas. *Journal of Physics: Conference Series*, 119(3):032032, 2008.

[13] Particle Data Group. Review of particle physics. *Phys. Rev. D*, 86:010001, Jul 2012.

[14] ATLAS Collaboration. Performance of the Reconstruction and Identification of Hadronic Tau Decays in ATLAS with 2011 Data. Technical Report ATLAS-CONF-2012-142, CERN, Geneva, Oct 2012.

[15] ATLAS Collaboration. Performance of Missing Transverse Momentum Reconstruction in Proton-Proton Collisions at 7 TeV with ATLAS. *Eur.Phys.J.*, C72:1844, 2012.

[16] R. Brun and F. Rademakers. Root - an object oriented data analysis framework. pages 81–86, September 1996.

[17] P. Adragna A. Dotti and R. A. Vitillo. The Online Histogram Presenter for the ATLAS experiment: a modular system for histogram visualization. Technical Report ATL-DAQ-PUB-2009-009, CERN, Geneva, Sep 2009.

[18] Y. Ilchenko et al. Data Quality Monitoring Display for ATLAS experiment. May 2009. Poster at CHEP 2009 conference.

[19] J. Adelman et al. ATLAS offline data quality monitoring. *Journal of Physics: Conference Series*, 219(4):042018, 2010.

[20] ATLAS Collaboration. Characterization of Interaction-Point Beam Parameters Using the pp Event-Vertex Distribution Reconstructed in the ATLAS Detector at the LHC. Technical Report ATLAS-CONF-2010-027, CERN, Geneva, May 2010.

[21] T. Golling et al. The ATLAS Data Quality Defect Database System. *Eur.Phys.J.*, C72:1960, 2012.

[22] ATLAS Collaboration. Charged-particle multiplicities in pp interactions measured with the atlas detector at the lhc. *New J. Phys.*, 13(arXiv:1012.5104. CERN-PH-EP-2010-079):053033. 70 p, Dec 2010. Comments: 57 pages plus author list (82 pages total), 19 figures (85 independent .eps files), 10 tables.

[23] G. D'Agostini. A multidimensional unfolding method based on Bayes' theorem. *Nucl. Instr. Meth. in Physics Research Section A*, 362(2–3):487 – 498, 1995.

[24] ATLAS Collaboration. Charged particle multiplicities in p p interactions at $\sqrt{s}$ = 0.9 and 7 TeV in a diffractive limited phase-space measured with the ATLAS detector at the LHC and new PYTHIA6 tune. Technical Report ATLAS-CONF-2010-031, CERN, Geneva, Jul 2010.

[25] R. Engel F. W. Bopp and J. Ranft. Rapidity gaps and the PHOJET Monte Carlo. pages 729–741, 1998.

[26] H. Miyazawa. Baryon Number Changing Currents. *Prog. Theor. Phys.*, 36 (6):1266–1276, 1966.

[27] S. Dimopoulos and H. Georgi. Softly Broken Supersymmetry and SU(5). *Nucl. Phys.*, B193:150, 1981.

[28] H. Goldberg. Constraint on the photino mass from cosmology. *Phys. Rev. Lett.*, 50:1419, 1983.

[29] J.R. Ellis, J.S. Hagelin, D.V. Nanopoulos, K.A. Olive, and M. Srednicki. Supersymmetric relics from the big bang. *Nucl. Phys.*, B238:453–476, 1984.

[30] S. Dimopoulos, S. Raby, and Frank Wilczek. Supersymmetry and the Scale of Unification. *Phys. Rev.*, D24:1681–1683, 1981.

[31] Michael Dine and Willy Fischler. A Phenomenological Model of Particle Physics Based on Supersymmetry. *Phys. Lett.*, B110:227, 1982.

[32] Luis Alvarez-Gaume, Mark Claudson, and Mark B. Wise. Low-Energy Supersymmetry. *Nucl. Phys.*, B207:96, 1982.

[33] Chiara R. Nappi and Burt A. Ovrut. Supersymmetric Extension of the SU(3) x SU(2) x U(1) Model. *Phys. Lett.*, B113:175, 1982.

[34] Michael Dine and Ann E. Nelson. Dynamical supersymmetry breaking at low-energies. *Phys. Rev.*, D48:1277–1287, 1993.

[35] Michael Dine, Ann E. Nelson, and Yuri Shirman. Low-energy dynamical supersymmetry breaking simplified. *Phys. Rev.*, D51:1362–1370, 1995.

[36] Michael Dine, Ann E. Nelson, Yosef Nir, and Yuri Shirman. New tools for low-energy dynamical supersymmetry breaking. *Phys. Rev.*, D53:2658–2669, 1996.

[37] G. Abbiendi et al. Search for chargino and neutralino production at $\sqrt{s}$ = 192 GeV to 209 GeV at LEP. *Eur.Phys.J.*, C35:1–20, 2004.

[38] ATLAS Collaboration. Expected performance of the ATLAS detector in GMSB models with tau final states. Technical Report ATL-PHYS-PUB-2009-089, CERN, Geneva, Nov 2009.

[39] Andy Buckley. PySLHA. `http://www.insectnation.org/projects/pyslha`. Accessed: 2012-08-20.

[40] S. Frixione and B. R. Webber. Matching NLO QCD computations and parton shower simulations. *JHEP*, 06:029, 2002.

[41] G. Corcella et al. HERWIG 6: An event generator for hadron emission reactions with interfering gluons (including supersymmetric processes). *JHEP*, 0101:010, 2001.

[42] B. P. Kersevan and E. Richter-Was. The Monte Carlo event generator AcerMC version 2.0 with interfaces to PYTHIA 6.2 and HERWIG 6.5. 2004.

[43] S. Mrenna T. Sjostrand and P. Z. Skands. PYTHIA 6.4 Physics and Manual. *JHEP*, 0605:026, 2006.

[44] M. L. Mangano et al. ALPGEN, a generator for hard multiparton processes in hadronic collisions. *JHEP*, 0307:001, 2003.

[45] J. R. Forshaw J. M. Butterworth and M. H. Seymour. Multiparton interactions in photoproduction at HERA. *Z.Phys.*, C72:637–646, 1996.

[46] S. D. Protopopescu H. Baer, F. E. Paige and X. Tata. ISAJET 7.48: A Monte Carlo event generator for p p, anti-p, p, and e+ e- reactions. 1999.

[47] ATLAS Collaboration. Selection of jets produced in proton-proton collisions with the ATLAS detector using 2011 data. Technical Report ATLAS-CONF-2012-020, CERN, Geneva, Mar 2012.

[48] Determination of the tau energy scale and the associated systematic uncertainty in proton-proton collisions at sqrts = 7 TeV with the ATLAS detector at the LHC in 2011. Technical Report ATLAS-CONF-2012-054, CERN, Geneva, Jun 2012.

[49] Jet energy scale and its systematic uncertainty in proton-proton collisions at sqrt(s)=7 TeV with ATLAS 2011 data. Technical Report ATLAS-CONF-2013-004, CERN, Geneva, Jan 2013.

[50] Glen Cowan, Kyle Cranmer, Eilam Gross, and Ofer Vitells. Asymptotic formulae for likelihood-based tests of new physics. *Eur.Phys.J.*, C71:1554, 2011.

[51] A. L. Read. Presentation of search results: the cl s technique. *Journal of Physics G: Nuclear and Particle Physics*, 28(10):2693, 2002.

Acronyms

AOD Analysis Object Data . . . 21
ATLAS A Toroidal LHC ApparatuS
BCID Bunch Crossing IDentification . . . 24
BDT Boosted Desicion Tree . . . 17
CP Combined Performance . . . 39
CR Control Region . . . 65
CSC Cathode Strip Chambers . . . 11
CoM Center of Mass . . . 1
DAQ Data AQuisition . . . 21
DB DataBase . . . 29
DM Dark Matter . . . 57
DQ Data Quality . . . 23
EF Event Filter . . . 20
EMES Electro-Magnetic Energy Scale . . . 11
ESD Event Summary Data . . . 21
fCal Forward Calorimeter . . . 8
GMSB Gauge Mediated Symmetry Breaking . . . 57
GRL Good Run List . . . 35
HEC Hadronic Endcap Calorimeter . . . 8
HLT High Level Trigger . . . 19
ID Inner Detector . . . 4
IP Impact Parameter . . . 17
JER Jet Energy Resolution . . . 80
JES Jet Energy Scale . . . 11
L1 Level one . . . 12
L2 Level two . . . 20

LAr	Liquid Argon Calorimeter . . . 8
LB	Luminosity Block . . . 14
LEP	Large Electron Positron Collider . . . 3
LHC	Large Hadron Collider . . . 1
LSP	Lightest Supersymmetric Particle . . . 58
MBTS	Minimum Bias Trigger Scintillator . . . 20
MC	Monte Carlo . . . 42
MDT	Monitored Drift Tubes . . . 11
MSSM	Minimal Supersymmetric Standard Model . . . 57
MS	Muon Spectrometer
NLSP	Next-to-Lightest Supersymmetric Particle . . . 58
PMT	PhotoMultiplier Tube . . . 10
QCD	Quantum Chromodynamics . . . 11
ROD	Read Out Driver . . . 24
RPC	Resistive Plate Chambers . . . 11
SCT	SemiConductor Tracker . . . 6
SF	Scale Factor . . . 65
SM	Standard Model . . . 1
SR	Signal Region . . . 60
SUSY	Supersymmetry . . . 13
TES	Tau Energy Scale . . . 16
TGC	Thin Gap Chambers . . . 11
TRT	Transition Radiation Tracker . . . 6
VEV	Vacuum Expectation Value . . . 58

List of Figures

List of Tables

Paper I

CERN-PH-EP-2010-079
(Accepted by New J. Phys.)

February 9, 2011

Charged-particle multiplicities in pp interactions measured with the ATLAS detector at the LHC

The ATLAS Collaboration

Abstract

Measurements are presented from proton-proton collisions at centre-of-mass energies of $\sqrt{s}$ = 0.9, 2.36 and 7 TeV recorded with the ATLAS detector at the LHC. Events were collected using a single-arm minimum-bias trigger. The charged-particle multiplicity, its dependence on transverse momentum and pseudorapidity and the relationship between the mean transverse momentum and charged-particle multiplicity are measured. Measurements in different regions of phase-space are shown, providing diffraction-reduced measurements as well as more inclusive ones. The observed distributions are corrected to well-defined phase-space regions, using model-independent corrections. The results are compared to each other and to various Monte Carlo models, including a new AMBT1 PYTHIA6 tune. In all the kinematic regions considered, the particle multiplicities are higher than predicted by the Monte Carlo models. The central charged-particle multiplicity per event and unit of pseudorapidity, for tracks with $p_{\mathrm{T}} > 100$ MeV, is measured to be 3.483 ± 0.009 (stat) ± 0.106 (syst) at $\sqrt{s}$ = 0.9 TeV and 5.630 ± 0.003 (stat) ± 0.169 (syst) at $\sqrt{s}$ = 7 TeV.

Contents

1 Introduction

Inclusive charged-particle distributions have been previously measured in pp and $p\bar{p}$ collisions at a range of different centre-of-mass energies [1–17]. These measurements provide insight into the strong interactions at low energy-scales. Several QCD-inspired models have been developed to interpret them. These models are frequently cast into Monte Carlo simulations with free parameters that can be constrained by measurements such as minimum bias distributions. These measurements contribute to the understanding of soft QCD; moreover, they are important to determination of biases on high-p_{T} phenomena due to underlying events and event pileup effects and are therefore of growing importance for future LHC physics. The measurements presented in this paper implement a similar strategy to that in [1]. A single-arm trigger overlapping with the acceptance of the tracking volume is used. Results are presented as inclusive-inelastic distributions, with minimal model-dependence; a minimum number of charged particles within well-defined p_{T} and η selection are required.

This paper reports on measurements of primary charged-particle multiplicity distributions using the first ~190 $\mu\mathrm{b}^{-1}$ of data recorded by the ATLAS experiment at 7 TeV and ~7 $\mu\mathrm{b}^{-1}$ at 0.9 TeV. At $\sqrt{s}$ = 0.9 TeV the sample is similar to that used for the first ATLAS minimum-bias publication [1]. Results are also presented at $\sqrt{s}$ = 2.36 TeV where the track reconstruction setup differs significantly from that at the other energies, due to the Silicon Tracker (SCT) not being at nominal voltage. The integrated luminosity at this energy is estimated to be ~0.1 $\mu\mathrm{b}^{-1}$.

The following distributions are measured in this paper:

$$\frac{1}{N_{\mathrm{ev}}}\cdot\frac{\mathrm{d}N_{\mathrm{ch}}}{\mathrm{d}\eta},\quad \frac{1}{N_{\mathrm{ev}}}\cdot\frac{1}{2\pi p_{\mathrm{T}}}\cdot\frac{\mathrm{d}^2N_{\mathrm{ch}}}{\mathrm{d}\eta\mathrm{d}p_{\mathrm{T}}},\quad \frac{1}{N_{\mathrm{ev}}}\cdot\frac{\mathrm{d}N_{\mathrm{ev}}}{\mathrm{d}n_{\mathrm{ch}}}\quad\text{and}\quad \langle p_{\mathrm{T}}\rangle \text{ vs. } n_{\mathrm{ch}},$$

where p_{T} is the charged particle momentum component transverse to the beam direction [1], η is the pseudorapidity of the particle, n_{ch} is the number of charged particles in an event, N_{ev} is the number of events with a minimum number of charged particles within the selected kinematic range, N_{ch} is the total number of charged particles in the data sample and $\langle p_{\mathrm{T}}\rangle$ is the average p_{T} for a given number of charged particles [2]. Primary charged particles are defined as charged particles with a mean lifetime $\tau > 0.3\cdot 10^{-10}$ s either directly produced in pp interactions or from subsequent decays of particles with a shorter lifetime.

The charged-particle multiplicity results are compared to particle level Monte Carlo (MC) predictions. Three different phase-space regions are considered in this paper, with varying selection both on the p_{T} and the number of charged particles per event; all phase-space regions require tracks within $|\eta| < 2.5$. Diffractive physics is expected to contribute mostly at low numbers of charged particles and at low track momentum. Therefore varying the selection on n_{ch} and p_{T} in effect varies the relative contribution from diffractive events. Appendix B shows the results for two additional phase-space regions useful for Monte Carlo tuning. This measurement, with refined corrections and systematic uncertainty determination supersedes the results presented in [1].

2 The ATLAS Detector

The ATLAS detector [18] at the Large Hadron Collider (LHC) [19] covers almost the whole solid angle around the collision point with layers of tracking detectors, calorimeters and muon chambers. It has been

[1] The ATLAS reference system is a Cartesian right-handed co-ordinate system, with the nominal collision point at the origin. The anti-clockwise beam direction defines the positive z-axis, while the positive x-axis is defined as pointing from the collision point to the centre of the LHC ring and the positive y-axis points upwards. The azimuthal angle ϕ is measured around the beam axis and the polar angle θ is measured with respect to the z-axis. The pseudorapidity is defined as $\eta = -\ln\tan(\theta/2)$.

[2] The factor $2\pi p_{\mathrm{T}}$ in the p_{T} spectrum comes from the Lorentz invariant definition of the cross section in terms of d^3p. Our results could thus be interpreted as the massless approximation to d^3p.

designed to study a wide range of physics topics at LHC energies. For the measurements presented in this paper, the tracking devices and the trigger system are of particular importance.

The ATLAS Inner Detector (ID) has full coverage in ϕ and covers the pseudorapidity range $|\eta| < 2.5$. It consists of a silicon pixel detector (Pixel), a silicon microstrip detector (SCT) and a transition radiation tracker (TRT). These detectors cover a sensitive radial distance from the interaction point of 50.5–150 mm, 299–560 mm and 563–1066 mm, respectively, and are immersed in a 2 T axial magnetic field. The inner-detector barrel (end-cap) parts consist of 3 (2×3) Pixel layers, 4 (2×9) double-layers of single-sided silicon microstrips with a 40 mrad stereo angle, and 73 (2×160) layers of TRT straws. Typical position resolutions are 10, 17 and 130 μm for the R-ϕ co-ordinate and, in case of the Pixel and SCT, 115 and 580 μm for the second measured co-ordinate. A track from a charged particle traversing the barrel detector would typically have 11 silicon hits [3](3 pixel clusters and 8 strip clusters) and more than 30 straw hits.

For the runs at $\sqrt{s} = 2.36$ TeV, stable beams were not declared by the LHC; the high voltage on the SCT detector was thus not turned up to its nominal operating voltage but was left in standby mode. The Pixel detector was at nominal conditions for these runs. The hit efficiency in the SCT is thus significantly lower and special track reconstruction algorithms are needed; the single hit efficiency at nominal voltage in the SCT barrel is above 99.7% [20], while in standby it drops to $\sim 60\%$ for tracks perpendicular to the silicon surface.

The ATLAS detector has a three-level trigger system: Level 1 (L1), Level 2 (L2) and Event Filter (EF). For this measurement, the trigger relies on the L1 signals from the Beam Pickup Timing devices (BPTX) and the Minimum Bias Trigger Scintillators (MBTS). The BPTX stations are composed of electrostatic button pick-up detectors attached to the beam pipe at ±175 m from the centre of the ATLAS detector. The coincidence of the BPTX signal between the two sides of the detector is used to determine when bunches are colliding in the centre of the ATLAS detector. The MBTS are mounted at each end of the detector in front of the liquid-argon end-cap calorimeter cryostats at $z = \pm 3.56$ m. They are segmented into eight sectors in azimuth and two rings in pseudorapidity ($2.09 < |\eta| < 2.82$ and $2.82 < |\eta| < 3.84$). Data were collected for this analysis using a trigger requiring a BPTX coincidence and MBTS trigger signals. The MBTS trigger used for this paper is configured to require one hit above threshold from either side of the detector, referred to as a single-arm trigger. The efficiency of this trigger is studied with a separate prescaled L1 BPTX trigger, filtered to obtain inelastic interactions by Inner Detector requirements at L2 and EF, the latter only for the 900 GeV data.

3 Monte Carlo Simulation

Inclusive minimum bias data are modelled using three components in the PYTHIA6 [21] Monte Carlo (MC) event generator: non-diffractive (ND), single- (SD) and double-diffractive (DD). Non-diffractive processes are modelled from two-to-two processes as described in this section. Diffractive process modelling is described in Sec. 3.1.

Low-p_{T} scattering processes may be described by lowest-order perturbative Quantum Chromodynamics (QCD) two-to-two parton scatters, where the divergence of the cross section at $p_{\mathrm{T}} = 0$ is regulated by phenomenological models. The PYTHIA6 MC event generator implements several of these models. The parameters of these models have been tuned to describe charged-hadron production and the underlying event in pp and $p\bar{p}$ data at centre-of-mass energies between 200 GeV and 1.96 TeV.

Samples of MC events were produced for single-diffractive, double-diffractive and non-diffractive processes using the PYTHIA6 generator [4]. The ATLAS MC09 PYTHIA tune [22] uses a specific set of

[3] A hit is a measurement point assigned to a track.

[4] PYTHIA version 6.4.21

optimised parameters; it employs the MRST LO* parton density functions (PDFs) [23] and the p_{T}-ordered parton shower [24]. A tune is a particular configuration or set of values of the parameters of the particular Monte Carlo model. These parameters were derived by tuning to the underlying event (UE) and minimum-bias data from the Tevatron at 630 GeV to 1.96 TeV. The MC samples generated with this tune are used to determine detector acceptances and efficiencies and to correct the data. MC samples were produced at all three centre-of-mass energies considered in this paper. The non-diffractive, single-diffractive and double-diffractive contributions in the generated samples are mixed according to the generator cross sections.

All the events are processed through the ATLAS detector simulation program [25], which is based on GEANT4 [26]. They are then reconstructed and analysed by the same program chain used for the data. Particular attention was devoted to the description in the simulation of the size and position of the collision beam spot and of the detailed detector conditions during data taking. The MC09 PYTHIA6 samples are used to derive the detector corrections for these measurements. The MC samples at 2.36 TeV were generated assuming nominal detector conditions.

For the purpose of comparing the present measurements to different phenomenological models describing minimum-bias events, the following additional particle level MC samples were generated:

- the new ATLAS Minimum Bias Tune 1 (AMBT1) PYTHIA6 tune described in Sec. 3.2;
- the DW [27] PYTHIA6 tune, which uses virtuality-ordered showers and was derived to describe the CDF Run II underlying event and Drell-Yan data;
- the PYTHIA8 generator [5] [28], in which the diffraction model produces much harder p_{T} and n_{ch} spectra for the single- and double-diffractive contributions than PYTHIA6. The default parton shower model is similar to the one used in PYTHIA6 MC09;
- the PHOJET generator [6] [29], which is used as an alternative model to PYTHIA-based generators. PHOJET relies on PYTHIA6 [7]for the fragmentation of partons.

3.1 Diffractive Models

PYTHIA6, PYTHIA8 and PHOJET model the diffractive components very differently. Here we mostly describe the model implemented in PYTHIA6. The PYTHIA6 diffraction is based on a Regge-based pomeron model to generate the cross-section and generate the diffractive mass and momentum transfer [30, 31]. To allow the Regge model to cover the full phase-space, empirical corrections are introduced [21]. These have the effect of enhancing the production of small masses and suppressing production near the kinematic limit. Particle production from low mass states ($M_X < 1$ GeV) is treated as an isotropic two body decay. Particle production from high mass states is based on the string model. Two string configurations are possible depending on whether the pomeron couples to a quark or gluon [21].

The PYTHIA8 model uses the same model as PYTHIA6 to generate the cross-section and generate the diffractive mass and momentum transfer. The particle production for low mass states uses the string model but for higher masses ($M_X > 10$ GeV) a perturbative element based on pomeron-proton scattering is introduced. The non-perturbative string model introduces a mass dependence on the relative probability of the pomeron scattering off a quark to scattering off a gluon, which enhances the gluon probability at high masses. The perturbative pomeron-proton scattering uses HERA diffractive PDFs [32] and the standard multiple interactions framework is used to generate the parton-parton scattering. The introduction of the perturbative pomeron-proton scattering results in a harder p_{T} and multiplicity spectrum for

[5] PYTHIA version 8.130
[6] PHOJET version 1.12.1.35
[7] PYTHIA version 6.1.15

diffractive events generated with PYTHIA8 compared to those generated with PYTHIA6 [33]. However, it should be noted that relatively little tuning has been made of the diffractive processes in PYTHIA6 and PYTHIA8.

PHOJET is based on the dual parton model. It generates a harder p_{T} and multiplicity spectrum in diffractive events than PYTHIA6. The new diffraction model of PYTHIA8 generates distributions quite similar to those from PHOJET [33].

3.2 PYTHIA 6 ATLAS Minimum Bias Tune 1

Before the start of the LHC, an ATLAS tune to PYTHIA6 with MRST LO* PDFs using Tevatron underlying event and minimum bias data was produced, the so-called MC09 tune [22]. The first ATLAS measurements of charged particle production at the LHC [1] measured the charged particle production at $\sqrt{s} = 0.9$ TeV in the central region to be 5–15% higher than the Monte Carlo models predict. In addition, neither the high n_{ch} nor the high p_{T} distributions were well described by this tune and the $\langle p_{\mathrm{T}} \rangle$ was overestimated in events with $n_{\mathrm{ch}} > 20$. A new tune, AMBT1, was developed in order to adapt the free parameters of the non-diffractive models to the new experimental data at $\sqrt{s} = 0.9$ TeV and $\sqrt{s} = 7$ TeV, using the same PDFs and PYTHIA6 model choices as MC09.

The AMBT1 tune is obtained by tuning to ATLAS minimum bias data at both $\sqrt{s} = 0.9$ TeV and $\sqrt{s} = 7$ TeV in a diffraction-reduced phase-space that is presented in this paper: $n_{\mathrm{ch}} \geq 6$, $p_{\mathrm{T}} > 500$ MeV, $|\eta| < 2.5$. The tune was derived using preliminary versions of these distributions [34]. The starting point for this tune is the ATLAS MC09c [22] PYTHIA6 tune. MC09c is an extension of the ATLAS MC09 tune where the strength of the colour reconnection (CR) was tuned to describe the $\langle p_{\mathrm{T}} \rangle$ vs. n_{ch} distributions measured by CDF in $p\bar{p}$ collisions at the Tevatron [7].

Charged particle distributions are sensitive to multi-parton interactions (MPI) and colour reconnection of the hadronic final state [35]; the MPI are regulated by a low p_{T} cut-off and the matter overlap distribution of the two protons in which the additional partonic scattering takes place. These are the main parameters varied for this new tune. Parameters related to final state radiation, hadronisation and fragmentation are not tuned, as these are constrained by many LEP results. No changes to the diffraction model are made. The model parameters are adapted in order to best describe these new distributions over the full range while maintaining consistency with the Tevatron results. For the data MC comparisons the RIVET [8] [36] package is used; the tuning is done using the PROFESSOR package [9] [37, 38]. Table 1 summarizes the parameters varied in this tune; the meaning of the parameters are given below.

MPI Parameters The size of the MPI component in the PYTHIA6 model is regulated by a simple cut-off parameter for the $\hat{p}_T$ of two-to-two scattering processes. This cut-off parameter is fixed at a reference energy, which is generally taken as 1.8 TeV. The cut-off at this reference scale is called PARP(82). It is then rescaled for other centre-of-mass energies using a parameter PARP(90). The rescaling is done according to the following formula:

$$p_{\mathrm{T}}^{min} = \mathrm{PARP(82)} \left(\frac{E}{1.8\ \mathrm{TeV}} \right)^{\mathrm{PARP(90)}} . \tag{1}$$

The amount of scattering is described by the matter overlap distribution between the two protons, which regulates how many central, hard scatterings and how many less central, softer scatterings occur. This distribution is modelled as a double Gaussian probability density function. The parameter PARP(83) describes the fraction of matter in the narrower of the two Gaussian functions. The size of this narrower Gaussian is given as a fraction PARP(84) of the wider, main radius. The optimal value for this parameter

[8] version 1.2.2a0
[9] version 1.0.0a0

was found in a first tuning run. Further variations of the matter fraction in the narrower cone were found to not have a significant influence on the main distributions used for tuning.

Colour Reconnection Parameters The colour reconnection scenario of PYTHIA used in MC09c minimises the total string length between partons. The probability that a given string piece does not participate in the CR is given by $(1 - \text{PARP}(78))^{n_{\text{MI}}}$, where n_{MI} is the number of multi-parton interactions [21]; the larger the parameter, the smaller the probability of the string piece not participating. In addition to this parameter, an additional parameter PARP(77) is present in PYTHIA; it is used to describe a suppression factor for the CR of fast moving string pieces. The suppression factor is given by $1/(1 + \text{PARP}(77)^2 \cdot p^2_{\text{avg}})$, where p^2_{avg} is a measure of the average squared momentum that hadrons produced by the string piece would have.

Additional Parameters Investigated In an initial study, the cut-off parameter for initial state radiation (PARP(62)) and the cut-off for momentum smearing in primordial $k_\perp$ (PARP(93)) were considered. The optimal values for these parameters were found in a first tuning run, further variation of those parameters was not found to have a significant influence on the main distributions used for tuning.

Distributions Used The tune described in this paper focuses on the ATLAS minimum bias data. It primarily attempts to improve the description of the high p_{T} and high n_{ch} distributions observed. For the p_{T} spectrum, only particles above 5 GeV are considered. For the n_{ch} spectrum, only events with 20 or more tracks are used in the tune. For the $\langle p_{\text{T}} \rangle$ vs. n_{ch} distribution, only events with ten or more tracks are considered. The full η distribution is used. For completeness, the preliminary underlying event results [39, 40] are included in the plateau region; however, due to the limited statistics, these data have only very small impact on the tune.

Tevatron data in the energy range of 630 GeV to 1.96 TeV are included in the tune, but with a weight which is ten times lower than that of the ATLAS data. This weighting allows a check of the consistency of the resulting tune with the Tevatron data while forcing the ATLAS data to drive the tuning process. Similar datasets were used for the MC09c tune. The charged particle multiplicity shown in [41] was not included in the tune as no variation of the tuning parameters considered was able to fit both the ATLAS and the CDF distributions simultaneously. App. A shows a full list of the distributions and the ranges considered by the tune.

Results The final parameter values resulting from the tune are shown in Table 1.

Parameter	Related model	MC09c value	scanning range	AMBT1 value
PARP(90)	MPI (energy extrapolation)	0.2487	0.18 – 0.28	0.250
PARP(82)	MPI (p_T^{min})	2.31	2.1 – 2.5	2.292
PARP(84)	MPI matter overlap (core size)	0.7	0.0 – 1.0	0.651
PARP(83)	MPI matter overlap (fraction in core)	0.8	fixed	0.356
PARP(78)	CR strength	0.224	0.2 – 0.6	0.538
PARP(77)	CR suppression	0.0	0.25 – 1.15	1.016
PARP(93)	Primordial $k_\perp$	5.0	fixed	10.0
PARP(62)	ISR cut-off	1.0	fixed	1.025

Table 1: Comparison of MC09c and AMBT1 parameters. The ranges of the parameter variations scanned are also given. The parameters declared as 'fixed' were fixed to the values obtained after an initial pass of the tuning.

4 Data Selection

Events in which the Inner Detector was fully operational and the solenoid magnet was on are used for this analysis for both $\sqrt{s} = 0.9$ TeV and $\sqrt{s} = 7$ TeV. During this data-taking period, more than 97% of the Pixel detector, 99% of the SCT and 98% of the TRT were operational. At $\sqrt{s} = 2.36$ TeV the requirements are the same, except for the SCT being in standby.

Events were selected from colliding proton bunches in which the MBTS trigger recorded one or more counters above threshold on either side. The maximum instantaneous luminosity is approximately 1.9×10^{27} cm^{-2} s^{-1} at 7 TeV. The probability of additional interactions in the same bunch crossing is estimated to be of the order of 0.1%. In order to perform an inclusive-inelastic measurement, no further requirements beyond the MBTS trigger are applied.

In order to better understand the track reconstruction performance at $\sqrt{s} = 2.36$ TeV, during which time the SCT was in standby, additional data at $\sqrt{s} = 0.9$ TeV were taken with the SCT in standby for part of a run. This enables the derivation of data-driven corrections to the track reconstruction efficiency, as described in Sec. 6.4.

4.1 Different Phase-Space Regions Considered

Three separate phase-space regions are considered in the main part of this paper with varying contributions from diffractive events:

- at least one charged particle in the kinematic range $|\eta| < 2.5$ and $p_{\mathrm{T}} > 500$ MeV,
- at least two charged particles in the kinematic range $|\eta| < 2.5$ and $p_{\mathrm{T}} > 100$ MeV,
- at least six charged particles in the kinematic range $|\eta| < 2.5$ and $p_{\mathrm{T}} > 500$ MeV.

The first of these phase-space regions is studied at all three centre-of-mass energies. This is the region that allows us to best investigate the evolution of charged-multiplicity distributions as a function of centre-of-mass energy and thus constrain the MC parameters that dictate the energy extrapolation of the models. The second measures the most inclusive charged-particle spectra and is also used as the basis for the model-dependent extrapolation to $p_{\mathrm{T}} = 0$; in this phase-space region results at $\sqrt{s} = 0.9$ and 7 TeV are shown. The third phase-space region considered is similar to the first but with a higher cut on the number of charged particles, thus reducing the expected contribution from diffractive events in the sample. These distributions are measured for both 0.9 and 7 TeV. This is the phase-space region which was used to produce the new AMBT1 tune. At 2.36 TeV only the first phase-space region is measured. Two additional phase-space regions are presented in App. B.

The relative contribution from diffractive events varies widely between Monte Carlo models and depends strongly on the phase-space region selection applied. The diffractive contribution is constrained very little by previous data. Table 2 shows the predicted fractions of simulated events originating from diffractive processes, as predicted by PYTHIA6, PYTHIA8 and PHOJET; the values for the different tunes of PYTHIA6 are found to be similar because the acceptances of the different non-diffractive models do not change significantly and the diffractive models are identical. The large difference in predictions between the models is one of the motivations for not making any model-dependent corrections to the experimental data, as such corrections would vary significantly depending on which MC model is used to derive them.

4.2 Event Selection

To reduce the contribution from background events and non-primary tracks, as well as to minimise the systematic uncertainties, the events are required to satisfy the following criteria:

Phase-Space Region		$\sqrt{s}$ = 0.9 TeV			$\sqrt{s}$ = 7 TeV		
min n_{ch}	min p_{T} (MeV)	PYTHIA6	PYTHIA8	PHOJET	PYTHIA6	PYTHIA8	PHOJET
2	100	22%	22%	20%	21%	21%	14%
1	500	16%	21%	19%	17%	21%	14%
6	500	0.4%	5%	8%	0.4%	10%	8%

Table 2: Fraction of simulated events originating from diffractive processes, as predicted by PYTHIA6, PYTHIA8 and PHOJET in the three phase-space regions measured in this paper at both $\sqrt{s}$ = 0.9 TeV and $\sqrt{s}$ = 7 TeV. All results are for $|\eta| < 2.5$.

- to have triggered the single-arm, single-counter level 1 minimum bias trigger scintillators
- the presence of a primary vertex [42] reconstructed using the beam spot information [43] and at least two tracks, each with:
  - $p_{\mathrm{T}} > 100$ MeV,
  - a transverse distance of closest approach with respect to the beam-spot position $|d_0^{\mathrm{BS}}| < 4$ mm;
- the rejection of events with a second vertex containing four or more tracks, to remove events with more than one interaction per bunch crossing;
- a minimum number of tracks, depending on the particular phase-space region, as described in Sec. 4.3.

4.3 Track Reconstruction Algorithms

Tracks are reconstructed offline within the full acceptance range $|\eta| < 2.5$ of the Inner Detector [44, 45]. Track candidates are reconstructed by requiring a minimum number of silicon hits and then extrapolated to include measurements in the TRT. Due to the SCT being in standby mode at 2.36 TeV, different track reconstruction algorithms are needed; at 0.9 and 7 TeV, the reconstruction algorithms are collectively referred to as full tracks. The analysis at $\sqrt{s}$ = 2.36 TeV has been performed using two complementary methods for reconstructing tracks. The first reconstructs tracks using pixel detector information only, denoted Pixel tracks. The second uses tracks reconstructed from the full Inner Detector information, denoted ID tracks [1].

4.3.1 Algorithms for 0.9 and 7 TeV

For the measurements at 0.9 and 7 TeV, two different track reconstruction algorithms are used. The algorithm used for the previous minimum-bias publication [1] is used with a lower p_{T} threshold cut at 100 MeV. An additional algorithm configuration is run using only the hits that have not been used by the first algorithm. This additional algorithm uses wider initial roads and has a looser requirement on the number of silicon hits. This second algorithm contributes around 60% of the tracks from 100 to 150 MeV, mostly due to the tracks having too low a momentum to go far enough in the SCT detector to satisfy the silicon hit requirement of the original algorithm; this fraction decreases rapidly, reaching less than 2% at 200 MeV.

Tracks are required to pass the selection criteria shown in Table 3; the column labelled Full Tracks refers to the algorithms used at 0.9 and 7 TeV. The transverse, d_0, and longitudinal, z_0, impact parameters

[1] In the context of the other analyses, ID tracks are referred to as track for brevity.

Criteria	$\sqrt{s}$ = 0.9 and 7 TeV	$\sqrt{s}$ = 2.36 TeV	
	Full Tracks	ID Tracks	Pixel Tracks
$p_{\mathrm{T}} > 100$ or 500 MeV	YES	YES	YES
$\lvert\eta\rvert < 2.5$	YES	YES	YES
layer-0 hit if expected	YES	YES	YES(*)
> 1 Pixel hit	YES	YES	YES
> 2, 4 or 6 SCT hits for tracks (**)	YES	NO	NO
$\lvert d_0\rvert < 1.5$ mm and $\lvert z_0\rvert \cdot \sin\theta < 1.5$ mm	YES	YES	YES(***)
χ^2 probability > 0.01 for $p_{\mathrm{T}} > 10$ GeV	YES	N/A	N/A

Table 3: Selection criteria applied to tracks for the full reconstruction, ID tracks and Pixel tracks. The transverse momentum cut applied depends on the phase-space region in question. (*) For the Pixel track method the layer-0 is required even if not expected. (**) The SCT hit selection are for $p_{\mathrm{T}} < 200$, $200 < p_{\mathrm{T}} < 300$ or $p_{\mathrm{T}} > 300$ MeV, respectively. (***) For the Pixel track method, the d_0 and z_0 selection are after the track refitting is performed (see Sec. 4.3.2).

are calculated with respect to the event primary vertex. The layer-0 selection requires a hit in the innermost layer of the Pixel detector if a hit is expected [2]. The track-fit χ^2 probability [3] cut is applied to remove tracks with mis-measured p_{T} due to mis-alignment or nuclear interactions.

These tracks are used to produce the corrected distributions and will be referred to as selected tracks. The multiplicity of selected tracks within an event is denoted by n_{sel}. The tracks used by the vertex reconstruction algorithm are very similar to those used for the analysis; the p_{T} threshold is also 100 MeV. Due to the requirement that the vertex be made from a minimum of two such tracks and the fact that we do not wish to correct our measurement outside of the observed phase-space region, the minimum number of particles per event for the phase-space region with $p_{\mathrm{T}} > 100$ MeV also needs to be set at two. Table 4 shows the total number of selected events and tracks for all phase-space regions considered.

Trigger and vertex reconstruction efficiencies are parameterised as a function of $n_{\mathrm{sel}}^{\mathrm{BS}}$. $n_{\mathrm{sel}}^{\mathrm{BS}}$ is defined as the number of tracks passing all of the track selection requirements except for the constraints with respect to the primary vertex; instead, the unsigned transverse impact parameter with respect to the beam spot, $|d_0^{\mathrm{BS}}|$, is required to be less than 1.8 mm.

Phase-Space Region		$\sqrt{s}$ = 0.9 TeV		$\sqrt{s}$ = 7 TeV		$\sqrt{s}$ = 2.36 TeV	
n_{ch}	min p_{T}	Full Tracks		Full Tracks		ID Tracks (Pixel Tracks)	
	(MeV)	Events	Tracks	Events	Tracks	Events	Tracks
2	100	357,523	4,532,663	10,066,072	209,809,430	-	-
1	500	334,411	1,854,930	9,619,049	97,224,268	5,929 (5,983)	38,983 (44,788)
6	500	124,782	1,287,898	5,395,381	85,587,104	-	-

Table 4: Number of events and tracks in the three phase-space regions at each centre-of-mass energy considered in this paper.

[2] A hit is expected if the extrapolated track crosses an active region of a Pixel module that has not been disabled.

[3] This probability function is computed as $1 - P(n_{\mathrm{dof}}/2, \chi^2/2)$, where $P(n_{\mathrm{dof}}/2, \chi^2/2)$ is the incomplete gamma function and n_{dof} is the number of degrees of freedom of the fit. It represents the probability that an observed χ^2 exceeds the observed value for a correct model.

4.3.2 Track Reconstruction Algorithms at 2.36 TeV

Operation of the SCT at standby voltage during 2.36 TeV data taking led to reduced SCT hit efficiency. Consequently, ID tracks are reconstructed at this centre-of-mass energy using looser requirements on the numbers of hits and holes [4] [44, 45]. There are no simulation samples that fully describe the SCT operating at reduced voltage. A technique to emulate the impact of operating the SCT in standby was developed in simulation; this corrects the Monte Carlo without re-simulation by modifying the silicon clusterisation algorithm used to study the tracking performance. However, the final ID track efficiency at $\sqrt{s} = 2.36$ TeV was determined using a correction to the track reconstruction efficiency derived from data at $\sqrt{s} = 0.9$ TeV.

Pixel tracks were reconstructed using the standard track reconstruction algorithms limited to Pixel hits and with different track requirements. There is little redundant information, because at least three measurement points are needed to obtain a momentum measurement and the average number of Pixel hits per track is three in the barrel. Therefore the Pixel track reconstruction efficiency is very sensitive to the location of inactive Pixel modules. The total distance between the first and the last measurement point in the pixel detector, as well as the limited number of measurement points per track, limit the momentum resolution of the tracks; therefore the Pixel tracks were refit using the reconstructed primary vertex as an additional measurement point. The refitting improves the momentum resolution by almost a factor of two. However, the Pixel track momentum resolution remains a factor of three worse than the resolution of ID tracks.

The selection criteria used to define good Pixel and ID tracks are shown in Table 3. The total number of accepted events and tracks at this energy are shown in Table 4. These two track reconstruction methods have different limitations; the method with the best possible measurement for a given variable is chosen when producing the final plots. The Pixel track method is used for the n_{ch} and η distributions, while the ID track method is used for the p_{T} spectrum measurement; the $\langle p_{\mathrm{T}} \rangle$ distribution is not produced for this energy as neither method is able to describe both the number of particles and their p_{T} accurately.

5 Background Contribution

5.1 Event Backgrounds

There are three possible sources of background events that can contaminate the selected sample: cosmic rays, beam-induced background and the presence of another collision inside the same bunch crossing. The fraction of cosmic ray background events was estimated in [1], where it was found to be smaller than 10^{-6}. Beam-induced backgrounds are estimated from non-colliding empty bunches using the same method as described in [1]; after final event selection, fewer than 0.1% of events are predicted to originate from beam-induced backgrounds. The reconstructed primary vertex requirement is particularly useful in suppressing the beam-induced background. The instantaneous luminosity at $\sqrt{s} = 7$ TeV is high enough that the effect of multiple collisions inside the same bunch crossing cannot be ignored. Events are rejected if they have a second vertex with four or more tracks [5]. After this cut, the fraction of events with more than one interaction in the same bunch crossing is measured to be about 0.1%; the residual effect is thus neglected. At the lower centre-of-mass energies, the rate of multiple interactions is lower and thus also neglected.

[4] A hole is defined as an absence of a hit when it is expected given the track trajectory.

[5] Events with two vertices with fewer than four tracks are dominated by events where a secondary interaction is reconstructed as another primary vertex and are thus not removed from our data samples.

5.2 Backgrounds to Primary Tracks

Primary charged-particle multiplicities are measured from selected-track distributions after correcting for the fraction of non-primary particles in the sample. Non-primary tracks are mostly due to hadronic interactions, photon conversions and decays of long-lived particles, as well as a small fraction of fake tracks. Their contribution is estimated using MC predictions for the shape of the d_0 distribution for primaries, non-primaries from electrons and other non-primaries. The separation between non-primaries from electrons and non-electrons is needed as the electrons are mostly from conversions in the detector material and would thus be sensitive to a mis-modeling of the detector material, whereas the non-electron non-primary tracks are mostly from long-lived particles and this fraction is thus also sensitive to the underlying physics. The Gaussian peak of the d_0 distribution, shown in Fig. 1 for $100 < p_{\mathrm{T}} < 150$ GeV, is dominated by the primary tracks and their resolution. The non-primary tracks populate the tails. The dominant contribution to non-primary tracks inside the acceptance cut on $|d_0|$ comes from non-electrons.

The primary, electron non-primary and non-electron non-primary d_0 distributions are obtained from MC and used as templates to extract the relative fractions in data. A fit is performed in the side-bands of the distribution, i.e. outside the range in d_0 used for selecting tracks. The fractions of primary, electron non-primary and non-electron non-primary tracks are all allowed to float with the total number of events constrained to that of the data. The contribution of non-primaries from electrons within the analysis acceptance of 1.5 mm is small, while it dominates at high values of $|d_0|$. The requirement on having a hit on layer-0 suppresses this contribution enough to allow the fit to be performed down to the lowest p_{T} region. The fit is performed in bins of 50 MeV in p_{T} from 100 to 500 MeV. A single fit is used for all tracks with $p_{\mathrm{T}} > 500$ MeV; in this bin the distinction is not made between the two sources of non-primary tracks. The fraction of non-primary tracks varies from 3.4% for $100 < p_{\mathrm{T}} < 150$ MeV to 1.6% above 500 MeV at $\sqrt{s} = 7$ TeV. Figure 1 shows the observed d_0 distribution for the bin $100 < p_{\mathrm{T}} < 150$ MeV compared to the MC predictions after the fit.

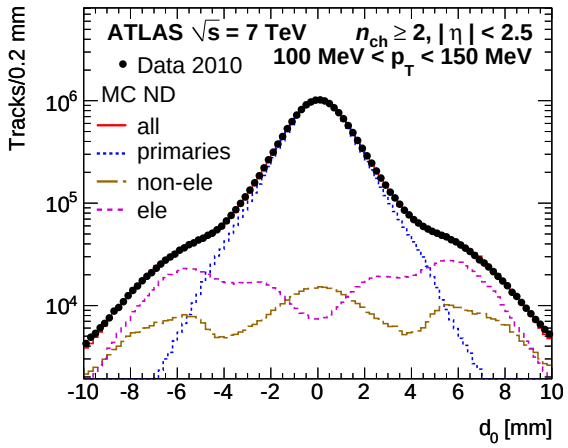

Figure 1: Transverse impact parameter, d_0, distribution at $\sqrt{s} = 7$ TeV for primary (blue short dashed) and non-primary particles after scaling them to the best fit value for $100 < p_{\mathrm{T}} < 150$ MeV. The non-primary particles are split into electrons (pink long-dashed) and non-electrons (green dot-dashed). The full red curve shows the non-diffractive (ND) MC prediction for the sum over the three components which agrees well with the data (black points).

Systematic Uncertainties The full difference between the non-primary fraction in MC and that in data obtained using the fit is taken as a systematic uncertainty. The largest difference is found to be an increase of non-primaries in data by 25% relative to the MC for $p_{\mathrm{T}} > 500$ MeV. This conservative estimate is

taken to be constant as a function of p_{T} and results in only a small effect, up to 0.9%, on the final corrected distributions. In order to estimate the effect of the choice of the variable used to obtain the fit, the fraction of primary and non-primary track contributions are obtained by fitting the z_0 distributions. The difference is measured to be 12% in the first bin, 8% in the last bin and less than 4% in all other bins; this difference is taken as a source of systematic uncertainty. The estimated number of non-primary tracks in $|d_0| < 1.5$ mm is found to be stable with respect to a change in the fit range of 1 mm in all p_{T} bins except the first one ($100 < p_{\mathrm{T}} < 150$ MeV), where a 10% difference is observed; this difference is taken as a systematic uncertainty. The fraction of non-primary tracks is found to be independent of n_{sel}, but shows a small dependence on η, taken as a small systematic uncertainty of 0.1%.

The total uncertainty on the fraction of non-primary tracks is taken as the sum in quadrature of all these effects. The total relative uncertainty on the measured distributions at $\sqrt{s} = 0.9$ TeV and $\sqrt{s} = 7$ TeV is 1.0% for the first p_{T} bin, decreasing to 0.5% above 500 MeV. At $\sqrt{s} = 2.36$ TeV this uncertainty for the Pixel track method is 0.6%.

6 Selection Efficiency

The data are corrected to obtain inclusive spectra for charged primary particles satisfying the different phase-space region requirements. These corrections include inefficiencies due to trigger selection, vertex and track reconstruction. They also account for effects due to the momentum scale and resolution and for the residual background from non-primary tracks.

In the following sections the methods used to obtain these efficiencies, as well as the systematic uncertainties associated with them are described. Plots are shown for the phase-space region $n_{\mathrm{ch}} \geq 2$, $p_{\mathrm{T}} > 100$ MeV, $|\eta| < 2.5$ at $\sqrt{s} = 7$ TeV, but similar conclusions can be drawn at the other energies and phase-space regions.

6.1 Trigger Efficiency

The trigger efficiency, $\varepsilon_{\mathrm{trig}}$, is measured from a data sample selected using a control trigger. The control trigger used for this analysis selects events from random filled bunch crossings which are then filtered at L2. At $\sqrt{s} = 0.9$ TeV the L2 filter requires a minimum of seven pixel clusters and seven SCT hits and the EF requires at least one track with $p_{\mathrm{T}} > 200$ MeV. At $\sqrt{s} = 7$ TeV the L2 requirement is loosened to four pixel clusters and four SCT hits. No EF requirements are made at this energy. The vertex requirement for selected tracks is removed for these trigger studies, to account for correlations between the trigger and vertex reconstruction efficiencies. The trigger efficiency is determined by taking the ratio of events from the control trigger in which the L1 MBTS also accepted the event, over the total number of events in the control sample. For $\sqrt{s} = 2.36$ TeV there is not sufficient data to measure the trigger efficiency and thus the $\sqrt{s} = 0.9$ TeV parametrisation is used to correct the 2.36 TeV data.

The trigger efficiency is parametrised as a function of $n_{\mathrm{sel}}^{\mathrm{BS}}$; it is 97% (99%) in the first $n_{\mathrm{sel}}^{\mathrm{BS}}$ bin and rapidly increases to nearly 100% for $n_{\mathrm{sel}}^{\mathrm{BS}} \geq 2$, $p_{\mathrm{T}} > 100$ MeV ($n_{\mathrm{sel}}^{\mathrm{BS}} \geq 1$, $p_{\mathrm{T}} > 500$ MeV). The trigger requirement is found to introduce no observable bias in the p_{T} and η distributions of selected tracks within the statistical uncertainties of the the data recorded with the control trigger. The resulting trigger efficiency is shown in Fig. 2a for the phase-space region with $n_{\mathrm{sel}}^{\mathrm{BS}} \geq 2$, $p_{\mathrm{T}} > 100$ MeV at $\sqrt{s} = 7$ TeV.

Systematic Uncertainties Since there is no vertex requirement in the data sample used to measure the trigger efficiency, it is not possible to make the same impact-parameter selection as is made on the final selected tracks. In order to study potential effects due to this, the trigger efficiency is measured after applying the impact-parameter constraints with respect to the primary vertex if available or with respect to the beam spot if not. The difference in the efficiency obtained this way and in the nominal way is

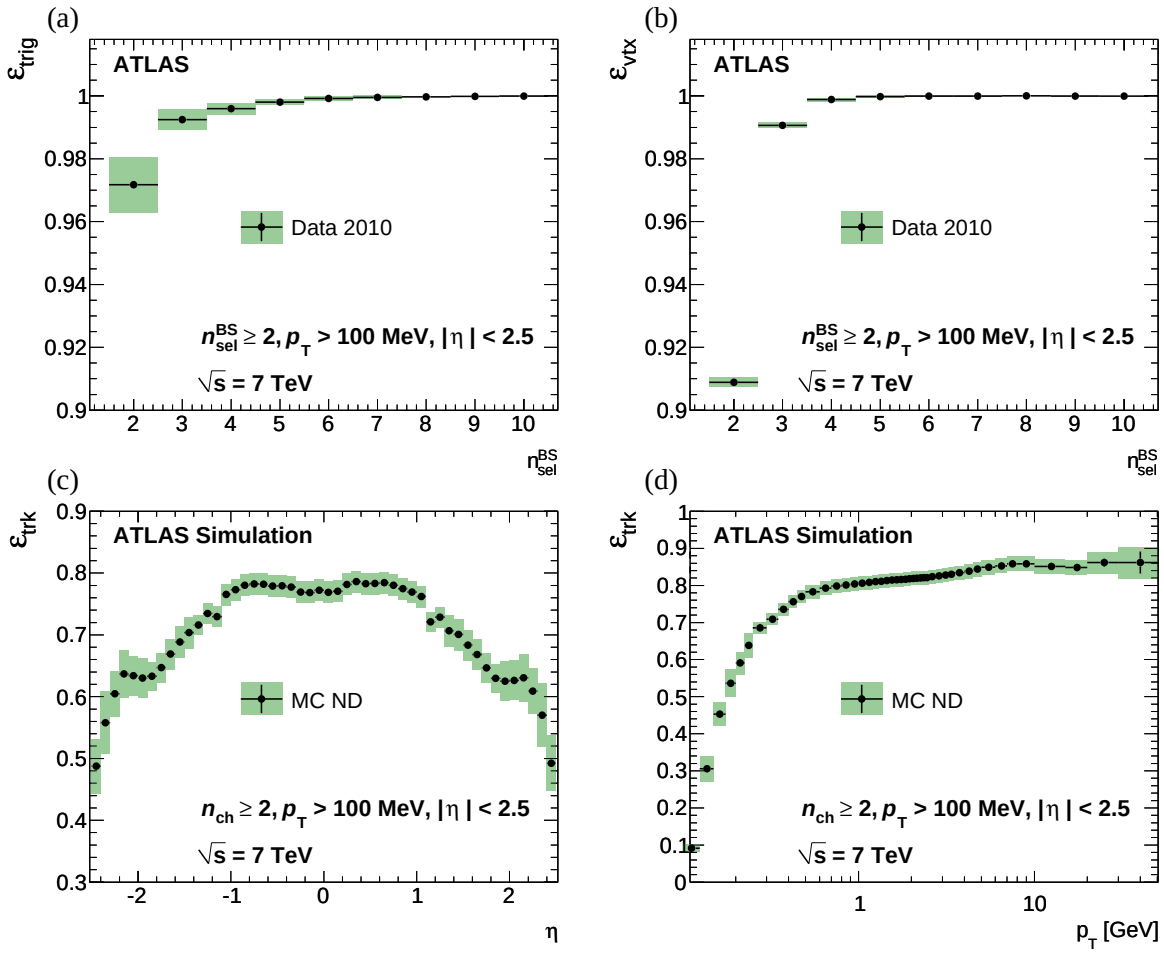

Figure 2: Trigger efficiency (a) and vertex reconstruction efficiency (b) with respect to the event selection, as a function of the number of reconstructed tracks before the vertex requirement ($n_{\mathrm{sel}}^{\mathrm{BS}}$). The track reconstruction efficiency as a function of η (c) and p_{T} (d) is derived from non-diffractive (ND) MC. The statistical errors are shown as black lines, the total errors as green shaded areas. All distributions are shown at $\sqrt{s} = 7$ TeV for $n_{\mathrm{ch}} \geq 2$, $p_{\mathrm{T}} > 100$ MeV, $|\eta| < 2.5$. For the vertex and trigger efficiencies, the selection requires $n_{\mathrm{sel}}^{\mathrm{BS}} \geq 2$.

considered as a systematic uncertainty. This variation provides a conservative estimate of the effect of beam-induced background and non-primary tracks on the trigger efficiency at low values of $n_{\mathrm{sel}}^{\mathrm{BS}}$. The systematic uncertainty arising from possible correlation of the MBTS trigger with the control trigger is studied using simulation, and the effect of correlations on the trigger efficiency is found to be less than 0.1%. The total systematic uncertainty on the trigger efficiency determination, which also includes the statistical uncertainty on the control sample, is of the order of 1% in first $n_{\mathrm{sel}}^{\mathrm{BS}}$ bin, decreasing rapidly as $n_{\mathrm{sel}}^{\mathrm{BS}}$ increases.

6.2 Vertex Reconstruction Efficiency

The vertex reconstruction efficiency, $\varepsilon_{\mathrm{vtx}}$, is determined from data by taking the ratio of triggered events with a reconstructed vertex to the total number of triggered events, after removing the expected contribution from beam background events. The efficiency is measured to be 90-92% in the first $n_{\mathrm{sel}}^{\mathrm{BS}}$ bin for the different energies and phase-space regions; it rapidly rises to 100% at higher track multiplicities. The vertex reconstruction efficiency at $\sqrt{s} = 7$ TeV for $n_{\mathrm{sel}}^{\mathrm{BS}} \geq 2$, $p_{\mathrm{T}} > 100$ MeV is shown in Fig. 2b as a function of $n_{\mathrm{sel}}^{\mathrm{BS}}$.

The dependence of the vertex reconstruction efficiency on the η and p_{T} of the selected tracks is studied as well as the dependence on the projection along the beam-axis of the separation between the perigees [6]of the tracks (Δz), for events with more than one track. For all phase-space regions, only the dominant effect is corrected for as the other effect is always found to be significantly smaller and would thus not affect the final result.

For the lower p_{T} threshold selection, a strong dependence is observed as a function of Δz for events with two tracks; this bias is corrected for in the analysis using two different parametrisations depending on the p_{T} of the lowest p_{T} track: one for tracks below 200 MeV and one for those above that threshold. The dependence on the vertex reconstruction efficiency due to the η of the tracks is found to be smaller than the Δz correction and is neglected for this phase-space region. For the 500 MeV p_{T} threshold selection, the η dependence is corrected for events with $n_{\mathrm{sel}}^{\mathrm{BS}} = 1$. For events with higher multiplicities the Δz dependence is found to be very small and is neglected.

Systematic Uncertainties The difference between the vertex reconstruction efficiency measured with beam background removal and the vertex reconstruction efficiency measured without beam background removal is assigned as the systematic uncertainty on the vertex reconstruction efficiency. For determination of this difference, the contribution of beam-related backgrounds is estimated using non-colliding bunches, as in [1]. The highest rate of beam-related background is found in the phase-space region with $p_{\mathrm{T}} > 100$ MeV at 900 GeV, where it is 0.8% without vertex selection and 0.2% with vertex selection, although it is found to decrease rapidly at higher multiplicities. (This beam-related background contribution is larger than that given if Sec. 5 where a reconstructed primary vertex was required.) The total uncertainty due to the vertex reconstruction efficiency is significantly below 1% for all phase-space regions at all energies. Fig 2b shows the total error for the phase-space region with $p_{\mathrm{T}} > 100$ MeV at $\sqrt{s} = 7$ TeV.

6.3 Track Reconstruction Efficiency for the 0.9 and 7 TeV Data Samples

The track reconstruction efficiency, $\varepsilon_{\mathrm{trk}}$, determined from MC, is parametrised in bins of p_{T} and η. The excellent agreement between data and MC of basic track quantities for tracks above 500 MeV was previously demonstrated [1]. Figure 3 highlights the agreement for tracks in the additional range covered in this paper, $100 < p_{\mathrm{T}} < 500$ MeV.

[6]The perigee of a track is here the point of closest approach of the track and the coordinate origin (0,0,0).

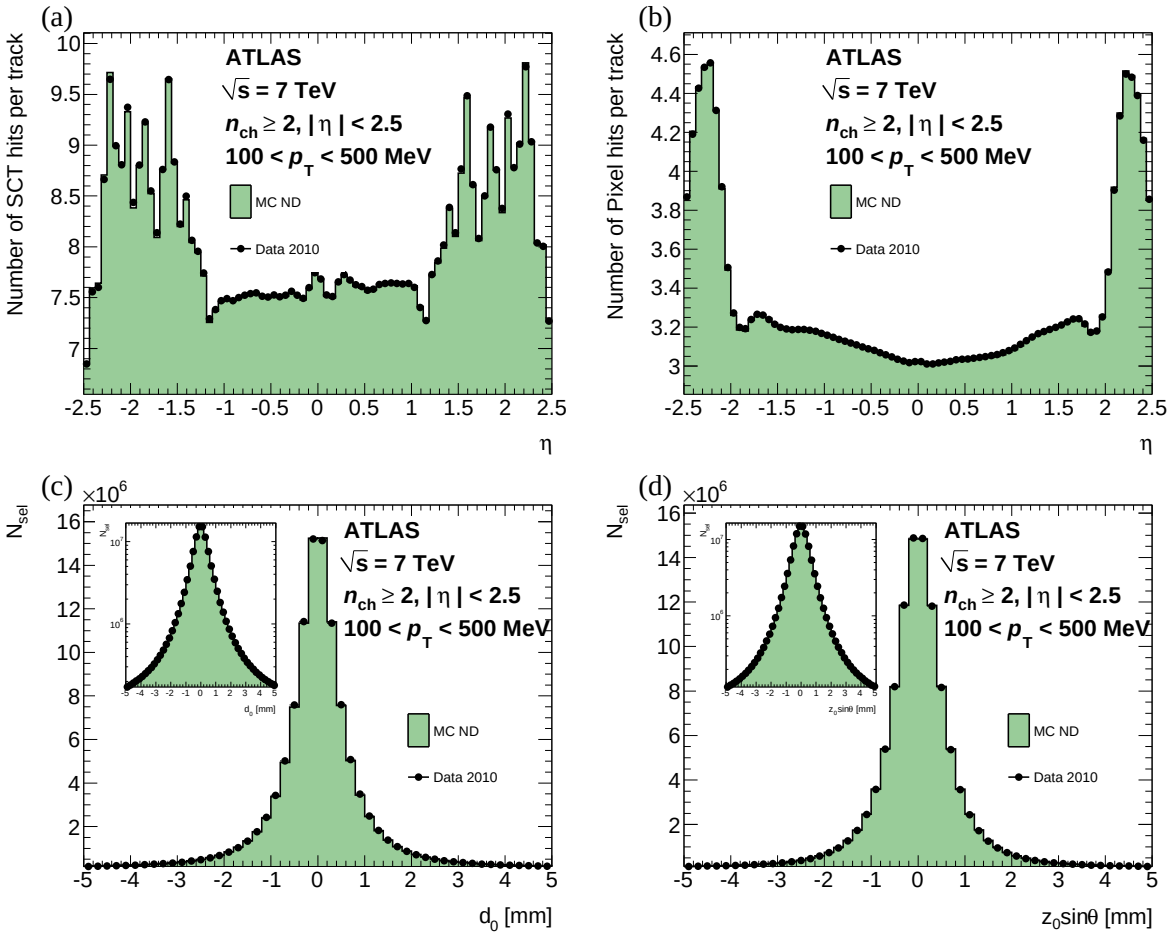

Figure 3: Comparison between data and simulation at $\sqrt{s} = 7$ TeV for tracks with transverse momentum between 100 and 500 MeV: the average number of silicon hits on reconstructed track as a function of η in the SCT (a) and Pixel (b) detectors, the transverse impact parameter (c) and longitudinal impact parameter multiplied by $\sin\theta$ (d). The inserts for the impact parameter plots show the log-scale plots. The p_{T} distribution of the tracks in non-diffractive (ND) MC is re-weighted to match the data and the number of events is scaled to the data.

The track reconstruction efficiency is defined as:

$$\varepsilon_{\mathrm{trk}}(p_{\mathrm{T}}, \eta) = \frac{N_{\mathrm{rec}}^{\mathrm{matched}}(p_{\mathrm{T}}, \eta)}{N_{\mathrm{gen}}(p_{\mathrm{T}}, \eta)},$$

where p_{T} and η are generated particle properties, $N_{\mathrm{rec}}^{\mathrm{matched}}(p_{\mathrm{T}}, \eta)$ is the number of reconstructed tracks matched to a generated charged particle and $N_{\mathrm{gen}}(p_{\mathrm{T}}, \eta)$ is the number of generated charged particles in that bin. The matching between a generated particle and a reconstructed track uses a cone-matching algorithm in the η–ϕ plane, associating the particle to the track with the smallest $\Delta R = \sqrt{(\Delta\phi)^2 + (\Delta\eta)^2}$ within a cone of radius 0.15. In addition, the particle trajectory must be compatible with the position of one of the pixel hits of the track. The larger cone size than in [1] is needed to account for the degraded resolution at lower track p_{T}.

The resulting reconstruction efficiency as a function of η integrated over p_{T} is shown in Fig. 2c at $\sqrt{s} = 7$ TeV for the phase-space region with the lowest p_{T} threshold. The track reconstruction efficiency is lower in the region $|\eta| > 1$ due to particles passing through more material in that region. Figure 2d

shows the efficiency as a function of p_{T} integrated over η. The initial rise with p_{T} is due to the requirement on the minimum number of silicon hits required in the analysis, which indirectly constrains the tracks to pass through a minimum number of detector layers and thus have a minimum p_{T}.

Systematic Uncertainties As the track reconstruction efficiency is determined from MC, the main systematic uncertainties result from the level of agreement between data and MC. The overwhelming majority of particles in the selected events are hadrons. These are known to suffer from hadronic interactions with the material in the detector. Thus a good description of the material in the detector is needed to get a good description of the track reconstruction efficiency. To quantify the influence of an imperfect description of the detector description, in particular the material in the simulation, two different data-driven methods are used. The first reconstructs the invariant mass of K_s^0 mesons decaying to two charged pions; the second compares the track lengths in data and simulation. The K_s^0 mass method studies the mass as a function of the decay radius of the meson; it has greatest sensitivity to small radii, while the track length study probes the material description in the simulation in terms of nuclear interaction length (λ) in the SCT detector. The combination of both methods provides good sensitivity throughout the silicon detectors. They allow us to constrain the material to better than 10% in the central barrel region and better than 30% at the highest $|\eta|$ measured. The material uncertainty is the largest uncertainty in almost all regions of all distributions plotted in this paper. In the barrel region, the total uncertainty due to the material is 8% at low p_{T}, going down to 2% above 500 MeV. The uncertainty increases with increasing $|\eta|$; the largest uncertainties are in the region $2.3 < |\eta| < 2.5$: 15% in the first p_{T} bin decreasing to 7% above 500 MeV.

The track-fit χ^2 probability cut has been found to offer powerful discrimination against tracks with mis-measured momenta. These are mostly very low momentum particles that are reconstructed with much higher momentum due to mis-alignment or nuclear interactions [7]. Mis-measured tracks are seen predominantly at the edges of the η acceptance where the distance between consecutive measurement points of the outer layer of the Pixel and the first layer of the SCT can reach up to ~ 1 m. The fraction of mis-measured tracks is observed to be significantly more in data than in Monte Carlo even after this cut is applied. Two different methods are used to estimate the fraction of mis-measured tracks in data. The first compares the momentum obtained from the tracks reconstructed using only the SCT hit information with that obtained for fully reconstructed tracks. After normalising the number of well-measured tracks in MC to data, the scaling of the MC high-p_{T} tails needed to model the data is obtained. The second method uses the difference between data and MC seen in the tails of the d_0 distributions at high p_{T} because mis-measured tracks tend to have poorly reconstructed d_0. Again a scaling factor is obtained to scale the MC tails in order to describe the data. These two methods give very similar results. Both methods are used to obtain the systematic uncertainty for all but the outer-most regions in η where the effect is the most significant. In this region an additional method is used that compares the η distributions, normalised in the central region, in bins of p_{T}. The variation with p_{T} of the η distribution due to physics is small compared to the differences observed due to mis-measured tracks. The additional tracks at high $|\eta|$, high p_{T} are considered to be due to mis-measured tracks and the fraction of mis-measured tracks in data is obtained. This third method gives the systematic uncertainty for the outer-most η bins. Averaged over the whole η region, the fraction of mis-measured tracks in data is found to be negligible for $p_{\mathrm{T}} < 10$ GeV, 3% for $10 < p_{\mathrm{T}} < 15$ GeV and increases to 30% for $30 < p_{\mathrm{T}} < 50$ GeV. An additional systematic on the track reconstruction efficiency of 10% is taken for all tracks with $p_{\mathrm{T}} > 10$ GeV due to different efficiencies of the χ^2 probability cut in data and MC. All systematic uncertainties on the mis-measured high-p_{T} tracks are taken as single-sided errors.

Studies using $Z \to \mu\mu$ events show that the resolution in data is about 10% worse than the nominal MC resolution above 10 GeV. The impact of a 10% Gaussian smearing of the reconstructed track p_{T} in

[7] Note that the momentum spectrum falls by many orders of magnitude in the measured range.

Systematic Uncertainty	Size	Region
Material	$\pm 2 - 15\%$	decreases with p_{T}, increases with $\lvert\eta\rvert$
χ^2 prob. cut	$\pm 10\%$	flat, only for $p_{\mathrm{T}} > 10$ GeV
Resolution	$\pm 5\%$ negligible -7%	$100 < p_{\mathrm{T}} < 150$ MeV $0.15 < p_{\mathrm{T}} < 10$ GeV $p_{\mathrm{T}} > 10$ GeV
Track Selection	$\pm 1\%$	flat in p_{T} and η
Truth Matching	$\pm 1\%$	only for $\sqrt{s} = 2.36$ TeV Pixel Tracks
Efficiency correction factor	$\pm 4\%$	only for $\sqrt{s} = 2.36$ TeV ID Track
Alignment and other high p_{T}	-3% to -30%	only for $p_{\mathrm{T}} > 10$ GeV averaged over η , increases with increasing p_{T}

Table 5: The systematic uncertainties on the track reconstruction efficiency for $\sqrt{s} = 0.9$ TeV, $\sqrt{s} = 7$ TeV and $\sqrt{s} = 2.36$ TeV Pixel Track and ID Track methods. Unless otherwise stated, the systematic is similar for all energies and phase-space regions. All uncertainties are quoted relative to the track reconstruction efficiency.

MC is performed and found to have a 7% effect for the binning used in this paper. This effect is taken as a systematic uncertainty on tracks above 10 GeV. This systematic uncertainty is single-sided and added linearly with the systematic uncertainty due to the mis-measured high-p_{T} tracks. The effect on tracks below 10 GeV is found to be negligible.

The p_{T} cut applied at various stages of the pattern recognition inside the track reconstruction algorithm introduces an inefficiency due to the momentum resolution. A different momentum resolution or a bias in the momentum estimation in data compared to MC can result in a change in the migration out of the first bin in p_{T} ($100 < p_{\mathrm{T}} < 150$ MeV) and thus a gain or loss of observed tracks. The default migration correction is derived using the resolution in Monte Carlo. The track p_{T} resolution at the seed finding stage in Monte Carlo is increased by a very conservative 10 MeV, making the p_{T} resolution effectively 15 MeV instead of 10 MeV. The effect of this shift on the track reconstruction efficiency in the first p_{T} bin is found to be about 5%; this difference is assigned as a systematic uncertainty.

A detailed comparison of track properties in data and simulation is performed by varying the track selection criteria. The largest deviations between data and MC are observed at high η and are found to be $\sim 1\%$. For simplicity, a constant 1% uncertainty is assigned over the whole range.

A summary of the track reconstruction systematic uncertainties is shown in Table 5. The total uncertainty due to the track reconstruction efficiency determination is obtained by adding all effects in quadrature except for tracks above 10 GeV where the resolution and mis-measured track effects are added linearly; asymmetric errors are considered for these effects.

6.4 Track-Reconstruction Efficiency for the 2.36 TeV Data Sample

Both the Pixel track and the ID track methods apply a data-driven correction to the primary track reconstruction efficiency, $\varepsilon_{\mathrm{MC}}$

$$\varepsilon(x) = \varepsilon_{\mathrm{MC}}(x) \cdot \varepsilon_{\mathrm{corr}}(\eta), \tag{2}$$

where $\varepsilon_{\mathrm{MC}}$ is derived from nominal simulation at $\sqrt{s} = 2.36$ TeV. Here x is either both p_{T} and η for the ID track or only η for the Pixel track method, as those are the parameters that the correction factors were found to depend on.

The correction, $\varepsilon_{\mathrm{corr}}$, is derived from the reference dataset taken at $\sqrt{s} = 0.9$ TeV where the high voltage on the SCT was lowered for part of the run.

For the Pixel track method, $\varepsilon_{\text{corr}}$ is the ratio of the relative Pixel track reconstruction efficiency, ε_{rel}, in data to simulation. The relative Pixel track efficiency is the efficiency to reconstruct a Pixel track if a track has been reconstructed using hits in the SCT and TRT detectors only.

$$\varepsilon_{\text{corr}}(\eta) = \frac{\varepsilon_{\text{rel}}^{\text{Data}}(\eta)}{\varepsilon_{\text{rel}}^{\text{MC}}(\eta)} \tag{3}$$

Figure 4a shows the relative Pixel track efficiency in data and simulation. The ratio of the two distributions, shown in the insert, is used to correct the track reconstruction efficiency for the Pixel track method at $\sqrt{s} = 2.36$ TeV.

For the ID track method the efficiency derived from simulation with nominal conditions is corrected by $\varepsilon_{\text{corr}}$ to account for the lower SCT efficiency in standby mode. Figure 4b shows the distribution of the number of reconstructed tracks in data in both SCT configurations at $\sqrt{s} = 0.9$ TeV normalised to the same number of events satisfying the trigger requirement. The ratio of the number of reconstructed tracks with the SCT in standby, $N_{\text{tr}}^{\text{sb}}$, to the number of reconstructed tracks with the SCT at nominal, $N_{\text{tr}}^{\text{nom}}$, shown in the inset, is used to correct the track reconstruction efficiency for the ID track method at $\sqrt{s} = 2.36$ TeV:

$$\varepsilon_{\text{corr}}(\eta) = \frac{N_{\text{tr}}^{\text{sb}}(\eta)}{N_{\text{tr}}^{\text{nom}}(\eta)}. \tag{4}$$

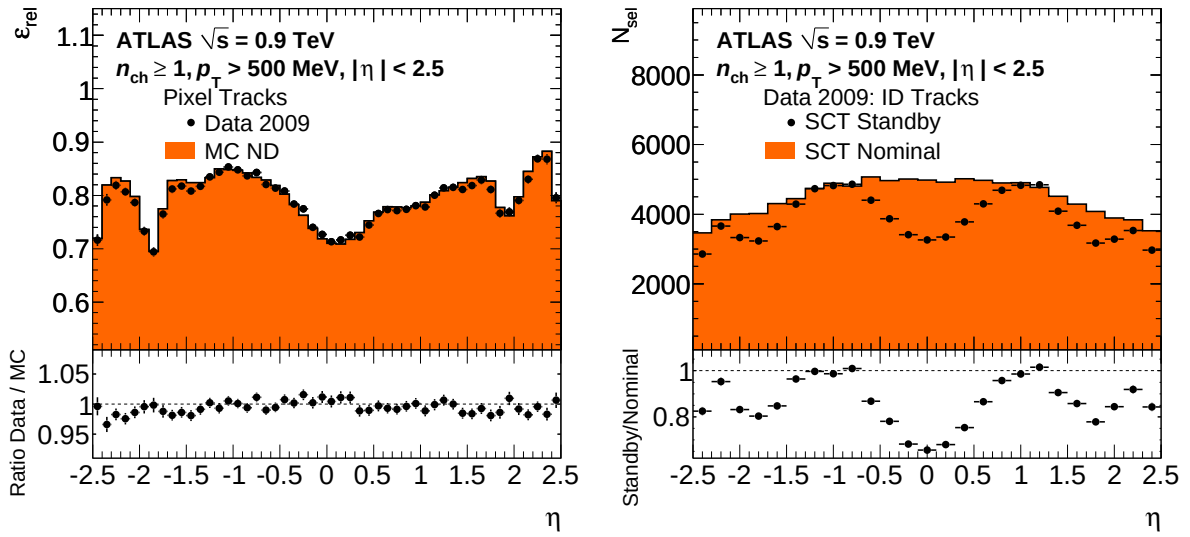

(a) (b)

Figure 4: Relative efficiency of Pixel tracks in data and non-diffractive (ND) MC simulation at $\sqrt{s} = 0.9$ TeV (a). Both Pixel track distributions are re-weighted to have the same beam spot distribution as the $\sqrt{s} = 2.36$ TeV data. The number of reconstructed ID tracks in data at $\sqrt{s} = 0.9$ TeV as a function of η with the SCT in nominal and standby (b). The ID track distributions are normalised to the number of events passing the trigger requirement.

Systematic Uncertainties Most systematic uncertainties on the ID track reconstruction efficiency are similar to the full tracking at other energies. The major additional systematic uncertainty is due to the

efficiency correction factor for the SCT configuration. The uncertainty due to the statistical limitations of the reference dataset is 2%. An additional 3% uncertainty accounts for the extrapolation from $\sqrt{s}$ = 0.9 TeV to $\sqrt{s}$ = 2.36 TeV, which was estimated by comparing the distributions of the number of ID tracks between $\sqrt{s}$ = 0.9 TeV and $\sqrt{s}$ = 2.36 TeV. The total uncertainty on the efficiency correction factor adds those two effects in quadrature to obtain a total uncertainty of 4%.

The material uncertainty is estimated using a similar method as for the other energies; the absolute uncertainty is found to be 2% (3%) for the Pixel (ID) track reconstruction efficiency. The uncertainty is larger for ID tracks, because such tracks are sensitive to the material throughout the whole silicon detector. The uncertainty due to the momentum resolution is negligible because the phase-space cuts are sufficiently far from the track algorithm cuts.

There is an additional 1% uncertainty on the Pixel track method due to the matching procedure. The relative Pixel track reconstruction efficiency differs from the primary efficiency due to material effects and contributions from non-primary tracks. There is an additional discrepancy of 4% in for $2.4 < |\eta| < 2.5$ that is assigned as a systematic uncertainty for those bins. At central η the total uncertainty on the Pixel (ID) track reconstruction efficiency is estimated to be 3.4% (6%). Table 5 shows the track reconstruction systematics at $\sqrt{s}$ = 2.36 TeV and the differences with respect to the uncertainties at other centre-of-mass energies are indicated.

7 Correction Procedure

The effect of events lost due to the trigger and vertex requirements is corrected using an event-by-event weight:

$$w_{\text{ev}}(n_{\text{sel}}^{\text{BS}}) = \frac{1}{\varepsilon_{\text{trig}}(n_{\text{sel}}^{\text{BS}})} \cdot \frac{1}{\varepsilon_{\text{vtx}}(n_{\text{sel}}^{\text{BS}}, x)},$$

where x is either the Δz between tracks or the η of the tracks, as described in Sec. 6.2.

The p_{T} and η distributions of selected tracks are corrected for using a track-by-track weight:

$$w_{\text{trk}}(p_{\text{T}}, \eta) = \frac{1}{\varepsilon_{\text{trk}}(p_{\text{T}}, \eta)} \cdot (1 - f_{\text{nonp}}(p_{\text{T}})) \cdot (1 - f_{\text{okr}}(p_{\text{T}}, \eta)),$$

where f_{nonp} is the fraction of non-primary tracks determined as described in Sec. 5.

The fraction of selected tracks passing the kinematic selection for which the corresponding primary particle is outside the kinematic range, $f_{\text{okr}}(p_{\text{T}}, \eta)$, originates from resolution effects and has been estimated from MC. The uncertainty on f_{okr} is mostly due to the resolution difference between data and MC. This uncertainty is negligible for all cases except at $\sqrt{s}$ = 2.36 TeV for the Pixel track method where the uncertainty is estimated to be 1%, due to the poor momentum resolution of the Pixel tracks. No additional corrections are needed for the η distribution; the additional corrections needed for the other distributions are described in the following sections.

For all distributions in all phase-space regions considered, closure tests are carried out. These are tests carried out on MC where the reconstructed samples are corrected according to the same procedure as used on the data; the resulting difference between the corrected distribution and the known particle level distribution is defined as the amount of non-closure; if the correction procedure were perfect, the non-closure would be zero. For this analysis, closure tests are carried out on all distributions in all phases-space regions and unless explicitly mentioned in the text the level of non-closure is less than 1%.

7.1 Correction to $\frac{\mathrm{d}N_{\text{ev}}}{\mathrm{d}n_{\text{ch}}}$

First, the observed n_{sel} distribution is corrected for the trigger and vertex reconstruction efficiencies. Then, an event-level correction is applied using Bayesian unfolding [46] to correct the observed track

multiplicity to the distribution of the number of primary charged particles, as follows. An unfolding matrix, $M_{\mathrm{ch,sel}}$, is defined that expresses the probability that a given selected track multiplicity, after all other event-level corrections are applied, n_{sel}, is due to n_{ch} primary particles. This matrix is normalised such that the number of events does not change except for the rare cases where $n_{\mathrm{sel}} > n_{\mathrm{ch}}$ and n_{ch} is below our acceptance selection. This matrix is populated from MC09 MC and applied to data to obtain the observed n_{ch} distribution. The resulting distribution is then used to re-populate the matrix and the correction is re-applied. This procedure is repeated without a regularisation term and converges after four iterations in data; convergence is defined as the first iteration in which the χ^2 difference between the result of the unfolding and the input distribution for that iteration is less than the number of bins used in the unfolding.

After the n_{sel} distribution has been unfolded, the resulting charged particle multiplicity distribution is corrected for events migrating out of the selected kinematic range ($n_{\mathrm{ch}} \geq X$), which the matrix does not account for. This is achieved by adding an additional term to the correction. The correction terms for the phase-space regions with $n_{\mathrm{ch}} \geq 2$ is

$$1/(1-(1-\varepsilon_{\mathrm{trk}})^{n_{\mathrm{ch}}} - n_{\mathrm{ch}} \cdot \varepsilon_{\mathrm{trk}} \cdot (1-\varepsilon_{\mathrm{trk}})^{(n_{\mathrm{ch}}-1)}) \tag{5}$$

where $\varepsilon_{\mathrm{trk}}$ is the mean effective track reconstruction efficiency for a given n_{ch} bin. Corresponding terms are used for the other phase-space regions. This track reconstruction efficiency can in principle be different for each n_{ch} bin, but the difference is found to be small and thus the mean effective track reconstruction efficiency for lowest n_{ch} bin is used.

Systematic Uncertainties The systematic uncertainties on the unfolding procedure are obtained by modifying the input distributions as described below, applying the unfolding procedure and comparing the output to that obtained when using the nominal input; the matrix and the correction factors are not modified.

There are two sources of systematic uncertainties considered. One of them is due to the track reconstruction efficiency uncertainties while the second one accounts for the different p_{T} spectrum reconstructed in data and MC. The first source of uncertainty is estimated by starting from the observed n_{sel} spectrum in data; tracks are randomly removed from the distribution according to the mean p_{T} and η of the tracks for each value of n_{sel} and the uncertainty on the track reconstruction efficiency for those p_{T} and η values. A new input distribution is obtained, put through the unfolding procedure and the difference with respect to the nominal n_{ch} distribution is taken as a systematic uncertainty. The uncertainty is then symmetrised. The uncertainty on n_{ch} due to the uncertainty on the track reconstruction efficiency is found to be $\sim 3\%$ to $\sim 25\%$ at $\sqrt{s} = 7$ TeV in the most inclusive phase-space region, $n_{\mathrm{ch}} \geq 2$, $p_{\mathrm{T}} > 100$ MeV, $|\eta| < 2.5$.

The other source of uncertainty originates from the unfolding method that is carried out in a single dimension at a time, in this case n_{ch}. There is some dependency on the p_{T} spectrum of the MC sample used to populate the matrix, due to the strong dependence of the track reconstruction efficiency on p_{T}. To investigate this effect, the average track reconstruction efficiency derived using the p_{T} spectrum in data and that obtained from MC are compared. The difference in these two mean efficiencies is then treated in the same way as the uncertainty on track reconstruction efficiency, described in the previous paragraph. This uncertainty is taken as being asymmetric; only the contribution from a shift of the spectrum in the direction of the data is taken. The mean value is kept as that given by the nominal p_{T} spectrum in MC. The uncertainty varies with increasing n_{ch} from -2% to $+40\%$ at $\sqrt{s} = 7$ TeV in the most inclusive phase-space region.

The only additional systematic uncertainty due to the tuning of the track reconstruction efficiency is due to the difference between the bias introduced by the vertex correction in MC and data. The estimation of this error is done by comparing the Δz_0 distribution in $n_{\mathrm{sel}}^{\mathrm{BS}}$=2 between data and MC. The

Δz_0 distribution is a very good probe of the correlation between $n_{\mathrm{sel}}/n_{\mathrm{ch}}$ and $n_{\mathrm{sel}}^{\mathrm{BS}}$ as events with high n_{sel} tend to have small Δz_0 values while events with n_{sel}<2 tend to have large Δz_0. Very good agreement is found between data and MC. Re-weighting the Δz_0 distribution in MC to match data or applying the vertex correction extracted from data to the MC closure test leads to a systematic uncertainty of the order of 0.1% for n_{ch}=2 where this effect is most pronounced. As this error is much smaller than other systematic uncertainties considered, it is neglected. The systematic uncertainty due to track-track correlation in a single event is small and is neglected everywhere in this analysis.

7.2 Corrections to N_{ev}

The total number of events, N_{ev}, used to normalise the final distributions, is defined as the integral of the n_{ch} distributions, after all corrections are applied.

Systematic Uncertainties The systematic uncertainties on N_{ev} are obtained in the same way as for the n_{ch} distributions. Only those systematics affecting the events entering or leaving the phase-space region have an impact on N_{ev}. The total uncertainty on N_{ev} at $\sqrt{s}$ = 7 TeV for the most inclusive phase-space region is 0.3%, due mostly to the track reconstruction efficiency. At $\sqrt{s}$ = 2.36 TeV the total uncertainty on N_{ev} is 1.4% for the Pixel track and 2.6% for the ID track methods.

7.3 Corrections to $\frac{1}{p_{\mathrm{T}}} \cdot \frac{\mathrm{d}N_{\mathrm{ch}}}{\mathrm{d}p_{\mathrm{T}}}$

The tracks are first corrected for the event level inefficiencies of the trigger and the vertex reconstruction. Then the tracks are corrected for the track reconstruction inefficiencies, non-primary track contamination and out of kinematic range factors. Finally, a similar unfolding method to that used on the n_{ch} distribution is used to correct the measured track p_{T} to the primary particle momentum. More bins are used for the unfolding than are shown in the final distributions; this is necessary in order to avoid amplification of small data MC differences with successive iterations, causing large fluctuations. For this distribution four iterations are required before convergence is reached; convergence is defined as for the n_{ch} distribution.

Systematic Uncertainties In order to estimate the effect on the final p_{T} distributions of the uncertainties affecting the correction steps prior to the unfolding, the unfolding procedure is re-run on the corrected p_{T} distribution shifting the distribution used as input to the unfolding procedure by the systematic uncertainties. This new p_{T} distribution is put through the unfolding procedure and the difference with respect to the nominal corrected p_{T} spectrum is taken as a systematic uncertainty.

The high-p_{T} systematic uncertainties are obtained using the MC samples. The systematic uncertainty associated to the mis-measured high-p_{T} tracks is obtained by scaling the number of mis-measured tracks in MC to match those found in data. This new input distribution is put through the unfolding procedure and the final difference with respect to the nominal MC is taken as a systematic uncertainty. The systematic uncertainty associated to the resolution is obtained by smearing the well-measured tracks, in MC, by the resolution uncertainty obtained in Sec. 6.3. The effect on the final unfolded distribution is taken as a systematic uncertainty. Those two high-p_{T} systematics are added linearly. Both cause only single-sided variations. This combined uncertainty is measured to be from -10% for p_{T} = 10 GeV to -30% for the last p_{T} bin ($30 < p_{\mathrm{T}} < 50$ GeV) at $\sqrt{s}$ = 7 TeV for the $n_{\mathrm{ch}} \geq 2$, $p_{\mathrm{T}} > 100$ MeV phase-space region. The variations for other phase-space regions at this energy are similar. At $\sqrt{s}$ = 0.9 TeV this uncertainty is found to be -20% for all three bins above p_{T} of 10 GeV.

In order to assess the stability of the results under varying starting hypotheses for the MC spectrum used to fill the matrix, a flat initial prior is used as an input. While convergence is only typically reached after seven iterations, instead of three for the nominal prior, the final difference in the unfolded spectra is

small. The difference between the resulting distribution obtained with a flat prior and that obtained with the MC p_{T} spectrum as a prior is taken as a systematic uncertainty. At $\sqrt{s} = 7$ TeV this uncertainty is less than 2% for nearly all pT bins, with the exception of a couple of bins around changes in bin width, where the effect is 3-5%. At $\sqrt{s} = 0.9$ TeV, due to more limited statistics in the MC, the largest change seen is 7% with a few others around 3-4%.

7.4 Mean p_{T} versus n_{ch}

The correction procedure for the $\langle p_{\mathrm{T}} \rangle$ vs. n_{ch} distribution is designed to correct separately two components: $\sum_i p_{\mathrm{T}}(i)$ vs. n_{ch} and $\sum_i 1$ vs. n_{ch} and take the ratio only after all corrections are applied. The sum is over all tracks and all events; the first sum is the total p_{T} of all tracks in that bin in n_{ch}; the second sum represents the total number of tracks in that bin. The sums will be referred to as the numerator and denominator, respectively. Each of these distributions, $\sum_i p_{\mathrm{T}}(i)$ and $\sum_i 1$, is corrected in two steps.

First the two distributions as a function of n_{sel} are corrected on a track-by-track basis by applying the appropriate track weights; this track-by-track correction is applied to the data distribution and thus no longer relies on the p_{T} spectrum of the MC. Second, the matrix obtained after the final iteration of the n_{ch} unfolding described in Sec. 7.1 is applied to each of the distributions to unfold n_{sel} to n_{ch}. Finally, the ratio of the two distributions is taken to obtain the corrected $\langle p_{\mathrm{T}} \rangle$ vs. n_{ch} distribution. For this distribution we exclude tracks with $p_{\mathrm{T}} > \sqrt{s}/2$ as they are clearly un-physical; this removes 1 track at $\sqrt{s} = 0.9$ TeV and 1 track at $\sqrt{s} = 7$ TeV.

This unfolding procedure assumes that the tracking efficiency depends only on p_{T} and η and is independent of the track particle multiplicity, and that the p_{T} spectrum of the tracks in events that migrate back from a given n_{sel} bin to a given n_{ch} bin is the same as the p_{T} spectrum of tracks in events in the corresponding n_{sel} bin. The fact that these assumptions are not completely valid is taken as a systematic uncertainty. This uncertainty is obtained by looking at the non-closure of the corrected distribution in the MC. This residual non-closure is, we believe, a consequence of the two main assumptions. A full parametrisation of the track reconstruction efficiency in terms of p_{T}, η and n_{ch} would remove the need for the first assumption, while a full two-dimensional unfolding as a single step where the two dimensions were p_{T} and n_{ch} would remove the need for the second. Both of these are beyond the scope of the current paper. In order to understand if the amount of non-closure is a realistic estimate of the uncertainty on the method when applied to data, in particular to investigate its dependence on the p_{T} spectrum, the whole unfolding procedure is carried out using PYTHIA6 DW tune samples and the PYTHIA8 samples; we varied both the input distribution and the matrix used to do the unfolding. The level of non-closure is found to be similar to that obtained with the MC09 PYTHIA6 samples. We thus conclude that the level of non-closure is not strongly dependent on the p_{T} spectrum. This allows us to use the residual non-closure as a systematic uncertainty on the unfolding method as described in the next section.

Systematic and Statistical Uncertainties For the calculation of the statistical uncertainty, the full correlation between the tracks inside the same event was not computed. The statistical uncertainty in the numerator and denominator are computed separately then added in quadrature after taking the ratio. This is found to be a conservative estimate of the uncertainty.

Systematic uncertainties considered for the $\langle p_{\mathrm{T}} \rangle$ vs. n_{ch} distribution are either due to assumptions made during the correction procedure or to uncertainties on quantities taken from the MC and used during the correction procedure.

The first category refers to the assumptions on the method, the effects of which are visible in the closure test. To account for these imperfections, we apply a systematic uncertainty of 2%, which covers the non-closure in MC, except for the highest n_{ch} bin and the first few n_{ch} bins in some of the phase-space regions. For these cases a larger systematic uncertainty is applied to cover the non-closure. For the

analyses with $p_{\mathrm{T}} > 500$ MeV, where the size of a non-closure is larger, a 3% systematic error is applied in the n_{ch}=1 bin. This systematic uncertainty also covers the difference in the non-closure between samples created using MC09 (default) and those with DW tune of PYTHIA6 and PYTHIA8. In the correction procedure we use the approximation that $n_{\mathrm{sel}} = n_{\mathrm{sel}}^{\mathrm{BS}}$. The effect of such an approximation is studied on simulation and found to be negligible with respect to the other sources of uncertainty.

The second category comprises uncertainties on the track correction weights $w_{\mathrm{ev}}(n_{\mathrm{sel}}^{\mathrm{BS}})$ and $w_{\mathrm{trk}}(p_{\mathrm{T}}, \eta)$ and on the migration probabilities obtained from the unfolding matrix. The dominant systematic uncertainties that affects both the track corrections weights and the migration probabilities are the same as those affecting the n_{ch} distribution unfolding: the uncertainty on the track reconstruction efficiency and the effect of the difference in the p_{T} spectra between data and MC. These uncertainties are propagated by varying the input distribution for both the $\sum_i p_{\mathrm{T}}(i)$ vs. n_{sel} and $\sum_i 1$ vs. n_{sel}.

Smaller effects are also studied, for example the uncertainty on the rate of non-primary tracks and the effect of the systematic uncertainties affecting the high-p_{T} tracks mentioned in Sec. 6.3. Excluding the systematic uncertainties due to the assumptions made during the correction procedure, the systematic uncertainties are between 0.5% and 2% for all bins in n_{ch}, all energies and all phase-space regions.

7.5 Correction for Different Minimum n_{ch} Requirements

The only difference in the correction procedure from track to particle level for $n_{\mathrm{ch}} \geq 6$ with respect to $n_{\mathrm{ch}} \geq 1$ is the need for an additional correction that takes into account the effect on the tracks due to the tighter cut on both the number of tracks and number of particles.

The n_{ch} distribution and the number of events N_{ev} are obtained by correcting and unfolding the multiplicity distribution of the whole spectrum and then applying the higher n_{ch} cut on the final distribution. For the p_{T} and η track distributions an extra correction is needed. For events with $n_{\mathrm{sel}} \geq 6$, the tracks are added to the distribution as for all other phase-space regions; a weight corresponding to the product of the track (w_{trk}) and event weights (w_{ev}) is applied. For events with $n_{\mathrm{sel}} < 6$ the tracks are added to the distribution with an additional weighting factor, $w_{n_{\mathrm{ch}}<6}$ that represents the probability that a track from an event with n_{sel} tracks is from an event with $n_{\mathrm{ch}} \geq 6$. This additional weight is taken from the final n_{ch} unfolding matrix, after the final iteration; each column in the matrix represents the probability that an event with n_{sel} tracks has n_{ch} particles. The total probability ($p(n_{\mathrm{ch}} \geq 6 \,|\, n_{\mathrm{sel}})$) for a given $n_{\mathrm{sel}} < 6$ is therfor the sum over the matrix elements for $n_{\mathrm{ch}} \geq 6$

$$w_{n_{\mathrm{ch}}<6} = p(n_{\mathrm{ch}} \geq 6 \,|\, n_{\mathrm{sel}}) = \sum_{n_{\mathrm{ch}} \geq 6} M_{\mathrm{n_{ch},n_{sel}}},$$

where $M_{\mathrm{n_{ch},n_{sel}}}$ is the entry in the unfolding matrix for n_{ch} and n_{sel}. This weight is about 65% for $n_{\mathrm{sel}} = 5$ and rapidly drops to 1% for $n_{\mathrm{sel}} = 2$.

Systematic Uncertainties All uncertainties related to the distributions with the lower n_{ch} cut are taken into account. In addition, an extra systematic uncertainty due to the uncertainty on the track reconstruction efficiency is needed for the correction to higher n_{ch} selection. By varying the track reconstruction efficiency down by its uncertainty, different $w_{n_{\mathrm{ch}}<6}$ weights are obtained. The shift in the resulting n_{ch} distribution is symmetrised and taken as an additional systematic uncertainty.

7.6 Extrapolation to $p_{\mathrm{T}} = 0$

Comparing the results in our well-defined phase-space regions to other inclusive measurements from other experiments requires additional model-dependent corrections. One such correction is described here, but applied only for comparative purposes. This particular correction is derived to extrapolate

the average multiplicity in the phase-space region with the lowest measured p_{T} to the multiplicity for all $p_{\mathrm{T}} > 0$. No attempt is made to correct for the $n_{\mathrm{ch}} \geq 2$ requirement. Results are quoted for the average multiplicity in the rapidity interval $|\eta| < 2.5$ and are not considered to be the main results of this paper. This correction is obtained using three independent methods: fitting the p_{T} spectrum to a given functional form, assuming a flat distribution at low p_{T} in the observed fully corrected $\frac{1}{p_{\mathrm{T}}} \cdot \frac{\mathrm{d}N_{\mathrm{ch}}}{\mathrm{d}p_{\mathrm{T}}}$ distribution and obtaining the correction factor from the AMBT1 PYTHIA6 MC.

In the first method, the corrected p_{T} spectrum is fit with a two-component Tsallis [47,48] distribution

$$f(p_{\mathrm{T}}) = \frac{1}{2\pi\eta'} \sum_{i=\pi,p} \left. \frac{dN_{\mathrm{ch}}}{dy}\right|_{y=0,i} \frac{(n_i-1)(n_i-2)}{(n_i T_i + m_{0,i}(n_i-1))(n_i T_i + m_{0,i})} \cdot \left[\frac{n_i T_i + m_T(p_{\mathrm{T}})_i}{n_i T_i + m_{0,i}}\right]^{-n_i} \tanh^{-1}\left(\frac{p_{\mathrm{T}} \sinh\eta'}{\sqrt{m_{0,i}^2 + p_{\mathrm{T}}^2 \cosh^2\eta'}}\right)\Bigg|_{\eta'=2.5},$$

where $m_T(p_{\mathrm{T}})$ is the transverse mass $m_T = \sqrt{p_{\mathrm{T}}^2 + m_0^2}$ and m_0 is the particle rest mass $m_0 = \{m_\pi, m_p\}$ and $dN_{\mathrm{ch}}/dy|_{y=0,i}$, T_i and n_i are the six parameters of the fit. η' represents the pseudorapidity at the edge of our acceptance, $\eta = 2.5$. $dN_{\mathrm{ch}}/dy|_{y=0}$ represents the integrated yield of the particle production at mid-rapidity, but is left here as a free parameter of the fit. Mesons (pions and kaons) are merged into a single Tsallis function since there is insufficient information in the measured distribution to fit three independent shapes. The $\tanh^{-1}$ factor accounts for the variation in E/p of each track over the entire measured pseudorapidity range. It is derived by integrating $\frac{dy}{d\eta} d\eta$ over $|\eta| < 2.5$.

From this functional form and using the parameters obtained from the fit, the fraction of particles with $p_{\mathrm{T}} < 100$ MeV is extracted. This procedure gives the correction factor to be applied to the mean charged-particle multiplicity per unit η, averaged over $|\eta| < 2.5$, in order to get the inclusive multiplicity. The correction factor from $p_{\mathrm{T}} > 100$ MeV to $p_{\mathrm{T}} > 0$ MeV is found to be 1.065 at $\sqrt{s} = 0.9$ TeV and 1.063 at $\sqrt{s} = 7$ TeV.

The second method assumes that the $\frac{1}{p_{\mathrm{T}}} \cdot \frac{\mathrm{d}N_{\mathrm{ch}}}{\mathrm{d}p_{\mathrm{T}}}$ distribution is flat at low p_{T}. One can thus use the value of this distribution in the lowest p_{T} bin ($100 < p_{\mathrm{T}} < 150$ MeV) to extract the value for tracks below 100 MeV. From this assumption, the fraction of particles below 100 MeV and the scale factor used to correct our observed distributions are derived. The scale factors are found to be 1.068 at $\sqrt{s} = 0.9$ TeV and 1.065 at $\sqrt{s} = 7$ TeV. The third and final method simply obtains the correction factor using one of the MC models. AMBT1 PYTHIA6 is chosen; the correction factors are found to be 1.055 at $\sqrt{s} = 0.9$ TeV and 1.051 at $\sqrt{s} = 7$ TeV. We chose to use the scale factor obtained from the functional form fit as the central value and consider the difference between this and the other two methods as a systematic uncertainty.

Systematic Uncertainties Several sources of systematic uncertainty on the calculated scale factor are considered. The dominant uncertainty comes from the difference in the scale factors obtained from the three different extrapolation methods. The largest difference between the value obtained from the fit and the values from the MC and from the flat extrapolation is considered as the uncertainty and then symmetrised. This uncertainty is found to be 0.007 at $\sqrt{s} = 0.9$ TeV and 0.012 at $\sqrt{s} = 7$ TeV.

The other sources of uncertainty are related to the fitting procedure such as the variation within the uncertainty on the fit parameters and the variation due to a change of the the fit range. All sources of uncertainty are assumed to be uncorrelated and thus added in quadrature. The final scale factors, with total uncertainty, are then $1.063 \pm 0.014_{\mathrm{tot}}$ at $\sqrt{s} = 7$ TeV and $1.065 \pm 0.011_{\mathrm{tot}}$ at $\sqrt{s} = 0.9$ TeV.

8 Total Systematic Uncertainties

The individual sources of systematic uncertainties have already been discussed in previous sections. The effect on the final distribution from each source is treated independently and propagated to the final distributions; the total error is the sum in quadrature from the different sources, unless explicitly mentioned in the text. In most bins of all distributions the largest uncertainty comes from the track reconstruction efficiency. The uncertainties at $\sqrt{s} = 2.36$ TeV are larger than at the other two energies due to the uncertainties related to the operation of the SCT at reduced bias voltage during 2.36 TeV data taking. The total uncertainties are shown as shaded bands in the final distributions presented in the next section.

9 Results and Discussion

The corrected distributions for primary charged particles for events in three separate phase-space regions are shown in Fig. 5 to 13. The results are compared to predictions of models tuned to a wide range of measurements. The measured distributions are presented as inclusive-inelastic distributions within a given phase-space region with minimal model-dependent corrections to facilitate the comparison with models.

9.1 Charged-Particle Multiplicities as a Function of the Pseudorapidity

Figures 5 and 6 show the charged-particle multiplicity as a function of pseudorapidity. Figure 5 shows the distribution at all three centre-of-mass energies in the phase-space region, $n_{\mathrm{ch}} \geq 1$, $p_{\mathrm{T}} > 500$ MeV, $|\eta| < 2.5$. The mean particle density is roughly constant for $|\eta| < 1.0$ and decreases at higher values of $|\eta|$. There is little shape variation between the models except for the DW PYTHIA6 tune which has a flatter spectrum and a more pronounced dip at central η , especially at low $\sqrt{s}$. At all three energies the AMBT1 PYTHIA6 tune gives the best shape and normalisation description of the data, although it was tuned for $n_{\mathrm{ch}} \geq 6$.

Figure 6a and b show the η distributions for the most inclusive phase-space region, $n_{\mathrm{ch}} \geq 2$, $p_{\mathrm{T}} > 100$ MeV, $|\eta| < 2.5$. There is less η variation than in the previous figure. At 900 GeV there is very little difference between the models both in shape and normalisation with the exception of PHOJET which shows an excellent agreement with the data; the other models show on average too few particles. The shape of the distribution is reasonably well described by all models. At 7 TeV again the shapes seem to all model reasonably well the observed spectrum, but at this energy the difference in normalisation among the models varies more widely and no model reproduces the data.

Figure 6c and d show the η distributions for the phase-space region with the least amount of diffraction, $n_{\mathrm{ch}} \geq 6$, $p_{\mathrm{T}} > 500$ MeV, $|\eta| < 2.5$. The distributions in this phase-space region have the largest drop at high $|\eta|$. All but PYTHIA6 DW and PHOJET at $\sqrt{s} = 7$ TeV show reasonable agreement in both shape and normalisation at both energies.

9.2 Charged-Particle Multiplicities as a Function of the Transverse Momentum

Figures 7 and 8 show the charged-particle multiplicities as a function of the transverse momentum. The first of these figures shows all three centre-of-mass energies considered in the phase-space region $n_{\mathrm{ch}} \geq 1$, $p_{\mathrm{T}} > 500$ MeV and $|\eta| < 2.5$. The observed p_{T} spectrum is not described by any of the models over the whole range. The region that the models have the most difficulty describing is the region above 1 GeV.

Figures 8a and b show the charged-particle multiplicities in the most-inclusive phase-space region. At 900 GeV PHOJET describes the data best over the whole range even though the agreement is still not

excellent. The other models tend to under-predict the number of low p_{T} particles while at higher p_{T} the models vary widely. At 7 TeV the effect at low p_{T} is more pronounced, while at high p_{T} the agreement of PYTHIA8 and PHOJET with the data is quite good. The AMBT1 and MC09 tunes of PYTHIA6 predict too many particles at higher p_{T}.

Figures 8c and d show the charged-particle multiplicities with the smallest contribution from diffractive events. This distribution carried the most weight in the AMBT1 tune. Considerable improvement in the agreement with data is seen between the older MC09 and the newly tuned AMBT1 but the parameters varied in this tune were not sufficient to describe the full spectrum.

9.3 Charged-Particle Multiplicity Distribution

Figure 9 shows the charged-particle multiplicity distributions for $n_{\mathrm{ch}} \geq 1$, $p_{\mathrm{T}} > 500$ MeV and $|\eta| < 2.5$ at all three centre-of-mass energies. At low number of charged particles, all models predict more events than observed in data, which is compensated by an under-prediction in the tails of the distributions. It should be noted that due to the normalisation, $1/N_{\mathrm{ev}}$, a deviation observed in one region needs to be compensated for by one in the other direction somewhere else. Although the predictions of PHOJET at 0.9 TeV model the data reasonably well, at 2.36 TeV and 7 TeV they do not model the observed spectrum. The new AMBT1 PYTHIA6 tune seems to provide the best agreement with data.

Figures 10a and b show the distribution for the most inclusive phase-space region. Here the variations between models at both low and high values of n_{ch} are increased and no model predicts the observed spectra.

Figures 10c and d show the distribution for the diffraction-reduced phase-space region. The distributions are very similar to those in Fig. 9 with a cut at $n_{\mathrm{ch}} \geq 6$; only the normalisation is different between the plots. The errors are also recomputed as there is a larger cancellation between the numerator and denominator for this phase-space region.

9.4 Average Transverse Momentum as a Function of the Number of Charged Particles

The final set of distributions discussed in the main part of this paper is the average transverse momentum as a function of particle multiplicity. The measurement of $\langle p_{\mathrm{T}} \rangle$ as a function of charged multiplicity at $\sqrt{s} = 2.36$ TeV is not shown because different track reconstruction methods are used for determining the p_{T} and multiplicity distributions, as discussed in Sec. 4.3.2. Figure 11 shows the results for events with $n_{\mathrm{ch}} \geq 1$, $p_{\mathrm{T}} > 500$ MeV and $|\eta| < 2.5$. At 900 GeV the slope vs. n_{ch} for high values of n_{ch} seems to be well described by most models but the absolute value is best modelled by PYTHIA6 DW. At the highest centre-of-mass energy above 20 particles the models vary widely both in slope and in absolute value; at low values of n_{ch} none of the models describe the data very well. In the more inclusive phase-space region, Fig. 12a and b, the models vary widely, especially at high $\sqrt{s}$.

9.5 $dn_{\mathrm{ch}}/d\eta$ at $\eta = 0$

The mean number of charged particles in the central region is computed by averaging over $|\eta| < 0.2$. The values for all three phase-space regions and all energies available are shown in Fig. 13 and in Table 6. The result quoted at $\sqrt{s} = 2.36$ TeV is the value obtained using the Pixel track method. The phase-space region with largest minimum p_{T} and highest minimum multiplicity ($p_{\mathrm{T}} > 500$ MeV; $n_{\mathrm{ch}} \geq 6$), which is the region with the least amount of diffraction, is the one where the models vary the least and the energy extrapolations of most models agree the best with the data. However, in this region the energy extrapolation of PYTHIA6 and PHOJET do not agree with the data. For the most inclusive measurements, none of the models agree with the data and the spread at 7 TeV in the expected values is almost one third

of the mean predicted value. The observed value is significantly higher at this energy than any of the models.

Phase-Space Region	Energy (TeV)	$dn_{\mathrm{ch}}/d\eta$ at $\eta = 0$	
		Measured	PYTHIA6 AMBT1 MC
$n_{\mathrm{ch}} \geq 2$, $p_{\mathrm{T}} > 100$ MeV	0.9	3.483 ± 0.009 (stat) ± 0.106 (syst)	3.01
	7	5.630 ± 0.003 (stat) ± 0.169 (syst)	4.93
$n_{\mathrm{ch}} \geq 1$, $p_{\mathrm{T}} > 500$ MeV	0.9	1.343 ± 0.004 (stat) ± 0.027 (syst)	1.28
	2.36	1.74 ± 0.019 (stat) ± 0.058 (syst)	1.70
	7	2.423 ± 0.001 (stat) ± 0.050 (syst)	2.36
$n_{\mathrm{ch}} \geq 6$, $p_{\mathrm{T}} > 500$ MeV	0.9	2.380 ± 0.009 (stat) ± 0.027 (syst)	2.33
	7	3.647 ± 0.002 (stat) ± 0.052 (syst)	3.63

Table 6: $dn_{\mathrm{ch}}/d\eta$ at $\eta = 0$ for the three different phase-space regions considered in this paper for the energies where results are available. For MC, sufficient statistics were generated such that the statistical uncertainty is smaller than the last digit quoted.

9.6 Extrapolation to $p_{\mathrm{T}} = 0$

The mean multiplicities of charged-particles with $p_{\mathrm{T}} > 100$ MeV within the full $|\eta| < 2.5$ region are computed as the mean of the distributions shown in Fig. 6a and b. They are found to be 3.614 ± 0.006 (stat) ± 0.170 (syst) at $\sqrt{s} = 0.9$ TeV and 5.881 ± 0.002 (stat) ± 0.276 (syst) at $\sqrt{s} = 7$ TeV. Multiplying these numbers by the model-dependent scale factors obtained in Sec. 7.6, the averaged inclusive charged-particle multiplicity for events with two or more particles is found to be 3.849 ± 0.006 (stat) ± 0.185 (syst) at $\sqrt{s} = 0.9$ TeV and 6.252 ± 0.002 (stat) ± 0.304 (syst) at $\sqrt{s} = 7$ TeV. This result is interpreted as the average total inelastic multiplicity for events with two or more particles within $|\eta| < 2.5$. Figure 14 compares these results to recently published ALICE results [5,6] for inclusive inelastic as well as inelastic with more than one particle. The ALICE results are quoted as averages over $|\eta| < 1.0$ and $|\eta| < 0.5$, respectively.

10 Conclusions

Charged-particle multiplicity measurements with the ATLAS detector using the first collisions delivered by the LHC during 2009 and 2010 are presented. Based on over three hundred thousand proton-proton inelastic interactions at 900 GeV, just under six thousand at 2.36 TeV and over ten million at 7 TeV, the properties of events in three well-defined phase-space regions were studied. The data were corrected with minimal model dependence to obtain inclusive distributions. The selected kinematic range and the precision of this analysis highlight clear differences between Monte Carlo models and the measured distributions. In all the kinematic regions considered, the particle multiplicities are higher than predicted by the Monte Carlo models.

The three different phase-space regions studied, from the most inclusive to the one with the smallest diffractive contribution, highlight various aspects of the charged-particle spectra. In general, the agreement between the models and the data is better in the phase-space regions with higher minimum p_{T} cutoff, where diffractive contributions are less significant.

For the $\sqrt{s} = 0.9$ TeV measurements with the p_{T} threshold of 500 MeV, these results supersede the results presented in [1].

11 Acknowledgements

We wish to thank CERN for the efficient commissioning and operation of the LHC during this initial high-energy data-taking period as well as the support staff from our institutions without whom ATLAS could not be operated efficiently.

We acknowledge the support of ANPCyT, Argentina; YerPhI, Armenia; ARC, Australia; BMWF, Austria; ANAS, Azerbaijan; SSTC, Belarus; CNPq and FAPESP, Brazil; NSERC, NRC and CFI, Canada; CERN; CONICYT, Chile; CAS, MOST and NSFC, China; COLCIENCIAS, Colombia; MSMT CR, MPO CR and VSC CR, Czech Republic; DNRF, DNSRC and Lundbeck Foundation, Denmark; ARTEMIS, European Union; IN2P3-CNRS, CEA-DSM/IRFU, France; GNAS, Georgia; BMBF, DFG, HGF, MPG and AvH Foundation, Germany; GSRT, Greece; ISF, MINERVA, GIF, DIP and Benoziyo Center, Israel; INFN, Italy; MEXT and JSPS, Japan; CNRST, Morocco; FOM and NWO, Netherlands; RCN, Norway; MNiSW, Poland; GRICES and FCT, Portugal; MERYS (MECTS), Romania; MES of Russia and ROSATOM, Russian Federation; JINR; MSTD, Serbia; MSSR, Slovakia; ARRS and MVZT, Slovenia; DST/NRF, South Africa; MICINN, Spain; SRC and Wallenberg Foundation, Sweden; SER, SNSF and Cantons of Bern and Geneva, Switzerland; NSC, Taiwan; TAEK, Turkey; STFC, the Royal Society and Leverhulme Trust, United Kingdom; DOE and NSF, United States of America.

The crucial computing support from all WLCG partners is acknowledged gratefully, in particular from CERN and the ATLAS Tier-1 facilities at TRIUMF (Canada), NDGF (Denmark, Norway, Sweden), CC-IN2P3 (France), KIT/GridKA (Germany), INFN-CNAF (Italy), NL-T1 (Netherlands), PIC (Spain), ASGC (Taiwan), RAL (UK) and BNL (USA) and in the Tier-2 facilities worldwide.

We thank Peter Skands for useful discussions concerning the AMBT1 tune.

References

[1] ATLAS Collaboration, G. Aad et al., *Charged-particle multiplicities in pp interactions at $\sqrt{s}$ = 900 GeV measured with the ATLAS detector at the LHC*, Phys. Lett. **B688** (2010) 21–42, arXiv:1003.3124 [hep-ex].

[2] CMS Collaboration, V. Khachatryan et al., *Charged particle multiplicities in pp interactions at $\sqrt{s}$ = 0.9, 2.36, and 7 TeV*, arXiv:1011.5531 [hep-ex]. Submitted to JHEP.

[3] CMS Collaboration, V. Khachatryan et al., *Transverse momentum and pseudorapidity distributions of charged hadrons in pp collisions at $\sqrt{s}$ = 7TeV*, Phys. Rev. Lett. **105** (2010) 022002, arXiv:1005.3299 [hep-ex].

[4] CMS Collaboration, V. Khachatryan et al., *Transverse momentum and pseudorapidity distributions of charged hadrons in pp collisions at $\sqrt{s}$ = 0.9 and 2.36 TeV*, JHEP **02** (2010) 041, arXiv:1002.0621 [hep-ex].

[5] ALICE Collaboration, K. Aamodt et al., *Charged-particle multiplicity measured in proton-proton collisions at $\sqrt{s}$ = 7 TeV with ALICE at LHC*, Eur. Phys. J. **C68** (2010) 345–354, arXiv:1004.3514 [hep-ex].

[6] ALICE Collaboration, K. Aamodt et al., *First proton–proton collisions at the LHC as observed with the ALICE detector: measurement of the charged particle pseudorapidity density at $\sqrt{s}$ = 900 GeV*, Eur. Phys. J. **C65** (2010) 111–125, arXiv:0911.5430 [hep-ex].

[7] CDF Collaboration, T. Aaltonen et al., *Measurement of Particle Production and Inclusive Differential Cross Sections in $p\bar{p}$ Collisions at $\sqrt{s}$ =1.96 TeV*, Phys. Rev. **D79** (2009) 112005, arXiv:0904.1098 [hep-ex].

[8] E735 Collaboration, T. Alexopoulos et al., *Multiplicity dependence of transverse momentum spectra of centrally produced hadrons in $\bar{p}p$ collisions at 0.3 TeV, 0.54 TeV, 0.9 TeV, and 1.8 TeV center-of-mass energy*, Phys. Lett. **B336** (1994) 599–604.

[9] UA1 Collaboration, C. Albajar et al., *A Study of the General Characteristics of $p\bar{p}$ Collisions at $\sqrt{s}$ = 0.2 TeV to 0.9 TeV*, Nucl. Phys. **B335** (1990) 261.

[10] CDF Collaboration, F. Abe et al., *Pseudorapidity distributions of charged particles produced in $\bar{p}p$ interactions at $\sqrt{s}$ = 630 GeV and 1800 GeV*, Phys. Rev. **D41** (1990) 2330.

[11] UA5 Collaboration, R. E. Ansorge et al., *Charged particle multiplicity distributions at 200 and 900 GeV c.m. energy*, Z. Phys. **C43** (1989) 357.

[12] UA5 Collaboration, R. E. Ansorge et al., *Charged particle correlations in $p\bar{p}$ collisions at c.m. energies of 200, 546, and 900 GeV*, Z. Phys. **C37** (1988) 191–213.

[13] CDF Collaboration, F. Abe et al., *Transverse momentum distributions of charged particles produced in $\bar{p}p$ interactions at $\sqrt{s}$ = 630 GeV and 1800 GeV*, Phys. Rev. Lett. **61** (1988) 1819.

[14] UA5 Collaboration, G. J. Alner et al., *UA5: A general study of proton-antiproton physics at $\sqrt{s}$ = 546 GeV*, Phys. Rept. **154** (1987) 247–383.

[15] UA5 Collaboration, R. E. Ansorge et al., *Diffraction dissociation at the CERN pulsed $p\bar{p}$ collider at c.m. energies of 900 and 200 GeV*, Z. Phys. **C33** (1986) 175.

[16] ABCDHW Collaboration, A. Breakstone et al., *Charged Multiplicity Distribution in pp Interactions at ISR Energies*, Phys. Rev. **D30** (1984) 528.

[17] UA1 Collaboration, G. Arnison et al., *Transverse Momentum Spectra for Charged Particles at the CERN Proton anti-Proton Collider*, Phys. Lett. **B118** (1982) 167.

[18] ATLAS Collaboration, G. Aad et al., *The ATLAS Experiment at the CERN Large Hadron Collider*, JINST **3** (2008) S08003.

[19] L. Evans, (ed.) and P. Bryant, (ed.), *LHC Machine*, JINST **3** (2008) S08001.

[20] ATLAS Collaboration, G. Aad et al., *The ATLAS Inner Detector commissioning and calibration*, Eur. Phys. J. **C70** (2010) 787–821, arXiv:1004.5293.

[21] T. Sjostrand, S. Mrenna, and P. Skands, *PYTHIA 6.4 Physics and Manual*, JHEP **05** (2006) 026, arXiv:hep-ph/0603175.

[22] ATLAS Collaboration, *ATLAS Monte Carlo Tunes for MC09*, ATL-PHYS-PUB-2010-002.

[23] A. Sherstnev and R. S. Thorne, *Parton Distributions for LO Generators*, Eur. Phys. J. **C55** (2008) 553–575, arXiv:0711.2473 [hep-ph].

[24] T. Sjostrand, *New Showers with transverse-momentum-ordering*, submitted to the proceedings of the Workshop on Physics at TeV Colliders, Les Houches, France. arXiv:hep-ph/0401061.

[25] ATLAS Collaboration, *The ATLAS Simulation Infrastructure*, Eur. Phys. J. **C70** (2010) 823–874, arXiv:1005.4568.

[26] GEANT4 Collaboration, S. Agostinelli et al., *GEANT4: A simulation toolkit*, Nucl. Instr. Meth. **A506** (2003) 250–303.

[27] M. G. Albrow et al., *Tevatron-for-LHC Report of the QCD Working Group*, arXiv:hep-ph/0610012.

[28] T. Sjostrand, S. Mrenna, and P. Skands, *Brief Introduction to PYTHIA 8.1*, Comput. Phys. Comm. **178** (2008) , arXiv:0710.3820.

[29] R. Engel, *Photoproduction within the two component dual parton model. 1. Amplitudes and cross-sections*, Z. Phys. **C66** (1995) 203–214.

[30] G. A. Schuler and T. Sjostrand, *Towards a complete description of high-energy photoproduction*, Nucl. Phys. **B407** (1993) 539.

[31] G. A. Schuler and T. Sjostrand, *Hadronic diffractive cross sections and the rise of the total cross section*, Phys. Rev. D **49** (1994) 2257–2267.

[32] A. Aktas et al. JHEP **0710** (2007) 042, arXiv:0708.3217.

[33] S.Navin, *Diffraction in Pythia*, arXiv:1005.3894.

[34] ATLAS Collaboration, *Charged particle multiplicities in pp interactions at $\sqrt{s}$ = 0.9 and 7 TeV in a diffractive limited phase space measured with the ATLAS detector at the LHC and a new* PYTHIA6 *tune*, ATLAS-CONF-2010-031.

[35] C. Buttar et al., *Les Houches physics at TeV colliders 2005, standard model and Higgs working group: Summary report*, arXiv:hep-ph/0604120.

[36] A. Buckley et al., *Rivet user manual*, arXiv:1003.0694 [hep-ph].

[37] A. Buckley, H. Hoeth, H. Lacker, H. Schulz, and J. E. von Seggern, *Systematic event generator tuning for the LHC*, Eur. Phys. J. **C65** (2010) 331–357, arXiv:0907.2973 [hep-ph].

[38] K. Hamacher and M. Weierstall, *The Next Round of Hadronic Generator Tuning Heavily Based on Identified Particle Data*, arXiv:hep-ex/9511011.

[39] ATLAS Collaboration, *Track-based underlying event measurements in pp collisions at $\sqrt{s}$ = 900 GeV and 7 TeV with the ATLAS Detector at the LHC*, ATLAS-CONF-2010-029.

[40] ATLAS Collaboration, G. Aad et al., *Measurement of underlying event characteristics using charged particles in pp collisions at $\sqrt{s}$ = 900 GeV and 7 TeV with the ATLAS detector*, arXiv:1012.0791 [hep-ex]. Submitted by Phys. Rev. **D**.

[41] CDF Collaboration, D. E. Acosta et al., *Soft and hard interactions in $p\bar{p}$ collisions at $\sqrt{s}$ = 1800-GeV and 630-GeV*, Phys. Rev. **D65** (2002) 072005.

[42] G. Piacquadio, K. Prokofiev, and A. Wildauer, *Primary vertex reconstruction in the ATLAS experiment at LHC*, J. Phys. Conf. Ser. **119** (2008) 032033.

[43] ATLAS Collaboration, *Characterization of Interaction-Point Beam Parameters Using the pp Event-Vertex Distribution Reconstructed in the ATLAS Detector at the LHC*, ATLAS-CONF-2010-027.

[44] T. Cornelissen et al., *Concepts, Design and Implementation of the ATLAS New Tracking (NEWT)*, ATL-SOFT-PUB-2007-007.

[45] T. Cornelissen et al., *The new ATLAS track reconstruction (NEWT)*, J. Phys. Conf. Ser. **119** (2008) 032014.

[46] G. D'Agostini, *A Multidimensional unfolding method based on Bayes' theorem*, Nucl. Instr. Meth. **A362** (1995) 487–498.

[47] C. Tsallis, *Possible Generalization of Boltzmann-Gibbs Statistics*, J. Stat. Phys. **52** (1988) 479–487.

[48] PHENIX Collaboration, A. Adare et al., *Measurement of neutral mesons in p + p collisions at* $\sqrt{s}$ *= 200 GeV and scaling properties of hadron production*, arXiv:1005.3674 [hep-ex].

[49] CDF Collaboration, D. E. Acosta et al., *Underlying Event in Inclusive Jet Production*, http://www-cdf.fnal.gov/physics/new/qcd/run2/ue/chgjet/index.html.

[50] CDF Collaboration, D. E. Acosta et al., *The underlying event in hard interactions at the Tevatron* $\bar{p}p$ *collider*, Phys. Rev. **D70** (2004) 072002.

[51] D0 Collaboration, V. M. Abazov et al., *Measurement of dijet azimuthal decorrelations at central rapidities in* $p\bar{p}$ *collisions at* $\sqrt{s} = 1.96$ *TeV*, Phys. Rev. Lett. **94** (2005) 221801.

[52] CDF Collaboration, T. Aaltonen et al., *Measurement of Particle Production and Inclusive Differential Cross Sections in* $p\bar{p}$ *Collisions at* $\sqrt{s} = 1.96$ *TeV*, Phys. Rev. **D79** (2009) 112005.

[53] CDF Collaboration, A. A. Affolder et al., *The transverse momentum and total cross section of* e^+e^- *pairs in the Z boson region from* $p\bar{p}$ *collisions at* $\sqrt{s} = 1.8$ *TeV*, Phys. Rev. Lett. **84** (2000) 845–850.

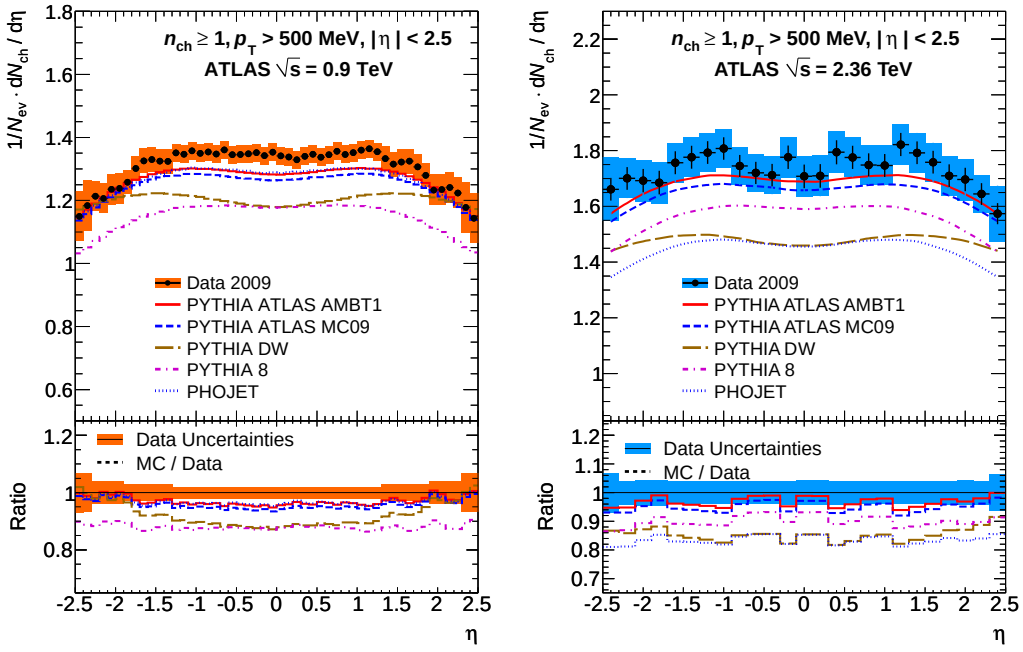

(a) (b)

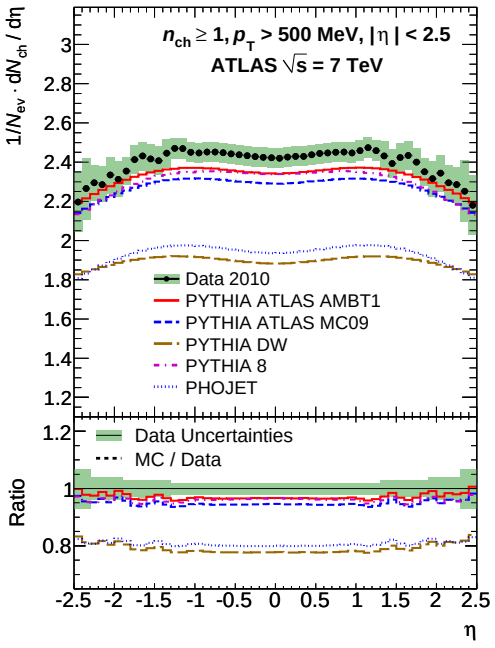

(c)

Figure 5: Charged-particle multiplicities as a function of the pseudorapidity for events with $n_{ch} \geq 1$, $p_T > 500$ MeV and $|\eta| < 2.5$ at $\sqrt{s} = 0.9$ TeV (a), $\sqrt{s} = 2.36$ TeV (b) and $\sqrt{s} = 7$ TeV (c). The dots represent the data and the curves the predictions from different MC models. The vertical bars represent the statistical uncertainties, while the shaded areas show statistical and systematic uncertainties added in quadrature. The bottom inserts show the ratio of the MC over the data. The values of the ratio histograms refer to the bin centroids.

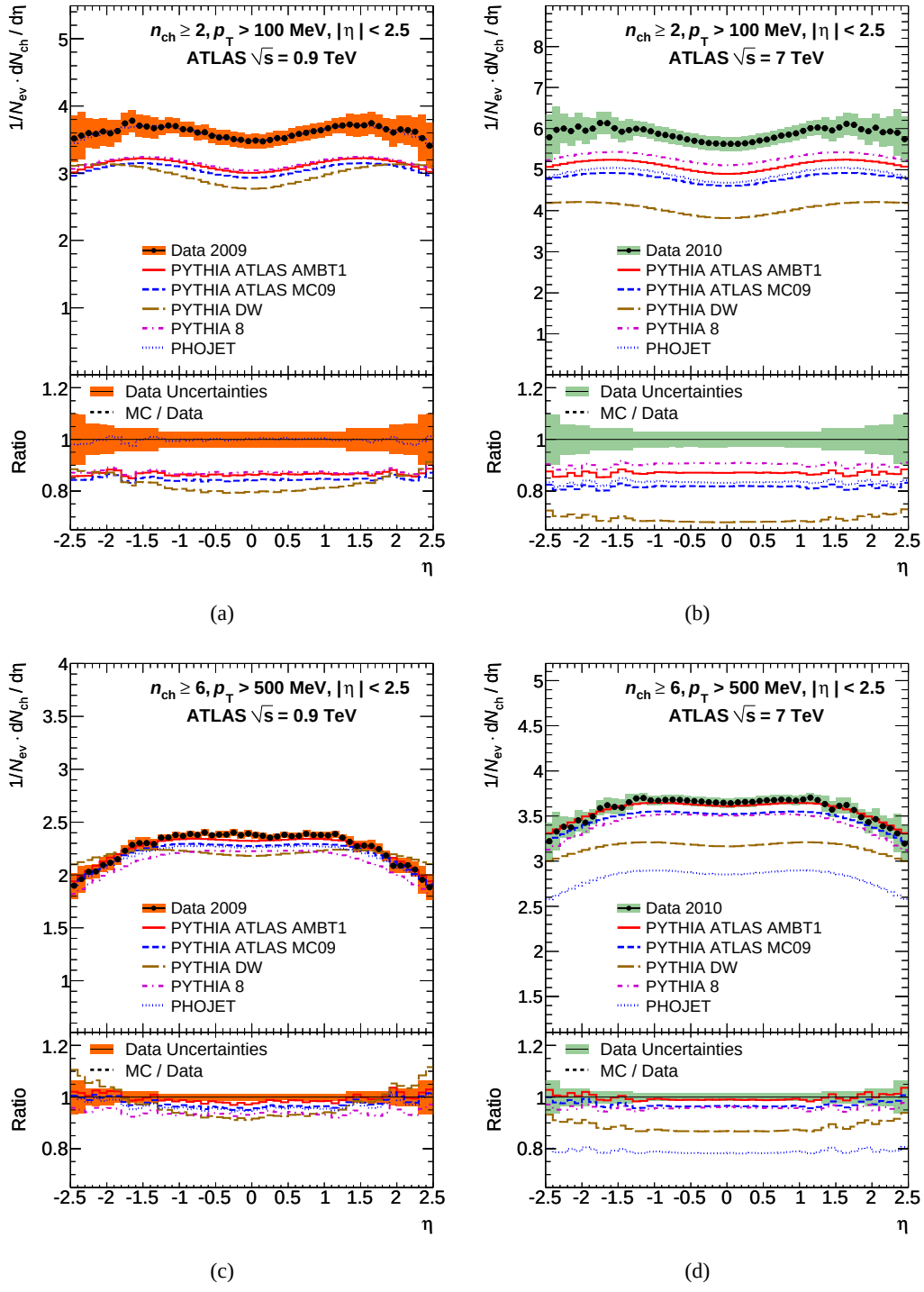

Figure 6: Charged-particle multiplicities as a function of the pseudorapidity for events with $n_{ch} \geq 2$, $p_T > 100$ MeV (a,b) and $n_{ch} \geq 6$, $p_T > 500$ MeV (c,d) and $|\eta| < 2.5$ at $\sqrt{s} = 0.9$ TeV (a,c) and $\sqrt{s} = 7$ TeV (b,d). The dots represent the data and the curves the predictions from different MC models. The vertical bars represent the statistical uncertainties, while the shaded areas show statistical and systematic uncertainties added in quadrature. The bottom inserts show the ratio of the MC over the data. The values of the ratio histograms refer to the bin centroids.

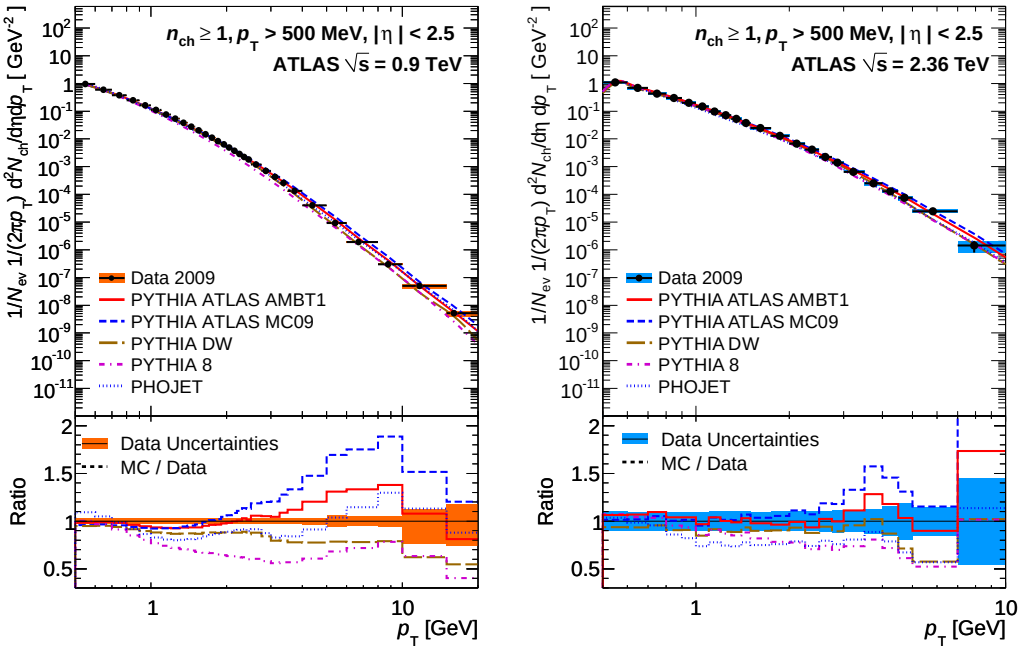

(a)

(b)

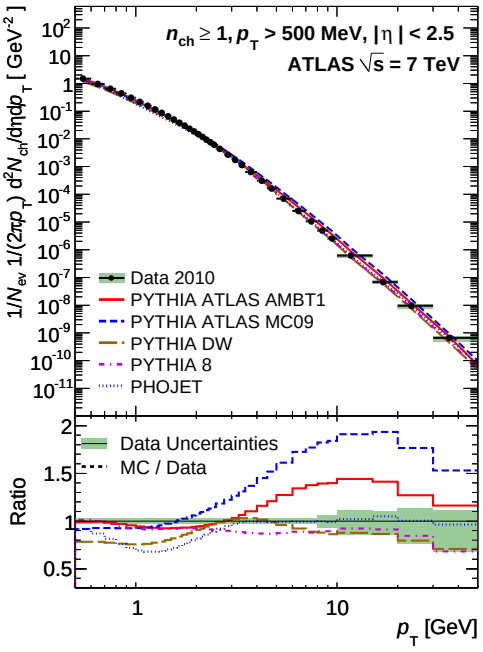

(c)

Figure 7: Charged-particle multiplicities as a function of the transverse momentum for events with $n_{\mathrm{ch}} \geq 1$, $p_{\mathrm{T}} > 500$ MeV and $|\eta| < 2.5$ at $\sqrt{s} = 0.9$ TeV(a), $\sqrt{s} = 2.36$ TeV(b) and $\sqrt{s} = 7$ TeV(c). The dots represent the data and the curves the predictions from different MC models. The vertical bars represent the statistical uncertainties, while the shaded areas show statistical and systematic uncertainties added in quadrature. The bottom inserts show the ratio of the MC over the data. The values of the ratio histograms refer to the bin centroids.

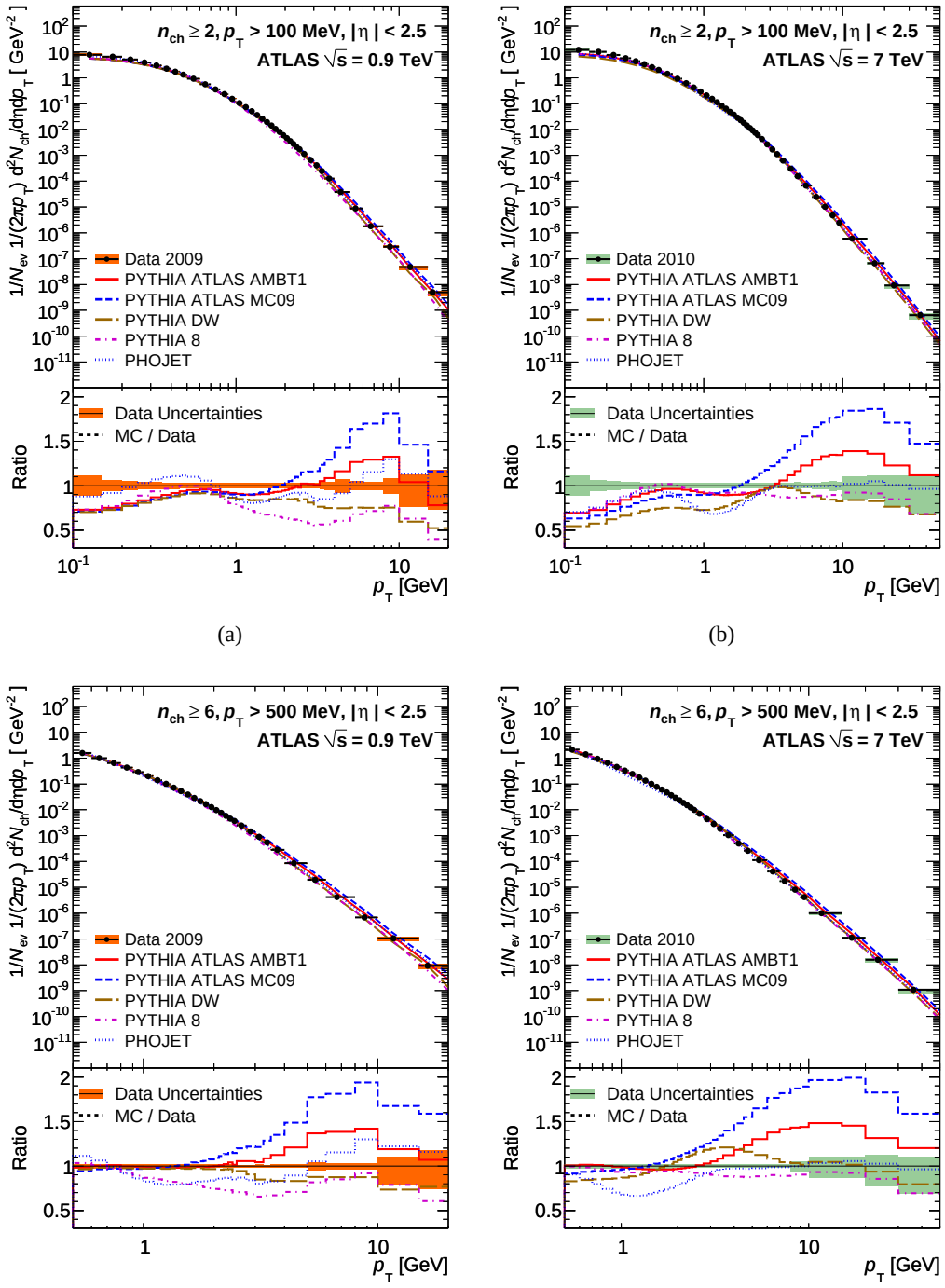

Figure 8: Charged-particle multiplicities as a function of the transverse momentum for events with $n_{\mathrm{ch}} \geq 2$, $p_{\mathrm{T}} > 100$ MeV (a,b) and $n_{\mathrm{ch}} \geq 6$, $p_{\mathrm{T}} > 500$ MeV (c,d) and $|\eta| < 2.5$ at $\sqrt{s} = 0.9$ TeV (a,c) and $\sqrt{s} = 7$ TeV (b,d). The dots represent the data and the curves the predictions from different MC models. The vertical bars represent the statistical uncertainties, while the shaded areas show statistical and systematic uncertainties added in quadrature. The bottom inserts show the ratio of the MC over the data. The values of the ratio histograms refer to the bin centroids.

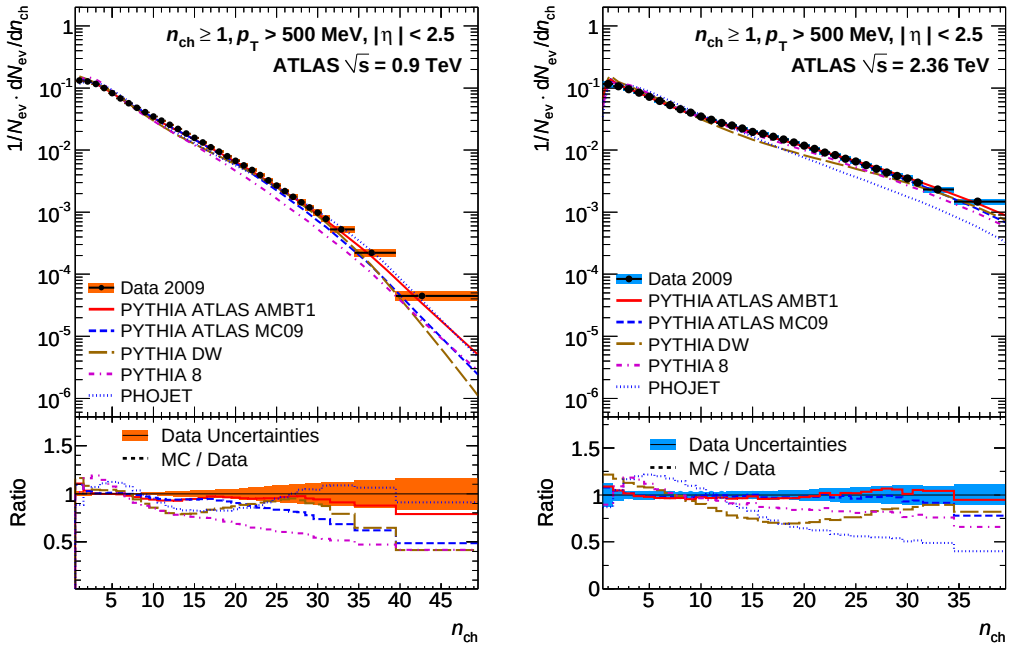

(a)

(b)

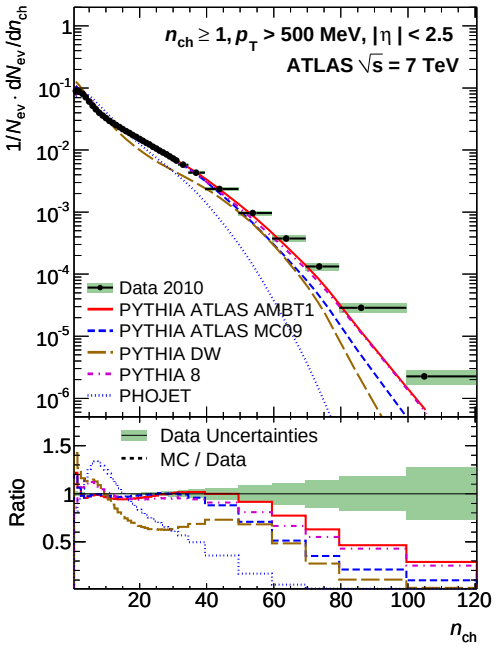

(c)

Figure 9: Charged-particle multiplicity distributions for events with $n_{ch} \geq 1$, $p_T > 500$ MeV and $|\eta| < 2.5$ at $\sqrt{s} = 0.9$ TeV(a), $\sqrt{s} = 2.36$ TeV(b) and $\sqrt{s} = 7$ TeV(c). The dots represent the data and the curves the predictions from different MC models. The vertical bars represent the statistical uncertainties, while the shaded areas show statistical and systematic uncertainties added in quadrature. The bottom inserts show the ratio of the MC over the data. The values of the ratio histograms refer to the bin centroids.

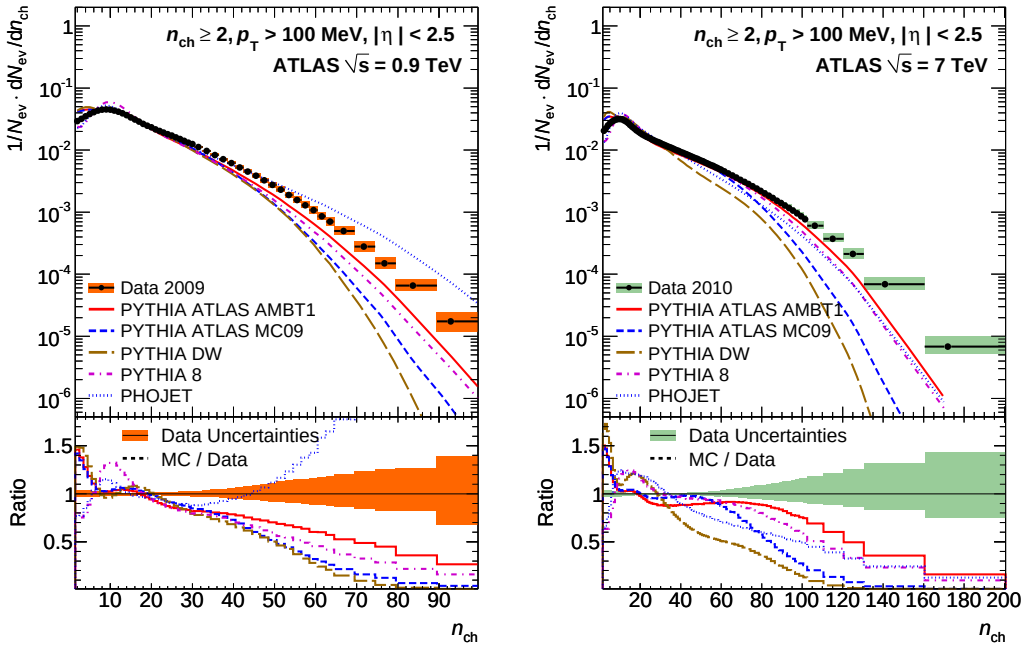

(a)

(b)

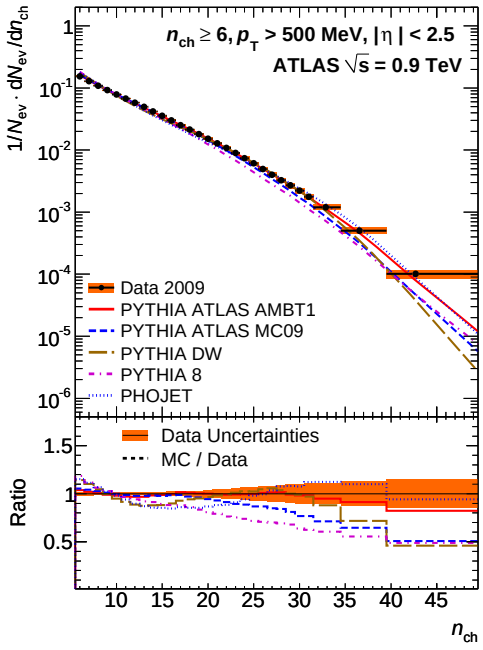

(c)

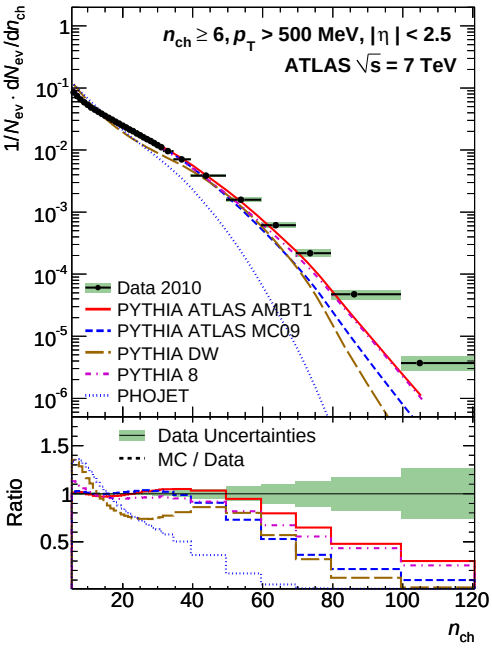

(d)

Figure 10: Charged-particle multiplicity distributions for events with $n_{ch} \geq 2$, $p_T > 100$ MeV (a,b) and $n_{ch} \geq 6$, $p_T > 500$ MeV (c,d) and $|\eta| < 2.5$ at $\sqrt{s} = 0.9$ TeV (a,c) and $\sqrt{s} = 7$ TeV (b,d). The dots represent the data and the curves the predictions from different MC models. The vertical bars represent the statistical uncertainties, while the shaded areas show statistical and systematic uncertainties added in quadrature. The bottom inserts show the ratio of the MC over the data. The values of the ratio histograms refer to the bin centroids.

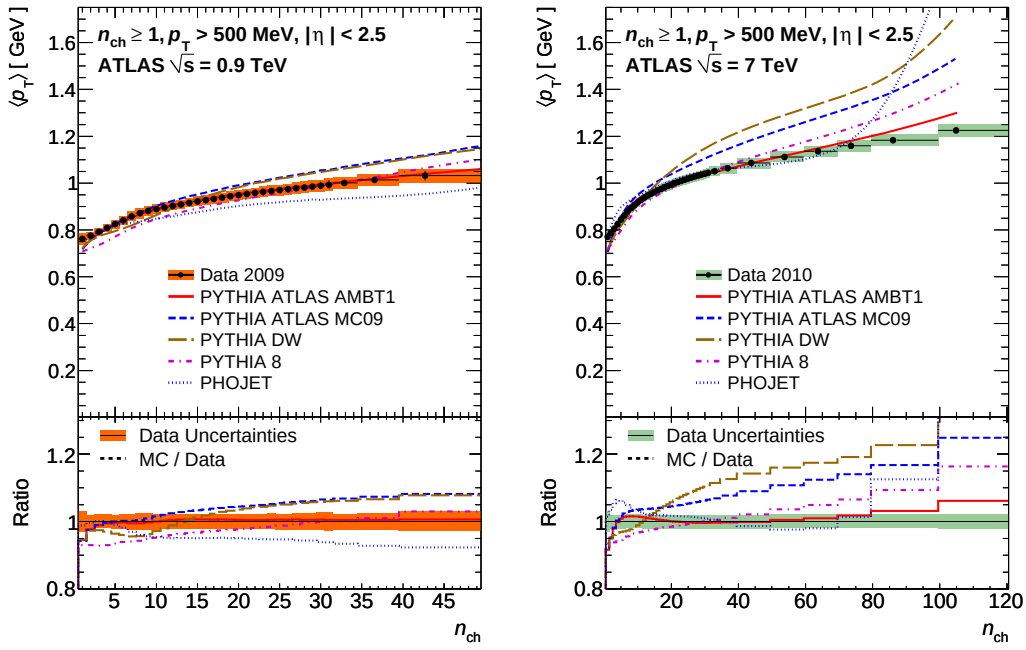

(a) (b)

Figure 11: Average transverse momentum as a function of the number of charged particles in the event for events with $n_{\mathrm{ch}} \geq 1$, $p_{\mathrm{T}} > 500$ MeV and $|\eta| < 2.5$ at $\sqrt{s} = 0.9$ TeV(a), and $\sqrt{s} = 7$ TeV(b). The dots represent the data and the curves the predictions from different MC models. The vertical bars represent the statistical uncertainties, while the shaded areas show statistical and systematic uncertainties added in quadrature. The bottom inserts show the ratio of the MC over the data. The values of the ratio histograms refer to the bin centroids.

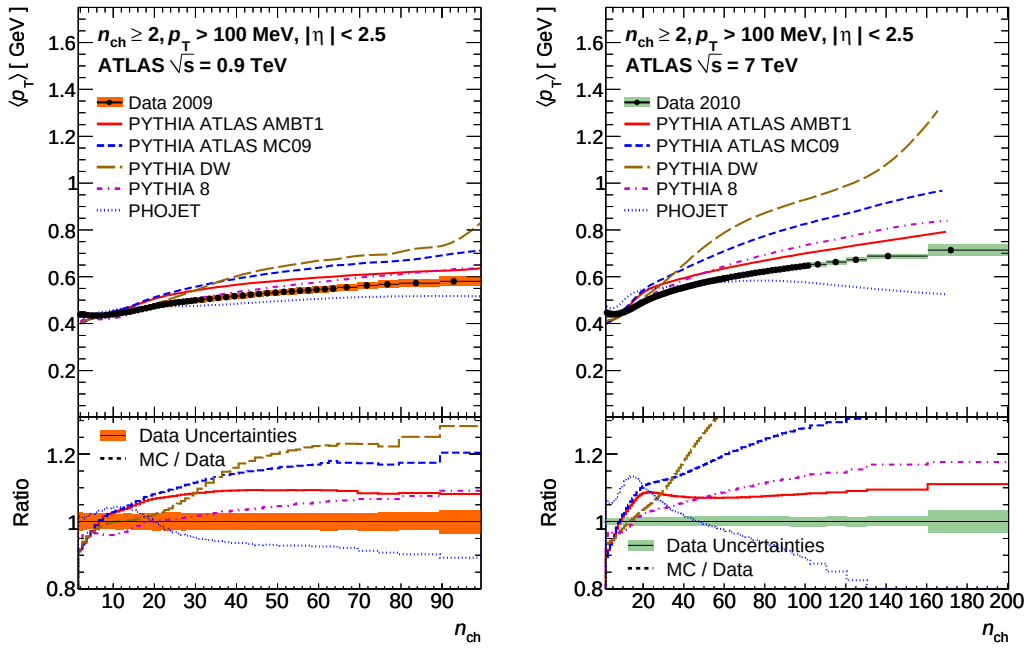

(a) (b)

Figure 12: Average transverse momentum as a function of the number of charged particles in the event for events with $n_{\mathrm{ch}} \geq 2$, $p_{\mathrm{T}} > 100$ MeV and $|\eta| < 2.5$ at $\sqrt{s} = 0.9$ TeV (a) and $\sqrt{s} = 7$ TeV (b). The dots represent the data and the curves the predictions from different MC models. The vertical bars represent the statistical uncertainties, while the shaded areas show statistical and systematic uncertainties added in quadrature. The bottom inserts show the ratio of the MC over the data. The values of the ratio histograms refer to the bin centroids.

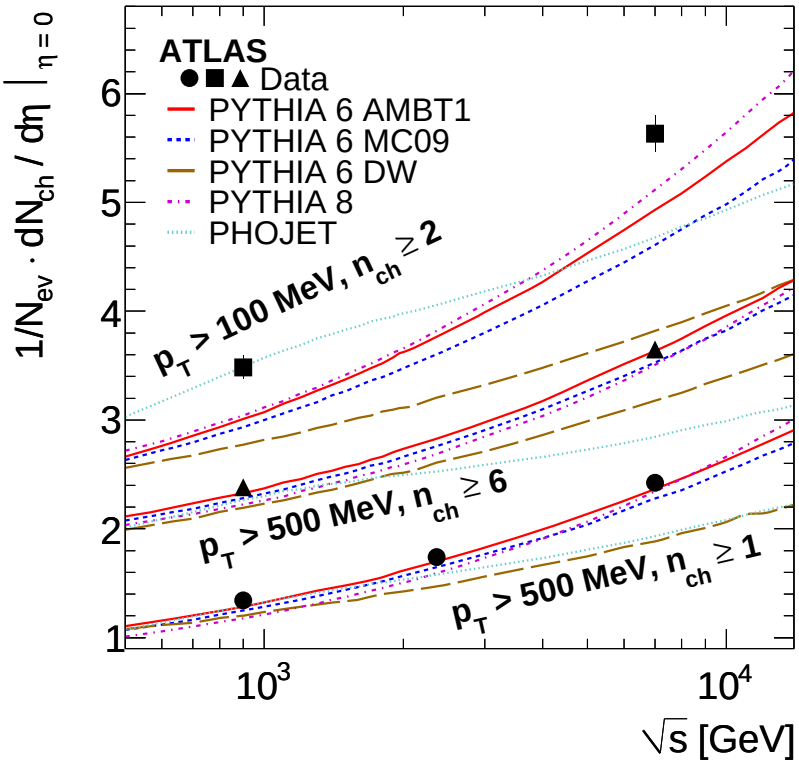

Figure 13: The average charged-particle multiplicity per unit of rapidity for $\eta = 0$ as a function of the centre-of-mass energy. The results with $n_{\mathrm{ch}} \geq 2$ within the kinematic range $p_{\mathrm{T}} > 100$ MeV and $|\eta| < 2.5$ are shown alongside the results with $n_{\mathrm{ch}} \geq 1$ within the kinematic range $p_{\mathrm{T}} > 500$ MeV and $|\eta| < 2.5$ at 0.9, 2.36 and 7 TeV. The data are compared to various particle level MC predictions. The vertical error bars on the data represent the total uncertainty.

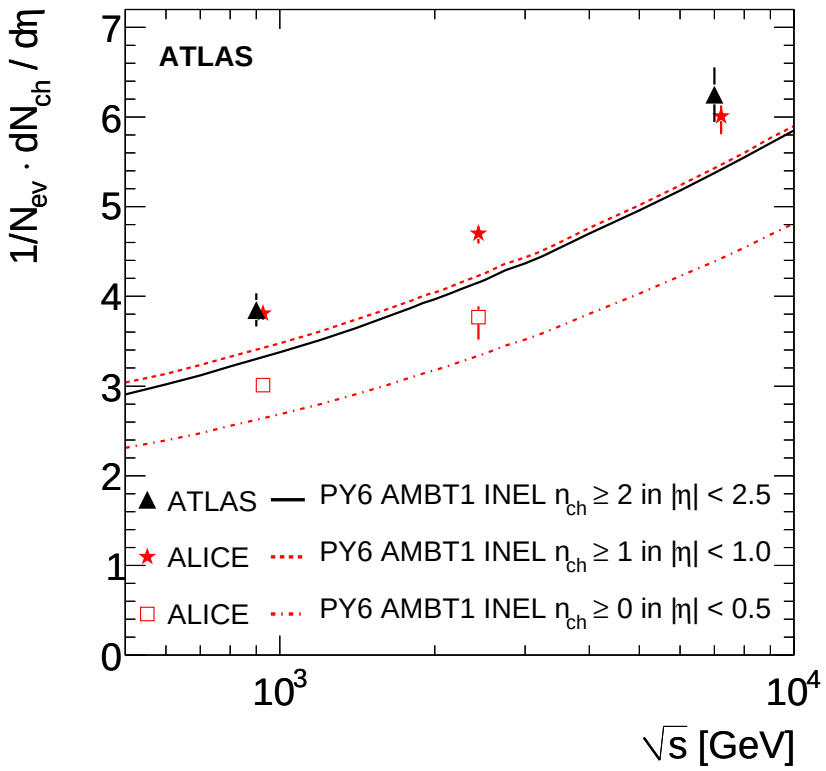

Figure 14: The average charged-particle multiplicity per unit of rapidity as a function of the centre-of-mass energy. The ATLAS results are for $n_{\mathrm{ch}} \geq 2$ in the region $|\eta| < 2.5$. For comparison ALICE results for $n_{\mathrm{ch}} \geq 1$ in the region $|\eta| < 1.0$ and $n_{\mathrm{ch}} \geq 0$ in the region $|\eta| < 0.5$ are shown. It should be noted that the ALICE points have been slightly shifted horizontally for clarity. The data points are compared to PYTHIA6 AMBT1 predictions for the same phase-space regions.

A Distributions Used in AMBT1 Tuning

Table 7 and 8 show the list of all distributions from ATLAS and the Tevatron, respectively, used in the ATLAS Minimum Bias Tune 1 (AMBT1). The Analysis column refers to the event selection used in the particular analysis. The Tuning range column refers to the portion of the phase-space region that is considered for the tune.

Analysis	Observable	Tuning range
ATLAS 0.9 TeV, minimum bias, $n_{\mathrm{ch}} \geq 6$	$\frac{1}{N_{\mathrm{ev}}} \cdot \frac{\mathrm{d}N_{\mathrm{ch}}}{\mathrm{d}\eta}$	$-2.5 < \eta < 2.5$
ATLAS 0.9 TeV, minimum bias, $n_{\mathrm{ch}} \geq 6$	$\frac{1}{N_{\mathrm{ev}}} \cdot \frac{1}{2\pi p_{\mathrm{T}}} \cdot \frac{\mathrm{d}^2 N_{\mathrm{ch}}}{\mathrm{d}\eta \mathrm{d}p_{\mathrm{T}}}$	$p_{\mathrm{T}} \geq 5.0$ GeV
ATLAS 0.9 TeV, minimum bias, $n_{\mathrm{ch}} \geq 6$	$\frac{1}{N_{\mathrm{ev}}} \cdot \frac{\mathrm{d}N_{\mathrm{ev}}}{\mathrm{d}n_{\mathrm{ch}}}$	$n_{\mathrm{ch}} \geq 20$
ATLAS 0.9 TeV, minimum bias, $n_{\mathrm{ch}} \geq 6$	$\langle p_{\mathrm{T}} \rangle$ vs. n_{ch}	$n_{\mathrm{ch}} \geq 10$
ATLAS 0.9 TeV, UE in minimum bias	$\langle \frac{\mathrm{d}^2 N_{\mathrm{ch}}}{\mathrm{d}\eta \mathrm{d}\phi} \rangle$ vs. $p_{\mathrm{T}}^{\mathrm{lead}}$ (towards)	$p_{\mathrm{T}}^{\mathrm{lead}} \geq 5.5\ GeV$
ATLAS 0.9 TeV, UE in minimum bias	$\langle \frac{\mathrm{d}^2 N_{\mathrm{ch}}}{\mathrm{d}\eta \mathrm{d}\phi} \rangle$ vs. $p_{\mathrm{T}}^{\mathrm{lead}}$ (transverse)	$p_{\mathrm{T}}^{\mathrm{lead}} \geq 5.5\ GeV$
ATLAS 0.9 TeV, UE in minimum bias	$\langle \frac{\mathrm{d}^2 N_{\mathrm{ch}}}{\mathrm{d}\eta \mathrm{d}\phi} \rangle$ vs. $p_{\mathrm{T}}^{\mathrm{lead}}$ (away)	$p_{\mathrm{T}}^{\mathrm{lead}} \geq 5.5\ GeV$
ATLAS 0.9 TeV, UE in minimum bias	$\langle \frac{\mathrm{d}^2 \sum p_{\mathrm{T}}}{\mathrm{d}\eta \mathrm{d}\phi} \rangle$ vs. $p_{\mathrm{T}}^{\mathrm{lead}}$ (towards)	$p_{\mathrm{T}}^{\mathrm{lead}} \geq 5.5\ GeV$
ATLAS 0.9 TeV, UE in minimum bias	$\langle \frac{\mathrm{d}^2 \sum p_{\mathrm{T}}}{\mathrm{d}\eta \mathrm{d}\phi} \rangle$ vs. $p_{\mathrm{T}}^{\mathrm{lead}}$ (transverse)	$p_{\mathrm{T}}^{\mathrm{lead}} \geq 5.5\ GeV$
ATLAS 0.9 TeV, UE in minimum bias	$\langle \frac{\mathrm{d}^2 \sum p_{\mathrm{T}}}{\mathrm{d}\eta \mathrm{d}\phi} \rangle$ vs. $p_{\mathrm{T}}^{\mathrm{lead}}$ (away)	$p_{\mathrm{T}}^{\mathrm{lead}} \geq 5.5\ GeV$
ATLAS 7 TeV, minimum bias, $n_{\mathrm{ch}} \geq 6$	$\frac{1}{N_{\mathrm{ev}}} \cdot \frac{\mathrm{d}N_{\mathrm{ch}}}{\mathrm{d}\eta}$	$-2.5 < \eta < 2.5$
ATLAS 7 TeV, minimum bias, $n_{\mathrm{ch}} \geq 6$	$\frac{1}{N_{\mathrm{ev}}} \cdot \frac{1}{2\pi p_{\mathrm{T}}} \cdot \frac{\mathrm{d}^2 N_{\mathrm{ch}}}{\mathrm{d}\eta \mathrm{d}p_{\mathrm{T}}}$	$p_{\mathrm{T}} \geq 5.0$ GeV
ATLAS 7 TeV, minimum bias, $n_{\mathrm{ch}} \geq 6$	$\frac{1}{N_{\mathrm{ev}}} \cdot \frac{\mathrm{d}N_{\mathrm{ev}}}{\mathrm{d}n_{\mathrm{ch}}}$	$n_{\mathrm{ch}} \geq 40$
ATLAS 7 TeV, minimum bias, $n_{\mathrm{ch}} \geq 6$	$\langle p_{\mathrm{T}} \rangle$ vs. n_{ch}	$n_{\mathrm{ch}} \geq 10$
ATLAS 7 TeV, UE in minimum bias	$\langle \frac{\mathrm{d}^2 N_{\mathrm{ch}}}{\mathrm{d}\eta \mathrm{d}\phi} \rangle$ vs. $p_{\mathrm{T}}^{\mathrm{lead}}$ (towards)	$p_{\mathrm{T}}^{\mathrm{lead}} \geq 10\ GeV$
ATLAS 7 TeV, UE in minimum bias	$\langle \frac{\mathrm{d}^2 N_{\mathrm{ch}}}{\mathrm{d}\eta \mathrm{d}\phi} \rangle$ vs. $p_{\mathrm{T}}^{\mathrm{lead}}$ (transverse)	$p_{\mathrm{T}}^{\mathrm{lead}} \geq 10\ GeV$
ATLAS 7 TeV, UE in minimum bias	$\langle \frac{\mathrm{d}^2 N_{\mathrm{ch}}}{\mathrm{d}\eta \mathrm{d}\phi} \rangle$ vs. $p_{\mathrm{T}}^{\mathrm{lead}}$ (away)	$p_{\mathrm{T}}^{\mathrm{lead}} \geq 10\ GeV$
ATLAS 7 TeV, UE in minimum bias	$\langle \frac{\mathrm{d}^2 \sum p_{\mathrm{T}}}{\mathrm{d}\eta \mathrm{d}\phi} \rangle$ vs. $p_{\mathrm{T}}^{\mathrm{lead}}$ (towards)	$p_{\mathrm{T}}^{\mathrm{lead}} \geq 10\ GeV$
ATLAS 7 TeV, UE in minimum bias	$\langle \frac{\mathrm{d}^2 \sum p_{\mathrm{T}}}{\mathrm{d}\eta \mathrm{d}\phi} \rangle$ vs. $p_{\mathrm{T}}^{\mathrm{lead}}$ (transverse)	$p_{\mathrm{T}}^{\mathrm{lead}} \geq 10\ GeV$
ATLAS 7 TeV, UE in minimum bias	$\langle \frac{\mathrm{d}^2 \sum p_{\mathrm{T}}}{\mathrm{d}\eta \mathrm{d}\phi} \rangle$ vs. $p_{\mathrm{T}}^{\mathrm{lead}}$ (away)	$p_{\mathrm{T}}^{\mathrm{lead}} \geq 10\ GeV$

Table 7: ATLAS observables and ranges of distributions used in the AMBT1 tuning.

Observables
CDF Run I underlying event in dijet events [49] (leading jet analysis)
N_{ch} density vs. leading jet p_{T} (transverse), JET20
N_{ch} density vs. leading jet p_{T} (toward), JET20
N_{ch} density vs. leading jet p_{T} (away), JET20
$\sum p_{\mathrm{T}}$ density vs. leading jet p_{T} (transverse), JET20
$\sum p_{\mathrm{T}}$ density vs. leading jet p_{T} (toward), JET20
$\sum p_{\mathrm{T}}$ density vs. leading jet p_{T} (away), JET20
N_{ch} density vs. leading jet p_{T} (transverse), min bias
N_{ch} density vs. leading jet p_{T} (toward), min bias
N_{ch} density vs. leading jet p_{T} (away), min bias
$\sum p_{\mathrm{T}}$ density vs. leading jet p_{T} (transverse), min bias
$\sum p_{\mathrm{T}}$ density vs. leading jet p_{T} (toward), min bias
$\sum p_{\mathrm{T}}$ density vs. leading jet p_{T} (away), min bias
p_{T} distribution (transverse), leading $p_{\mathrm{T}} > 5$ GeV
p_{T} distribution (transverse), leading $p_{\mathrm{T}} > 30$ GeV
CDF Run I underlying event in MIN/MAX-cones [50] ("MIN-MAX" analysis)
$\langle p_T^{\mathrm{max}} \rangle$ vs. E_T^{lead}, $\sqrt{s} = 1800$ GeV
$\langle p_T^{\mathrm{min}} \rangle$ vs. E_T^{lead}, $\sqrt{s} = 1800$ GeV
$\langle p_T^{\mathrm{diff}} \rangle$ vs. E_T^{lead}, $\sqrt{s} = 1800$ GeV
$\langle N_{\mathrm{max}} \rangle$ vs. E_T^{lead}, $\sqrt{s} = 1800$ GeV
$\langle N_{\mathrm{min}} \rangle$ vs. E_T^{lead}, $\sqrt{s} = 1800$ GeV
Swiss Cheese p_T^{sum} vs. E_T^{lead} (2 jets), $\sqrt{s} = 1800$ GeV
$\langle p_T^{\mathrm{max}} \rangle$ vs. E_T^{lead}, $\sqrt{s} = 630$ GeV
$\langle p_T^{\mathrm{min}} \rangle$ vs. E_T^{lead}, $\sqrt{s} = 630$ GeV
$\langle p_T^{\mathrm{diff}} \rangle$ vs. E_T^{lead}, $\sqrt{s} = 630$ GeV
Swiss Cheese $p_{\mathrm{T}}^{\mathrm{sum}}$ vs. E_T^{lead} (2 jets), $\sqrt{s} = 630$ GeV
D0 Run II dijet angular correlations [51]
Dijet azimuthal angle, $p_T^{\mathrm{max}} \in [75, 100]$ GeV
Dijet azimuthal angle, $p_T^{\mathrm{max}} \in [100, 130]$ GeV
Dijet azimuthal angle, $p_T^{\mathrm{max}} \in [130, 180]$ GeV
Dijet azimuthal angle, $p_T^{\mathrm{max}} >180$ GeV
CDF Run II minimum bias [52]
$\langle p_{\mathrm{T}} \rangle$ of charged particles vs. N_{ch}, $\sqrt{s} = 1960$ GeV
CDF Run I Z p_{T} [53]
$\frac{d\sigma}{dp_{\mathrm{T}}^Z}$, $\sqrt{s} = 1800$ GeV

Table 8: Tevatron datasets used in the AMBT1 tuning. No specific cuts on the tuning ranges were made.

B Additional Phase-Space Regions

Two additional phase-space regions are considered in this appendix:

- at least twenty charged particles in the kinematic range $|\eta| < 2.5$ and $p_T > 100$ MeV,
- at least one charged particle in the kinematic range $|\eta| < 2.5$ and $p_T > 2.5$ GeV.

The correction procedures as well as methods used to extract the systematic uncertainties are identical to the three phase-space regions presented in the main part of the paper. The first phase-space region is chosen to be compared with the other diffraction-reduced phase-space region with six particles above 500 MeV and allows the study of the interplay between the number of particles and the p_T, in particular for the study of diffraction models. The second additional phase-space region is chosen so as to be less influenced by non-perturbative parts of the non-diffractive modeling and to be useful for predicting high-p_T particle rates, for example for trigger studies.

Table 9 shows the number of selected events and tracks for these two additional phase-space regions at both $\sqrt{s} = 0.9$ TeV and $\sqrt{s} = 7$ TeV. Figures 15 to 18 show the four kinematic distributions. Table 10 shows the results for the mean track multiplicity at central eta (obtained as the average between $-0.2 < \eta < 0.2$). Figure 19 shows the mean track multiplicity at central rapidity for all centre-of-mass energies and phase-space regions presented in this paper, along with predictions from PYTHIA6 AMBT1.

Phase-Space Region		$\sqrt{s} = 0.9$ TeV		$\sqrt{s} = 7$ TeV	
n_{ch}	min p_T	Events	Tracks	Events	Tracks
20	100 MeV	69,833	1,966,059	4,029,563	153,553,344
1	2.5 GeV	19,016	22,233	1,715,637	2,690,534

Table 9: Number of events and tracks in the two additional phase-space regions and energies considered in this appendix.

Phase-Space Region	Energy (TeV)	$dn_{ch}/d\eta$ at $\eta = 0$ Measured
$n_{ch} \geq 20$, $p_T > 100$ MeV	0.9	6.596 ± 0.025 (stat) ± 0.080 (syst)
	7	9.077 ± 0.005 (stat) ± 0.157 (syst)
$n_{ch} \geq 1$, $p_T > 2.5$ GeV	0.9	0.281 ± 0.006 (stat) ± 0.0005 (syst)
	7	0.362 ± 0.001 (stat) ± 0.002 (syst)

Table 10: $dn_{ch}/d\eta$ at $\eta = 0$ for the additional two different phase-space regions considered in this paper for $\sqrt{s} = 0.9$ TeV and $\sqrt{s} = 7$ TeV.

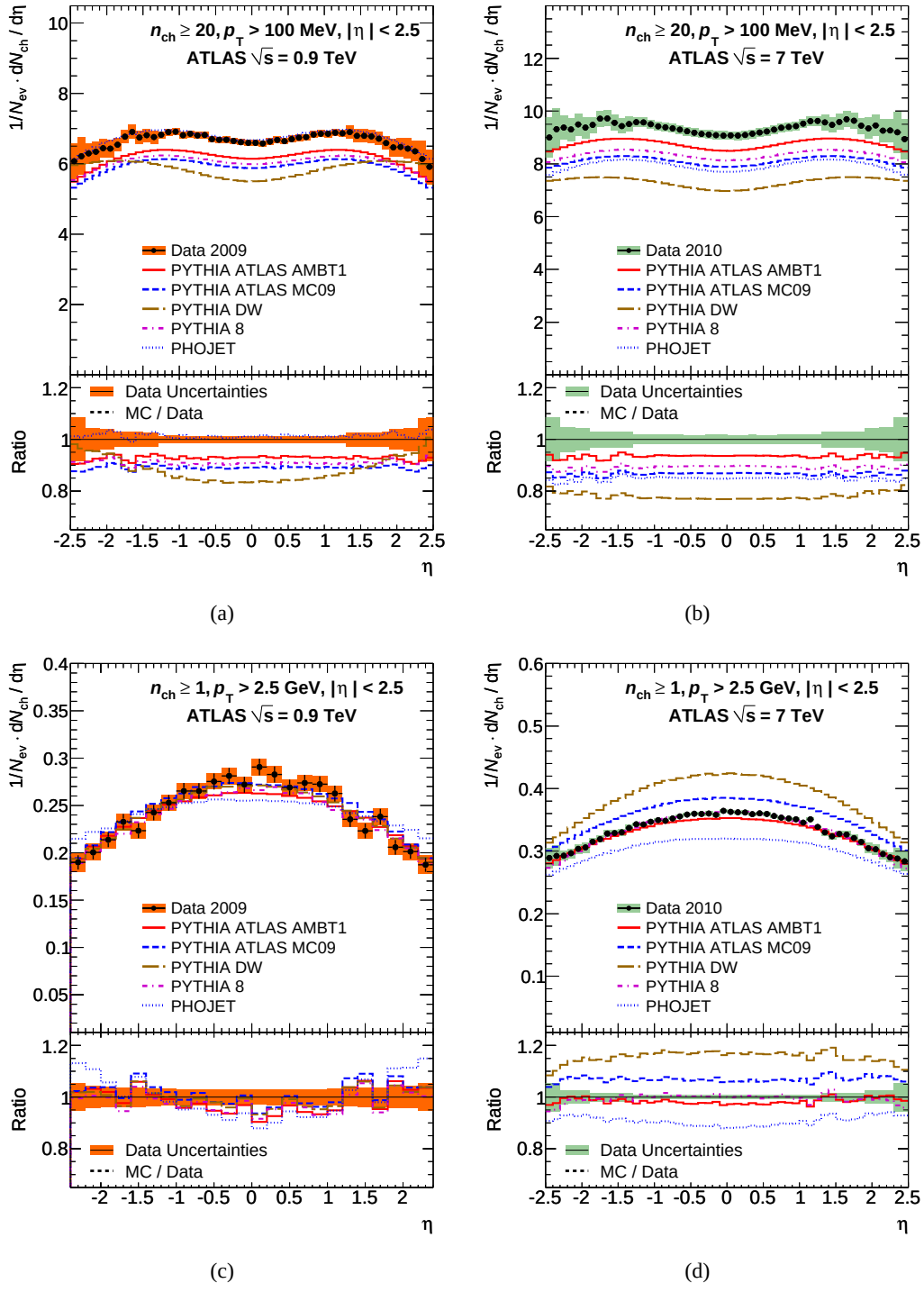

Figure 15: Charged-particle multiplicities as a function of the pseudorapidity for events with $n_{ch} \geq 20$, $p_T > 100$ MeV (a,b) and $n_{ch} \geq 1$, $p_T > 2.5$ GeV (c,d) and $|\eta| < 2.5$ at $\sqrt{s} = 0.9$ TeV (a,c) and $\sqrt{s} = 7$ TeV (b,d). The dots represent the data and the curves the predictions from different MC models. The vertical bars represent the statistical uncertainties, while the shaded areas show statistical and systematic uncertainties added in quadrature. The bottom inserts show the ratio of the MC over the data. The values of the ratio histograms refer to the bin centroids.

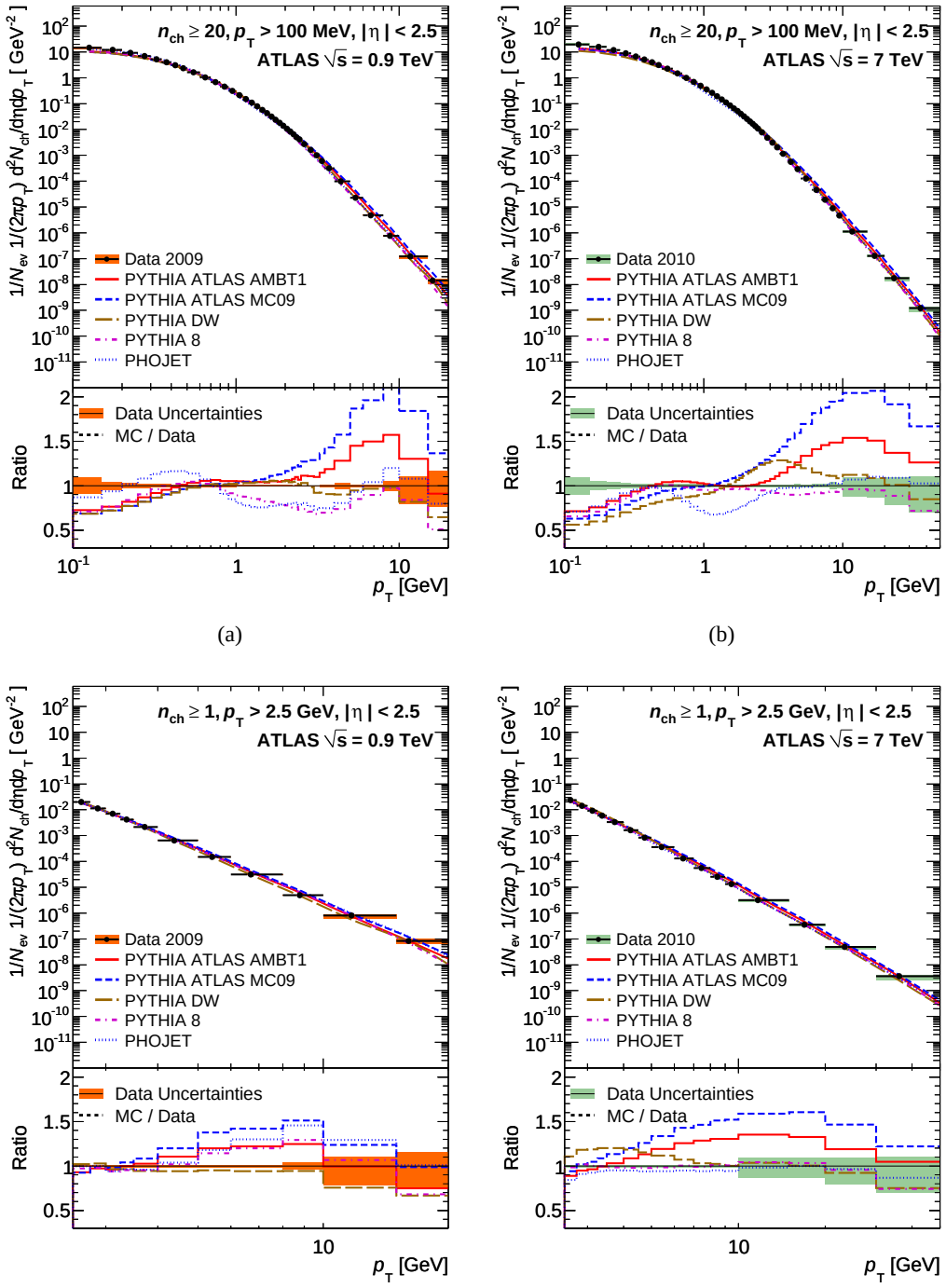

Figure 16: Charged-particle multiplicities as a function of the transverse momentum for events with $n_{ch} \geq 20$, $p_T > 100$ MeV (a,b) and $n_{ch} \geq 1$, $p_T > 2.5$ GeV (c,d) and $|\eta| < 2.5$ at $\sqrt{s} = 0.9$ TeV (a,c) and $\sqrt{s} = 7$ TeV (b,d). The dots represent the data and the curves the predictions from different MC models. The vertical bars represent the statistical uncertainties, while the shaded areas show statistical and systematic uncertainties added in quadrature. The bottom inserts show the ratio of the MC over the data. The values of the ratio histograms refer to the bin centroids.

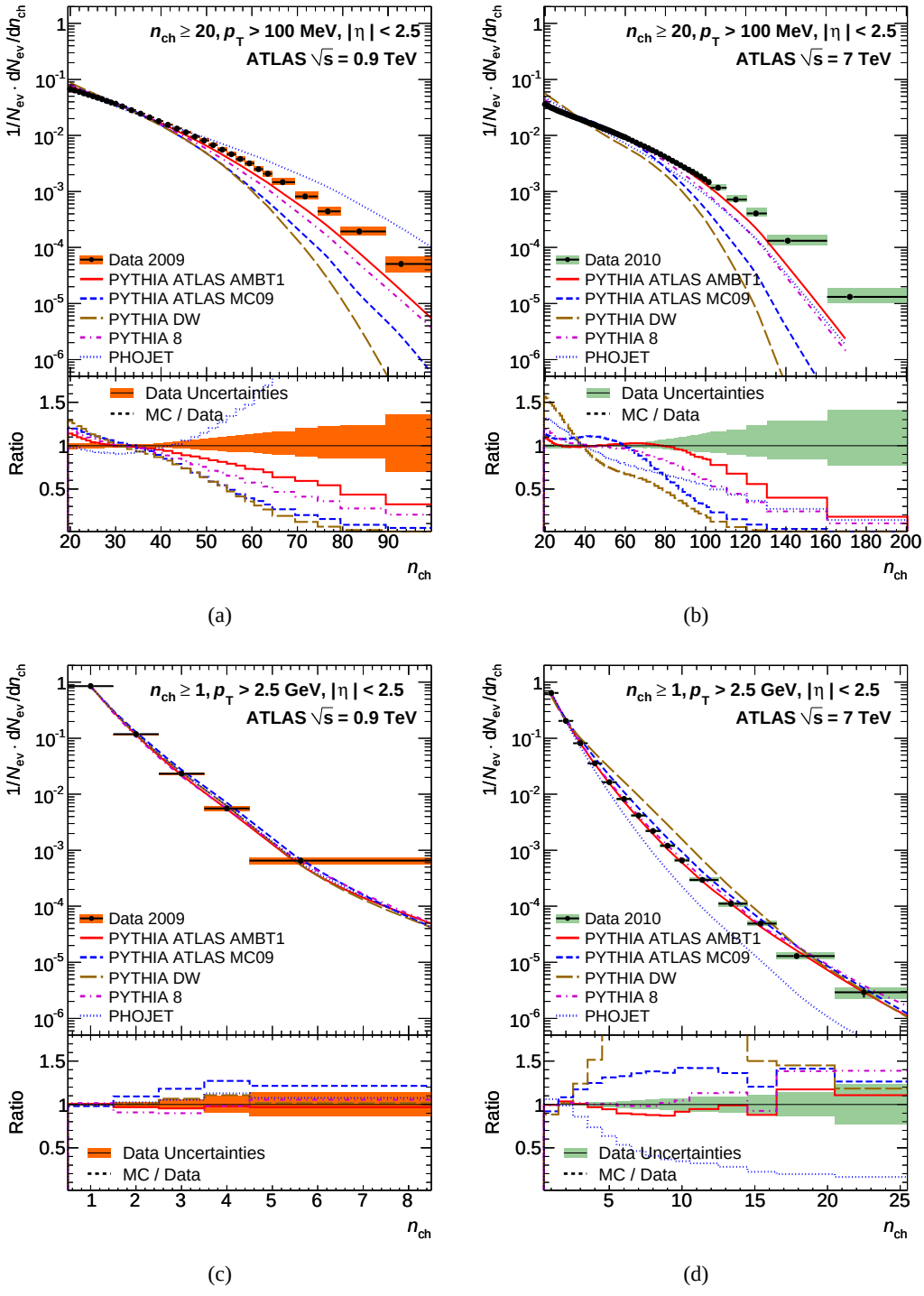

Figure 17: Charged-particle multiplicity distributions for events with $n_{ch} \geq 20$, $p_T > 100$ MeV (a,b) and $n_{ch} \geq 1$, $p_T > 2.5$ GeV (c,d) and $|\eta| < 2.5$ at $\sqrt{s} = 0.9$ TeV (a,c) and $\sqrt{s} = 7$ TeV (b,d). The dots represent the data and the curves the predictions from different MC models. The vertical bars represent the statistical uncertainties, while the shaded areas show statistical and systematic uncertainties added in quadrature. The bottom inserts show the ratio of the MC over the data. The values of the ratio histograms refer to the bin centroids.

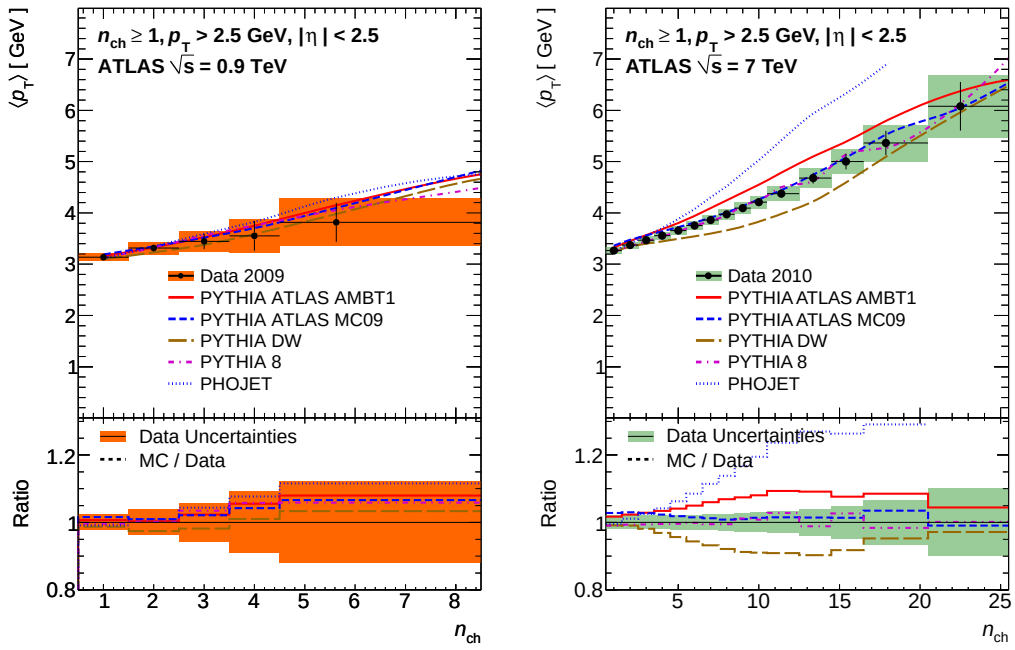

(a) (b)

Figure 18: Average transverse momentum as a function of the number of charged particles in the event for events with $n_{\mathrm{ch}} \geq 1$, $p_{\mathrm{T}} > 2.5$ GeV and $|\eta| < 2.5$ at $\sqrt{s} = 0.9$ TeV (a) and $\sqrt{s} = 7$ TeV (b). The dots represent the data and the curves the predictions from different MC models. The vertical bars represent the statistical uncertainties, while the shaded areas show statistical and systematic uncertainties added in quadrature. The bottom inserts show the ratio of the MC over the data. The values of the ratio histograms refer to the bin centroids.

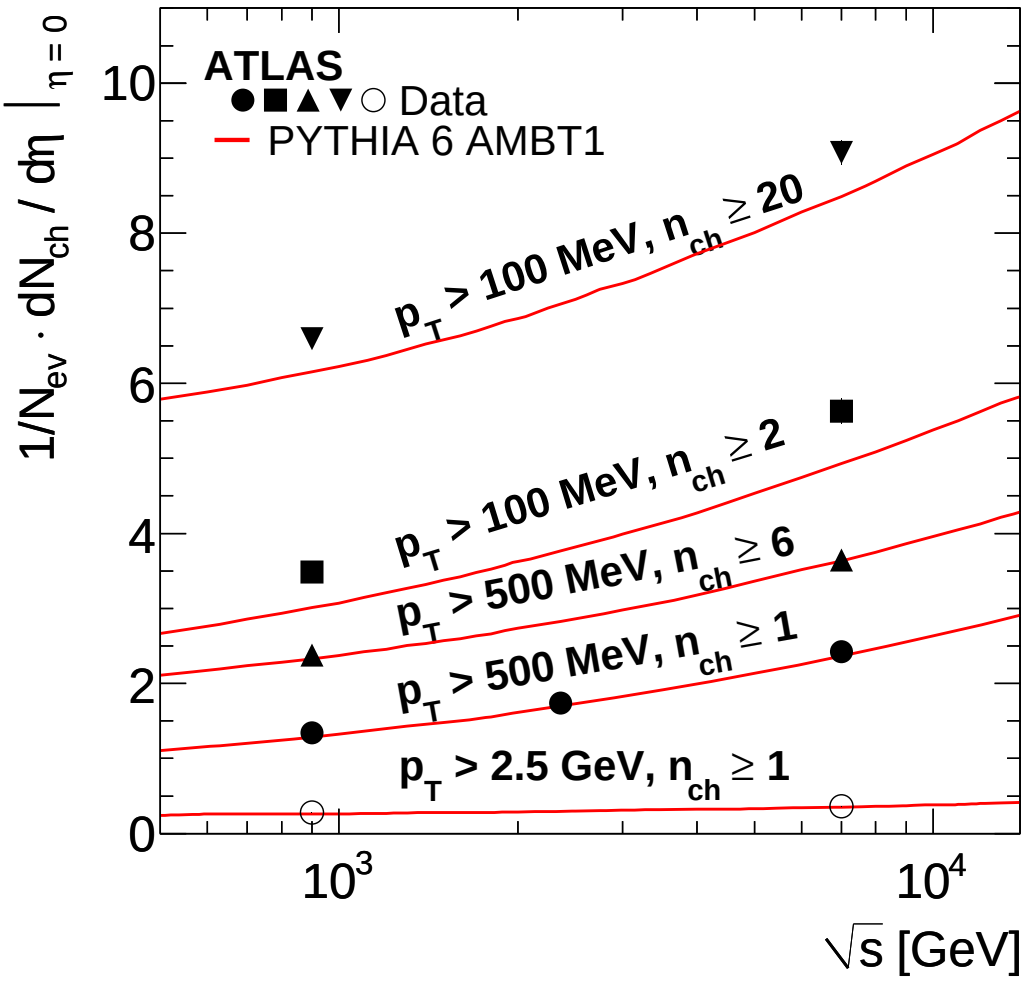

Figure 19: The average charged particle multiplicity per unit of rapidity for $\eta = 0$ as a function of the centre-of-mass energy. All the measured phase-space regions and energies are shown as triangles and compared to predictions from PYTHIA6 AMBT1 tune. The phase-space region label is above the corresponding curves and points. Combined statistical and systematic uncertainties are approximately equal to or smaller than the data points.

The ATLAS Collaboration

G. Aad[48], B. Abbott[111], J. Abdallah[11], A.A. Abdelalim[49], A. Abdesselam[118], O. Abdinov[10], B. Abi[112], M. Abolins[88], H. Abramowicz[153], H. Abreu[115], E. Acerbi[89a,89b], B.S. Acharya[164a,164b], M. Ackers[20], D.L. Adams[24], T.N. Addy[56], J. Adelman[175], M. Aderholz[99], S. Adomeit[98], P. Adragna[75], T. Adye[129], S. Aefsky[22], J.A. Aguilar-Saavedra[124b,a], M. Aharrouche[81], S.P. Ahlen[21], F. Ahles[48], A. Ahmad[148], M. Ahsan[40], G. Aielli[133a,133b], T. Akdogan[18a], T.P.A. Åkesson[79], G. Akimoto[155], A.V. Akimov [94], M.S. Alam[1], M.A. Alam[76], S. Albrand[55], M. Aleksa[29], I.N. Aleksandrov[65], M. Aleppo[89a,89b], F. Alessandria[89a], C. Alexa[25a], G. Alexander[153], G. Alexandre[49], T. Alexopoulos[9], M. Alhroob[20], M. Aliev[15], G. Alimonti[89a], J. Alison[120], M. Aliyev[10], P.P. Allport[73], S.E. Allwood-Spiers[53], J. Almond[82], A. Aloisio[102a,102b], R. Alon[171], A. Alonso[79], J. Alonso[14], M.G. Alviggi[102a,102b], K. Amako[66], P. Amaral[29], C. Amelung[22], V.V. Ammosov[128], A. Amorim[124a,b], G. Amorós[167], N. Amram[153], C. Anastopoulos[139], T. Andeen[34], C.F. Anders[20], K.J. Anderson[30], A. Andreazza[89a,89b], V. Andrei[58a], M-L. Andrieux[55], X.S. Anduaga[70], A. Angerami[34], F. Anghinolfi[29], N. Anjos[124a], A. Annovi[47], A. Antonaki[8], M. Antonelli[47], S. Antonelli[19a,19b], J. Antos[144b], F. Anulli[132a], S. Aoun[83], L. Aperio Bella[4], R. Apolle[118], G. Arabidze[88], I. Aracena[143], Y. Arai[66], A.T.H. Arce[44], J.P. Archambault[28], S. Arfaoui[29,c], J-F. Arguin[14], E. Arik[18a,*], M. Arik[18a], A.J. Armbruster[87], K.E. Arms[109], S.R. Armstrong[24], O. Arnaez[81], C. Arnault[115], A. Artamonov[95], G. Artoni[132a,132b], D. Arutinov[20], S. Asai[155], J. Silva[124a,d], R. Asfandiyarov[172], S. Ask[27], B. Åsman[146a,146b], L. Asquith[5], K. Assamagan[24], A. Astbury[169], A. Astvatsatourov[52], G. Atoian[175], B. Aubert[4], B. Auerbach[175], E. Auge[115], K. Augsten[127], M. Aurousseau[4], N. Austin[73], R. Avramidou[9], D. Axen[168], C. Ay[54], G. Azuelos[93,e], Y. Azuma[155], M.A. Baak[29], G. Baccaglioni[89a], C. Bacci[134a,134b], A.M. Bach[14], H. Bachacou[136], K. Bachas[29], G. Bachy[29], M. Backes[49], E. Badescu[25a], P. Bagnaia[132a,132b], S. Bahinipati[2], Y. Bai[32a], D.C. Bailey [158], T. Bain[158], J.T. Baines[129], O.K. Baker[175], S. Baker[77], F. Baltasar Dos Santos Pedrosa[29], E. Banas[38], P. Banerjee[93], Sw. Banerjee[169], D. Banfi[89a,89b], A. Bangert[137], V. Bansal[169], H.S. Bansil[17], L. Barak[171], S.P. Baranov[94], A. Barashkou[65], A. Barbaro Galtieri[14], T. Barber[27], E.L. Barberio[86], D. Barberis[50a,50b], M. Barbero[20], D.Y. Bardin[65], T. Barillari[99], M. Barisonzi[174], T. Barklow[143], N. Barlow[27], B.M. Barnett[129], R.M. Barnett[14], A. Baroncelli[134a], A.J. Barr[118], F. Barreiro[80], J. Barreiro Guimarães da Costa[57], P. Barrillon[115], R. Bartoldus[143], A.E. Barton[71], D. Bartsch[20], R.L. Bates[53], L. Batkova[144a], J.R. Batley[27], A. Battaglia[16], M. Battistin[29], G. Battistoni[89a], F. Bauer[136], H.S. Bawa[143], B. Beare[158], T. Beau[78], P.H. Beauchemin[118], R. Beccherle[50a], P. Bechtle[41], H.P. Beck[16], M. Beckingham[48], K.H. Becks[174], A.J. Beddall[18c], A. Beddall[18c], V.A. Bednyakov[65], C. Bee[83], M. Begel[24], S. Behar Harpaz[152], P.K. Behera[63], M. Beimforde[99], C. Belanger-Champagne[166], P.J. Bell[49], W.H. Bell[49], G. Bella[153], L. Bellagamba[19a], F. Bellina[29], G. Bellomo[89a,89b], M. Bellomo[119a], A. Belloni[57], K. Belotskiy[96], O. Beltramello[29], S. Ben Ami[152], O. Benary[153], D. Benchekroun[135a], C. Benchouk[83], M. Bendel[81], B.H. Benedict[163], N. Benekos[165], Y. Benhammou[153], D.P. Benjamin[44], M. Benoit[115], J.R. Bensinger[22], K. Benslama[130], S. Bentvelsen[105], D. Berge[29], E. Bergeaas Kuutmann[41], N. Berger[4], F. Berghaus[169], E. Berglund[49], J. Beringer[14], K. Bernardet[83], P. Bernat[115], R. Bernhard[48], C. Bernius[24], T. Berry[76], A. Bertin[19a,19b], F. Bertinelli[29], F. Bertolucci[122a,122b], M.I. Besana[89a,89b], N. Besson[136], S. Bethke[99], W. Bhimji[45], R.M. Bianchi[29], M. Bianco[72a,72b], O. Biebel[98], J. Biesiada[14], M. Biglietti[132a,132b], H. Bilokon[47], M. Bindi[19a,19b], A. Bingul[18c], C. Bini[132a,132b], C. Biscarat[177], U. Bitenc[48], K.M. Black[21], R.E. Blair[5], J.-B. Blanchard[115], G. Blanchot[29], C. Blocker[22], J. Blocki[38], A. Blondel[49], W. Blum[81], U. Blumenschein[54], G.J. Bobbink[105], V.B. Bobrovnikov[107], A. Bocci[44], R. Bock[29], C.R. Boddy[118], M. Boehler[41], J. Boek[174], N. Boelaert[35], S. Böser[77], J.A. Bogaerts[29], A. Bogdanchikov[107], A. Bogouch[90,*], C. Bohm[146a], V. Boisvert[76], T. Bold[163,f], V. Boldea[25a], M. Boonekamp[136], G. Boorman[76], C.N. Booth[139], P. Booth[139], J.R.A. Booth[17], S. Bordoni[78], C. Borer[16], A. Borisov[128], G. Borissov[71], I. Borjanovic[12a], S. Borroni[132a,132b], K. Bos[105], D. Boscherini[19a], M. Bosman[11], H. Boterenbrood[105], D. Botterill[129], J. Bouchami[93], J. Boudreau[123], E.V. Bouhova-Thacker[71],

C. Boulahouache[123], C. Bourdarios[115], N. Bousson[83], A. Boveia[30], J. Boyd[29], I.R. Boyko[65], N.I. Bozhko[128], I. Bozovic-Jelisavcic[12b], J. Bracinik[17], A. Braem[29], E. Brambilla[72a,72b], P. Branchini[134a], G.W. Brandenburg[57], A. Brandt[7], G. Brandt[41], O. Brandt[54], U. Bratzler[156], B. Brau[84], J.E. Brau[114], H.M. Braun[174], B. Brelier[158], J. Bremer[29], R. Brenner[166], S. Bressler[152], D. Breton[115], N.D. Brett[118], P.G. Bright-Thomas[17], D. Britton[53], F.M. Brochu[27], I. Brock[20], R. Brock[88], T.J. Brodbeck[71], E. Brodet[153], F. Broggi[89a], C. Bromberg[88], G. Brooijmans[34], W.K. Brooks[31b], G. Brown[82], E. Brubaker[30], P.A. Bruckman de Renstrom[38], D. Bruncko[144b], R. Bruneliere[48], S. Brunet[61], A. Bruni[19a], G. Bruni[19a], M. Bruschi[19a], T. Buanes[13], F. Bucci[49], J. Buchanan[118], N.J. Buchanan[2], P. Buchholz[141], R.M. Buckingham[118], A.G. Buckley[45], S.I. Buda[25a], I.A. Budagov[65], B. Budick[108], V. Büscher[81], L. Bugge[117], D. Buira-Clark[118], E.J. Buis[105], O. Bulekov[96], M. Bunse[42], T. Buran[117], H. Burckhart[29], S. Burdin[73], T. Burgess[13], S. Burke[129], E. Busato[33], P. Bussey[53], C.P. Buszello[166], F. Butin[29], B. Butler[143], J.M. Butler[21], C.M. Buttar[53], J.M. Butterworth[77], W. Buttinger[27], T. Byatt[77], S. Cabrera Urbán[167], M. Caccia[89a,89b,*g*], D. Caforio[19a,19b], O. Cakir[3a], P. Calafiura[14], G. Calderini[78], P. Calfayan[98], R. Calkins[106], L.P. Caloba[23a], R. Caloi[132a,132b], D. Calvet[33], S. Calvet[33], A. Camard[78], P. Camarri[133a,133b], M. Cambiaghi[119a,119b], D. Cameron[117], J. Cammin[20], S. Campana[29], M. Campanelli[77], V. Canale[102a,102b], F. Canelli[30], A. Canepa[159a], J. Cantero[80], L. Capasso[102a,102b], M.D.M. Capeans Garrido[29], I. Caprini[25a], M. Caprini[25a], D. Capriotti[99], M. Capua[36a,36b], R. Caputo[148], C. Caramarcu[25a], R. Cardarelli[133a], T. Carli[29], G. Carlino[102a], L. Carminati[89a,89b], B. Caron[159a], S. Caron[48], C. Carpentieri[48], G.D. Carrillo Montoya[172], S. Carron Montero[158], A.A. Carter[75], J.R. Carter[27], J. Carvalho[124a,*h*], D. Casadei[108], M.P. Casado[11], M. Cascella[122a,122b], C. Caso[50a,50b,*], A.M. Castaneda Hernandez[172], E. Castaneda-Miranda[172], V. Castillo Gimenez[167], N.F. Castro[124b,*a*], G. Cataldi[72a], F. Cataneo[29], A. Catinaccio[29], J.R. Catmore[71], A. Cattai[29], G. Cattani[133a,133b], S. Caughron[88], A. Cavallari[132a,132b], P. Cavalleri[78], D. Cavalli[89a], M. Cavalli-Sforza[11], V. Cavasinni[122a,122b], A. Cazzato[72a,72b], F. Ceradini[134a,134b], C. Cerna[83], A.S. Cerqueira[23a], A. Cerri[29], L. Cerrito[75], F. Cerutti[47], S.A. Cetin[18b], F. Cevenini[102a,102b], A. Chafaq[135a], D. Chakraborty[106], K. Chan[2], B. Chapleau[85], J.D. Chapman[27], J.W. Chapman[87], E. Chareyre[78], D.G. Charlton[17], V. Chavda[82], S. Cheatham[71], S. Chekanov[5], S.V. Chekulaev[159a], G.A. Chelkov[65], H. Chen[24], L. Chen[2], S. Chen[32c], T. Chen[32c], X. Chen[172], S. Cheng[32a], A. Cheplakov[65], V.F. Chepurnov[65], R. Cherkaoui El Moursli[135d], V. Chernyatin[24], E. Cheu[6], S.L. Cheung[158], L. Chevalier[136], F. Chevallier[136], G. Chiefari[102a,102b], L. Chikovani[51], J.T. Childers[58a], A. Chilingarov[71], G. Chiodini[72a], M.V. Chizhov[65], G. Choudalakis[30], S. Chouridou[137], I.A. Christidi[77], A. Christov[48], D. Chromek-Burckhart[29], M.L. Chu[151], J. Chudoba[125], G. Ciapetti[132a,132b], A.K. Ciftci[3a], R. Ciftci[3a], D. Cinca[33], V. Cindro[74], M.D. Ciobotaru[163], C. Ciocca[19a,19b], A. Ciocio[14], M. Cirilli[87,*i*], M. Ciubancan[25a], A. Clark[49], P.J. Clark[45], W. Cleland[123], J.C. Clemens[83], B. Clement[55], C. Clement[146a,146b], R.W. Clifft[129], Y. Coadou[83], M. Cobal[164a,164c], A. Coccaro[50a,50b], J. Cochran[64], P. Coe[118], J.G. Cogan[143], J. Coggeshall[165], E. Cogneras[177], C.D. Cojocaru[28], J. Colas[4], A.P. Colijn[105], C. Collard[115], N.J. Collins[17], C. Collins-Tooth[53], J. Collot[55], G. Colon[84], R. Coluccia[72a,72b], G. Comune[88], P. Conde Muiño[124a], E. Coniavitis[118], M.C. Conidi[11], M. Consonni[104], S. Constantinescu[25a], C. Conta[119a,119b], F. Conventi[102a,*j*], J. Cook[29], M. Cooke[14], B.D. Cooper[75], A.M. Cooper-Sarkar[118], N.J. Cooper-Smith[76], K. Copic[34], T. Cornelissen[50a,50b], M. Corradi[19a], S. Correard[83], F. Corriveau[85,*k*], A. Cortes-Gonzalez[165], G. Cortiana[99], G. Costa[89a], M.J. Costa[167], D. Costanzo[139], T. Costin[30], D. Côté[29], R. Coura Torres[23a], L. Courneyea[169], G. Cowan[76], C. Cowden[27], B.E. Cox[82], K. Cranmer[108], M. Cristinziani[20], G. Crosetti[36a,36b], R. Crupi[72a,72b], S. Crépé-Renaudin[55], C. Cuenca Almenar[175], T. Cuhadar Donszelmann[139], S. Cuneo[50a,50b], M. Curatolo[47], C.J. Curtis[17], P. Cwetanski[61], H. Czirr[141], Z. Czyczula[117], S. D'Auria[53], M. D'Onofrio[73], A. D'Orazio[132a,132b], A. Da Rocha Gesualdi Mello[23a], P.V.M. Da Silva[23a], C. Da Via[82], W. Dabrowski[37], A. Dahlhoff[48], T. Dai[87], C. Dallapiccola[84], S.J. Dallison[129,*], M. Dam[35], M. Dameri[50a,50b], D.S. Damiani[137], H.O. Danielsson[29], R. Dankers[105], D. Dannheim[99], V. Dao[49],

G. Darbo[50a], G.L. Darlea[25b], C. Daum[105], J.P. Dauvergne [29], W. Davey[86], T. Davidek[126], N. Davidson[86], R. Davidson[71], M. Davies[93], A.R. Davison[77], E. Dawe[142], I. Dawson[139], J.W. Dawson[5,*], R.K. Daya[39], K. De[7], R. de Asmundis[102a], S. De Castro[19a,19b], S. De Cecco[78], J. de Graat[98], N. De Groot[104], P. de Jong[105], E. De La Cruz-Burelo[87], C. De La Taille[115], B. De Lotto[164a,164c], L. De Mora[71], L. De Nooij[105], M. De Oliveira Branco[29], D. De Pedis[132a], P. de Saintignon[55], A. De Salvo[132a], U. De Sanctis[164a,164c], A. De Santo[149], J.B. De Vivie De Regie[115], S. Dean[77], G. Dedes[99], D.V. Dedovich[65], J. Degenhardt[120], M. Dehchar[118], M. Deile[98], C. Del Papa[164a,164c], J. Del Peso[80], T. Del Prete[122a,122b], A. Dell'Acqua[29], L. Dell'Asta[89a,89b], M. Della Pietra[102a,l], D. della Volpe[102a,102b], M. Delmastro[29], P. Delpierre[83], N. Delruelle[29], P.A. Delsart[55], C. Deluca[148], S. Demers[175], M. Demichev[65], B. Demirkoz[11], J. Deng[163], S.P. Denisov[128], C. Dennis[118], D. Derendarz[38], J.E. Derkaoui[135c], F. Derue[78], P. Dervan[73], K. Desch[20], E. Devetak[148], P.O. Deviveiros[158], A. Dewhurst[129], B. DeWilde[148], S. Dhaliwal[158], R. Dhullipudi[24,m], A. Di Ciaccio[133a,133b], L. Di Ciaccio[4], A. Di Girolamo[29], B. Di Girolamo[29], S. Di Luise[134a,134b], A. Di Mattia[88], R. Di Nardo[133a,133b], A. Di Simone[133a,133b], R. Di Sipio[19a,19b], M.A. Diaz[31a], F. Diblen[18c], E.B. Diehl[87], H. Dietl[99], J. Dietrich[48], T.A. Dietzsch[58a], S. Diglio[115], K. Dindar Yagci[39], J. Dingfelder[20], C. Dionisi[132a,132b], P. Dita[25a], S. Dita[25a], F. Dittus[29], F. Djama[83], R. Djilkibaev[108], T. Djobava[51], M.A.B. do Vale[23a], A. Do Valle Wemans[124a], T.K.O. Doan[4], M. Dobbs[85], R. Dobinson [29,*], D. Dobos[42], E. Dobson[29], M. Dobson[163], J. Dodd[34], O.B. Dogan[18a,*], C. Doglioni[118], T. Doherty[53], Y. Doi[66,*], J. Dolejsi[126], I. Dolenc[74], Z. Dolezal[126], B.A. Dolgoshein[96], T. Dohmae[155], M. Donadelli[23b], M. Donega[120], J. Donini[55], J. Dopke[174], A. Doria[102a], A. Dos Anjos[172], M. Dosil[11], A. Dotti[122a,122b], M.T. Dova[70], J.D. Dowell[17], A.D. Doxiadis[105], A.T. Doyle[53], Z. Drasal[126], J. Drees[174], N. Dressnandt[120], H. Drevermann[29], C. Driouichi[35], M. Dris[9], J.G. Drohan[77], J. Dubbert[99], T. Dubbs[137], S. Dube[14], E. Duchovni[171], G. Duckeck[98], A. Dudarev[29], F. Dudziak[115], M. Dührssen [29], I.P. Duerdoth[82], L. Duflot[115], M-A. Dufour[85], M. Dunford[29], H. Duran Yildiz[3b], R. Duxfield[139], M. Dwuznik[37], F. Dydak [29], D. Dzahini[55], M. Düren[52], J. Ebke[98], S. Eckert[48], S. Eckweiler[81], K. Edmonds[81], C.A. Edwards[76], I. Efthymiopoulos[49], W. Ehrenfeld[41], T. Ehrich[99], T. Eifert[29], G. Eigen[13], K. Einsweiler[14], E. Eisenhandler[75], T. Ekelof[166], M. El Kacimi[4], M. Ellert[166], S. Elles[4], F. Ellinghaus[81], K. Ellis[75], N. Ellis[29], J. Elmsheuser[98], M. Elsing[29], R. Ely[14], D. Emeliyanov[129], R. Engelmann[148], A. Engl[98], B. Epp[62], A. Eppig[87], J. Erdmann[54], A. Ereditato[16], D. Eriksson[146a], J. Ernst[1], M. Ernst[24], J. Ernwein[136], D. Errede[165], S. Errede[165], E. Ertel[81], M. Escalier[115], C. Escobar[167], X. Espinal Curull[11], B. Esposito[47], F. Etienne[83], A.I. Etienvre[136], E. Etzion[153], D. Evangelakou[54], H. Evans[61], L. Fabbri[19a,19b], C. Fabre[29], K. Facius[35], R.M. Fakhrutdinov[128], S. Falciano[132a], A.C. Falou[115], Y. Fang[172], M. Fanti[89a,89b], A. Farbin[7], A. Farilla[134a], J. Farley[148], T. Farooque[158], S.M. Farrington[118], P. Farthouat[29], D. Fasching[172], P. Fassnacht[29], D. Fassouliotis[8], B. Fatholahzadeh[158], A. Favareto[89a,89b], L. Fayard[115], S. Fazio[36a,36b], R. Febbraro[33], P. Federic[144a], O.L. Fedin[121], I. Fedorko[29], W. Fedorko[88], M. Fehling-Kaschek[48], L. Feligioni[83], D. Fellmann[5], C.U. Felzmann[86], C. Feng[32d], E.J. Feng[30], A.B. Fenyuk[128], J. Ferencei[144b], D. Ferguson[172], J. Ferland[93], B. Fernandes[124a,n], W. Fernando[109], S. Ferrag[53], J. Ferrando[118], V. Ferrara[41], A. Ferrari[166], P. Ferrari[105], R. Ferrari[119a], A. Ferrer[167], M.L. Ferrer[47], D. Ferrere[49], C. Ferretti[87], A. Ferretto Parodi[50a,50b], M. Fiascaris[30], F. Fiedler[81], A. Filipčič[74], A. Filippas[9], F. Filthaut[104], M. Fincke-Keeler[169], M.C.N. Fiolhais[124a,h], L. Fiorini[11], A. Firan[39], G. Fischer[41], P. Fischer [20], M.J. Fisher[109], S.M. Fisher[129], J. Flammer[29], M. Flechl[48], I. Fleck[141], J. Fleckner[81], P. Fleischmann[173], S. Fleischmann[20], T. Flick[174], L.R. Flores Castillo[172], M.J. Flowerdew[99], F. Föhlisch[58a], M. Fokitis[9], T. Fonseca Martin[16], D.A. Forbush[138], A. Formica[136], A. Forti[82], D. Fortin[159a], J.M. Foster[82], D. Fournier[115], A. Foussat[29], A.J. Fowler[44], K. Fowler[137], H. Fox[71], P. Francavilla[122a,122b], S. Franchino[119a,119b], D. Francis[29], T. Frank[171], M. Franklin[57], S. Franz[29], M. Fraternali[119a,119b], S. Fratina[120], S.T. French[27], R. Froeschl[29], D. Froidevaux[29], J.A. Frost[27], C. Fukunaga[156], E. Fullana Torregrosa[29], J. Fuster[167], C. Gabaldon[29], O. Gabizon[171], T. Gadfort[24], S. Gadomski[49],

G. Gagliardi[50a,50b], P. Gagnon[61], C. Galea[98], E.J. Gallas[118], M.V. Gallas[29], V. Gallo[16], B.J. Gallop[129], P. Gallus[125], E. Galyaev[40], K.K. Gan[109], Y.S. Gao[143,o], V.A. Gapienko[128], A. Gaponenko[14], F. Garberson[175], M. Garcia-Sciveres[14], C. García[167], J.E. García Navarro[49], R.W. Gardner[30], N. Garelli[29], H. Garitaonandia[105], V. Garonne[29], J. Garvey[17], C. Gatti[47], G. Gaudio[119a], O. Gaumer[49], B. Gaur[141], L. Gauthier[136], I.L. Gavrilenko[94], C. Gay[168], G. Gaycken[20], J-C. Gayde[29], E.N. Gazis[9], P. Ge[32d], C.N.P. Gee[129], Ch. Geich-Gimbel[20], K. Gellerstedt[146a,146b], C. Gemme[50a], M.H. Genest[98], S. Gentile[132a,132b], F. Georgatos[9], S. George[76], P. Gerlach[174], A. Gershon[153], C. Geweniger[58a], H. Ghazlane[135d], P. Ghez[4], N. Ghodbane[33], B. Giacobbe[19a], S. Giagu[132a,132b], V. Giakoumopoulou[8], V. Giangiobbe[122a,122b], F. Gianotti[29], B. Gibbard[24], A. Gibson[158], S.M. Gibson[29], G.F. Gieraltowski[5], L.M. Gilbert[118], M. Gilchriese[14], O. Gildemeister[29], V. Gilewsky[91], D. Gillberg[28], A.R. Gillman[129], D.M. Gingrich[2,p], J. Ginzburg[153], N. Giokaris[8], R. Giordano[102a,102b], F.M. Giorgi[15], P. Giovannini[99], P.F. Giraud[136], D. Giugni[89a], P. Giusti[19a], B.K. Gjelsten[117], L.K. Gladilin[97], C. Glasman[80], J. Glatzer[48], A. Glazov[41], K.W. Glitza[174], G.L. Glonti[65], J. Godfrey[142], J. Godlewski[29], M. Goebel[41], T. Göpfert[43], C. Goeringer[81], C. Gössling[42], T. Göttfert[99], S. Goldfarb[87], D. Goldin[39], T. Golling[175], N.P. Gollub[29], S.N. Golovnia[128], A. Gomes[124a,q], L.S. Gomez Fajardo[41], R. Gonçalo[76], L. Gonella[20], C. Gong[32b], A. Gonidec[29], S. Gonzalez[172], S. González de la Hoz[167], M.L. Gonzalez Silva[26], S. Gonzalez-Sevilla[49], J.J. Goodson[148], L. Goossens[29], P.A. Gorbounov[95], H.A. Gordon[24], I. Gorelov[103], G. Gorfine[174], B. Gorini[29], E. Gorini[72a,72b], A. Gorišek[74], E. Gornicki[38], S.A. Gorokhov[128], B.T. Gorski[29], V.N. Goryachev[128], B. Gosdzik[41], M. Gosselink[105], M.I. Gostkin[65], M. Gouanère[4], I. Gough Eschrich[163], M. Gouighri[135a], D. Goujdami[135a], M.P. Goulette[49], A.G. Goussiou[138], C. Goy[4], I. Grabowska-Bold[163,r], V. Grabski[176], P. Grafström[29], C. Grah[174], K-J. Grahn[147], F. Grancagnolo[72a], S. Grancagnolo[15], V. Grassi[148], V. Gratchev[121], N. Grau[34], H.M. Gray[34,s], J.A. Gray[148], E. Graziani[134a], O.G. Grebenyuk[121], D. Greenfield[129], T. Greenshaw[73], Z.D. Greenwood[24,t], I.M. Gregor[41], P. Grenier[143], E. Griesmayer[46], J. Griffiths[138], N. Grigalashvili[65], A.A. Grillo[137], K. Grimm[148], S. Grinstein[11], P.L.Y. Gris[33], Y.V. Grishkevich[97], J.-F. Grivaz[115], J. Grognuz[29], M. Groh[99], E. Gross[171], J. Grosse-Knetter[54], J. Groth-Jensen[79], M. Gruwe[29], K. Grybel[141], V.J. Guarino[5], C. Guicheney[33], A. Guida[72a,72b], T. Guillemin[4], S. Guindon[54], H. Guler[85,u], J. Gunther[125], B. Guo[158], J. Guo[34], A. Gupta[30], Y. Gusakov[65], V.N. Gushchin[128], A. Gutierrez[93], P. Gutierrez[111], N. Guttman[153], O. Gutzwiller[172], C. Guyot[136], C. Gwenlan[118], C.B. Gwilliam[73], A. Haas[143], S. Haas[29], C. Haber[14], R. Hackenburg[24], H.K. Hadavand[39], D.R. Hadley[17], P. Haefner[99], F. Hahn[29], S. Haider[29], Z. Hajduk[38], H. Hakobyan[176], J. Haller[54], K. Hamacher[174], A. Hamilton[49], S. Hamilton[161], H. Han[32a], L. Han[32b], K. Hanagaki[116], M. Hance[120], C. Handel[81], P. Hanke[58a], C.J. Hansen[166], J.R. Hansen[35], J.B. Hansen[35], J.D. Hansen[35], P.H. Hansen[35], P. Hansson[143], K. Hara[160], G.A. Hare[137], T. Harenberg[174], D. Harper[87], R.D. Harrington[21], O.M. Harris[138], K. Harrison[17], J.C. Hart[129], J. Hartert[48], F. Hartjes[105], T. Haruyama[66], A. Harvey[56], S. Hasegawa[101], Y. Hasegawa[140], S. Hassani[136], M. Hatch[29], D. Hauff[99], S. Haug[16], M. Hauschild[29], R. Hauser[88], M. Havranek[125], B.M. Hawes[118], C.M. Hawkes[17], R.J. Hawkings[29], D. Hawkins[163], T. Hayakawa[67], D Hayden[76], H.S. Hayward[73], S.J. Haywood[129], E. Hazen[21], M. He[32d], S.J. Head[17], V. Hedberg[79], L. Heelan[28], S. Heim[88], B. Heinemann[14], S. Heisterkamp[35], L. Helary[4], M. Heldmann[48], M. Heller[115], S. Hellman[146a,146b], C. Helsens[11], R.C.W. Henderson[71], M. Henke[58a], A. Henrichs[54], A.M. Henriques Correia[29], S. Henrot-Versille[115], F. Henry-Couannier[83], C. Hensel[54], T. Henß[174], Y. Hernández Jiménez[167], R. Herrberg[15], A.D. Hershenhorn[152], G. Herten[48], R. Hertenberger[98], L. Hervas[29], N.P. Hessey[105], A. Hidvegi[146a], E. Higón-Rodriguez[167], D. Hill[5,*], J.C. Hill[27], N. Hill[5], K.H. Hiller[41], S. Hillert[20], S.J. Hillier[17], I. Hinchliffe[14], E. Hines[120], M. Hirose[116], F. Hirsch[42], D. Hirschbuehl[174], J. Hobbs[148], N. Hod[153], M.C. Hodgkinson[139], P. Hodgson[139], A. Hoecker[29], M.R. Hoeferkamp[103], J. Hoffman[39], D. Hoffmann[83], M. Hohlfeld[81], M. Holder[141], A. Holmes[118], S.O. Holmgren[146a], T. Holy[127], J.L. Holzbauer[88], R.J. Homer[17], Y. Homma[67], T. Horazdovsky[127], C. Horn[143], S. Horner[48], K. Horton[118], J-Y. Hostachy[55], T. Hott[99], S. Hou[151], M.A. Houlden[73], A. Hoummada[135a], J. Howarth[82],

D.F. Howell[118], I. Hristova [41], J. Hrivnac[115], I. Hruska[125], T. Hryn'ova[4], P.J. Hsu[175], S.-C. Hsu[14], G.S. Huang[111], Z. Hubacek[127], F. Hubaut[83], F. Huegging[20], T.B. Huffman[118], E.W. Hughes[34], G. Hughes[71], R.E. Hughes-Jones[82], M. Huhtinen[29], P. Hurst[57], M. Hurwitz[14], U. Husemann[41], N. Huseynov[10], J. Huston[88], J. Huth[57], G. Iacobucci[102a], G. Iakovidis[9], M. Ibbotson[82], I. Ibragimov[141], R. Ichimiya[67], L. Iconomidou-Fayard[115], J. Idarraga[115], M. Idzik[37], P. Iengo[4], O. Igonkina[105], Y. Ikegami[66], M. Ikeno[66], Y. Ilchenko[39], D. Iliadis[154], D. Imbault[78], M. Imhaeuser[174], M. Imori[155], T. Ince[20], J. Inigo-Golfin[29], P. Ioannou[8], M. Iodice[134a], G. Ionescu[4], A. Irles Quiles[167], K. Ishii[66], A. Ishikawa[67], M. Ishino[66], R. Ishmukhametov[39], T. Isobe[155], C. Issever[118], S. Istin[18a], Y. Itoh[101], A.V. Ivashin[128], W. Iwanski[38], H. Iwasaki[66], J.M. Izen[40], V. Izzo[102a], B. Jackson[120], J.N. Jackson[73], P. Jackson[143], M.R. Jaekel[29], V. Jain[61], K. Jakobs[48], S. Jakobsen[35], J. Jakubek[127], D.K. Jana[111], E. Jankowski[158], E. Jansen[77], A. Jantsch[99], M. Janus[20], G. Jarlskog[79], L. Jeanty[57], K. Jelen[37], I. Jen-La Plante[30], P. Jenni[29], A. Jeremie[4], P. Jež[35], S. Jézéquel[4], H. Ji[172], W. Ji[81], J. Jia[148], Y. Jiang[32b], M. Jimenez Belenguer[29], G. Jin[32b], S. Jin[32a], O. Jinnouchi[157], M.D. Joergensen[35], D. Joffe[39], L.G. Johansen[13], M. Johansen[146a,146b], K.E. Johansson[146a], P. Johansson[139], S. Johnert[41], K.A. Johns[6], K. Jon-And[146a,146b], G. Jones[82], R.W.L. Jones[71], T.W. Jones[77], T.J. Jones[73], O. Jonsson[29], K.K. Joo[158,*v*], C. Joram[29], P.M. Jorge[124a,*b*], J. Joseph[14], X. Ju[130], V. Juranek[125], P. Jussel[62], V.V. Kabachenko[128], S. Kabana[16], M. Kaci[167], A. Kaczmarska[38], P. Kadlecik[35], M. Kado[115], H. Kagan[109], M. Kagan[57], S. Kaiser[99], E. Kajomovitz[152], S. Kalinin[174], L.V. Kalinovskaya[65], S. Kama[39], N. Kanaya[155], M. Kaneda[155], T. Kanno[157], V.A. Kantserov[96], J. Kanzaki[66], B. Kaplan[175], A. Kapliy[30], J. Kaplon[29], D. Kar[43], M. Karagoz[118], M. Karnevskiy[41], K. Karr[5], V. Kartvelishvili[71], A.N. Karyukhin[128], L. Kashif[57], A. Kasmi[39], R.D. Kass[109], A. Kastanas[13], M. Kataoka[4], Y. Kataoka[155], E. Katsoufis[9], J. Katzy[41], V. Kaushik[6], K. Kawagoe[67], T. Kawamoto[155], G. Kawamura[81], M.S. Kayl[105], V.A. Kazanin[107], M.Y. Kazarinov[65], S.I. Kazi[86], J.R. Keates[82], R. Keeler[169], R. Kehoe[39], M. Keil[54], G.D. Kekelidze[65], M. Kelly[82], J. Kennedy[98], C.J. Kenney[143], M. Kenyon[53], O. Kepka[125], N. Kerschen[29], B.P. Kerševan[74], S. Kersten[174], K. Kessoku[155], C. Ketterer[48], M. Khakzad[28], F. Khalil-zada[10], H. Khandanyan[165], A. Khanov[112], D. Kharchenko[65], A. Khodinov[148], A.G. Kholodenko[128], A. Khomich[58a], T.J. Khoo[27], G. Khoriauli[20], N. Khovanskiy[65], V. Khovanskiy[95], E. Khramov[65], J. Khubua[51], G. Kilvington[76], H. Kim[7], M.S. Kim[2], P.C. Kim[143], S.H. Kim[160], N. Kimura[170], O. Kind[15], B.T. King[73], M. King[67], R.S.B. King[118], J. Kirk[129], G.P. Kirsch[118], L.E. Kirsch[22], A.E. Kiryunin[99], D. Kisielewska[37], T. Kittelmann[123], A.M. Kiver[128], H. Kiyamura[67], E. Kladiva[144b], J. Klaiber-Lodewigs[42], M. Klein[73], U. Klein[73], K. Kleinknecht[81], M. Klemetti[85], A. Klier[171], A. Klimentov[24], R. Klingenberg[42], E.B. Klinkby[35], T. Klioutchnikova[29], P.F. Klok[104], S. Klous[105], E.-E. Kluge[58a], T. Kluge[73], P. Kluit[105], S. Kluth[99], E. Kneringer[62], J. Knobloch[29], A. Knue[54], B.R. Ko[44], T. Kobayashi[155], M. Kobel[43], B. Koblitz[29], M. Kocian[143], A. Kocnar[113], P. Kodys[126], K. Köneke[29], A.C. König[104], S. Koenig[81], S. König[48], L. Köpke[81], F. Koetsveld[104], P. Koevesarki[20], T. Koffas[29], E. Koffeman[105], F. Kohn[54], Z. Kohout[127], T. Kohriki[66], T. Koi[143], T. Kokott[20], G.M. Kolachev[107], H. Kolanoski[15], V. Kolesnikov[65], I. Koletsou[89a,89b], J. Koll[88], D. Kollar[29], M. Kollefrath[48], S.D. Kolya[82], A.A. Komar[94], J.R. Komaragiri[142], T. Kondo[66], T. Kono[41,*w*], A.I. Kononov[48], R. Konoplich[108,*x*], N. Konstantinidis[77], A. Kootz[174], S. Koperny[37], S.V. Kopikov[128], K. Korcyl[38], K. Kordas[154], V. Koreshev[128], A. Korn[14], A. Korol[107], I. Korolkov[11], E.V. Korolkova[139], V.A. Korotkov[128], O. Kortner[99], S. Kortner[99], V.V. Kostyukhin[20], M.J. Kotamäki[29], S. Kotov[99], V.M. Kotov[65], C. Kourkoumelis[8], A. Koutsman[105], R. Kowalewski[169], T.Z. Kowalski[37], W. Kozanecki[136], A.S. Kozhin[128], V. Kral[127], V.A. Kramarenko[97], G. Kramberger[74], O. Krasel[42], M.W. Krasny[78], A. Krasznahorkay[108], J. Kraus[88], A. Kreisel[153], F. Krejci[127], J. Kretzschmar[73], N. Krieger[54], P. Krieger[158], K. Kroeninger[54], H. Kroha[99], J. Kroll[120], J. Kroseberg[20], J. Krstic[12a], U. Kruchonak[65], H. Krüger[20], Z.V. Krumshteyn[65], A. Kruth[20], T. Kubota[155], S. Kuehn[48], A. Kugel[58c], T. Kuhl[174], D. Kuhn[62], V. Kukhtin[65], Y. Kulchitsky[90], S. Kuleshov[31b], C. Kummer[98], M. Kuna[83], N. Kundu[118], J. Kunkle[120], A. Kupco[125], H. Kurashige[67], M. Kurata[160], Y.A. Kurochkin[90], V. Kus[125],

W. Kuykendall[138], M. Kuze[157], P. Kuzhir[91], O. Kvasnicka[125], R. Kwee[15], A. La Rosa[29], L. La Rotonda[36a,36b], L. Labarga[80], J. Labbe[4], C. Lacasta[167], F. Lacava[132a,132b], H. Lacker[15], D. Lacour[78], V.R. Lacuesta[167], E. Ladygin[65], R. Lafaye[4], B. Laforge[78], T. Lagouri[80], S. Lai[48], E. Laisne[55], M. Lamanna[29], C.L. Lampen[6], W. Lampl[6], E. Lancon[136], U. Landgraf[48], M.P.J. Landon[75], H. Landsman[152], J.L. Lane[82], C. Lange[41], A.J. Lankford[163], F. Lanni[24], K. Lantzsch[29], V.V. Lapin[128,*], S. Laplace[4], C. Lapoire[20], J.F. Laporte[136], T. Lari[89a], A.V. Larionov [128], A. Larner[118], C. Lasseur[29], M. Lassnig[29], W. Lau[118], P. Laurelli[47], A. Lavorato[118], W. Lavrijsen[14], P. Laycock[73], A.B. Lazarev[65], A. Lazzaro[89a,89b], O. Le Dortz[78], E. Le Guirriec[83], C. Le Maner[158], E. Le Menedeu[136], M. Leahu[29], A. Lebedev[64], C. Lebel[93], T. LeCompte[5], F. Ledroit-Guillon[55], H. Lee[105], J.S.H. Lee[150], S.C. Lee[151], L. Lee JR[175], M. Lefebvre[169], M. Legendre[136], A. Leger[49], B.C. LeGeyt[120], F. Legger[98], C. Leggett[14], M. Lehmacher[20], G. Lehmann Miotto[29], M. Lehto[139], X. Lei[6], M.A.L. Leite[23b], R. Leitner[126], D. Lellouch[171], J. Lellouch[78], M. Leltchouk[34], V. Lendermann[58a], K.J.C. Leney[145b], T. Lenz[174], G. Lenzen[174], B. Lenzi[136], K. Leonhardt[43], S. Leontsinis[9], C. Leroy[93], J-R. Lessard[169], J. Lesser[146a], C.G. Lester[27], A. Leung Fook Cheong[172], J. Levêque[83], D. Levin[87], L.J. Levinson[171], M.S. Levitski[128], M. Lewandowska[21], M. Leyton[15], B. Li[83], H. Li[172], S. Li[32b], X. Li[87], Z. Liang[39], Z. Liang[118,*y*], B. Liberti[133a], P. Lichard[29], M. Lichtnecker[98], K. Lie[165], W. Liebig[13], R. Lifshitz[152], J.N. Lilley[17], A. Limosani[86], M. Limper[63], S.C. Lin[151,*z*], F. Linde[105], J.T. Linnemann[88], E. Lipeles[120], L. Lipinsky[125], A. Lipniacka[13], T.M. Liss[165], A. Lister[49], A.M. Litke[137], C. Liu[28], D. Liu[151,*aa*], H. Liu[87], J.B. Liu[87], M. Liu[32b], S. Liu[2], Y. Liu[32b], M. Livan[119a,119b], S.S.A. Livermore[118], A. Lleres[55], S.L. Lloyd[75], E. Lobodzinska[41], P. Loch[6], W.S. Lockman[137], S. Lockwitz[175], T. Loddenkoetter[20], F.K. Loebinger[82], A. Loginov[175], C.W. Loh[168], T. Lohse[15], K. Lohwasser[48], M. Lokajicek[125], J. Loken [118], V.P. Lombardo[89a,89b], R.E. Long[71], L. Lopes[124a,*b*], D. Lopez Mateos[34,*ab*], M. Losada[162], P. Loscutoff[14], F. Lo Sterzo[132a,132b], M.J. Losty[159a], X. Lou[40], A. Lounis[115], K.F. Loureiro[162], J. Love[21], P.A. Love[71], A.J. Lowe[143], F. Lu[32a], J. Lu[2], L. Lu[39], H.J. Lubatti[138], C. Luci[132a,132b], A. Lucotte[55], A. Ludwig[43], D. Ludwig[41], I. Ludwig[48], J. Ludwig[48], F. Luehring[61], G. Luijckx[105], D. Lumb[48], L. Luminari[132a], E. Lund[117], B. Lund-Jensen[147], B. Lundberg[79], J. Lundberg[146a,146b], J. Lundquist[35], M. Lungwitz[81], A. Lupi[122a,122b], G. Lutz[99], D. Lynn[24], J. Lys[14], E. Lytken[79], H. Ma[24], L.L. Ma[172], M. Maaßen[48], J.A. Macana Goia[93], G. Maccarrone[47], A. Macchiolo[99], B. Maček[74], J. Machado Miguens[124a,*b*], D. Macina[49], R. Mackeprang[35], R.J. Madaras[14], W.F. Mader[43], R. Maenner[58c], T. Maeno[24], P. Mättig[174], S. Mättig[41], P.J. Magalhaes Martins[124a,*h*], L. Magnoni[29], E. Magradze[51], C.A. Magrath[104], Y. Mahalalel[153], K. Mahboubi[48], G. Mahout[17], C. Maiani[132a,132b], C. Maidantchik[23a], A. Maio[124a,*q*], S. Majewski[24], Y. Makida[66], N. Makovec[115], P. Mal[6], Pa. Malecki[38], P. Malecki[38], V.P. Maleev[121], F. Malek[55], U. Mallik[63], D. Malon[5], S. Maltezos[9], V. Malyshev[107], S. Malyukov[65], R. Mameghani[98], J. Mamuzic[12b], A. Manabe[66], L. Mandelli[89a], I. Mandić[74], R. Mandrysch[15], J. Maneira[124a], P.S. Mangeard[88], I.D. Manjavidze[65], A. Mann[54], P.M. Manning[137], A. Manousakis-Katsikakis[8], B. Mansoulie[136], A. Manz[99], A. Mapelli[29], L. Mapelli[29], L. March [80], J.F. Marchand[29], F. Marchese[133a,133b], M. Marchesotti[29], G. Marchiori[78], M. Marcisovsky[125], A. Marin[21,*], C.P. Marino[61], F. Marroquim[23a], R. Marshall[82], Z. Marshall[34,*ab*], F.K. Martens[158], S. Marti-Garcia[167], A.J. Martin[175], B. Martin[29], B. Martin[88], F.F. Martin[120], J.P. Martin[93], Ph. Martin[55], T.A. Martin[17], B. Martin dit Latour[49], M. Martinez[11], V. Martinez Outschoorn[57], A.C. Martyniuk[82], M. Marx[82], F. Marzano[132a], A. Marzin[111], L. Masetti[81], T. Mashimo[155], R. Mashinistov[94], J. Masik[82], A.L. Maslennikov[107], M. Maß[42], I. Massa[19a,19b], G. Massaro[105], N. Massol[4], A. Mastroberardino[36a,36b], T. Masubuchi[155], M. Mathes[20], P. Matricon[115], H. Matsumoto[155], H. Matsunaga[155], T. Matsushita[67], C. Mattravers[118,*ac*], J.M. Maugain[29], S.J. Maxfield[73], E.N. May[5], A. Mayne[139], R. Mazini[151], M. Mazur[20], M. Mazzanti[89a], E. Mazzoni[122a,122b], S.P. Mc Kee[87], A. McCarn[165], R.L. McCarthy[148], T.G. McCarthy[28], N.A. McCubbin[129], K.W. McFarlane[56], J.A. Mcfayden[139], H. McGlone[53], G. Mchedlidze[51], R.A. McLaren[29], T. Mclaughlan[17], S.J. McMahon[129], T.R. McMahon[76], T.J. McMahon[17], R.A. McPherson[169,*k*], A. Meade[84], J. Mechnich[105], M. Mechtel[174], M. Medinnis[41],

R. Meera-Lebbai[111], T. Meguro[116], R. Mehdiyev[93], S. Mehlhase[41], A. Mehta[73], K. Meier[58a], J. Meinhardt[48], B. Meirose[79], C. Melachrinos[30], B.R. Mellado Garcia[172], L. Mendoza Navas[162], Z. Meng[151,ad], A. Mengarelli[19a,19b], S. Menke[99], C. Menot[29], E. Meoni[11], D. Merkl[98], P. Mermod[118], L. Merola[102a,102b], C. Meroni[89a], F.S. Merritt[30], A. Messina[29], J. Metcalfe[103], A.S. Mete[64], S. Meuser[20], C. Meyer[81], J-P. Meyer[136], J. Meyer[173], J. Meyer[54], T.C. Meyer[29], W.T. Meyer[64], J. Miao[32d], S. Michal[29], L. Micu[25a], R.P. Middleton[129], P. Miele[29], S. Migas[73], L. Mijović[41], G. Mikenberg[171], M. Mikestikova[125], B. Mikulec[49], M. Mikuž[74], D.W. Miller[143], R.J. Miller[88], W.J. Mills[168], C. Mills[57], A. Milov[171], D.A. Milstead[146a,146b], D. Milstein[171], A.A. Minaenko[128], M. Miñano[167], I.A. Minashvili[65], A.I. Mincer[108], B. Mindur[37], M. Mineev[65], Y. Ming[130], L.M. Mir[11], G. Mirabelli[132a], L. Miralles Verge[11], A. Misiejuk[76], A. Mitra[118], J. Mitrevski[137], G.Y. Mitrofanov[128], V.A. Mitsou[167], S. Mitsui[66], P.S. Miyagawa[82], K. Miyazaki[67], J.U. Mjörnmark[79], T. Moa[146a,146b], P. Mockett[138], S. Moed[57], V. Moeller[27], K. Mönig[41], N. Möser[20], S. Mohapatra[148], B. Mohn[13], W. Mohr[48], S. Mohrdieck-Möck[99], A.M. Moisseev[128,*], R. Moles-Valls[167], J. Molina-Perez[29], L. Moneta[49], J. Monk[77], E. Monnier[83], S. Montesano[89a,89b], F. Monticelli[70], S. Monzani[19a,19b], R.W. Moore[2], G.F. Moorhead[86], C. Mora Herrera[49], A. Moraes[53], A. Morais[124a,b], N. Morange[136], J. Morel[54], G. Morello[36a,36b], D. Moreno[81], M. Moreno Llácer[167], P. Morettini[50a], M. Morii[57], J. Morin[75], Y. Morita[66], A.K. Morley[29], G. Mornacchi[29], M-C. Morone[49], J.D. Morris[75], H.G. Moser[99], M. Mosidze[51], J. Moss[109], R. Mount[143], E. Mountricha[9], S.V. Mouraviev[94], E.J.W. Moyse[84], M. Mudrinic[12b], F. Mueller[58a], J. Mueller[123], K. Mueller[20], T.A. Müller[98], D. Muenstermann[42], A. Muijs[105], A. Muir[168], Y. Munwes[153], K. Murakami[66], W.J. Murray[129], I. Mussche[105], E. Musto[102a,102b], A.G. Myagkov[128], M. Myska[125], J. Nadal[11], K. Nagai[160], K. Nagano[66], Y. Nagasaka[60], A.M. Nairz[29], Y. Nakahama[115], K. Nakamura[155], I. Nakano[110], G. Nanava[20], A. Napier[161], M. Nash[77,ae], I. Nasteva[82], N.R. Nation[21], T. Nattermann[20], T. Naumann[41], G. Navarro[162], H.A. Neal[87], E. Nebot[80], P. Nechaeva[94], A. Negri[119a,119b], G. Negri[29], S. Nektarijevic[49], A. Nelson[64], S. Nelson[143], T.K. Nelson[143], S. Nemecek[125], P. Nemethy[108], A.A. Nepomuceno[23a], M. Nessi[29], S.Y. Nesterov[121], M.S. Neubauer[165], A. Neusiedl[81], R.M. Neves[108], P. Nevski[24], P.R. Newman[17], R.B. Nickerson[118], R. Nicolaidou[136], L. Nicolas[139], B. Nicquevert[29], F. Niedercorn[115], J. Nielsen[137], T. Niinikoski[29], A. Nikiforov[15], V. Nikolaenko[128], K. Nikolaev[65], I. Nikolic-Audit[78], K. Nikolopoulos[24], H. Nilsen[48], P. Nilsson[7], Y. Ninomiya [155], A. Nisati[132a], T. Nishiyama[67], R. Nisius[99], L. Nodulman[5], M. Nomachi[116], I. Nomidis[154], H. Nomoto[155], M. Nordberg[29], B. Nordkvist[146a,146b], O. Norniella Francisco[11], P.R. Norton[129], J. Novakova[126], M. Nozaki[66], M. Nožička[41], I.M. Nugent[159a], A.-E. Nuncio-Quiroz[20], G. Nunes Hanninger[20], T. Nunnemann[98], E. Nurse[77], T. Nyman[29], B.J. O'Brien[45], S.W. O'Neale[17,*], D.C. O'Neil[142], V. O'Shea[53], F.G. Oakham[28,af], H. Oberlack[99], J. Ocariz[78], A. Ochi[67], S. Oda[155], S. Odaka[66], J. Odier[83], G.A. Odino[50a,50b], H. Ogren[61], A. Oh[82], S.H. Oh[44], C.C. Ohm[146a,146b], T. Ohshima[101], H. Ohshita[140], T.K. Ohska[66], T. Ohsugi[59], S. Okada[67], H. Okawa[163], Y. Okumura[101], T. Okuyama[155], M. Olcese[50a], A.G. Olchevski[65], M. Oliveira[124a,h], D. Oliveira Damazio[24], E. Oliver Garcia[167], D. Olivito[120], A. Olszewski[38], J. Olszowska[38], C. Omachi[67,ag], A. Onofre[124a,ah], P.U.E. Onyisi[30], C.J. Oram[159a], G. Ordonez[104], M.J. Oreglia[30], F. Orellana[49], Y. Oren[153], D. Orestano[134a,134b], I. Orlov[107], C. Oropeza Barrera[53], R.S. Orr[158], E.O. Ortega[130], B. Osculati[50a,50b], R. Ospanov[120], C. Osuna[11], G. Otero y Garzon[26], J.P Ottersbach[105], M. Ouchrif[135c], F. Ould-Saada[117], A. Ouraou[136], Q. Ouyang[32a], M. Owen[82], S. Owen[139], A. Oyarzun[31b], O.K. Øye[13], V.E. Ozcan[77], N. Ozturk[7], A. Pacheco Pages[11], C. Padilla Aranda[11], E. Paganis[139], F. Paige[24], K. Pajchel[117], S. Palestini[29], D. Pallin[33], A. Palma[124a,b], J.D. Palmer[17], Y.B. Pan[172], E. Panagiotopoulou[9], B. Panes[31a], N. Panikashvili[87], S. Panitkin[24], D. Pantea[25a], M. Panuskova[125], V. Paolone[123], A. Paoloni[133a,133b], A. Papadelis[146a], Th.D. Papadopoulou[9], A. Paramonov[5], S.J. Park[54], W. Park[24,ai], M.A. Parker[27], F. Parodi[50a,50b], J.A. Parsons[34], U. Parzefall[48], E. Pasqualucci[132a], A. Passeri[134a], F. Pastore[134a,134b], Fr. Pastore[29], G. Pásztor [49,aj], S. Pataraia[172], N. Patel[150], J.R. Pater[82], S. Patricelli[102a,102b], T. Pauly[29], M. Pecsy[144a],

M.I. Pedraza Morales[172], S.V. Peleganchuk[107], H. Peng[172], R. Pengo[29], A. Penson[34], J. Penwell[61], M. Perantoni[23a], K. Perez[34,ab], T. Perez Cavalcanti[41], E. Perez Codina[11], M.T. Pérez García-Estañ[167], V. Perez Reale[34], I. Peric[20], L. Perini[89a,89b], H. Pernegger[29], R. Perrino[72a], P. Perrodo[4], S. Persembe[3a], P. Perus[115], V.D. Peshekhonov[65], O. Peters[105], B.A. Petersen[29], J. Petersen[29], T.C. Petersen[35], E. Petit[83], A. Petridis[154], C. Petridou[154], E. Petrolo[132a], F. Petrucci[134a,134b], D. Petschull[41], M. Petteni[142], R. Pezoa[31b], A. Phan[86], A.W. Phillips[27], P.W. Phillips[129], G. Piacquadio[29], E. Piccaro[75], M. Piccinini[19a,19b], A. Pickford[53], R. Piegaia[26], J.E. Pilcher[30], A.D. Pilkington[82], J. Pina[124a,q], M. Pinamonti[164a,164c], J.L. Pinfold[2], J. Ping[32c], B. Pinto[124a,b], O. Pirotte[29], C. Pizio[89a,89b], R. Placakyte[41], M. Plamondon[169], W.G. Plano[82], M.-A. Pleier[24], A.V. Pleskach[128], A. Poblaguev[24], S. Poddar[58a], F. Podlyski[33], L. Poggioli[115], T. Poghosyan[20], M. Pohl[49], F. Polci[55], G. Polesello[119a], A. Policicchio[138], A. Polini[19a], J. Poll[75], V. Polychronakos[24], D.M. Pomarede[136], D. Pomeroy[22], K. Pommès[29], L. Pontecorvo[132a], B.G. Pope[88], G.A. Popeneciu[25a], D.S. Popovic[12a], A. Poppleton[29], X. Portell Bueso[48], R. Porter[163], C. Posch[21], G.E. Pospelov[99], S. Pospisil[127], I.N. Potrap[99], C.J. Potter[149], C.T. Potter[85], G. Poulard[29], J. Poveda[172], R. Prabhu[77], P. Pralavorio[83], S. Prasad[57], R. Pravahan[7], S. Prell[64], K. Pretzl[16], L. Pribyl[29], D. Price[61], L.E. Price[5], M.J. Price[29], P.M. Prichard[73], D. Prieur[123], M. Primavera[72a], K. Prokofiev[29], F. Prokoshin[31b], S. Protopopescu[24], J. Proudfoot[5], X. Prudent[43], H. Przysiezniak[4], S. Psoroulas[20], E. Ptacek[114], J. Purdham[87], M. Purohit[24,ak], P. Puzo[115], Y. Pylypchenko[117], J. Qian[87], Z. Qian[83], Z. Qin[41], A. Quadt[54], D.R. Quarrie[14], W.B. Quayle[172], F. Quinonez[31a], M. Raas[104], V. Radescu[58b], B. Radics[20], T. Rador[18a], F. Ragusa[89a,89b], G. Rahal[177], A.M. Rahimi[109], S. Rajagopalan[24], S. Rajek[42], M. Rammensee[48], M. Rammes[141], M. Ramstedt[146a,146b], K. Randrianarivony[28], P.N. Ratoff[71], F. Rauscher[98], E. Rauter[99], M. Raymond[29], A.L. Read[117], D.M. Rebuzzi[119a,119b], A. Redelbach[173], G. Redlinger[24], R. Reece[120], K. Reeves[40], A. Reichold[105], E. Reinherz-Aronis[153], A. Reinsch[114], I. Reisinger[42], D. Reljic[12a], C. Rembser[29], Z.L. Ren[151], A. Renaud[115], P. Renkel[39], B. Rensch[35], M. Rescigno[132a], S. Resconi[89a], B. Resende[136], P. Reznicek[98], R. Rezvani[158], A. Richards[77], R. Richter[99], E. Richter-Was[38,al], M. Ridel[78], S. Rieke[81], M. Rijpstra[105], M. Rijssenbeek[148], A. Rimoldi[119a,119b], L. Rinaldi[19a], R.R. Rios[39], I. Riu[11], G. Rivoltella[89a,89b], F. Rizatdinova[112], E. Rizvi[75], S.H. Robertson[85,k], A. Robichaud-Veronneau[49], D. Robinson[27], J.E.M. Robinson[77], M. Robinson[114], A. Robson[53], J.G. Rocha de Lima[106], C. Roda[122a,122b], D. Roda Dos Santos[29], S. Rodier[80], D. Rodriguez[162], Y. Rodriguez Garcia[15], A. Roe[54], S. Roe[29], O. Røhne[117], V. Rojo[1], S. Rolli[161], A. Romaniouk[96], V.M. Romanov[65], G. Romeo[26], D. Romero Maltrana[31a], L. Roos[78], E. Ros[167], S. Rosati[138], M. Rose[76], G.A. Rosenbaum[158], E.I. Rosenberg[64], P.L. Rosendahl[13], L. Rosselet[49], V. Rossetti[11], E. Rossi[102a,102b], L.P. Rossi[50a], L. Rossi[89a,89b], M. Rotaru[25a], I. Roth[171], J. Rothberg[138], I. Rottländer[20], D. Rousseau[115], C.R. Royon[136], A. Rozanov[83], Y. Rozen[152], X. Ruan[115], I. Rubinskiy[41], B. Ruckert[98], N. Ruckstuhl[105], V.I. Rud[97], G. Rudolph[62], F. Rühr[6], A. Ruiz-Martinez[64], E. Rulikowska-Zarebska[37], V. Rumiantsev[91,*], L. Rumyantsev[65], K. Runge[48], O. Runolfsson[20], Z. Rurikova[48], N.A. Rusakovich[65], D.R. Rust[61], J.P. Rutherfoord[6], C. Ruwiedel[14], P. Ruzicka[125], Y.F. Ryabov[121], V. Ryadovikov[128], P. Ryan[88], M. Rybar[126], G. Rybkin[115], N.C. Ryder[118], S. Rzaeva[10], A.F. Saavedra[150], I. Sadeh[153], H.F-W. Sadrozinski[137], R. Sadykov[65], F. Safai Tehrani[132a,132b], H. Sakamoto[155], G. Salamanna[105], A. Salamon[133a], M. Saleem[111], D. Salihagic[99], A. Salnikov[143], J. Salt[167], B.M. Salvachua Ferrando[5], D. Salvatore[36a,36b], F. Salvatore[149], A. Salzburger[29], D. Sampsonidis[154], B.H. Samset[117], H. Sandaker[13], H.G. Sander[81], M.P. Sanders[98], M. Sandhoff[174], P. Sandhu[158], T. Sandoval[27], R. Sandstroem[105], S. Sandvoss[174], D.P.C. Sankey[129], A. Sansoni[47], C. Santamarina Rios[85], C. Santoni[33], R. Santonico[133a,133b], H. Santos[124a], J.G. Saraiva[124a,q], T. Sarangi[172], E. Sarkisyan-Grinbaum[7], F. Sarri[122a,122b], G. Sartisohn[174], O. Sasaki[66], T. Sasaki[66], N. Sasao[68], I. Satsounkevitch[90], G. Sauvage[4], J.B. Sauvan[115], P. Savard[158,af], V. Savinov[123], P. Savva [9], L. Sawyer[24,am], D.H. Saxon[53], L.P. Says[33], C. Sbarra[19a,19b], A. Sbrizzi[19a,19b], O. Scallon[93], D.A. Scannicchio[163], J. Schaarschmidt[43], P. Schacht[99], U. Schäfer[81], S. Schaetzel[58b], A.C. Schaffer[115], D. Schaile[98], R.D. Schamberger[148], A.G. Schamov[107],

V. Scharf[58a], V.A. Schegelsky[121], D. Scheirich[87], M.I. Scherzer[14], C. Schiavi[50a,50b], J. Schieck[98], M. Schioppa[36a,36b], S. Schlenker[29], J.L. Schlereth[5], E. Schmidt[48], M.P. Schmidt[175,*], K. Schmieden[20], C. Schmitt[81], M. Schmitz[20], A. Schöning[58b], M. Schott[29], D. Schouten[142], J. Schovancova[125], M. Schram[85], A. Schreiner[63], C. Schroeder[81], N. Schroer[58c], S. Schuh[29], G. Schuler[29], J. Schultes[174], H.-C. Schultz-Coulon[58a], H. Schulz[15], J.W. Schumacher[20], M. Schumacher[48], B.A. Schumm[137], Ph. Schune[136], C. Schwanenberger[82], A. Schwartzman[143], Ph. Schwemling[78], R. Schwienhorst[88], R. Schwierz[43], J. Schwindling[136], W.G. Scott[129], J. Searcy[114], E. Sedykh[121], E. Segura[11], S.C. Seidel[103], A. Seiden[137], F. Seifert[43], J.M. Seixas[23a], G. Sekhniaidze[102a], D.M. Seliverstov[121], B. Sellden[146a], G. Sellers[73], M. Seman[144b], N. Semprini-Cesari[19a,19b], C. Serfon[98], L. Serin[115], R. Seuster[99], H. Severini[111], M.E. Sevior[86], A. Sfyrla[29], E. Shabalina[54], M. Shamim[114], L.Y. Shan[32a], J.T. Shank[21], Q.T. Shao[86], M. Shapiro[14], P.B. Shatalov[95], L. Shaver[6], C. Shaw[53], K. Shaw[164a,164c], D. Sherman[175], P. Sherwood[77], A. Shibata[108], S. Shimizu[29], M. Shimojima[100], T. Shin[56], A. Shmeleva[94], M.J. Shochet[30], D. Short[118], M.A. Shupe[6], P. Sicho[125], A. Sidoti[15], A. Siebel[174], F. Siegert[48], J. Siegrist[14], Dj. Sijacki[12a], O. Silbert[171], Y. Silver[153], D. Silverstein[143], S.B. Silverstein[146a], V. Simak[127], Lj. Simic[12a], S. Simion[115], B. Simmons[77], M. Simonyan[35], P. Sinervo[158], N.B. Sinev[114], V. Sipica[141], G. Siragusa[81], A.N. Sisakyan[65], S.Yu. Sivoklokov[97], J. Sjölin[146a,146b], T.B. Sjursen[13], L.A. Skinnari[14], K. Skovpen[107], P. Skubic[111], N. Skvorodnev[22], M. Slater[17], T. Slavicek[127], K. Sliwa[161], T.J. Sloan[71], J. Sloper[29], V. Smakhtin[171], S.Yu. Smirnov[96], L.N. Smirnova[97], O. Smirnova[79], B.C. Smith[57], D. Smith[143], K.M. Smith[53], M. Smizanska[71], K. Smolek[127], A.A. Snesarev[94], S.W. Snow[82], J. Snow[111], J. Snuverink[105], S. Snyder[24], M. Soares[124a], R. Sobie[169,*k*], J. Sodomka[127], A. Soffer[153], C.A. Solans[167], M. Solar[127], J. Solc[127], U. Soldevila[167], E. Solfaroli Camillocci[132a,132b], A.A. Solodkov[128], O.V. Solovyanov[128], J. Sondericker[24], N. Soni[2], V. Sopko[127], B. Sopko[127], M. Sorbi[89a,89b], M. Sosebee[7], A. Soukharev[107], S. Spagnolo[72a,72b], F. Spanò[34], R. Spighi[19a], G. Spigo[29], F. Spila[132a,132b], E. Spiriti[134a], R. Spiwoks[29], M. Spousta[126], T. Spreitzer[158], B. Spurlock[7], R.D. St. Denis[53], T. Stahl[141], J. Stahlman[120], R. Stamen[58a], E. Stanecka[29], R.W. Stanek[5], C. Stanescu[134a], S. Stapnes[117], E.A. Starchenko[128], J. Stark[55], P. Staroba[125], P. Starovoitov[91], A. Staude[98], P. Stavina[144a], G. Stavropoulos[14], G. Steele[53], P. Steinbach[43], P. Steinberg[24], I. Stekl[127], B. Stelzer[142], H.J. Stelzer[41], O. Stelzer-Chilton[159a], H. Stenzel[52], K. Stevenson[75], G.A. Stewart[53], T. Stockmanns[20], M.C. Stockton[29], K. Stoerig[48], G. Stoicea[25a], S. Stonjek[99], P. Strachota[126], A.R. Stradling[7], A. Straessner[43], J. Strandberg[87], S. Strandberg[146a,146b], A. Strandlie[117], M. Strang[109], E. Strauss[143], M. Strauss[111], P. Strizenec[144b], R. Ströhmer[173], D.M. Strom[114], J.A. Strong[76,*], R. Stroynowski[39], J. Strube[129], B. Stugu[13], I. Stumer[24,*], J. Stupak[148], P. Sturm[174], D.A. Soh[151,*y*], D. Su[143], S. Subramania[2], Y. Sugaya[116], T. Sugimoto[101], C. Suhr[106], K. Suita[67], M. Suk[126], V.V. Sulin[94], S. Sultansoy[3d], T. Sumida[29], X. Sun[55], J.E. Sundermann[48], K. Suruliz[164a,164b], S. Sushkov[11], G. Susinno[36a,36b], M.R. Sutton[139], Y. Suzuki[66], Yu.M. Sviridov[128], S. Swedish[168], I. Sykora[144a], T. Sykora[126], B. Szeless[29], J. Sánchez[167], D. Ta[105], K. Tackmann[29], A. Taffard[163], R. Tafirout[159a], A. Taga[117], N. Taiblum[153], Y. Takahashi[101], H. Takai[24], R. Takashima[69], H. Takeda[67], T. Takeshita[140], M. Talby[83], A. Talyshev[107], M.C. Tamsett[24], J. Tanaka[155], R. Tanaka[115], S. Tanaka[131], S. Tanaka[66], Y. Tanaka[100], K. Tani[67], N. Tannoury[83], G.P. Tappern[29], S. Tapprogge[81], D. Tardif[158], S. Tarem[152], F. Tarrade[24], G.F. Tartarelli[89a], P. Tas[126], M. Tasevsky[125], E. Tassi[36a,36b], M. Tatarkhanov[14], C. Taylor[77], F.E. Taylor[92], G. Taylor[137], G.N. Taylor[86], W. Taylor[159b], M. Teixeira Dias Castanheira[75], P. Teixeira-Dias[76], K.K. Temming[48], H. Ten Kate[29], P.K. Teng[151], Y.D. Tennenbaum-Katan[152], S. Terada[66], K. Terashi[155], J. Terron[80], M. Terwort[41,*an*], M. Testa[47], R.J. Teuscher[158,*k*], C.M. Tevlin[82], J. Thadome[174], J. Therhaag[20], T. Theveneaux-Pelzer[78], M. Thioye[175], S. Thoma[48], J.P. Thomas[17], E.N. Thompson[84], P.D. Thompson[17], P.D. Thompson[158], A.S. Thompson[53], E. Thomson[120], M. Thomson[27], R.P. Thun[87], T. Tic[125], V.O. Tikhomirov[94], Y.A. Tikhonov[107], C.J.W.P. Timmermans[104], P. Tipton[175], F.J. Tique Aires Viegas[29], S. Tisserant[83], J. Tobias[48], B. Toczek[37], T. Todorov[4], S. Todorova-Nova[161], B. Toggerson[163], J. Tojo[66], S. Tokár[144a], K. Tokunaga[67], K. Tokushuku[66],

K. Tollefson[88], M. Tomoto[101], L. Tompkins[14], K. Toms[103], A. Tonazzo[134a,134b], G. Tong[32a], A. Tonoyan[13], C. Topfel[16], N.D. Topilin[65], I. Torchiani[29], E. Torrence[114], E. Torró Pastor[167], J. Toth[83,aj], F. Touchard[83], D.R. Tovey[139], D. Traynor[75], T. Trefzger[173], J. Treis[20], L. Tremblet[29], A. Tricoli[29], I.M. Trigger[159a], S. Trincaz-Duvoid[78], T.N. Trinh[78], M.F. Tripiana[70], N. Triplett[64], W. Trischuk[158], A. Trivedi[24,ao], B. Trocmé[55], C. Troncon[89a], M. Trottier-McDonald[142], A. Trzupek[38], C. Tsarouchas[29], J.C-L. Tseng[118], M. Tsiakiris[105], P.V. Tsiareshka[90], D. Tsionou[139], G. Tsipolitis[9], V. Tsiskaridze[48], E.G. Tskhadadze[51], I.I. Tsukerman[95], V. Tsulaia[123], J.-W. Tsung[20], S. Tsuno[66], D. Tsybychev[148], A. Tua[139], J.M. Tuggle[30], M. Turala[38], D. Turecek[127], I. Turk Cakir[3e], E. Turlay[105], P.M. Tuts[34], A. Tykhonov[74], M. Tylmad[146a,146b], M. Tyndel[129], D. Typaldos[17], H. Tyrvainen[29], G. Tzanakos[8], K. Uchida[20], I. Ueda[155], R. Ueno[28], M. Ugland[13], M. Uhlenbrock[20], M. Uhrmacher[54], F. Ukegawa[160], G. Unal[29], D.G. Underwood[5], A. Undrus[24], G. Unel[163], Y. Unno[66], D. Urbaniec[34], E. Urkovsky[153], P. Urquijo[49,ap], P. Urrejola[31a], G. Usai[7], M. Uslenghi[119a,119b], L. Vacavant[83], V. Vacek[127], B. Vachon[85], S. Vahsen[14], C. Valderanis[99], J. Valenta[125], P. Valente[132a], S. Valentinetti[19a,19b], S. Valkar[126], E. Valladolid Gallego[167], S. Vallecorsa[152], J.A. Valls Ferrer[167], H. van der Graaf[105], E. van der Kraaij[105], E. van der Poel[105], D. van der Ster[29], B. Van Eijk[105], N. van Eldik[84], P. van Gemmeren[5], Z. van Kesteren[105], I. van Vulpen[105], W. Vandelli[29], G. Vandoni[29], A. Vaniachine[5], P. Vankov[41], F. Vannucci[78], F. Varela Rodriguez[29], R. Vari[132a], E.W. Varnes[6], D. Varouchas[14], A. Vartapetian[7], K.E. Varvell[150], V.I. Vassilakopoulos[56], F. Vazeille[33], G. Vegni[89a,89b], J.J. Veillet[115], C. Vellidis[8], F. Veloso[124a], R. Veness[29], S. Veneziano[132a], A. Ventura[72a,72b], D. Ventura[138], S. Ventura [47], M. Venturi[48], N. Venturi[16], V. Vercesi[119a], M. Verducci[138], W. Verkerke[105], J.C. Vermeulen[105], A. Vest[43], M.C. Vetterli[142,af], I. Vichou[165], T. Vickey[145b,aq], G.H.A. Viehhauser[118], S. Viel[168], M. Villa[19a,19b], M. Villaplana Perez[167], E. Vilucchi[47], M.G. Vincter[28], E. Vinek[29], V.B. Vinogradov[65], M. Virchaux[136,*], S. Viret[33], J. Virzi[14], A. Vitale [19a,19b], O. Vitells[171], I. Vivarelli[48], F. Vives Vaque[11], S. Vlachos[9], M. Vlasak[127], N. Vlasov[20], A. Vogel[20], P. Vokac[127], M. Volpi[11], G. Volpini[89a], H. von der Schmitt[99], J. von Loeben[99], H. von Radziewski[48], E. von Toerne[20], V. Vorobel[126], A.P. Vorobiev[128], V. Vorwerk[11], M. Vos[167], R. Voss[29], T.T. Voss[174], J.H. Vossebeld[73], A.S. Vovenko[128], N. Vranjes[12a], M. Vranjes Milosavljevic[12a], V. Vrba[125], M. Vreeswijk[105], T. Vu Anh[81], R. Vuillermet[29], I. Vukotic[115], W. Wagner[174], P. Wagner[120], H. Wahlen[174], J. Wakabayashi[101], J. Walbersloh[42], S. Walch[87], J. Walder[71], R. Walker[98], W. Walkowiak[141], R. Wall[175], P. Waller[73], C. Wang[44], H. Wang[172], J. Wang[151], J. Wang[32d], J.C. Wang[138], R. Wang[103], S.M. Wang[151], A. Warburton[85], C.P. Ward[27], M. Warsinsky[48], P.M. Watkins[17], A.T. Watson[17], M.F. Watson[17], G. Watts[138], S. Watts[82], A.T. Waugh[150], B.M. Waugh[77], J. Weber[42], M. Weber[129], M.S. Weber[16], P. Weber[54], A.R. Weidberg[118], J. Weingarten[54], C. Weiser[48], H. Wellenstein[22], P.S. Wells[29], M. Wen[47], T. Wenaus[24], S. Wendler[123], Z. Weng[151,ar], T. Wengler[29], S. Wenig[29], N. Wermes[20], M. Werner[48], P. Werner[29], M. Werth[163], M. Wessels[58a], K. Whalen[28], S.J. Wheeler-Ellis[163], S.P. Whitaker[21], A. White[7], M.J. White[86], S. White[24], S.R. Whitehead[118], D. Whiteson[163], D. Whittington[61], F. Wicek[115], D. Wicke[174], F.J. Wickens[129], W. Wiedenmann[172], M. Wielers[129], P. Wienemann[20], C. Wiglesworth[73], L.A.M. Wiik[48], A. Wildauer[167], M.A. Wildt[41,an], I. Wilhelm[126], H.G. Wilkens[29], J.Z. Will[98], E. Williams[34], H.H. Williams[120], W. Willis[34], S. Willocq[84], J.A. Wilson[17], M.G. Wilson[143], A. Wilson[87], I. Wingerter-Seez[4], S. Winkelmann[48], F. Winklmeier[29], M. Wittgen[143], M.W. Wolter[38], H. Wolters[124a,h], G. Wooden[118], B.K. Wosiek[38], J. Wotschack[29], M.J. Woudstra[84], K. Wraight[53], C. Wright[53], B. Wrona[73], S.L. Wu[172], X. Wu[49], Y. Wu[32b,as], E. Wulf[34], R. Wunstorf[42], B.M. Wynne[45], L. Xaplanteris[9], S. Xella[35], S. Xie[48], Y. Xie[32a], C. Xu[32b], D. Xu[139], G. Xu[32a], B. Yabsley[150], M. Yamada[66], A. Yamamoto[66], K. Yamamoto[64], S. Yamamoto[155], T. Yamamura[155], J. Yamaoka[44], T. Yamazaki[155], Y. Yamazaki[67], Z. Yan[21], H. Yang[87], U.K. Yang[82], Y. Yang[61], Y. Yang[32a], Z. Yang[146a,146b], S. Yanush[91], W-M. Yao[14], Y. Yao[14], Y. Yasu[66], J. Ye[39], S. Ye[24], M. Yilmaz[3c], R. Yoosoofmiya[123], K. Yorita[170], R. Yoshida[5], C. Young[143], S. Youssef[21], D. Yu[24], J. Yu[7], J. Yu[32c,at], L. Yuan[32a,au], A. Yurkewicz[148], V.G. Zaets [128], R. Zaidan[63], A.M. Zaitsev[128], Z. Zajacova[29],

Yo.K. Zalite [121], L. Zanello[132a,132b], P. Zarzhitsky[39], A. Zaytsev[107], M. Zdrazil[14], C. Zeitnitz[174], M. Zeller[175], P.F. Zema[29], A. Zemla[38], C. Zendler[20], A.V. Zenin[128], O. Zenin[128], T. Ženiš[144a], Z. Zenonos[122a,122b], S. Zenz[14], D. Zerwas[115], G. Zevi della Porta[57], Z. Zhan[32d], D. Zhang[32b,av], H. Zhang[88], J. Zhang[5], X. Zhang[32d], Z. Zhang[115], L. Zhao[108], T. Zhao[138], Z. Zhao[32b], A. Zhemchugov[65], S. Zheng[32a], J. Zhong[151,aw], B. Zhou[87], N. Zhou[163], Y. Zhou[151], C.G. Zhu[32d], H. Zhu[41], Y. Zhu[172], X. Zhuang[98], V. Zhuravlov[99], D. Zieminska[61], B. Zilka[144a], R. Zimmermann[20], S. Zimmermann[20], S. Zimmermann[48], M. Ziolkowski[141], R. Zitoun[4], L. Živković[34], V.V. Zmouchko[128,*], G. Zobernig[172], A. Zoccoli[19a,19b], Y. Zolnierowski[4], A. Zsenei[29], M. zur Nedden[15], V. Zutshi[106], L. Zwalinski[29].

[1] University at Albany, 1400 Washington Ave, Albany, NY 12222, United States of America
[2] University of Alberta, Department of Physics, Centre for Particle Physics, Edmonton, AB T6G 2G7, Canada
[3] Ankara University[(a)], Faculty of Sciences, Department of Physics, TR 061000 Tandogan, Ankara; Dumlupinar University[(b)], Faculty of Arts and Sciences, Department of Physics, Kutahya; Gazi University[(c)], Faculty of Arts and Sciences, Department of Physics, 06500, Teknikokullar, Ankara; TOBB University of Economics and Technology[(d)], Faculty of Arts and Sciences, Division of Physics, 06560, Sogutozu, Ankara; Turkish Atomic Energy Authority[(e)], 06530, Lodumlu, Ankara, Turkey
[4] LAPP, Université de Savoie, CNRS/IN2P3, Annecy-le-Vieux, France
[5] Argonne National Laboratory, High Energy Physics Division, 9700 S. Cass Avenue, Argonne IL 60439, United States of America
[6] University of Arizona, Department of Physics, Tucson, AZ 85721, United States of America
[7] The University of Texas at Arlington, Department of Physics, Box 19059, Arlington, TX 76019, United States of America
[8] University of Athens, Nuclear & Particle Physics, Department of Physics, Panepistimiopouli, Zografou, GR 15771 Athens, Greece
[9] National Technical University of Athens, Physics Department, 9-Iroon Polytechniou, GR 15780 Zografou, Greece
[10] Institute of Physics, Azerbaijan Academy of Sciences, H. Javid Avenue 33, AZ 143 Baku, Azerbaijan
[11] Institut de Física d'Altes Energies, IFAE, Edifici Cn, Universitat Autònoma de Barcelona, ES - 08193 Bellaterra (Barcelona), Spain
[12] University of Belgrade[(a)], Institute of Physics, P.O. Box 57, 11001 Belgrade; Vinca Institute of Nuclear Sciences[(b)]M. Petrovica Alasa 12-14, 11000 Belgrade, Serbia, Serbia
[13] University of Bergen, Department for Physics and Technology, Allegaten 55, NO - 5007 Bergen, Norway
[14] Lawrence Berkeley National Laboratory and University of California, Physics Division, MS50B-6227, 1 Cyclotron Road, Berkeley, CA 94720, United States of America
[15] Humboldt University, Institute of Physics, Berlin, Newtonstr. 15, D-12489 Berlin, Germany
[16] University of Bern, Albert Einstein Center for Fundamental Physics, Laboratory for High Energy Physics, Sidlerstrasse 5, CH - 3012 Bern, Switzerland
[17] University of Birmingham, School of Physics and Astronomy, Edgbaston, Birmingham B15 2TT, United Kingdom
[18] Bogazici University[(a)], Faculty of Sciences, Department of Physics, TR - 80815 Bebek-Istanbul; Dogus University[(b)], Faculty of Arts and Sciences, Department of Physics, 34722, Kadikoy, Istanbul; [(c)]Gaziantep University, Faculty of Engineering, Department of Physics Engineering, 27310, Sehitkamil, Gaziantep, Turkey; Istanbul Technical University[(d)], Faculty of Arts and Sciences, Department of Physics, 34469, Maslak, Istanbul, Turkey
[19] INFN Sezione di Bologna[(a)]; Università di Bologna, Dipartimento di Fisica[(b)], viale C. Berti Pichat, 6/2, IT - 40127 Bologna, Italy

[20] University of Bonn, Physikalisches Institut, Nussallee 12, D - 53115 Bonn, Germany
[21] Boston University, Department of Physics, 590 Commonwealth Avenue, Boston, MA 02215, United States of America
[22] Brandeis University, Department of Physics, MS057, 415 South Street, Waltham, MA 02454, United States of America
[23] Universidade Federal do Rio De Janeiro, COPPE/EE/IF [(a)], Caixa Postal 68528, Ilha do Fundao, BR - 21945-970 Rio de Janeiro; [(b)]Universidade de Sao Paulo, Instituto de Fisica, R.do Matao Trav. R.187, Sao Paulo - SP, 05508 - 900, Brazil
[24] Brookhaven National Laboratory, Physics Department, Bldg. 510A, Upton, NY 11973, United States of America
[25] National Institute of Physics and Nuclear Engineering[(a)]Bucharest-Magurele, Str. Atomistilor 407, P.O. Box MG-6, R-077125, Romania; University Politehnica Bucharest[(b)], Rectorat - AN 001, 313 Splaiul Independentei, sector 6, 060042 Bucuresti; West University[(c)] in Timisoara, Bd. Vasile Parvan 4, Timisoara, Romania
[26] Universidad de Buenos Aires, FCEyN, Dto. Fisica, Pab I - C. Universitaria, 1428 Buenos Aires, Argentina
[27] University of Cambridge, Cavendish Laboratory, J J Thomson Avenue, Cambridge CB3 0HE, United Kingdom
[28] Carleton University, Department of Physics, 1125 Colonel By Drive, Ottawa ON K1S 5B6, Canada
[29] CERN, CH - 1211 Geneva 23, Switzerland
[30] University of Chicago, Enrico Fermi Institute, 5640 S. Ellis Avenue, Chicago, IL 60637, United States of America
[31] Pontificia Universidad Católica de Chile, Facultad de Fisica, Departamento de Fisica[(a)], Avda. Vicuna Mackenna 4860, San Joaquin, Santiago; Universidad Técnica Federico Santa María, Departamento de Física[(b)], Avda. Espãna 1680, Casilla 110-V, Valparaíso, Chile
[32] Institute of High Energy Physics, Chinese Academy of Sciences[(a)], P.O. Box 918, 19 Yuquan Road, Shijing Shan District, CN - Beijing 100049; University of Science & Technology of China (USTC), Department of Modern Physics[(b)], Hefei, CN - Anhui 230026; Nanjing University, Department of Physics[(c)], Nanjing, CN - Jiangsu 210093; Shandong University, High Energy Physics Group[(d)], Jinan, CN - Shandong 250100, China
[33] Laboratoire de Physique Corpusculaire, Clermont Université, Université Blaise Pascal, CNRS/IN2P3, FR - 63177 Aubiere Cedex, France
[34] Columbia University, Nevis Laboratory, 136 So. Broadway, Irvington, NY 10533, United States of America
[35] University of Copenhagen, Niels Bohr Institute, Blegdamsvej 17, DK - 2100 Kobenhavn 0, Denmark
[36] INFN Gruppo Collegato di Cosenza[(a)]; Università della Calabria, Dipartimento di Fisica[(b)], IT-87036 Arcavacata di Rende, Italy
[37] Faculty of Physics and Applied Computer Science of the AGH-University of Science and Technology, (FPACS, AGH-UST), al. Mickiewicza 30, PL-30059 Cracow, Poland
[38] The Henryk Niewodniczanski Institute of Nuclear Physics, Polish Academy of Sciences, ul. Radzikowskiego 152, PL - 31342 Krakow, Poland
[39] Southern Methodist University, Physics Department, 106 Fondren Science Building, Dallas, TX 75275-0175, United States of America
[40] University of Texas at Dallas, 800 West Campbell Road, Richardson, TX 75080-3021, United States of America
[41] DESY, Notkestr. 85, D-22603 Hamburg and Platanenallee 6, D-15738 Zeuthen, Germany
[42] TU Dortmund, Experimentelle Physik IV, DE - 44221 Dortmund, Germany
[43] Technical University Dresden, Institut für Kern- und Teilchenphysik, Zellescher Weg 19, D-01069

Dresden, Germany
[44] Duke University, Department of Physics, Durham, NC 27708, United States of America
[45] University of Edinburgh, School of Physics & Astronomy, James Clerk Maxwell Building, The Kings Buildings, Mayfield Road, Edinburgh EH9 3JZ, United Kingdom
[46] Fachhochschule Wiener Neustadt; Johannes Gutenbergstrasse 3 AT - 2700 Wiener Neustadt, Austria
[47] INFN Laboratori Nazionali di Frascati, via Enrico Fermi 40, IT-00044 Frascati, Italy
[48] Albert-Ludwigs-Universität, Fakultät für Mathematik und Physik, Hermann-Herder Str. 3, D - 79104 Freiburg i.Br., Germany
[49] Université de Genève, Section de Physique, 24 rue Ernest Ansermet, CH - 1211 Geneve 4, Switzerland
[50] INFN Sezione di Genova[(a)]; Università di Genova, Dipartimento di Fisica[(b)], via Dodecaneso 33, IT - 16146 Genova, Italy
[51] Institute of Physics of the Georgian Academy of Sciences, 6 Tamarashvili St., GE - 380077 Tbilisi; Tbilisi State University, HEP Institute, University St. 9, GE - 380086 Tbilisi, Georgia
[52] Justus-Liebig-Universität Giessen, II Physikalisches Institut, Heinrich-Buff Ring 16, D-35392 Giessen, Germany
[53] University of Glasgow, Department of Physics and Astronomy, Glasgow G12 8QQ, United Kingdom
[54] Georg-August-Universität, II. Physikalisches Institut, Friedrich-Hund Platz 1, D-37077 Göttingen, Germany
[55] LPSC, CNRS/IN2P3 and Univ. Joseph Fourier Grenoble, 53 avenue des Martyrs, FR-38026 Grenoble Cedex, France
[56] Hampton University, Department of Physics, Hampton, VA 23668, United States of America
[57] Harvard University, Laboratory for Particle Physics and Cosmology, 18 Hammond Street, Cambridge, MA 02138, United States of America
[58] Ruprecht-Karls-Universität Heidelberg: Kirchhoff-Institut für Physik[(a)], Im Neuenheimer Feld 227, D-69120 Heidelberg; Physikalisches Institut[(b)], Philosophenweg 12, D-69120 Heidelberg; ZITI Ruprecht-Karls-University Heidelberg[(c)], Lehrstuhl für Informatik V, B6, 23-29, DE - 68131 Mannheim, Germany
[59] Hiroshima University, Faculty of Science, 1-3-1 Kagamiyama, Higashihiroshima-shi, JP - Hiroshima 739-8526, Japan
[60] Hiroshima Institute of Technology, Faculty of Applied Information Science, 2-1-1 Miyake Saeki-ku, Hiroshima-shi, JP - Hiroshima 731-5193, Japan
[61] Indiana University, Department of Physics, Swain Hall West 117, Bloomington, IN 47405-7105, United States of America
[62] Institut für Astro- und Teilchenphysik, Technikerstrasse 25, A - 6020 Innsbruck, Austria
[63] University of Iowa, 203 Van Allen Hall, Iowa City, IA 52242-1479, United States of America
[64] Iowa State University, Department of Physics and Astronomy, Ames High Energy Physics Group, Ames, IA 50011-3160, United States of America
[65] Joint Institute for Nuclear Research, JINR Dubna, RU-141980 Moscow Region, Russia, Russia
[66] KEK, High Energy Accelerator Research Organization, 1-1 Oho, Tsukuba-shi, Ibaraki-ken 305-0801, Japan
[67] Kobe University, Graduate School of Science, 1-1 Rokkodai-cho, Nada-ku, JP Kobe 657-8501, Japan
[68] Kyoto University, Faculty of Science, Oiwake-cho, Kitashirakawa, Sakyou-ku, Kyoto-shi, JP - Kyoto 606-8502, Japan
[69] Kyoto University of Education, 1 Fukakusa, Fujimori, fushimi-ku, Kyoto-shi, JP - Kyoto 612-8522, Japan
[70] Universidad Nacional de La Plata, FCE, Departamento de Física, IFLP (CONICET-UNLP), C.C. 67, 1900 La Plata, Argentina

[71] Lancaster University, Physics Department, Lancaster LA1 4YB, United Kingdom
[72] INFN Sezione di Lecce[(a)]; Università del Salento, Dipartimento di Fisica[(b)]Via Arnesano IT - 73100 Lecce, Italy
[73] University of Liverpool, Oliver Lodge Laboratory, P.O. Box 147, Oxford Street, Liverpool L69 3BX, United Kingdom
[74] Jožef Stefan Institute and University of Ljubljana, Department of Physics, SI-1000 Ljubljana, Slovenia
[75] Queen Mary University of London, Department of Physics, Mile End Road, London E1 4NS, United Kingdom
[76] Royal Holloway, University of London, Department of Physics, Egham Hill, Egham, Surrey TW20 0EX, United Kingdom
[77] University College London, Department of Physics and Astronomy, Gower Street, London WC1E 6BT, United Kingdom
[78] Laboratoire de Physique Nucléaire et de Hautes Energies, Université Pierre et Marie Curie (Paris 6), Université Denis Diderot (Paris-7), CNRS/IN2P3, Tour 33, 4 place Jussieu, FR - 75252 Paris Cedex 05, France
[79] Fysiska institutionen, Lunds universitet, Box 118, SE - 221 00 Lund, Sweden
[80] Universidad Autonoma de Madrid, Facultad de Ciencias, Departamento de Fisica Teorica, ES - 28049 Madrid, Spain
[81] Universität Mainz, Institut für Physik, Staudinger Weg 7, DE - 55099 Mainz, Germany
[82] University of Manchester, School of Physics and Astronomy, Manchester M13 9PL, United Kingdom
[83] CPPM, Aix-Marseille Université, CNRS/IN2P3, Marseille, France
[84] University of Massachusetts, Department of Physics, 710 North Pleasant Street, Amherst, MA 01003, United States of America
[85] McGill University, High Energy Physics Group, 3600 University Street, Montreal, Quebec H3A 2T8, Canada
[86] University of Melbourne, School of Physics, AU - Parkville, Victoria 3010, Australia
[87] The University of Michigan, Department of Physics, 2477 Randall Laboratory, 500 East University, Ann Arbor, MI 48109-1120, United States of America
[88] Michigan State University, Department of Physics and Astronomy, High Energy Physics Group, East Lansing, MI 48824-2320, United States of America
[89] INFN Sezione di Milano[(a)]; Università di Milano, Dipartimento di Fisica[(b)], via Celoria 16, IT - 20133 Milano, Italy
[90] B.I. Stepanov Institute of Physics, National Academy of Sciences of Belarus, Independence Avenue 68, Minsk 220072, Republic of Belarus
[91] National Scientific & Educational Centre for Particle & High Energy Physics, NC PHEP BSU, M. Bogdanovich St. 153, Minsk 220040, Republic of Belarus
[92] Massachusetts Institute of Technology, Department of Physics, Room 24-516, Cambridge, MA 02139, United States of America
[93] University of Montreal, Group of Particle Physics, C.P. 6128, Succursale Centre-Ville, Montreal, Quebec, H3C 3J7 , Canada
[94] P.N. Lebedev Institute of Physics, Academy of Sciences, Leninsky pr. 53, RU - 117 924 Moscow, Russia
[95] Institute for Theoretical and Experimental Physics (ITEP), B. Cheremushkinskaya ul. 25, RU 117 218 Moscow, Russia
[96] Moscow Engineering & Physics Institute (MEPhI), Kashirskoe Shosse 31, RU - 115409 Moscow, Russia
[97] Lomonosov Moscow State University Skobeltsyn Institute of Nuclear Physics (MSU SINP), 1(2),

Leninskie gory, GSP-1, Moscow 119991 Russian Federation, Russia
[98] Ludwig-Maximilians-Universität München, Fakultät für Physik, Am Coulombwall 1, DE - 85748 Garching, Germany
[99] Max-Planck-Institut für Physik, (Werner-Heisenberg-Institut), Föhringer Ring 6, 80805 München, Germany
[100] Nagasaki Institute of Applied Science, 536 Aba-machi, JP Nagasaki 851-0193, Japan
[101] Nagoya University, Graduate School of Science, Furo-Cho, Chikusa-ku, Nagoya, 464-8602, Japan
[102] INFN Sezione di Napoli[(a)]; Università di Napoli, Dipartimento di Scienze Fisiche[(b)], Complesso Universitario di Monte Sant'Angelo, via Cinthia, IT - 80126 Napoli, Italy
[103] University of New Mexico, Department of Physics and Astronomy, MSC07 4220, Albuquerque, NM 87131 USA, United States of America
[104] Radboud University Nijmegen/NIKHEF, Department of Experimental High Energy Physics, Heyendaalseweg 135, NL-6525 AJ, Nijmegen, Netherlands
[105] Nikhef National Institute for Subatomic Physics, and University of Amsterdam, Science Park 105, 1098 XG Amsterdam, Netherlands
[106] Department of Physics, Northern Illinois University, LaTourette Hall Normal Road, DeKalb, IL 60115, United States of America
[107] Budker Institute of Nuclear Physics (BINP), RU - Novosibirsk 630 090, Russia
[108] New York University, Department of Physics, 4 Washington Place, New York NY 10003, USA, United States of America
[109] Ohio State University, 191 West Woodruff Ave, Columbus, OH 43210-1117, United States of America
[110] Okayama University, Faculty of Science, Tsushimanaka 3-1-1, Okayama 700-8530, Japan
[111] University of Oklahoma, Homer L. Dodge Department of Physics and Astronomy, 440 West Brooks, Room 100, Norman, OK 73019-0225, United States of America
[112] Oklahoma State University, Department of Physics, 145 Physical Sciences Building, Stillwater, OK 74078-3072, United States of America
[113] Palacký University, 17.listopadu 50a, 772 07 Olomouc, Czech Republic
[114] University of Oregon, Center for High Energy Physics, Eugene, OR 97403-1274, United States of America
[115] LAL, Univ. Paris-Sud, IN2P3/CNRS, Orsay, France
[116] Osaka University, Graduate School of Science, Machikaneyama-machi 1-1, Toyonaka, Osaka 560-0043, Japan
[117] University of Oslo, Department of Physics, P.O. Box 1048, Blindern, NO - 0316 Oslo 3, Norway
[118] Oxford University, Department of Physics, Denys Wilkinson Building, Keble Road, Oxford OX1 3RH, United Kingdom
[119] INFN Sezione di Pavia[(a)]; Università di Pavia, Dipartimento di Fisica Nucleare e Teorica[(b)], Via Bassi 6, IT-27100 Pavia, Italy
[120] University of Pennsylvania, Department of Physics, High Energy Physics Group, 209 S. 33rd Street, Philadelphia, PA 19104, United States of America
[121] Petersburg Nuclear Physics Institute, RU - 188 300 Gatchina, Russia
[122] INFN Sezione di Pisa[(a)]; Università di Pisa, Dipartimento di Fisica E. Fermi[(b)], Largo B. Pontecorvo 3, IT - 56127 Pisa, Italy
[123] University of Pittsburgh, Department of Physics and Astronomy, 3941 O'Hara Street, Pittsburgh, PA 15260, United States of America
[124] Laboratorio de Instrumentacao e Fisica Experimental de Particulas - LIP[(a)], Avenida Elias Garcia 14-1, PT - 1000-149 Lisboa, Portugal; Universidad de Granada, Departamento de Fisica Teorica y del Cosmos and CAFPE[(b)], E-18071 Granada, Spain

[125] Institute of Physics, Academy of Sciences of the Czech Republic, Na Slovance 2, CZ - 18221 Praha 8, Czech Republic
[126] Charles University in Prague, Faculty of Mathematics and Physics, Institute of Particle and Nuclear Physics, V Holesovickach 2, CZ - 18000 Praha 8, Czech Republic
[127] Czech Technical University in Prague, Zikova 4, CZ - 166 35 Praha 6, Czech Republic
[128] State Research Center Institute for High Energy Physics, Moscow Region, 142281, Protvino, Pobeda street, 1, Russia
[129] Rutherford Appleton Laboratory, Science and Technology Facilities Council, Harwell Science and Innovation Campus, Didcot OX11 0QX, United Kingdom
[130] University of Regina, Physics Department, Canada
[131] Ritsumeikan University, Noji Higashi 1 chome 1-1, JP - Kusatsu, Shiga 525-8577, Japan
[132] INFN Sezione di Roma I[(a)]; Università La Sapienza, Dipartimento di Fisica[(b)], Piazzale A. Moro 2, IT- 00185 Roma, Italy
[133] INFN Sezione di Roma Tor Vergata[(a)]; Università di Roma Tor Vergata, Dipartimento di Fisica[(b)] , via della Ricerca Scientifica, IT-00133 Roma, Italy
[134] INFN Sezione di Roma Tre[(a)]; Università Roma Tre, Dipartimento di Fisica[(b)], via della Vasca Navale 84, IT-00146 Roma, Italy
[135] Réseau Universitaire de Physique des Hautes Energies (RUPHE): Université Hassan II, Faculté des Sciences Ain Chock[(a)], B.P. 5366, MA - Casablanca; Centre National de l'Energie des Sciences Techniques Nucleaires (CNESTEN)[(b)], B.P. 1382 R.P. 10001 Rabat 10001; Université Mohamed Premier[(c)], LPTPM, Faculté des Sciences, B.P.717. Bd. Mohamed VI, 60000, Oujda ; Université Mohammed V, Faculté des Sciences[(d)]4 Avenue Ibn Battouta, BP 1014 RP, 10000 Rabat, Morocco
[136] CEA, DSM/IRFU, Centre d'Etudes de Saclay, FR - 91191 Gif-sur-Yvette, France
[137] University of California Santa Cruz, Santa Cruz Institute for Particle Physics (SCIPP), Santa Cruz, CA 95064, United States of America
[138] University of Washington, Seattle, Department of Physics, Box 351560, Seattle, WA 98195-1560, United States of America
[139] University of Sheffield, Department of Physics & Astronomy, Hounsfield Road, Sheffield S3 7RH, United Kingdom
[140] Shinshu University, Department of Physics, Faculty of Science, 3-1-1 Asahi, Matsumoto-shi, JP - Nagano 390-8621, Japan
[141] Universität Siegen, Fachbereich Physik, D 57068 Siegen, Germany
[142] Simon Fraser University, Department of Physics, 8888 University Drive, CA - Burnaby, BC V5A 1S6, Canada
[143] SLAC National Accelerator Laboratory, Stanford, California 94309, United States of America
[144] Comenius University, Faculty of Mathematics, Physics & Informatics[(a)], Mlynska dolina F2, SK - 84248 Bratislava; Institute of Experimental Physics of the Slovak Academy of Sciences, Dept. of Subnuclear Physics[(b)], Watsonova 47, SK - 04353 Kosice, Slovak Republic
[145] [(a)]University of Johannesburg, Department of Physics, PO Box 524, Auckland Park, Johannesburg 2006; [(b)]School of Physics, University of the Witwatersrand, Private Bag 3, Wits 2050, Johannesburg, South Africa, South Africa
[146] Stockholm University: Department of Physics[(a)]; The Oskar Klein Centre[(b)], AlbaNova, SE - 106 91 Stockholm, Sweden
[147] Royal Institute of Technology (KTH), Physics Department, SE - 106 91 Stockholm, Sweden
[148] Stony Brook University, Department of Physics and Astronomy, Nicolls Road, Stony Brook, NY 11794-3800, United States of America
[149] University of Sussex, Department of Physics and Astronomy Pevensey 2 Building, Falmer, Brighton BN1 9QH, United Kingdom

[150] University of Sydney, School of Physics, AU - Sydney NSW 2006, Australia
[151] Insitute of Physics, Academia Sinica, TW - Taipei 11529, Taiwan
[152] Technion, Israel Inst. of Technology, Department of Physics, Technion City, IL - Haifa 32000, Israel
[153] Tel Aviv University, Raymond and Beverly Sackler School of Physics and Astronomy, Ramat Aviv, IL - Tel Aviv 69978, Israel
[154] Aristotle University of Thessaloniki, Faculty of Science, Department of Physics, Division of Nuclear & Particle Physics, University Campus, GR - 54124, Thessaloniki, Greece
[155] The University of Tokyo, International Center for Elementary Particle Physics and Department of Physics, 7-3-1 Hongo, Bunkyo-ku, JP - Tokyo 113-0033, Japan
[156] Tokyo Metropolitan University, Graduate School of Science and Technology, 1-1 Minami-Osawa, Hachioji, Tokyo 192-0397, Japan
[157] Tokyo Institute of Technology, Department of Physics, 2-12-1 O-Okayama, Meguro, Tokyo 152-8551, Japan
[158] University of Toronto, Department of Physics, 60 Saint George Street, Toronto M5S 1A7, Ontario, Canada
[159] TRIUMF[(a)], 4004 Wesbrook Mall, Vancouver, B.C. V6T 2A3; [(b)]York University, Department of Physics and Astronomy, 4700 Keele St., Toronto, Ontario, M3J 1P3, Canada
[160] University of Tsukuba, Institute of Pure and Applied Sciences, 1-1-1 Tennoudai, Tsukuba-shi, JP - Ibaraki 305-8571, Japan
[161] Tufts University, Science & Technology Center, 4 Colby Street, Medford, MA 02155, United States of America
[162] Universidad Antonio Narino, Centro de Investigaciones, Cra 3 Este No.47A-15, Bogota, Colombia
[163] University of California, Irvine, Department of Physics & Astronomy, CA 92697-4575, United States of America
[164] INFN Gruppo Collegato di Udine[(a)]; ICTP[(b)], Strada Costiera 11, IT-34014, Trieste; Università di Udine, Dipartimento di Fisica[(c)], via delle Scienze 208, IT - 33100 Udine, Italy
[165] University of Illinois, Department of Physics, 1110 West Green Street, Urbana, Illinois 61801, United States of America
[166] University of Uppsala, Department of Physics and Astronomy, P.O. Box 516, SE -751 20 Uppsala, Sweden
[167] Instituto de Física Corpuscular (IFIC) Centro Mixto UVEG-CSIC, Apdo. 22085 ES-46071 Valencia, Dept. Física At. Mol. y Nuclear; Dept. Ing. Electrónica; Univ. of Valencia, and Inst. de Microelectrónica de Barcelona (IMB-CNM-CSIC) 08193 Bellaterra, Spain
[168] University of British Columbia, Department of Physics, 6224 Agricultural Road, CA - Vancouver, B.C. V6T 1Z1, Canada
[169] University of Victoria, Department of Physics and Astronomy, P.O. Box 3055, Victoria B.C., V8W 3P6, Canada
[170] Waseda University, WISE, 3-4-1 Okubo, Shinjuku-ku, Tokyo, 169-8555, Japan
[171] The Weizmann Institute of Science, Department of Particle Physics, P.O. Box 26, IL - 76100 Rehovot, Israel
[172] University of Wisconsin, Department of Physics, 1150 University Avenue, WI 53706 Madison, Wisconsin, United States of America
[173] Julius-Maximilians-University of Würzburg, Physikalisches Institute, Am Hubland, 97074 Würzburg, Germany
[174] Bergische Universität, Fachbereich C, Physik, Postfach 100127, Gauss-Strasse 20, D- 42097 Wuppertal, Germany
[175] Yale University, Department of Physics, PO Box 208121, New Haven CT, 06520-8121, United States of America

[176] Yerevan Physics Institute, Alikhanian Brothers Street 2, AM - 375036 Yerevan, Armenia
[177] Centre de Calcul CNRS/IN2P3, Domaine scientifique de la Doua, 27 bd du 11 Novembre 1918, 69622 Villeurbanne Cedex, France
[a] Also at LIP, Portugal
[b] Also at Faculdade de Ciencias, Universidade de Lisboa, Portugal
[c] Also at CPPM, Marseille, France.
[d] Also at Centro de Fisica Nuclear da Universidade de Lisboa, Portugal
[e] Also at TRIUMF, Vancouver, Canada
[f] Also at FPACS, AGH-UST, Cracow, Poland
[g] Now at Universita' dell'Insubria, Dipartimento di Fisica e Matematica
[h] Also at Department of Physics, University of Coimbra, Portugal
[i] Now at CERN
[j] Also at Università di Napoli Parthenope, Napoli, Italy
[k] Also at Institute of Particle Physics (IPP), Canada
[l] Also at Università di Napoli Parthenope, via A. Acton 38, IT - 80133 Napoli, Italy
[m] Louisiana Tech University, 305 Wisteria Street, P.O. Box 3178, Ruston, LA 71272, United States of America
[n] Also at Universidade de Lisboa, Portugal
[o] At California State University, Fresno, USA
[p] Also at TRIUMF, 4004 Wesbrook Mall, Vancouver, B.C. V6T 2A3, Canada
[q] Also at Faculdade de Ciencias, Universidade de Lisboa, Portugal and at Centro de Fisica Nuclear da Universidade de Lisboa, Portugal
[r] Also at FPACS, AGH-UST, Cracow, Poland
[s] Also at California Institute of Technology, Pasadena, USA
[t] Louisiana Tech University, Ruston, USA
[u] Also at University of Montreal, Montreal, Canada
[v] Now at Chonnam National University, Chonnam, Korea 500-757
[w] Also at Institut für Experimentalphysik, Universität Hamburg, Luruper Chaussee 149, 22761 Hamburg, Germany
[x] Also at Manhattan College, NY, USA
[y] Also at School of Physics and Engineering, Sun Yat-sen University, China
[z] Also at Taiwan Tier-1, ASGC, Academia Sinica, Taipei, Taiwan
[aa] Also at School of Physics, Shandong University, Jinan, China
[ab] Also at California Institute of Technology, Pasadena, USA
[ac] Also at Rutherford Appleton Laboratory, Didcot, UK
[ad] Also at school of physics, Shandong University, Jinan
[ae] Also at Rutherford Appleton Laboratory, Didcot , UK
[af] Also at TRIUMF, Vancouver, Canada
[ag] Now at KEK
[ah] Also at Departamento de Fisica, Universidade de Minho, Portugal
[ai] University of South Carolina, Columbia, USA
[aj] Also at KFKI Research Institute for Particle and Nuclear Physics, Budapest, Hungary
[ak] University of South Carolina, Dept. of Physics and Astronomy, 700 S. Main St, Columbia, SC 29208, United States of America
[al] Also at Institute of Physics, Jagiellonian University, Cracow, Poland
[am] Louisiana Tech University, Ruston, USA
[an] Also at Institut für Experimentalphysik, Universität Hamburg, Hamburg, Germany
[ao] University of South Carolina, Columbia, USA

[ap] Transfer to LHCb 31.01.2010
[aq] Also at Oxford University, Department of Physics, Denys Wilkinson Building, Keble Road, Oxford OX1 3RH, United Kingdom
[ar] Also at school of physics and engineering, Sun Yat-sen University, China
[as] Determine the Muon T0s using 2009 and 2010 beam splash events for MDT chambers and for each mezzanine card, starting from 2009/09/15
[at] Also at CEA
[au] Also at LPNHE, Paris, France
[av] has been working on Muon MDT noise study and calibration since 2009/10, contact as Tiesheng Dai and Muon convener
[aw] Also at Nanjing University, China
[*] Deceased

Paper II

Eur. Phys. J. C (2012) 72:2215
DOI 10.1140/epjc/s10052-012-2215-7

THE EUROPEAN PHYSICAL JOURNAL C

Letter

Search for supersymmetry in events with large missing transverse momentum, jets, and at least one tau lepton in 7 TeV proton-proton collision data with the ATLAS detector

The ATLAS Collaboration*
CERN, 1211 Geneva 23, Switzerland

Received: 4 October 2012

Abstract A search for supersymmetry (SUSY) in events with large missing transverse momentum, jets, and at least one hadronically decaying τ lepton, with zero or one additional light lepton (e/μ), has been performed using 4.7 fb^{-1} of proton-proton collision data at $\sqrt{s} = 7$ TeV recorded with the ATLAS detector at the Large Hadron Collider. No excess above the Standard Model background expectation is observed and a 95 % confidence level visible cross-section upper limit for new phenomena is set. In the framework of gauge-mediated SUSY-breaking models, lower limits on the mass scale Λ are set at 54 TeV in the regions where the $\tilde{\tau}_1$ is the next-to-lightest SUSY particle ($\tan\beta > 20$). These limits provide the most stringent tests to date of GMSB models in a large part of the parameter space considered.

1 Introduction

This paper reports on the search for supersymmetry (SUSY) [1–9] in events with large missing transverse momentum, jets and at least one hadronically decaying τ lepton. Four different topologies with a τ in the final state have been studied: one τ lepton, at least two τ leptons, one τ lepton and precisely one additional muon and one τ lepton and precisely one additional electron. The minimal gauge-mediated supersymmetry-breaking (GMSB) model [10–15] is considered as benchmark to evaluate the reach of this analysis.

SUSY introduces a symmetry between fermions and bosons, resulting in a SUSY partner (sparticle) for each Standard Model (SM) particle with identical mass and quantum numbers except a difference by half a unit of spin. Assuming R-parity conservation [16–20], sparticles are produced in pairs. These would then decay through cascades involving other sparticles until the lightest SUSY particle (LSP), which is stable, is produced. Since equal mass SUSY partners are excluded, SUSY must be a broken symmetry. Minimal GMSB models can be described by six parameters: the SUSY-breaking mass scale in the low-energy sector (Λ), the messenger mass (M_{mess}), the number of SU(5) messenger fields (N_5), the ratio of the vacuum expectation values of the two Higgs doublets ($\tan\beta$), the Higgs-sector mixing parameter (μ) and the scale factor for the gravitino mass (C_{grav}). For the analysis presented in this paper, Λ and $\tan\beta$ are treated as free parameters, and the other parameters are fixed to the values already used in Refs. [21, 22]: $M_{\text{mess}} = 250$ TeV, $N_5 = 3$, $\mu > 0$ and $C_{\text{grav}} = 1$. The C_{grav} parameter determines the lifetime of next-to-lightest SUSY particle (NLSP); for $C_{\text{grav}} = 1$ the NLSP decays promptly ($c\tau_{\text{NLSP}} < 0.1$ mm). With this choice of parameters, at moderate Λ the production of gluino and/or squark pairs is expected to dominate at the LHC; these sparticles will decay into the next-to-lightest SUSY particle (NLSP), which subsequently decays to the LSP. In GMSB models, the LSP is the very light gravitino ($\tilde{G}$). The NLSP is the dominant sparticle decaying to the LSP and this leads to experimental signatures which are largely determined by the nature of the NLSP. This can be either the lightest stau ($\tilde{\tau}_1$), a right-handed slepton ($\tilde{\ell}_R$), the lightest neutralino ($\tilde{\chi}_1^0$), or a sneutrino ($\tilde{\nu}$), dominantly leading to final states containing τ leptons, light leptons ($\ell = e, \mu$), photons, b-jets, or neutrinos. At large values of $\tan\beta$, the $\tilde{\tau}_1$ is the NLSP for most of the parameter space, which leads to final states containing at least two τ leptons. In the so-called CoNLSP region, where the mass difference between the $\tilde{\tau}_1$ and the $\tilde{\ell}_R$ is smaller than the sum of the τ and light-lepton masses, both the $\tilde{\tau}_1$ and the $\tilde{\ell}_R$ decay directly into the LSP and are therefore NLSPs.

* e-mail: atlas.publications@cern.ch

Published online: 20 November 2012

Previous searches for $\tilde{\tau}_1$ pair production, with the subsequent decay $\tilde{\tau}_1 \to \tau\tilde{G}$ in the minimal GMSB model, have been reported by the LEP Collaborations ALEPH [23], DELPHI [24] and OPAL [25]. The analysis reported in this paper extends the searches in 2 fb^{-1} of data presented in Refs. [21, 22]. It comprises the full 2011 dataset, corresponding to an integrated luminosity of (4.7 ± 0.1) fb^{-1} [26, 27] after applying beam, detector and data-quality requirements. A complementary search interpreted in GMSB, requiring two light leptons, has also been performed using the same dataset by the ATLAS Collaboration [28]. The CMS Collaboration has searched for new phenomena in same-sign τ-pair events [29] and multi-lepton events including two τ leptons in the final state [30] using 35 pb^{-1} of data, where the minimal GMSB model was not considered.

2 ATLAS detector

The ATLAS experiment [31] is a multi-purpose detector with a forward-backward symmetric cylindrical geometry and nearly 4π solid angle coverage. The inner tracking detector (ID) consists of a silicon pixel detector, a silicon microstrip detector and a transition radiation tracker. The ID is surrounded by a thin superconducting solenoid providing a 2 T magnetic field and by fine-granularity lead/liquid-argon (LAr) electromagnetic calorimeters. An iron/scintillator-tile calorimeter provides hadronic coverage in the central pseudorapidity[1] range. The endcap and forward regions are instrumented with liquid-argon calorimeters for both electromagnetic and hadronic measurements. An extensive muon spectrometer system that incorporates large superconducting toroidal magnets surrounds the calorimeters.

3 Simulated samples

The Monte Carlo (MC) simulations used to evaluate the expected backgrounds and selection efficiencies for the SUSY models considered are very similar to the ones used in Refs. [21, 22]. A suite of generators is used to aid in the estimate of SM background contributions. The ALPGEN generator [32] is used to simulate samples of W and Z/γ^* events with up to five (for Z events) or six (for W events) accompanying jets, where CTEQ6L1 [33] is used for the parton distribution functions (PDFs). Z/γ^* events with $m_{\ell\ell} < 40$ GeV are referred to in this paper as "Drell-Yan". Top quark pair production, single top production and diboson (WW and WZ) pair production are simulated with MC@NLO [34–36] and the next-to-leading-order (NLO) PDF set CT10 [37]. Fragmentation and hadronization are performed with Herwig [38], using JIMMY [39] for the underlying event simulation. The decay of τ leptons and radiation of photons are simulated using TAUOLA [40, 41] and PHOTOS [42], respectively. The production of multi-jet events is simulated with PYTHIA 6.4.25 [43] using the AUET2B tune [44] and MRST2007 LO* [45] PDFs. The SUSY mass spectra are calculated using ISAJET 7.80 [46]. The MC signal samples are produced using Herwig++ 2.4.2 [47] with MRST2007 LO* PDFs. Signal cross-sections are calculated to next-to-leading order in the strong coupling constant, adding the resummation of soft gluon emission at next-to-leading-logarithmic accuracy (NLO+NLL) [48–52]. The nominal SUSY production cross-sections and their uncertainties are taken from an envelope of cross-section predictions using different PDF sets and factorisation and renormalization scales, as described in Ref. [53]. The GMSB signal samples are generated on a grid ranging from $\Lambda = 10$ TeV to $\Lambda = 80$ TeV and from $\tan\beta = 2$ to $\tan\beta = 67$, with the cross-section dropping from 100 pb for $\Lambda = 15$ TeV to 5.0 fb for $\Lambda = 80$ TeV.

All samples are processed through the GEANT4-based simulation [54] of the ATLAS detector [55]. The full simulation also includes a realistic treatment of the variation of the number of pp interactions per bunch crossing (pile-up) in the data, with an average of nine interactions per crossing.

4 Object reconstruction

Jets are reconstructed using the anti-k_t jet clustering algorithm [56] with radius parameter $R = 0.4$. Jet energies are calibrated to correct for upstream material, calorimeter non-compensation, pile-up, and other effects [57]. Jets are required to have transverse momenta (p_{T}) greater than 25 GeV and $|\eta| < 2.8$, except in the computation of the missing transverse momentum, where $|\eta| < 4.5$ and p_{T} greater than 20 GeV is required.

Muon candidates are identified as tracks in the ID matched to track segments in the muon spectrometer [58]. They are required to have $p_{\mathrm{T}} > 10$ GeV and $|\eta| < 2.4$. Electron candidates are constructed by matching electromagnetic clusters with tracks in the ID. They are then required to satisfy $p_{\mathrm{T}} > 20$ GeV, $|\eta| < 2.47$ and to pass the "tight" identification criteria described in Ref. [59], re-optimized for 2011 conditions.

[1] ATLAS uses a right-handed coordinate system with its origin at the nominal interaction point (IP) in the centre of the detector and the z-axis along the beam pipe. The x-axis points from the IP to the centre of the LHC ring and the y-axis points upward. Cylindrical coordinates (r, ϕ) are used in the transverse plane, ϕ being the azimuthal angle around the beam pipe. The pseudorapidity is defined in terms of the polar angle θ as $\eta = -\ln\tan(\theta/2)$.

Electrons or muons are required to be isolated, i.e. the scalar sum of the transverse momenta of tracks within a cone of $\Delta R = \sqrt{(\Delta\phi)^2 + (\Delta\eta)^2} < 0.2$ around the lepton candidate, excluding the lepton candidate track itself, must be less than 10 % of the lepton's transverse energy for electrons and less than 1.8 GeV for muons. Tracks selected for the electron and muon isolation requirement defined above have $p_{\mathrm{T}} > 1$ GeV and are associated to the primary vertex of the event.

The missing transverse momentum vector $\mathbf{p}_{\mathrm{T}}^{\mathrm{miss}}$ (and its magnitude $E_{\mathrm{T}}^{\mathrm{miss}}$) is measured from the transverse momenta of identified jets, electrons, muons and all calorimeter clusters with $|\eta| < 4.5$ not associated to such objects [60]. For the purpose of the measurement of $E_{\mathrm{T}}^{\mathrm{miss}}$, τ leptons are not distinguished from jets.

Jets originating from decays of b-quarks are identified and used to separate the W and $t\bar{t}$ background contributions. They are identified by a neural-network-based algorithm, which combines information from the track impact parameters with a search for decay vertices along the jet axis [61]. A working point corresponding to 60 % tagging efficiency for b-jets and <1 % mis-identification of light-flavour or gluon jets is chosen [62].

The τ leptons considered in this search are reconstructed through their hadronic decays. The τ reconstruction is seeded from anti-k_t jets ($R = 0.4$) with $p_{\mathrm{T}} > 10$ GeV. An η- and p_{T}-dependent energy calibration to the hadronic τ energy scale is applied. Discriminating variables based on track information and observables sensitive to the transverse and longitudinal shape of the energy deposits of τ candidates in the calorimeter are used. These quantities are combined in a boosted decision tree (BDT) discriminator [63] to optimize their impact. Calorimeter information and measurements of transition radiation are used to veto electrons mis-identified as τ leptons. Suitable τ lepton candidates must satisfy $p_{\mathrm{T}} > 20$ GeV, $|\eta| < 2.5$, and have one or three associated tracks of $p_{\mathrm{T}} > 1$ GeV with a charge sum of ± 1. A sample of $Z \to \tau\tau$ events is used to measure the efficiency of the BDT τ identification. The "loose" and "medium" working points in Ref. [63] are used herein and correspond to efficiencies of about 60 % and 40 % respectively, independent of p_{T}, with a rejection factor of 20–50 against τ candidates built from hadronic jets ("fake" τ leptons).

5 Event selection

Four mutually exclusive final states are considered for this search: events with only one "medium" τ, no additional "loose" τ candidates and no muons or electrons, referred to as '1τ'; events with two or more "loose" τ candidates and no muons or electrons, referred to as '2τ'; events with at least one "medium" τ and exactly one muon ('$\tau + \mu$') or electron ('$\tau + e$').

In the 1τ and 2τ final states, candidate events are triggered by requiring a jet with high transverse momentum and high $E_{\mathrm{T}}^{\mathrm{miss}}$ ('jetMET') [65], both measured at the electromagnetic scale[2]. In the $\tau + \mu$ final state, events are selected by a muon trigger and a muon-plus-jet trigger ('muon+jet'), while in the $\tau + e$ final state, a single-electron trigger requirement is imposed [65]. The trigger requirements have been optimized to ensure a uniform trigger efficiency for all data-taking periods, which exceeds 98 % with respect to the offline selection for all final states considered.

Pre-selected events are required to have a reconstructed primary vertex with at least five tracks (with $p_{\mathrm{T}} > 0.4$ GeV). To suppress soft multi-jet events in the 1τ and 2τ final states, a second jet with $p_{\mathrm{T}} > 30$ GeV is required. Remaining multi-jet events, where highly energetic jets are mismeasured, are suppressed by requiring the azimuthal angle between the missing transverse momentum vector and either of the two leading jets to be greater than 0.3 rad. Three quantities characterising the kinematic properties of the event are used to further suppress the main background processes (W + jets, Z + jets and $t\bar{t}$ events) in all four final states:

- the transverse mass $m_{\mathrm{T}}^{\tau,\ell}$ formed by $E_{\mathrm{T}}^{\mathrm{miss}}$ and either the p_{T} of the τ lepton in the 1τ and 2τ channels, or of the light lepton (e/μ) in the $\tau + \mu$ and $\tau + e$ ones: $m_{\mathrm{T}}^{\tau,\ell} = \sqrt{2 p_{\mathrm{T}}^{\tau,\ell} E_{\mathrm{T}}^{\mathrm{miss}} (1 - \cos(\Delta\phi(\tau/\ell, E_{\mathrm{T}}^{\mathrm{miss}})))}$;
- the scalar sum H_{T} of the transverse momenta of τ lepton candidates and the two highest momentum jets in the events: $H_{\mathrm{T}} = \sum p_{\mathrm{T}}^{\tau} + \sum_{i=1,2} p_{\mathrm{T}}^{\mathrm{jet_i}}$;
- the effective mass $m_{\mathrm{eff}} = H_{\mathrm{T}} + E_{\mathrm{T}}^{\mathrm{miss}}$.

For each of the four final states, specific criteria are applied to the above quantities in order to define a signal region (SR), as summarized in Table 1.

Figure 1 shows the m_{T} and $m_{\mathrm{T}}^{\tau_1} + m_{\mathrm{T}}^{\tau_2}$ distributions for the 1τ and 2τ channels after all the requirements of the analysis except the final requirement on H_{T}. Similarly, Fig. 2 shows the $m_{\mathrm{T}}^{e,\mu}$ distributions for the $\tau + \mu$ and $\tau + e$ channels after all the requirements of the analysis except the final m_{eff} requirement.

Figures 3 and 4 show the H_{T} distributions in the 1τ and 2τ channels, and m_{eff} distributions in the $\tau + \mu$ and $\tau + e$ channels, respectively, after all other selection criteria have been imposed.

[2]The electromagnetic scale is the basic calorimeter signal scale for the ATLAS calorimeters. It has been established using test-beam measurements for electrons and muons to give the correct response for the energy deposited in electromagnetic showers, although it does not correct for the lower response of the calorimeter to hadrons.

Table 1 Event selection for the four final states presented in this paper. Numbers in parentheses are the minimum transverse momenta required for the objects. Pairs of numbers separated by a slash denote different selection criteria imposed in different data-taking periods

–	1τ	2τ	$\tau+\mu$	$\tau+e$
Trigger	jetMET $p_{\mathrm{T}}^{\mathrm{jet}} > 75$ GeV $E_{\mathrm{T}}^{\mathrm{miss}} > 45/55$ GeV	jetMET $p_{\mathrm{T}}^{\mathrm{jet}} > 75$ GeV $E_{\mathrm{T}}^{\mathrm{miss}} > 45/55$ GeV	muon/muon+jet $p_{\mathrm{T}}^{\mu} > 18$ GeV $p_{\mathrm{T}}^{\mathrm{jet}} > 10$ GeV	electron $p_{\mathrm{T}}^{e} > 20/22$ GeV
Jet req.	$\geq$2 jets (130, 30 GeV)	$\geq$2 jets (130, 30 GeV)	$\geq$1 jet (50 GeV)	–
$E_{\mathrm{T}}^{\mathrm{miss}}$ req.	$E_{\mathrm{T}}^{\mathrm{miss}} > 130/150$ GeV	$E_{\mathrm{T}}^{\mathrm{miss}} > 130/150$ GeV	–	–
$N_{e,\mu}$	0	0	1μ (20 GeV)	$1e$ (25 GeV)
N_{τ}	=1 medium (20 GeV), =0 loose	$\geq$2 loose (20 GeV)	$\geq$1 medium (20 GeV)	$\geq$1 medium (20 GeV)
Kinematic criteria	$\Delta(\phi_{\mathrm{jet}_{1,2}}-\mathbf{p}_{\mathrm{T}}^{\mathrm{miss}}) > 0.3$ $E_{\mathrm{T}}^{\mathrm{miss}}/m_{\mathrm{eff}} > 0.3$ $m_{\mathrm{T}} > 110$ GeV $H_{\mathrm{T}} > 775$ GeV	$\Delta(\phi_{\mathrm{jet}_{1,2}}-\mathbf{p}_{\mathrm{T}}^{\mathrm{miss}}) > 0.3$ $m_{\mathrm{T}}^{\tau_1}+m_{\mathrm{T}}^{\tau_2} > 100$ GeV $H_{\mathrm{T}} > 650$ GeV	$m_{\mathrm{T}}^{e,\mu} > 100$ GeV $m_{\mathrm{eff}} > 1000$ GeV	$m_{\mathrm{T}}^{e,\mu} > 100$ GeV $m_{\mathrm{eff}} > 1000$ GeV

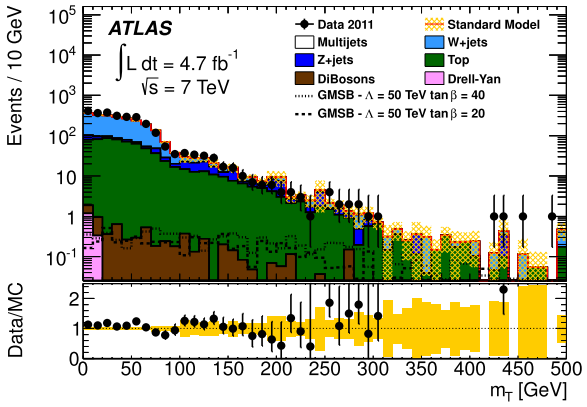

(a) m_{T} distribution for the 1τ final state.

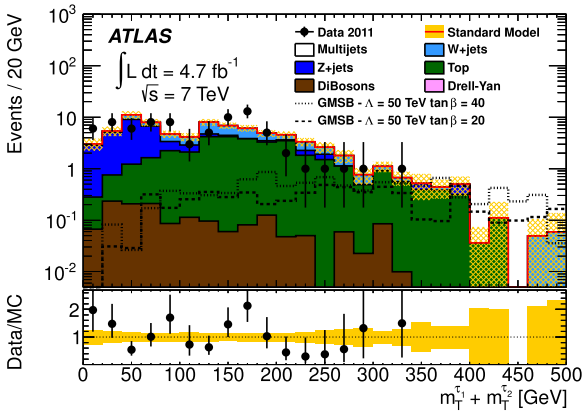

(b) $m_{\mathrm{T}}^{\tau_1}+m_{\mathrm{T}}^{\tau_2}$ distribution for the 2τ final state.

Fig. 1 Distribution of (**a**) m_{T} and (**b**) $m_{\mathrm{T}}^{\tau_1}+m_{\mathrm{T}}^{\tau_2}$ for the 1τ and 2τ final states, respectively, after all analysis requirements but the final requirement on H_{T}. Data are represented by the *points*, with statistical uncertainty only. The SM prediction includes the data-driven corrections discussed in the text. The band centred around the total SM background indicates the uncertainty due to finite MC sample sizes on the background expectation. Also shown is the expected signal from two typical GMSB samples ($\Lambda = 50$ TeV, $\tan\beta = 40$, $\Lambda = 50$ TeV, $\tan\beta = 20$)

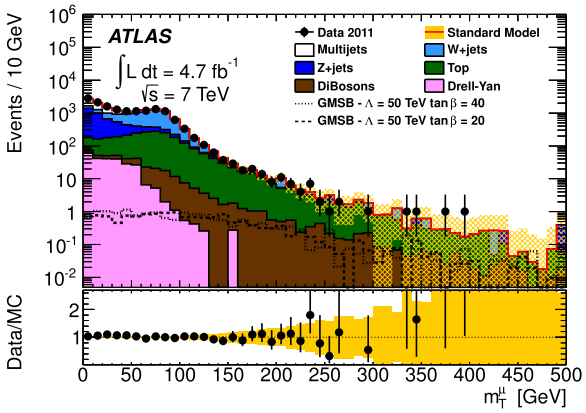

(a) m_{T}^{μ} distribution for the $\tau+\mu$ final state.

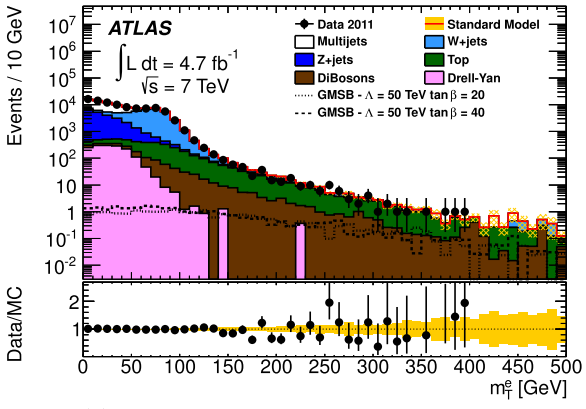

(b) m_{T}^{e} distribution for the $\tau+e$ final state.

Fig. 2 Distribution of $m_{\mathrm{T}}^{e,\mu}$ for the (**a**) $\tau+\mu$ and (**b**) $\tau+e$ final states after all analysis requirements but the final requirement on m_{eff}. Data are represented by the *points*, with statistical uncertainty only. The SM prediction includes the data-driven corrections discussed in the text. The band centred around the total SM background indicates the uncertainty due to finite MC sample sizes on the background expectation. Also shown is the expected signal from two typical GMSB samples ($\Lambda = 50$ TeV, $\tan\beta = 40$, $\Lambda = 50$ TeV, $\tan\beta = 20$)

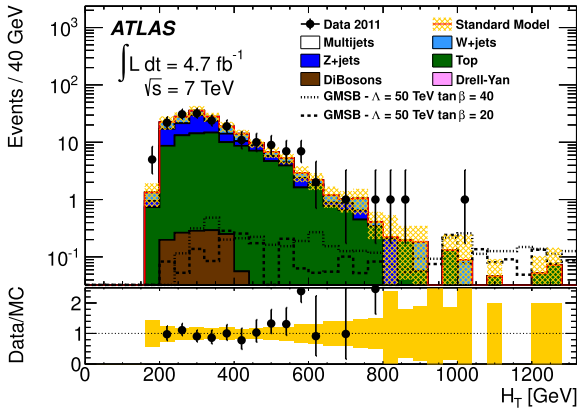

(a) H_{T} distribution for the 1τ final state.

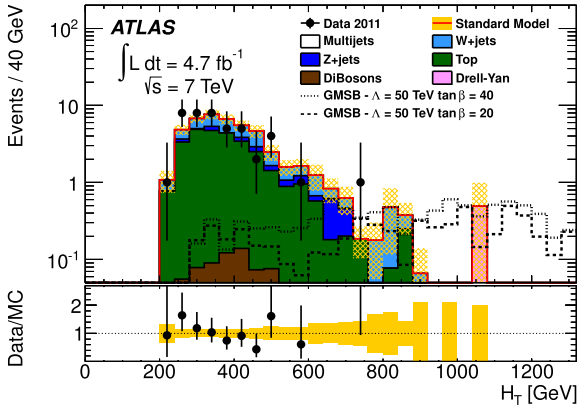

(b) H_{T} distribution for the 2τ final state.

Fig. 3 Distribution of H_{T} for the (**a**) 1τ and (**b**) 2τ final states after all analysis requirements. Data are represented by the *points*, with statistical uncertainty only. The SM prediction includes the data-driven corrections discussed in the text. The band centred around the total SM background indicates the uncertainty due to finite MC sample sizes on the background expectation. Also shown is the expected signal from two typical GMSB samples ($\Lambda = 50$ TeV, $\tan\beta = 40$, $\Lambda = 50$ TeV, $\tan\beta = 20$)

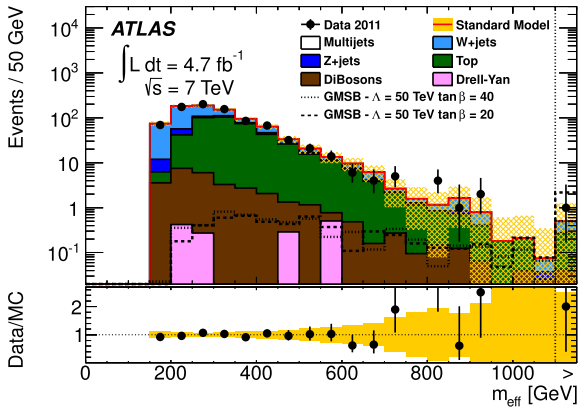

(a) m_{eff} distribution for the $\tau+\mu$ final state.

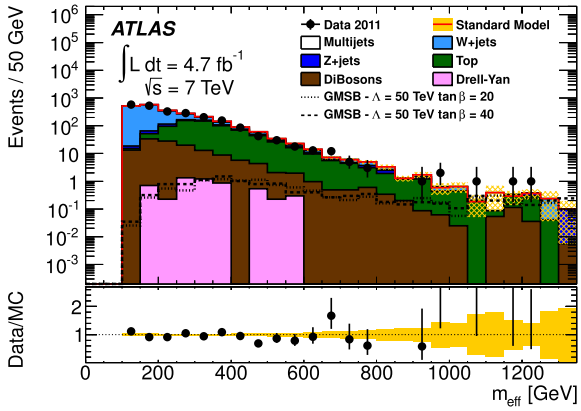

(b) m_{eff} distribution for the $\tau+e$ final state.

Fig. 4 Distribution of m_{eff} for the (**a**) $\tau + \mu$ and (**b**) $\tau + e$ final states after all analysis requirements. Data are represented by the *points*, with statistical uncertainty only. The SM prediction includes the data-driven corrections discussed in the text. The band centred around the total SM background indicates the uncertainty due to finite MC sample sizes on the background expectation. Also shown is the expected signal from two typical GMSB samples ($\Lambda = 50$ TeV, $\tan\beta = 40$, $\Lambda = 50$ TeV, $\tan\beta = 20$). In the *top figure*, the event in data surviving all the analysis requirements is shown in the overflow bin

6 Background estimation

The SM background expectation predicted by simulation in the SR is corrected by means of control regions (CRs), which are chosen such that a specific background process is enriched while any overlap with the SR is avoided. Data/MC comparison in the CRs show that MC overestimates the number of events compared to data, mainly due to mis-modelling of τ mis-identification probabilities and kinematics. Scaling factors are therefore obtained from the ratio of the number of observed events to the number of simulated background events in the control region where a given background contribution is enriched. Studies comparing data with MC simulations show that the τ mis-identification probability is, to a good approximation, independent of the kinematic variables used to separate the SR from the CRs, so that the measured ratio of the data to MC event yields in the CR can be used to compute scaling factors to correct the MC background prediction in the SR.

The dominant background contributions in the SR arise from top quark pair and single top events (hereafter generically indicated as 'top'), W + jets, Z + jets and multi-jet events. The latter background does not contribute significantly to the $\tau + \mu$ final state. The CR definitions used to estimate these background contributions in the various channels are summarized in Table 2.

6.1 Background estimation in the 2τ channel

The W and top background contributions are dominated by events in which one τ candidate is a true τ and the others are mis-reconstructed from hadronic activity in the fi-

Table 2 Definition of the background control regions (CRs) used to estimate the normalization of background samples in the four final states: 1τ, 2τ, $\tau+\mu$ and $\tau+e$

Background	1τ	2τ	$\tau+\mu$ $\tau+e$
$t\bar{t}$	$\Delta(\phi_{\text{jet}_{1,2}-\mathbf{p}_{\text{T}}^{\text{miss}}}) > 0.3$ rad $m_{\text{T}} < 70$ GeV $E_{\text{T}}^{\text{miss}}/m_{\text{eff}} > 0.3$ b-tag template fit	$\Delta(\phi_{\text{jet}_{1,2}-\mathbf{p}_{\text{T}}^{\text{miss}}}) > 0.3$ rad $m_{\text{T}}^{\tau_1} + m_{\text{T}}^{\tau_2} \geq 100$ GeV $H_{\text{T}} < 550$ GeV $N_{b\text{-tag}} \geq 1$	$30\text{ GeV} < E_{\text{T}}^{\text{miss}} < 100$ GeV $50\text{ GeV} < m_{\text{T}}^{e,\mu} < 150$ GeV $N_{b\text{-tag}} \geq 1$
$W+\text{jets}$	$\Delta(\phi_{\text{jet}_{1,2}-\mathbf{p}_{\text{T}}^{\text{miss}}}) > 0.3$ rad $m_{\text{T}} < 70$ GeV $E_{\text{T}}^{\text{miss}}/m_{\text{eff}} > 0.3$	$\Delta(\phi_{\text{jet}_{1,2}-\mathbf{p}_{\text{T}}^{\text{miss}}}) > 0.3$ rad $m_{\text{T}}^{\tau_1} + m_{\text{T}}^{\tau_2} \geq 100$ GeV $H_{\text{T}} < 550$ GeV $N_{b\text{-tag}} = 0$	$30\text{ GeV} < E_{\text{T}}^{\text{miss}} < 100$ GeV $50\text{ GeV} < m_{\text{T}}^{e,\mu} < 150$ GeV $N_{b\text{-tag}} = 0$
$Z+\text{jets}$	2μ (20 GeV), $\lvert\eta\rvert < 2.4$ $\geq$2 jets (130, 30 GeV) $N_{b\text{-tag}} = 0$	$\Delta(\phi_{\text{jet}_{1,2}-\mathbf{p}_{\text{T}}^{\text{miss}}}) > 0.3$ rad $m_{\text{T}}^{\tau_1} + m_{\text{T}}^{\tau_2} < 80$ GeV $H_{\text{T}} < 550$ GeV	MC-based normalization
Multi-jet	$\Delta(\phi_{\text{jet}_{1,2}-\mathbf{p}_{\text{T}}^{\text{miss}}}) < 0.3$ rad $E_{\text{T}}^{\text{miss}}/m_{\text{eff}} < 0.3$	$\Delta(\phi_{\text{jet}_{1,2}-\mathbf{p}_{\text{T}}^{\text{miss}}}) < 0.3$ rad $E_{\text{T}}^{\text{miss}}/m_{\text{eff}} < 0.4$	Compare events with and without lepton isolation [64]

nal state. The background from $Z+\text{jets}$ events is dominated by final states with $Z \to \tau\tau$ decays. The CRs defined for the estimation of these background contributions have a very small contamination from multi-jet events due to the requirement on $\Delta(\phi_{\text{jet}_{1,2}-\mathbf{p}_{\text{T}}^{\text{miss}}})$ and the presence of two or more τ leptons. The signal contribution in these CRs is expected to be at less than 0.1 % for the models considered. Correlations between different samples in the various CRs are taken into account by considering the matrix equation $\mathbf{N}^{\text{data}} = A\boldsymbol{\omega}$, where $\mathbf{N}^{\text{data}}$ is the observed number of data events in each of the CRs defined in Table 2, after subtracting the expected number of multi-jet events and any remaining sub-dominant background contribution, obtained from MC simulation. The matrix A is obtained from the MC expectation for the number of events originating from each of the background contributions (top, W and Z). The vector $\boldsymbol{\omega}$ of scaling factors is then computed by inverting the matrix A. To obtain the uncertainties for the scaling factors, all contributing parameters are varied according to their uncertainties, the procedure is repeated and new scaling factors are obtained. The width of the distribution of each resulting scaling factor is used as its uncertainty. The typical scaling factors obtained with this procedure are between 0.75 and 1, with uncertainty of order 40 %. The multi-jet background expectation is computed in a multi-jet-dominated CR defined by inverting the $\Delta(\phi_{\text{jet}_{1,2}-\mathbf{p}_{\text{T}}^{\text{miss}}})$ requirement and not applying the $m_{\text{T}}^{\tau_1} + m_{\text{T}}^{\tau_2}$ and H_{T} selection. In addition, an upper limit is imposed on the ratio $E_{\text{T}}^{\text{miss}}/m_{\text{eff}}$ to increase the purity of this CR sample.

6.2 Background estimation in the 1τ channel

The number of events from $W+\text{jets}$ and WZ processes in the SR is estimated by scaling the number of corresponding MC events with the ratio of data to MC events in the $W+\text{jets}$ CR. The corresponding scaling factors are computed separately for the cases in which the τ candidates from W/top decays are true τ leptons and for those in which they are misreconstructed from hadronic activity in the final state. It has been checked that the same scaling factors can be applied to both $W+\text{jets}$ and WZ processes. In the case of $W+\text{jets}$ background events with true τ candidates, the charge asymmetry method [66, 67] is used. To estimate the background from top events with true τ candidates, a scaling-factor-based-technique is also used, where the number of b-tagged events in data in the top CR is fitted to a template from MC simulation ('template fit'). For background events in both W/top processes due to fake τ candidates, the matrix method already discussed for the 2τ background estimation is employed, where the parameters in the vector $\boldsymbol{\omega}$ of scaling factors are ω_W^{fake}, ω_W^{true}, $\omega_{\text{top}}^{\text{fake}}$ and $\omega_{\text{top}}^{\text{true}}$. The region dominated by fake τ candidates is defined by $m_{\text{T}} > 110$ GeV and $H_{\text{T}} < 600$ GeV, while the one dominated by true τ candidates is defined by requiring $m_{\text{T}} < 70$ GeV. The values of $\omega_{\text{top}}^{\text{true}}$ obtained from this method and from the template fit are in very good agreement. The factor ω_W^{true} obtained with the charge asymmetry method agrees within 2σ with the one obtained with the matrix inversion method. The difference between the two ω_W^{true} values is then assigned as a systematic uncertainty on the $W+\text{jets}$ background estimation procedure. The background from $Z+\text{jets}$ events is due to events where the Z decays to a pair of neutrinos, and contributes fully to the observed $E_{\text{T}}^{\text{miss}}$. The background contribution in the SR is estimated from data by measuring the data/MC ratio from $Z \to \ell^+\ell^-$ decays in the $Z+\text{jets}$ CR defined in Table 2. Typical scaling factors are between 0.75 and 1.2, with uncertainty of order 20 %. The multi-jet background expectation is computed in the same way as in the 2τ channel.

Table 3 Number of expected background events and data yields in the four final states discussed. Where possible, the uncertainties are separated into statistical and systematic parts. The SM prediction is computed taking into account correlations between the different uncertainties. Also shown are the number of expected signal MC events for one GMSB point ($\Lambda = 50$ TeV, $\tan\beta = 20$), the 95 % confidence level (CL) upper limit on the number of observed (expected) signal events and corresponding cross-section from any new physics scenario that can be set for each of the four final states, taking into account the observed events in the data and the background expectations

–	1τ	2τ	$\tau + \mu$	$\tau + e$
Multi-jet	$0.17 \pm 0.04 \pm 0.11$	$0.17 \pm 0.15 \pm 0.36$	<0.01	0.22 ± 0.30
$W +$ jets	$0.31 \pm 0.16 \pm 0.16$	$1.11 \pm 0.67 \pm 0.30$	$0.27 \pm 0.21 \pm 0.13$	$0.24 \pm 0.17 \pm 0.27$
$Z +$ jets	$0.22 \pm 0.22 \pm 0.09$	$0.36 \pm 0.26 \pm 0.35$	$0.05 \pm 0.05 \pm 0.01$	$0.17 \pm 0.12 \pm 0.05$
Top	$0.61 \pm 0.25 \pm 0.11$	$0.76 \pm 0.31 \pm 0.31$	$0.36 \pm 0.18 \pm 0.26$	$1.41 \pm 0.27 \pm 0.84$
Diboson	<0.05	$0.02 \pm 0.01 \pm 0.07$	$0.11 \pm 0.04 \pm 0.02$	$0.26 \pm 0.12 \pm 0.11$
Drell-Yan	<0.36	$0.49 \pm 0.49 \pm 0.21$	<0.002	<0.002
Total background	$1.31 \pm 0.37 \pm 0.65$	$2.91 \pm 0.89 \pm 0.76$	$0.79 \pm 0.28 \pm 0.39$	$2.31 \pm 0.40 \pm 1.40$
Signal MC Events ($\Lambda = 50$ TeV, $\tan\beta = 20$)	$2.36 \pm 0.30 \pm 0.60$	$4.94 \pm 0.45 \pm 0.74$	$2.48 \pm 0.30 \pm 0.39$	$4.21 \pm 0.38 \pm 0.46$
Data	4	1	1	3
Obs. (exp.) upper limit on number of signal events	7.7 (4.5)	3.2 (4.7)	3.7 (3.4)	5.2 (4.6)
Obs. (exp.) upper limit on visible cross-section (fb)	1.67 (0.95)	0.68 (0.99)	0.78 (0.72)	1.10 (0.98)

6.3 Background estimation in the $\tau + \mu$ and $\tau + e$ channels

The top background contribution consists of events where the muon (electron) candidate is a true muon (electron), and the τ candidate can either be a true τ or a hadronic jet mis-identified as a τ. On the other hand, the $W +$ jets background consists mainly of events where the τ candidate is mis-reconstructed from hadronic activity in the final state. For this reason, the top CR is divided into two subregions: one dominated by true τ candidates, defined by $100\ \text{GeV} < m_{\text{T}}^{e,\mu} < 150\ \text{GeV}$, and one dominated by fake ones ($50\ \text{GeV} < m_{\text{T}}^{e,\mu} < 100\ \text{GeV}$). The same matrix approach already described is then used to estimate the true/fake top and $W +$ jets background contributions to the SR. The scaling factors obtained are about 0.6–0.8, with typical uncertainty of 15 %. The $Z +$ jets background is much smaller than the $W +$ jets one, and it is estimated using MC simulated events. The multi-jet background arises from mis-identified prompt leptons. By comparing the rates of events with and without the lepton isolation requirement, a data-driven estimate is obtained following the method described in Ref. [64].

The contribution from other sources of background considered (Drell-Yan and diboson events) is estimated in all analyses using directly the MC normalizations, without applying any further scaling factor.

Table 3 summarizes the estimated numbers of background events in the SR for each channel.

7 Systematic uncertainties on the background

Various systematic uncertainties were studied and the effect on the number of expected background events in each channel presented was evaluated, following the approach of Refs. [21, 22]. The dominant systematic uncertainties in the different channels are summarized in Table 4.

Table 4 Overview of the major systematic uncertainties and the MC statistical uncertainty for the background estimates in the four channels presented in this paper

Source of uncertainty	1τ	2τ	$\tau + \mu$	$\tau + e$
CR to SR extrapolation	27 %	12 %	26 %	29 %
Jet energy resolution	21 %	6.5 %	5.4 %	13 %
Jet energy scale	20 %	4.8 %	11 %	8.5 %
τ energy scale	10 %	8.5 %	0.3 %	4.3 %
Pile-up modelling	5.1 %	14 %	20 %	3.5 %
MC statistics	21 %	32 %	39 %	46 %

The theoretical uncertainty on the MC-based corrected extrapolation of the $W +$ jets and top backgrounds from the CR into the SR is estimated using alternative MC samples. These MC samples were obtained by varying the renormalization and factorisation scales, the functional form of the factorisation scale and the matching threshold in the parton shower process in the generators used for the simulation of the events described in Sect. 3.

Systematic uncertainties on the jet energy scale (JES) and jet energy resolution (JER) [57] are applied in MC events to the selected jets and propagated throughout the analysis. The difference in the number of expected background events obtained with the nominal MC simulation after applying these changes is taken as the systematic uncertainty.

The effect of the τ energy scale (TES) uncertainty on the expected background is estimated in a similar way. The un-

certainties from the jet and τ energy scale are treated as fully correlated.

The uncertainties on the background estimation due to the τ identification efficiency depend on the τ identification algorithm ("loose" or "medium"), the kinematics of the τ sample and the number of associated tracks. In the different channels, they vary between 2–5 %.

A systematic uncertainty associated with the simulation of pile-up in the MC events is also taken into account, with uncertainties varying between 5–20 %.

The effect of the 1.8 % uncertainty on the luminosity measurement [26, 27] is also considered on the normalization of the background contributions for which scale factors derived from CR regions were not applied (Drell-Yan and diboson in all channels, and $Z+$jets in the $\tau+\mu$ and $\tau+e$ channels).

The total systematic uncertainties obtained in the 1τ, 2τ, $\tau+\mu$ and $\tau+e$ channels are 52 %, 26 %, 49 % and 60 %, respectively. The limited size of the MC samples used for background estimation gives rise to a statistical error ranging from 21 % in the 1τ channel to 46 % in the $\tau+e$ channel.

8 Signal efficiencies and systematic uncertainties

The GMSB signal samples are described in Sect. 3. The total cross-section drops from 100 pb for $\Lambda = 15$ TeV to 5.0 fb for $\Lambda = 80$ TeV. The cross-section for strong production, for which this analysis has the largest efficiency, decreases faster than the cross-sections for slepton and gaugino production, such that for large values of Λ the selection efficiency with respect to the total SUSY production decreases. For the different final states, in the $\tilde{\tau}_1$ NLSP region the efficiency is about 3 % for the 2τ channel, 1 % for the $\tau+\mu$ and $\tau+e$ channels, and 0.5 % for the 1τ channel. In the non-$\tilde{\tau}_1$ NLSP regions and for high Λ values it drops to 0.1–0.2 % for all final states. The total systematic uncertainty on the signal selection from the various sources discussed in Sect. 7 ranges between 10–15 % for the 1τ channel, 15–18 % for the 2τ channel, 8–16 % for the $\tau+\mu$ channel and 11–17 % for the $\tau+e$ channel over the GMSB signal grid.

Theoretical uncertainties related to the GMSB cross-section predictions are obtained using the same procedure as detailed in Ref. [22]. These uncertainties are calculated for individual SUSY production processes and for each model point in the GMSB grid, leading to overall theoretical cross-section uncertainties between 5 % and 25 %.

9 Results

Table 3 summarizes the number of observed data events and the number of expected background events in the four channels, with separate statistical and systematic uncertainties. No significant excess is observed in any of the four signal regions. From the numbers of observed data events and expected background events, upper limits at 95 % confidence level (CL) of 7.7, 3.2, 3.7 and 5.2 signal events from any scenario of physics beyond the SM are calculated in the 1τ, 2τ, $\tau+\mu$ and $\tau+e$ channels, respectively. Using only the background predictions, expected limits of 4.5, 4.7, 3.4 and 4.6 events are obtained for the four channels (1τ, 2τ, $\tau+\mu$ and $\tau+e$). The limits on the number of signal events are computed using the profile likelihood method [68] and the CL_s criterion [69]. Uncertainties on the background and signal expectations are treated as Gaussian-distributed nuisance parameters in the likelihood fit. The signal-event upper limits translate into a 95 % CL observed (expected) upper limit on the visible cross-section for new phenomena for each of the four final states, defined by the product of cross-section, branching fraction, acceptance and efficiency for the selections defined in Sect. 5. The results are summarized in Table 3 for all channels. In order to produce the strongest possible 95 % CL limit on the GMSB model parameters Λ and $\tan\beta$, a statistical combination of the four channels is performed. The likelihood function representing the outcome of the combination includes the statistical independence of the four final states considered. The resulting observed and expected lower limits for the combination of the four final states are shown in Fig. 5. These limits are calculated in-

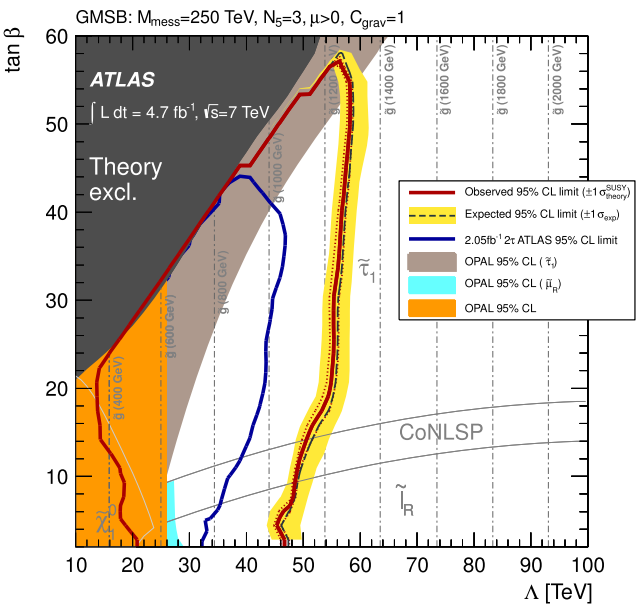

Fig. 5 Expected and observed 95 % CL lower limits on the minimal GMSB model parameters Λ and $\tan\beta$. The *dark grey area* indicates the region which is theoretically excluded due to unphysical sparticle mass values. The different NLSP regions are indicated. In the CoNLSP region the $\tilde{\tau}_1$ and the $\tilde{\ell}_R$ are the NLSPs. Additional model parameters are $M_{\text{mess}} = 250$ TeV, $N_5 = 3$, $\mu > 0$ and $C_{\text{grav}} = 1$. The limits from the OPAL experiment [25] are shown for comparison. The recent ATLAS limit [22] obtained on a subset (2 fb^{-1}) of the 2011 data in the 2τ final state is also shown

cluding all experimental and theoretical uncertainties on the background and signal expectations. Excluding the theoretical uncertainties on the signal cross-section from the limit calculation has a negligible effect on the limits obtained. Figure 5 also includes the limits from OPAL [25] for comparison. The best exclusion from the combination of all final states is obtained for $\Lambda = 58$ TeV for values of $\tan\beta$ between 45 and 55. The results extend previous limits and values of $\Lambda < 54$ TeV are now excluded at 95 % CL, in the regions where the $\tilde{\tau}_1$ is the next-to-lightest SUSY particle ($\tan\beta > 20$).

10 Conclusions

A search for SUSY in final states with jets, $E_{\mathrm{T}}^{\mathrm{miss}}$, light leptons ($e/\mu$) and hadronically decaying τ leptons is performed using 4.7 fb^{-1} of $\sqrt{s} = 7$ TeV pp collision data recorded with the ATLAS detector at the LHC. In the four final states studied, no significant excess is found above the expected SM backgrounds. The results are used to set model-independent 95 % CL upper limits on the number of signal events from new phenomena and corresponding upper limits on the visible cross-section for the four different final states. Limits on the model parameters are set for a minimal GMSB model. A lower limit on the SUSY breaking scale Λ of 54 TeV is determined in the regions where the $\tilde{\tau}_1$ is the next-to-lightest SUSY particle ($\tan\beta > 20$) by statistically combining the result of the four analyses described in this paper. The limit on Λ increases to 58 TeV for $\tan\beta$ between 45 and 55. These results provide the most stringent test to date of GMSB SUSY breaking models in a large part of the parameter space considered.

Acknowledgements We thank CERN for the very successful operation of the LHC, as well as the support staff from our institutions without whom ATLAS could not be operated efficiently.

We acknowledge the support of ANPCyT, Argentina; YerPhI, Armenia; ARC, Australia; BMWF and FWF, Austria; ANAS, Azerbaijan; SSTC, Belarus; CNPq and FAPESP, Brazil; NSERC, NRC and CFI, Canada; CERN; CONICYT, Chile; CAS, MOST and NSFC, China; COLCIENCIAS, Colombia; MSMT CR, MPO CR and VSC CR, Czech Republic; DNRF, DNSRC and Lundbeck Foundation, Denmark; EPLANET and ERC, European Union; IN2P3-CNRS, CEA-DSM/IRFU, France; GNSF, Georgia; BMBF, DFG, HGF, MPG and AvH Foundation, Germany; GSRT, Greece; ISF, MINERVA, GIF, DIP and Benoziyo Center, Israel; INFN, Italy; MEXT and JSPS, Japan; CNRST, Morocco; FOM and NWO, Netherlands; BRF and RCN, Norway; MNiSW, Poland; GRICES and FCT, Portugal; MERYS (MECTS), Romania; MES of Russia and ROSATOM, Russian Federation; JINR; MSTD, Serbia; MSSR, Slovakia; ARRS and MVZT, Slovenia; DST/NRF, South Africa; MICINN, Spain; SRC and Wallenberg Foundation, Sweden; SER, SNSF and Cantons of Bern and Geneva, Switzerland; NSC, Taiwan; TAEK, Turkey; STFC, the Royal Society and Leverhulme Trust, United Kingdom; DOE and NSF, United States of America.

The crucial computing support from all WLCG partners is acknowledged gratefully, in particular from CERN and the ATLAS Tier-1 facilities at TRIUMF (Canada), NDGF (Denmark, Norway, Sweden), CC-IN2P3 (France), KIT/GridKA (Germany), INFN-CNAF (Italy), NL-T1 (Netherlands), PIC (Spain), ASGC (Taiwan), RAL (UK) and BNL (USA) and in the Tier-2 facilities worldwide.

References

1. H. Miyazawa, Prog. Theor. Phys. **36**(6), 1266–1276 (1966)
2. P. Ramond, Phys. Rev. D **3**, 2415–2418 (1971)
3. Y.A. Golfand, E.P. Likhtman, JETP Lett. **13**, 323 (1971)
4. A. Neveu, J.H. Schwarz, Nucl. Phys. B **31**, 86 (1971)
5. A. Neveu, J.H. Schwarz, Phys. Rev. D **4**, 1109 (1971)
6. J. Gervais, B. Sakita, Nucl. Phys. B **34**, 632–639 (1971)
7. D.V. Volkov, V.P. Akulov, Phys. Lett. B **46**, 109 (1973)
8. J. Wess, B. Zumino, Phys. Lett. B **49**, 52 (1974)
9. J. Wess, B. Zumino, Nucl. Phys. B **70**, 39 (1974)
10. M. Dine, W. Fischler, Phys. Lett. B **110**, 227 (1982)
11. L. Alvarez-Gaume, M. Claudson, M. Wise, Nucl. Phys. B **207**, 96 (1982)
12. C.R. Nappi, B.A. Ovrut, Phys. Lett. B **113**, 175 (1982)
13. M. Dine, A.E. Nelson, Phys. Rev. D **48**, 1277 (1993). arXiv:hep-ph/9303230
14. M. Dine, A.E. Nelson, Y. Shirman, Phys. Rev. D **51**, 1362 (1995). arXiv:hep-ph/9408384
15. M. Dine, A.E. Nelson, Y. Nir, Y. Shirman, Phys. Rev. D **53**, 2658 (1996). arXiv:hep-ph/9507378
16. P. Fayet, Phys. Lett. B **64**, 159 (1976)
17. P. Fayet, Phys. Lett. B **69**, 489 (1977)
18. G.R. Farrar, P. Fayet, Phys. Lett. B **76**, 575 (1978)
19. P. Fayet, Phys. Lett. B **84**, 416 (1979)
20. S. Dimopoulos, H. Georgi, Nucl. Phys. B **193**, 150 (1981)
21. ATLAS Collaboration, Phys. Lett. B **714**, 197 (2012). arXiv:1204.3852 [hep-ex]
22. ATLAS Collaboration, Phys. Lett. B **714**, 180 (2012). arXiv:1203.6580 [hep-ex]
23. A. Heister et al. (ALEPH Collaboration), Eur. Phys. J. C **25**, 339 (2002). arXiv:hep-ex/0203024
24. J. Abdallah et al. (DELPHI Collaboration), Eur. Phys. J. C **27**, 153 (2003). arXiv:hep-ex/0303025
25. G. Abbiendi et al. (OPAL Collaboration), Eur. Phys. J. C **46**, 307 (2006). arXiv:hep-ex/0507048
26. ATLAS Collaboration, Updated luminosity determination in pp collisions at $\sqrt{s} = 7$ TeV using the ATLAS detector, ATLAS-CONF-2012-080, 2012. https://cdsweb.cern.ch/record/1460392
27. ATLAS Collaboration, Eur. Phys. J. C **71**, 1630 (2011). arXiv:1101.2185 [hep-ex]
28. ATLAS Collaboration, Further search for supersymmetry at $\sqrt{s} = 7$ TeV in final states with jets, missing transverse momentum and isolated leptons with the ATLAS detector. arXiv:1208.4688 [hep-ex]
29. CMS Collaboration, J. High Energy Phys. **1106**, 077 (2011). arXiv:1104.3168 [hep-ex]
30. CMS Collaboration, Phys. Lett. B **704**, 411 (2011). arXiv:1106.0933 [hep-ex]
31. ATLAS Collaboration, J. Instrum. **3**, S08003 (2008)
32. M.L. Mangano et al., J. High Energy Phys. **0307**, 001 (2003). arXiv:hep-ph/0206293
33. J. Pumplin et al., J. High Energy Phys. **0207**, 012 (2002). arXiv:hep-ph/0201195

34. S. Frixione, B.R. Webber, J. High Energy Phys. **0206**, 029 (2002). arXiv:hep-ph/0204244
35. S. Frixione, P. Nason, B.R. Webber, J. High Energy Phys. **0308**, 007 (2003). arXiv:hep-ph/0305252
36. S. Frixione, E. Laenen, P. Motylinski, B.R. Webber, J. High Energy Phys. **0603**, 092 (2006). arXiv:hep-ph/0512250
37. H.L. Lai, Phys. Rev. D **82**, 074024 (2010)
38. G. Corcella et al., J. High Energy Phys. **0101**, 010 (2001). arXiv:hep-ph/0011363
39. J. Butterworth, J.R. Forshaw, M. Seymour, Z. Phys. C **72**, 637 (1996). arXiv:hep-ph/9601371
40. S. Jadach, Z. Was, R. Decker, J.H. Kuhn, Comput. Phys. Commun. **76**, 361 (1993)
41. P. Golonka et al., Comput. Phys. Commun. **174**, 818 (2006)
42. E. Barberio, Z. Was, Comput. Phys. Commun. **79**, 291 (1994)
43. T. Sjostrand, S. Mrenna, P. Skands, J. High Energy Phys. **0605**, 026 (2006). arXiv:hep-ph/0603175
44. ATLAS Collaboration, ATLAS tunes for PYTHIA6 and PYTHIA8 for MC11, ATLAS-PHYS-PUB-2011-009, July 2011. https://cdsweb.cern.ch/record/1363300
45. A. Sherstnev, R.S. Thorne, Eur. Phys. J. C **55**, 553 (2008). arXiv:0711.2473 [hep-ph]
46. F.E. Paige, S.D. Protopopescu, H. Baer, X. Tata, ISAJET 7.69: A Monte Carlo event generator for pp, $\bar{p}p$, and e^+e^- reactions. arXiv:hep-ph/0312045
47. M. Bahr et al., Eur. Phys. J. C **58**, 639–707 (2008). arXiv:0803.0883v3 [hep-ph]
48. W. Beenakker, R. Hopker, M. Spira, P. Zerwas, Nucl. Phys. B **492**, 51 (1997). arXiv:hep-ph/9610490
49. A. Kulesza, L. Motyka, Phys. Rev. Lett. **102**, 111802 (2009). arXiv:0807.2405 [hep-ph]
50. A. Kulesza, L. Motyka, Phys. Rev. D **80**, 095004 (2009). arXiv:0905.4749 [hep-ph]
51. W. Beenakker et al., J. High Energy Phys. **0912**, 041 (2009). arXiv:0909.4418 [hep-ph]
52. W. Beenakker et al., Int. J. Mod. Phys. A **26**, 2637–2664 (2011). arXiv:1105.1110 [hep-ph]
53. M. Krämer et al., Supersymmetry production cross sections in pp collisions at $\sqrt{s} = 7$ TeV. arXiv:1206.2892 [hep-ph]
54. S. Agostinelli et al. (GEANT4 Collaboration), Nucl. Instrum. Methods Phys. Res. A **506**, 250 (2003)
55. ATLAS Collaboration, Eur. Phys. J. C **70**, 823 (2010). arXiv:1005.4568 [physics.ins-det]
56. M. Cacciari, G.P. Salam, G. Soyez, J. High Energy Phys. **0804**, 063 (2008). arXiv:0802.1189 [hep-ph]
57. ATLAS Collaboration, Jet energy measurement with the ATLAS detector in pp collisions at $\sqrt{s} = 7$ TeV. Eur. Phys. J. C (2011, submitted). arXiv:1112.6426 [hep-ex]
58. ATLAS Collaboration, J. High Energy Phys. **1012**, 060 (2010). arXiv:1010.2130 [hep-ex]
59. ATLAS Collaboration, Eur. Phys. J. C **72**, 1909 (2012). arXiv:1110.3174 [hep-ex]
60. ATLAS Collaboration, Eur. Phys. J. C **72**, 1844 (2012). arXiv:1108.5602 [hep-ex]
61. ATLAS Collaboration, Commissioning of the ATLAS high-performance b-tagging algorithms in the 7 TeV collision data, ATLAS-CONF-2011-102, July 2011. http://cdsweb.cern.ch/record/1369219
62. ATLAS Collaboration, Measurement of the b-tag efficiency in a sample of jets containing muons with 5 fb^{-1} of data from the ATLAS detector, ATLAS-CONF-2012-043, March 2012. http://cdsweb.cern.ch/record/1435197
63. ATLAS Collaboration, Performance of the reconstruction and identification of hadronic tau decays with ATLAS, ATLAS-CONF-2011-152, November 2011. http://cdsweb.cern.ch/record/1398195
64. ATLAS Collaboration, Eur. Phys. J. C **71**, 1577 (2011). arXiv:1012.1792 [hep-ex]
65. ATLAS Collaboration, Eur. Phys. J. C **72**, 1849 (2012). arXiv:1110.1530 [hep-ex]
66. ATLAS Collaboration, Phys. Rev. D **85**, 072004 (2012). arXiv:1109.5141 [hep-ex]
67. ATLAS Collaboration, Eur. Phys. J. C **72**, 2039 (2012). arXiv:1203.4211 [hep-ex]
68. G. Cowan, K. Cranmer, E. Gross, O. Vitells, Eur. Phys. J. C **71**, 1554 (2011). arXiv:1007.1727 [physics.data-an]
69. A.L. Read, J. Phys. G **28**, 2693 (2002)

The ATLAS Collaboration

G. Aad[48], T. Abajyan[21], B. Abbott[111], J. Abdallah[12], S. Abdel Khalek[115], A.A. Abdelalim[49], O. Abdinov[11], R. Aben[105], B. Abi[112], M. Abolins[88], O.S. AbouZeid[158], H. Abramowicz[153], H. Abreu[136], B.S. Acharya[164a,164b], L. Adamczyk[38], D.L. Adams[25], T.N. Addy[56], J. Adelman[176], S. Adomeit[98], P. Adragna[75], T. Adye[129], S. Aefsky[23], J.A. Aguilar-Saavedra[124b,a], M. Agustoni[17], M. Aharrouche[81], S.P. Ahlen[22], F. Ahles[48], A. Ahmad[148], M. Ahsan[41], G. Aielli[133a,133b], T. Akdogan[19a], T.P.A. Åkesson[79], G. Akimoto[155], A.V. Akimov[94], M.S. Alam[2], M.A. Alam[76], J. Albert[169], S. Albrand[55], M. Aleksa[30], I.N. Aleksandrov[64], F. Alessandria[89a], C. Alexa[26a], G. Alexander[153], G. Alexandre[49], T. Alexopoulos[10], M. Alhroob[164a,164c], M. Aliev[16], G. Alimonti[89a], J. Alison[120], B.M.M. Allbrooke[18], P.P. Allport[73], S.E. Allwood-Spiers[53], J. Almond[82], A. Aloisio[102a,102b], R. Alon[172], A. Alonso[79], F. Alonso[70], A. Altheimer[35], B. Alvarez Gonzalez[88], M.G. Alviggi[102a,102b], K. Amako[65], C. Amelung[23], V.V. Ammosov[128,*], S.P. Amor Dos Santos[124a], A. Amorim[124a,b], N. Amram[153], C. Anastopoulos[30], L.S. Ancu[17], N. Andari[115], T. Andeen[35], C.F. Anders[58b], G. Anders[58a], K.J. Anderson[31], A. Andreazza[89a,89b], V. Andrei[58a], M-L. Andrieux[55], X.S. Anduaga[70], S. Angelidakis[9], P. Anger[44], A. Angerami[35], F. Anghinolfi[30], A. Anisenkov[107], N. Anjos[124a], A. Annovi[47], A. Antonaki[9], M. Antonelli[47], A. Antonov[96], J. Antos[144b], F. Anulli[132a], M. Aoki[101], S. Aoun[83], L. Aperio Bella[5], R. Apolle[118,c], G. Arabidze[88], I. Aracena[143], Y. Arai[65], A.T.H. Arce[45], S. Arfaoui[148], J-F. Arguin[93], E. Arik[19a,*], M. Arik[19a], A.J. Armbruster[87], O. Arnaez[81], V. Arnal[80], C. Arnault[115], A. Artamonov[95], G. Artoni[132a,132b], D. Arutinov[21], S. Asai[155], S. Ask[28], B. Åsman[146a,146b], L. Asquith[6],

K. Assamagan[25], A. Astbury[169], M. Atkinson[165], B. Aubert[5], E. Auge[115], K. Augsten[127], M. Aurousseau[145a], G. Avolio[30], R. Avramidou[10], D. Axen[168], G. Azuelos[93,d], Y. Azuma[155], M.A. Baak[30], G. Baccaglioni[89a], C. Bacci[134a,134b], A.M. Bach[15], H. Bachacou[136], K. Bachas[30], M. Backes[49], M. Backhaus[21], J. Backus Mayes[143], E. Badescu[26a], P. Bagnaia[132a,132b], S. Bahinipati[3], Y. Bai[33a], D.C. Bailey[158], T. Bain[158], J.T. Baines[129], O.K. Baker[176], M.D. Baker[25], S. Baker[77], P. Balek[126], E. Banas[39], P. Banerjee[93], Sw. Banerjee[173], D. Banfi[30], A. Bangert[150], V. Bansal[169], H.S. Bansil[18], L. Barak[172], S.P. Baranov[94], A. Barbaro Galtieri[15], T. Barber[48], E.L. Barberio[86], D. Barberis[50a,50b], M. Barbero[21], D.Y. Bardin[64], T. Barillari[99], M. Barisonzi[175], T. Barklow[143], N. Barlow[28], B.M. Barnett[129], R.M. Barnett[15], A. Baroncelli[134a], G. Barone[49], A.J. Barr[118], F. Barreiro[80], J. Barreiro Guimarães da Costa[57], P. Barrillon[115], R. Bartoldus[143], A.E. Barton[71], V. Bartsch[149], A. Basye[165], R.L. Bates[53], L. Batkova[144a], J.R. Batley[28], A. Battaglia[17], M. Battistin[30], F. Bauer[136], H.S. Bawa[143,e], S. Beale[98], T. Beau[78], P.H. Beauchemin[161], R. Beccherle[50a], P. Bechtle[21], H.P. Beck[17], A.K. Becker[175], S. Becker[98], M. Beckingham[138], K.H. Becks[175], A.J. Beddall[19c], A. Beddall[19c], S. Bedikian[176], V.A. Bednyakov[64], C.P. Bee[83], L.J. Beemster[105], M. Begel[25], S. Behar Harpaz[152], P.K. Behera[62], M. Beimforde[99], C. Belanger-Champagne[85], P.J. Bell[49], W.H. Bell[49], G. Bella[153], L. Bellagamba[20a], M. Bellomo[30], A. Belloni[57], O. Beloborodova[107,f], K. Belotskiy[96], O. Beltramello[30], O. Benary[153], D. Benchekroun[135a], K. Bendtz[146a,146b], N. Benekos[165], Y. Benhammou[153], E. Benhar Noccioli[49], J.A. Benitez Garcia[159b], D.P. Benjamin[45], M. Benoit[115], J.R. Bensinger[23], K. Benslama[130], S. Bentvelsen[105], D. Berge[30], E. Bergeaas Kuutmann[42], N. Berger[5], F. Berghaus[169], E. Berglund[105], J. Beringer[15], P. Bernat[77], R. Bernhard[48], C. Bernius[25], T. Berry[76], C. Bertella[83], A. Bertin[20a,20b], F. Bertolucci[122a,122b], M.I. Besana[89a,89b], G.J. Besjes[104], N. Besson[136], S. Bethke[99], W. Bhimji[46], R.M. Bianchi[30], L. Bianchini[23], M. Bianco[72a,72b], O. Biebel[98], S.P. Bieniek[77], K. Bierwagen[54], J. Biesiada[15], M. Biglietti[134a], H. Bilokon[47], M. Bindi[20a,20b], S. Binet[115], A. Bingul[19c], C. Bini[132a,132b], C. Biscarat[178], B. Bittner[99], K.M. Black[22], R.E. Blair[6], J.-B. Blanchard[136], G. Blanchot[30], T. Blazek[144a], I. Bloch[42], C. Blocker[23], J. Blocki[39], A. Blondel[49], W. Blum[81], U. Blumenschein[54], G.J. Bobbink[105], V.B. Bobrovnikov[107], S.S. Bocchetta[79], A. Bocci[45], C.R. Boddy[118], M. Boehler[48], J. Boek[175], N. Boelaert[36], J.A. Bogaerts[30], A. Bogdanchikov[107], A. Bogouch[90,*], C. Bohm[146a], J. Bohm[125], V. Boisvert[76], T. Bold[38], V. Boldea[26a], N.M. Bolnet[136], M. Bomben[78], M. Bona[75], M. Boonekamp[136], S. Bordoni[78], C. Borer[17], A. Borisov[128], G. Borissov[71], I. Borjanovic[13a], M. Borri[82], S. Borroni[87], J. Bortfeldt[98], V. Bortolotto[134a,134b], K. Bos[105], D. Boscherini[20a], M. Bosman[12], H. Boterenbrood[105], J. Bouchami[93], J. Boudreau[123], E.V. Bouhova-Thacker[71], D. Boumediene[34], C. Bourdarios[115], N. Bousson[83], A. Boveia[31], J. Boyd[30], I.R. Boyko[64], I. Bozovic-Jelisavcic[13b], J. Bracinik[18], P. Branchini[134a], A. Brandt[8], G. Brandt[118], O. Brandt[54], U. Bratzler[156], B. Brau[84], J.E. Brau[114], H.M. Braun[175,*], S.F. Brazzale[164a,164c], B. Brelier[158], J. Bremer[30], K. Brendlinger[120], R. Brenner[166], S. Bressler[172], D. Britton[53], F.M. Brochu[28], I. Brock[21], R. Brock[88], F. Broggi[89a], C. Bromberg[88], J. Bronner[99], G. Brooijmans[35], T. Brooks[76], W.K. Brooks[32b], G. Brown[82], H. Brown[8], P.A. Bruckman de Renstrom[39], D. Bruncko[144b], R. Bruneliere[48], S. Brunet[60], A. Bruni[20a], G. Bruni[20a], M. Bruschi[20a], T. Buanes[14], Q. Buat[55], F. Bucci[49], J. Buchanan[118], P. Buchholz[141], R.M. Buckingham[118], A.G. Buckley[46], S.I. Buda[26a], I.A. Budagov[64], B. Budick[108], V. Büscher[81], L. Bugge[117], O. Bulekov[96], A.C. Bundock[73], M. Bunse[43], T. Buran[117], H. Burckhart[30], S. Burdin[73], T. Burgess[14], S. Burke[129], E. Busato[34], P. Bussey[53], C.P. Buszello[166], B. Butler[143], J.M. Butler[22], C.M. Buttar[53], J.M. Butterworth[77], W. Buttinger[28], S. Cabrera Urbán[167], D. Caforio[20a,20b], O. Cakir[4a], P. Calafiura[15], G. Calderini[78], P. Calfayan[98], R. Calkins[106], L.P. Caloba[24a], R. Caloi[132a,132b], D. Calvet[34], S. Calvet[34], R. Camacho Toro[34], P. Camarri[133a,133b], D. Cameron[117], L.M. Caminada[15], R. Caminal Armadans[12], S. Campana[30], M. Campanelli[77], V. Canale[102a,102b], F. Canelli[31,g], A. Canepa[159a], J. Cantero[80], R. Cantrill[76], L. Capasso[102a,102b], M.D.M. Capeans Garrido[30], I. Caprini[26a], M. Caprini[26a], D. Capriotti[99], M. Capua[37a,37b], R. Caputo[81], R. Cardarelli[133a], T. Carli[30], G. Carlino[102a], L. Carminati[89a,89b], B. Caron[85], S. Caron[104], E. Carquin[32b], G.D. Carrillo-Montoya[173], A.A. Carter[75], J.R. Carter[28], J. Carvalho[124a,h], D. Casadei[108], M.P. Casado[12], M. Cascella[122a,122b], C. Caso[50a,50b,*], A.M. Castaneda Hernandez[173,i], E. Castaneda-Miranda[173], V. Castillo Gimenez[167], N.F. Castro[124a], G. Cataldi[72a], P. Catastini[57], A. Catinaccio[30], J.R. Catmore[30], A. Cattai[30], G. Cattani[133a,133b], S. Caughron[88], V. Cavaliere[165], P. Cavalleri[78], D. Cavalli[89a], M. Cavalli-Sforza[12], V. Cavasinni[122a,122b], F. Ceradini[134a,134b], A.S. Cerqueira[24b], A. Cerri[30], L. Cerrito[75], F. Cerutti[47], S.A. Cetin[19b], A. Chafaq[135a], D. Chakraborty[106], I. Chalupkova[126], K. Chan[3], P. Chang[165], B. Chapleau[85], J.D. Chapman[28], J.W. Chapman[87], E. Chareyre[78], D.G. Charlton[18], V. Chavda[82], C.A. Chavez Barajas[30], S. Cheatham[85], S. Chekanov[6], S.V. Chekulaev[159a], G.A. Chelkov[64], M.A. Chelstowska[104], C. Chen[63], H. Chen[25], S. Chen[33c], X. Chen[173], Y. Chen[35], Y. Cheng[31], A. Cheplakov[64], R. Cherkaoui El Moursli[135e], V. Chernyatin[25], E. Cheu[7], S.L. Cheung[158], L. Chevalier[136], G. Chiefari[102a,102b], L. Chikovani[51a,*], J.T. Childers[30], A. Chilingarov[71], G. Chiodini[72a], A.S. Chisholm[18], R.T. Chislett[77], A. Chitan[26a], M.V. Chizhov[64], G. Choudalakis[31], S. Chouridou[137], I.A. Christidi[77], A. Christov[48], D. Chromek-Burckhart[30], M.L. Chu[151], J. Chudoba[125], G. Ciapetti[132a,132b], A.K. Ciftci[4a], R. Ciftci[4a], D. Cinca[34], V. Cindro[74], C. Ciocca[20a,20b], A. Ciocio[15], M. Cirilli[87], P. Cirkovic[13b], Z.H. Citron[172], M. Citterio[89a], M. Ciubancan[26a], A. Clark[49], P.J. Clark[46], R.N. Clarke[15], W. Cleland[123], J.C. Clemens[83], B. Clement[55], C. Clement[146a,146b], Y. Coadou[83], M. Cobal[164a,164c], A. Coccaro[138], J. Cochran[63], L. Coffey[23], J.G. Cogan[143], J. Coggeshall[165], E. Cogneras[178], J. Colas[5], S. Cole[106], A.P. Colijn[105],

N.J. Collins[18], C. Collins-Tooth[53], J. Collot[55], T. Colombo[119a,119b], G. Colon[84], G. Compostella[99], P. Conde Muiño[124a], E. Coniavitis[166], M.C. Conidi[12], S.M. Consonni[89a,89b], V. Consorti[48], S. Constantinescu[26a], C. Conta[119a,119b], G. Conti[57], F. Conventi[102a,j], M. Cooke[15], B.D. Cooper[77], A.M. Cooper-Sarkar[118], K. Copic[15], T. Cornelissen[175], M. Corradi[20a], F. Corriveau[85,k], A. Cortes-Gonzalez[165], G. Cortiana[99], G. Costa[89a], M.J. Costa[167], D. Costanzo[139], D. Côté[30], L. Courneyea[169], G. Cowan[76], C. Cowden[28], B.E. Cox[82], K. Cranmer[108], F. Crescioli[122a,122b], M. Cristinziani[21], G. Crosetti[37a,37b], S. Crépé-Renaudin[55], C.-M. Cuciuc[26a], C. Cuenca Almenar[176], T. Cuhadar Donszelmann[139], M. Curatolo[47], C.J. Curtis[18], C. Cuthbert[150], P. Cwetanski[60], H. Czirr[141], P. Czodrowski[44], Z. Czyczula[176], S. D'Auria[53], M. D'Onofrio[73], A. D'Orazio[132a,132b], M.J. Da Cunha Sargedas De Sousa[124a], C. Da Via[82], W. Dabrowski[38], A. Dafinca[118], T. Dai[87], C. Dallapiccola[84], M. Dam[36], M. Dameri[50a,50b], D.S. Damiani[137], H.O. Danielsson[30], V. Dao[49], G. Darbo[50a], G.L. Darlea[26b], J.A. Dassoulas[42], W. Davey[21], T. Davidek[126], N. Davidson[86], R. Davidson[71], E. Davies[118,c], M. Davies[93], O. Davignon[78], A.R. Davison[77], Y. Davygora[58a], E. Dawe[142], I. Dawson[139], R.K. Daya-Ishmukhametova[23], K. De[8], R. de Asmundis[102a], S. De Castro[20a,20b], S. De Cecco[78], J. de Graat[98], N. De Groot[104], P. de Jong[105], C. De La Taille[115], H. De la Torre[80], F. De Lorenzi[63], L. de Mora[71], L. De Nooij[105], D. De Pedis[132a], A. De Salvo[132a], U. De Sanctis[164a,164c], A. De Santo[149], J.B. De Vivie De Regie[115], G. De Zorzi[132a,132b], W.J. Dearnaley[71], R. Debbe[25], C. Debenedetti[46], B. Dechenaux[55], D.V. Dedovich[64], J. Degenhardt[120], J. Del Peso[80], T. Del Prete[122a,122b], T. Delemontex[55], M. Deliyergiyev[74], A. Dell'Acqua[30], L. Dell'Asta[22], M. Della Pietra[102a,j], D. della Volpe[102a,102b], M. Delmastro[5], P.A. Delsart[55], C. Deluca[105], S. Demers[176], M. Demichev[64], B. Demirkoz[12,l], J. Deng[163], S.P. Denisov[128], D. Derendarz[39], J.E. Derkaoui[135d], F. Derue[78], P. Dervan[73], K. Desch[21], E. Devetak[148], P.O. Deviveiros[105], A. Dewhurst[129], B. DeWilde[148], S. Dhaliwal[158], R. Dhullipudi[25,m], A. Di Ciaccio[133a,133b], L. Di Ciaccio[5], C. Di Donato[102a,102b], A. Di Girolamo[30], B. Di Girolamo[30], S. Di Luise[134a,134b], A. Di Mattia[173], B. Di Micco[30], R. Di Nardo[47], A. Di Simone[133a,133b], R. Di Sipio[20a,20b], M.A. Diaz[32a], E.B. Diehl[87], J. Dietrich[42], T.A. Dietzsch[58a], S. Diglio[86], K. Dindar Yagci[40], J. Dingfelder[21], F. Dinut[26a], C. Dionisi[132a,132b], P. Dita[26a], S. Dita[26a], F. Dittus[30], F. Djama[83], T. Djobava[51b], M.A.B. do Vale[24c], A. Do Valle Wemans[124a,n], T.K.O. Doan[5], M. Dobbs[85], D. Dobos[30], E. Dobson[30,o], J. Dodd[35], C. Doglioni[49], T. Doherty[53], Y. Doi[65,*], J. Dolejsi[126], I. Dolenc[74], Z. Dolezal[126], B.A. Dolgoshein[96,*], T. Dohmae[155], M. Donadelli[24d], J. Donini[34], J. Dopke[30], A. Doria[102a], A. Dos Anjos[173], A. Dotti[122a,122b], M.T. Dova[70], A.D. Doxiadis[105], A.T. Doyle[53], N. Dressnandt[120], M. Dris[10], J. Dubbert[99], S. Dube[15], E. Duchovni[172], G. Duckeck[98], D. Duda[175], A. Dudarev[30], F. Dudziak[63], M. Dührssen[30], I.P. Duerdoth[82], L. Duflot[115], M-A. Dufour[85], L. Duguid[76], M. Dunford[58a], H. Duran Yildiz[4a], R. Duxfield[139], M. Dwuznik[38], F. Dydak[30], M. Düren[52], W.L. Ebenstein[45], J. Ebke[98], S. Eckweiler[81], K. Edmonds[81], W. Edson[2], C.A. Edwards[76], N.C. Edwards[53], W. Ehrenfeld[42], T. Eifert[143], G. Eigen[14], K. Einsweiler[15], E. Eisenhandler[75], T. Ekelof[166], M. El Kacimi[135c], M. Ellert[166], S. Elles[5], F. Ellinghaus[81], K. Ellis[75], N. Ellis[30], J. Elmsheuser[98], M. Elsing[30], D. Emeliyanov[129], R. Engelmann[148], A. Engl[98], B. Epp[61], J. Erdmann[54], A. Ereditato[17], D. Eriksson[146a], J. Ernst[2], M. Ernst[25], J. Ernwein[136], D. Errede[165], S. Errede[165], E. Ertel[81], M. Escalier[115], H. Esch[43], C. Escobar[123], X. Espinal Curull[12], B. Esposito[47], F. Etienne[83], A.I. Etienvre[136], E. Etzion[153], D. Evangelakou[54], H. Evans[60], L. Fabbri[20a,20b], C. Fabre[30], R.M. Fakhrutdinov[128], S. Falciano[132a], Y. Fang[173], M. Fanti[89a,89b], A. Farbin[8], A. Farilla[134a], J. Farley[148], T. Farooque[158], S. Farrell[163], S.M. Farrington[170], P. Farthouat[30], F. Fassi[167], P. Fassnacht[30], D. Fassouliotis[9], B. Fatholahzadeh[158], A. Favareto[89a,89b], L. Fayard[115], S. Fazio[37a,37b], R. Febbraro[34], P. Federic[144a], O.L. Fedin[121], W. Fedorko[88], M. Fehling-Kaschek[48], L. Feligioni[83], D. Fellmann[6], C. Feng[33d], E.J. Feng[6], A.B. Fenyuk[128], J. Ferencei[144b], W. Fernando[6], S. Ferrag[53], J. Ferrando[53], V. Ferrara[42], A. Ferrari[166], P. Ferrari[105], R. Ferrari[119a], D.E. Ferreira de Lima[53], A. Ferrer[167], D. Ferrere[49], C. Ferretti[87], A. Ferretto Parodi[50a,50b], M. Fiascaris[31], F. Fiedler[81], A. Filipčič[74], F. Filthaut[104], M. Fincke-Keeler[169], M.C.N. Fiolhais[124a,h], L. Fiorini[167], A. Firan[40], G. Fischer[42], M.J. Fisher[109], M. Flechl[48], I. Fleck[141], J. Fleckner[81], P. Fleischmann[174], S. Fleischmann[175], T. Flick[175], A. Floderus[79], L.R. Flores Castillo[173], M.J. Flowerdew[99], T. Fonseca Martin[17], A. Formica[136], A. Forti[82], D. Fortin[159a], D. Fournier[115], A.J. Fowler[45], H. Fox[71], P. Francavilla[12], M. Franchini[20a,20b], S. Franchino[119a,119b], D. Francis[30], T. Frank[172], M. Franklin[57], S. Franz[30], M. Fraternali[119a,119b], S. Fratina[120], S.T. French[28], C. Friedrich[42], F. Friedrich[44], R. Froeschl[30], D. Froidevaux[30], J.A. Frost[28], C. Fukunaga[156], E. Fullana Torregrosa[30], B.G. Fulsom[143], J. Fuster[167], C. Gabaldon[30], O. Gabizon[172], T. Gadfort[25], S. Gadomski[49], G. Gagliardi[50a,50b], P. Gagnon[60], C. Galea[98], B. Galhardo[124a], E.J. Gallas[118], V. Gallo[17], B.J. Gallop[129], P. Gallus[125], K.K. Gan[109], Y.S. Gao[143,e], A. Gaponenko[15], F. Garberson[176], M. Garcia-Sciveres[15], C. García[167], J.E. García Navarro[167], R.W. Gardner[31], N. Garelli[30], H. Garitaonandia[105], V. Garonne[30], C. Gatti[47], G. Gaudio[119a], B. Gaur[141], L. Gauthier[136], P. Gauzzi[132a,132b], I.L. Gavrilenko[94], C. Gay[168], G. Gaycken[21], E.N. Gazis[10], P. Ge[33d], Z. Gecse[168], C.N.P. Gee[129], D.A.A. Geerts[105], Ch. Geich-Gimbel[21], K. Gellerstedt[146a,146b], C. Gemme[50a], A. Gemmell[53], M.H. Genest[55], S. Gentile[132a,132b], M. George[54], S. George[76], P. Gerlach[175], A. Gershon[153], C. Geweniger[58a], H. Ghazlane[135b], N. Ghodbane[34], B. Giacobbe[20a], S. Giagu[132a,132b], V. Giakoumopoulou[9], V. Giangiobbe[12], F. Gianotti[30], B. Gibbard[25], A. Gibson[158], S.M. Gibson[30], M. Gilchriese[15], D. Gillberg[29], A.R. Gillman[129], D.M. Gingrich[3,d], J. Ginzburg[153], N. Giokaris[9], M.P. Giordani[164c], R. Giordano[102a,102b], F.M. Giorgi[16], P. Giovannini[99], P.F. Giraud[136], D. Giugni[89a],

M. Giunta[93], P. Giusti[20a], B.K. Gjelsten[117], L.K. Gladilin[97], C. Glasman[80], J. Glatzer[21], A. Glazov[42], K.W. Glitza[175], G.L. Glonti[64], J.R. Goddard[75], J. Godfrey[142], J. Godlewski[30], M. Goebel[42], T. Göpfert[44], C. Goeringer[81], C. Gössling[43], S. Goldfarb[87], T. Golling[176], A. Gomes[124a,b], L.S. Gomez Fajardo[42], R. Gonçalo[76], J. Goncalves Pinto Firmino Da Costa[42], L. Gonella[21], S. González de la Hoz[167], G. Gonzalez Parra[12], M.L. Gonzalez Silva[27], S. Gonzalez-Sevilla[49], J.J. Goodson[148], L. Goossens[30], P.A. Gorbounov[95], H.A. Gordon[25], I. Gorelov[103], G. Gorfine[175], B. Gorini[30], E. Gorini[72a,72b], A. Gorišek[74], E. Gornicki[39], B. Gosdzik[42], A.T. Goshaw[6], M. Gosselink[105], M.I. Gostkin[64], I. Gough Eschrich[163], M. Gouighri[135a], D. Goujdami[135c], M.P. Goulette[49], A.G. Goussiou[138], C. Goy[5], S. Gozpinar[23], I. Grabowska-Bold[38], P. Grafström[20a,20b], K-J. Grahn[42], E. Gramstad[117], F. Grancagnolo[72a], S. Grancagnolo[16], V. Grassi[148], V. Gratchev[121], N. Grau[35], H.M. Gray[30], J.A. Gray[148], E. Graziani[134a], O.G. Grebenyuk[121], T. Greenshaw[73], Z.D. Greenwood[25,m], K. Gregersen[36], I.M. Gregor[42], P. Grenier[143], J. Griffiths[8], N. Grigalashvili[64], A.A. Grillo[137], S. Grinstein[12], Ph. Gris[34], Y.V. Grishkevich[97], J.-F. Grivaz[115], E. Gross[172], J. Grosse-Knetter[54], J. Groth-Jensen[172], K. Grybel[141], D. Guest[176], C. Guicheney[34], S. Guindon[54], U. Gul[53], J. Gunther[125], B. Guo[158], J. Guo[35], P. Gutierrez[111], N. Guttman[153], O. Gutzwiller[173], C. Guyot[136], C. Gwenlan[118], C.B. Gwilliam[73], A. Haas[108], S. Haas[30], C. Haber[15], H.K. Hadavand[8], D.R. Hadley[18], P. Haefner[21], F. Hahn[30], S. Haider[30], Z. Hajduk[39], H. Hakobyan[177], D. Hall[118], K. Hamacher[175], P. Hamal[113], K. Hamano[86], M. Hamer[54], A. Hamilton[145b,p], S. Hamilton[161], L. Han[33b], K. Hanagaki[116], K. Hanawa[160], M. Hance[15], C. Handel[81], P. Hanke[58a], J.R. Hansen[36], J.B. Hansen[36], J.D. Hansen[36], P.H. Hansen[36], P. Hansson[143], K. Hara[160], G.A. Hare[137], T. Harenberg[175], S. Harkusha[90], D. Harper[87], R.D. Harrington[46], O.M. Harris[138], J. Hartert[48], F. Hartjes[105], T. Haruyama[65], A. Harvey[56], S. Hasegawa[101], Y. Hasegawa[140], S. Hassani[136], S. Haug[17], M. Hauschild[30], R. Hauser[88], M. Havranek[21], C.M. Hawkes[18], R.J. Hawkings[30], A.D. Hawkins[79], T. Hayakawa[66], T. Hayashi[160], D. Hayden[76], C.P. Hays[118], H.S. Hayward[73], S.J. Haywood[129], S.J. Head[18], V. Hedberg[79], L. Heelan[8], S. Heim[88], B. Heinemann[15], S. Heisterkamp[36], L. Helary[22], C. Heller[98], M. Heller[30], S. Hellman[146a,146b], D. Hellmich[21], C. Helsens[12], R.C.W. Henderson[71], M. Henke[58a], A. Henrichs[176], A.M. Henriques Correia[30], S. Henrot-Versille[115], C. Hensel[54], T. Henß[175], C.M. Hernandez[8], Y. Hernández Jiménez[167], R. Herrberg[16], G. Herten[48], R. Hertenberger[98], L. Hervas[30], G.G. Hesketh[77], N.P. Hessey[105], E. Higón-Rodriguez[167], J.C. Hill[28], K.H. Hiller[42], S. Hillert[21], S.J. Hillier[18], I. Hinchliffe[15], E. Hines[120], M. Hirose[116], F. Hirsch[43], D. Hirschbuehl[175], J. Hobbs[148], N. Hod[153], M.C. Hodgkinson[139], P. Hodgson[139], A. Hoecker[30], M.R. Hoeferkamp[103], J. Hoffman[40], D. Hoffmann[83], M. Hohlfeld[81], M. Holder[141], S.O. Holmgren[146a], T. Holy[127], J.L. Holzbauer[88], T.M. Hong[120], L. Hooft van Huysduynen[108], S. Horner[48], J-Y. Hostachy[55], S. Hou[151], A. Hoummada[135a], J. Howard[118], J. Howarth[82], I. Hristova[16], J. Hrivnac[115], T. Hryn'ova[5], P.J. Hsu[81], S.-C. Hsu[15], D. Hu[35], Z. Hubacek[127], F. Hubaut[83], F. Huegging[21], A. Huettmann[42], T.B. Huffman[118], E.W. Hughes[35], G. Hughes[71], M. Huhtinen[30], M. Hurwitz[15], N. Huseynov[64,q], J. Huston[88], J. Huth[57], G. Iacobucci[49], G. Iakovidis[10], M. Ibbotson[82], I. Ibragimov[141], L. Iconomidou-Fayard[115], J. Idarraga[115], P. Iengo[102a], O. Igonkina[105], Y. Ikegami[65], M. Ikeno[65], D. Iliadis[154], N. Ilic[158], T. Ince[99], J. Inigo-Golfin[30], P. Ioannou[9], M. Iodice[134a], K. Iordanidou[9], V. Ippolito[132a,132b], A. Irles Quiles[167], C. Isaksson[166], M. Ishino[67], M. Ishitsuka[157], R. Ishmukhametov[109], C. Issever[118], S. Istin[19a], A.V. Ivashin[128], W. Iwanski[39], H. Iwasaki[65], J.M. Izen[41], V. Izzo[102a], B. Jackson[120], J.N. Jackson[73], P. Jackson[1], M.R. Jaekel[30], V. Jain[60], K. Jakobs[48], S. Jakobsen[36], T. Jakoubek[125], J. Jakubek[127], D.O. Jamin[151], D.K. Jana[111], E. Jansen[77], H. Jansen[30], A. Jantsch[99], M. Janus[48], G. Jarlskog[79], L. Jeanty[57], I. Jen-La Plante[31], D. Jennens[86], P. Jenni[30], A.E. Loevschall-Jensen[36], P. Ježˇ[36], S. Jézéquel[5], M.K. Jha[20a], H. Ji[173], W. Ji[81], J. Jia[148], Y. Jiang[33b], M. Jimenez Belenguer[42], S. Jin[33a], O. Jinnouchi[157], M.D. Joergensen[36], D. Joffe[40], M. Johansen[146a,146b], K.E. Johansson[146a], P. Johansson[139], S. Johnert[42], K.A. Johns[7], K. Jon-And[146a,146b], G. Jones[170], R.W.L. Jones[71], T.J. Jones[73], C. Joram[30], P.M. Jorge[124a], K.D. Joshi[82], J. Jovicevic[147], T. Jovin[13b], X. Ju[173], C.A. Jung[43], R.M. Jungst[30], V. Juranek[125], P. Jussel[61], A. Juste Rozas[12], S. Kabana[17], M. Kaci[167], A. Kaczmarska[39], P. Kadlecik[36], M. Kado[115], H. Kagan[109], M. Kagan[57], E. Kajomovitz[152], S. Kalinin[175], L.V. Kalinovskaya[64], S. Kama[40], N. Kanaya[155], M. Kaneda[30], S. Kaneti[28], T. Kanno[157], V.A. Kantserov[96], J. Kanzaki[65], B. Kaplan[108], A. Kapliy[31], J. Kaplon[30], D. Kar[53], M. Karagounis[21], K. Karakostas[10], M. Karnevskiy[42], V. Kartvelishvili[71], A.N. Karyukhin[128], L. Kashif[173], G. Kasieczka[58b], R.D. Kass[109], A. Kastanas[14], M. Kataoka[5], Y. Kataoka[155], E. Katsoufis[10], J. Katzy[42], V. Kaushik[7], K. Kawagoe[69], T. Kawamoto[155], G. Kawamura[81], M.S. Kayl[105], S. Kazama[155], V.A. Kazanin[107], M.Y. Kazarinov[64], R. Keeler[169], P.T. Keener[120], R. Kehoe[40], M. Keil[54], G.D. Kekelidze[64], J.S. Keller[138], M. Kenyon[53], O. Kepka[125], N. Kerschen[30], B.P. Kerševan[74], S. Kersten[175], K. Kessoku[155], J. Keung[158], F. Khalil-zada[11], H. Khandanyan[146a,146b], A. Khanov[112], D. Kharchenko[64], A. Khodinov[96], A. Khomich[58a], T.J. Khoo[28], G. Khoriauli[21], A. Khoroshilov[175], V. Khovanskiy[95], E. Khramov[64], J. Khubua[51b], H. Kim[146a,146b], S.H. Kim[160], N. Kimura[171], O. Kind[16], B.T. King[73], M. King[66], R.S.B. King[118], J. Kirk[129], A.E. Kiryunin[99], T. Kishimoto[66], D. Kisielewska[38], T. Kitamura[66], T. Kittelmann[123], K. Kiuchi[160], E. Kladiva[144b], M. Klein[73], U. Klein[73], K. Kleinknecht[81], M. Klemetti[85], A. Klier[172], P. Klimek[146a,146b], A. Klimentov[25], R. Klingenberg[43], J.A. Klinger[82], E.B. Klinkby[36], T. Klioutchnikova[30], P.F. Klok[104], S. Klous[105], E.-E. Kluge[58a], T. Kluge[73], P. Kluit[105], S. Kluth[99], E. Kneringer[61], E.B.F.G. Knoops[83], A. Knue[54], B.R. Ko[45], T. Kobayashi[155], M. Kobel[44], M. Kocian[143], P. Kodys[126],

K. Köneke[30], A.C. König[104], S. Koenig[81], L. Köpke[81], F. Koetsveld[104], P. Koevesarki[21], T. Koffas[29], E. Koffeman[105], L.A. Kogan[118], S. Kohlmann[175], F. Kohn[54], Z. Kohout[127], T. Kohriki[65], T. Koi[143], G.M. Kolachev[107,*], H. Kolanoski[16], V. Kolesnikov[64], I. Koletsou[89a], J. Koll[88], A.A. Komar[94], Y. Komori[155], T. Kondo[65], T. Kono[42,r], A.I. Kononov[48], R. Konoplich[108,s], N. Konstantinidis[77], R. Kopeliansky[152], S. Koperny[38], K. Korcyl[39], K. Kordas[154], A. Korn[118], A. Korol[107], I. Korolkov[12], E.V. Korolkova[139], V.A. Korotkov[128], O. Kortner[99], S. Kortner[99], V.V. Kostyukhin[21], S. Kotov[99], V.M. Kotov[64], A. Kotwal[45], C. Kourkoumelis[9], V. Kouskoura[154], A. Koutsman[159a], R. Kowalewski[169], T.Z. Kowalski[38], W. Kozanecki[136], A.S. Kozhin[128], V. Kral[127], V.A. Kramarenko[97], G. Kramberger[74], M.W. Krasny[78], A. Krasznahorkay[108], J.K. Kraus[21], S. Kreiss[108], F. Krejci[127], J. Kretzschmar[73], N. Krieger[54], P. Krieger[158], K. Kroeninger[54], H. Kroha[99], J. Kroll[120], J. Kroseberg[21], J. Krstic[13a], U. Kruchonak[64], H. Krüger[21], T. Kruker[17], N. Krumnack[63], Z.V. Krumshteyn[64], M.K. Kruse[45], T. Kubota[86], S. Kuday[4a], S. Kuehn[48], A. Kugel[58c], T. Kuhl[42], D. Kuhn[61], V. Kukhtin[64], Y. Kulchitsky[90], S. Kuleshov[32b], C. Kummer[98], M. Kuna[78], J. Kunkle[120], A. Kupco[125], H. Kurashige[66], M. Kurata[160], Y.A. Kurochkin[90], V. Kus[125], E.S. Kuwertz[147], M. Kuze[157], J. Kvita[142], R. Kwee[16], A. La Rosa[49], L. La Rotonda[37a,37b], L. Labarga[80], J. Labbe[5], S. Lablak[135a], C. Lacasta[167], F. Lacava[132a,132b], J. Lacey[29], H. Lacker[16], D. Lacour[78], V.R. Lacuesta[167], E. Ladygin[64], R. Lafaye[5], B. Laforge[78], T. Lagouri[176], S. Lai[48], E. Laisne[55], M. Lamanna[30], L. Lambourne[77], C.L. Lampen[7], W. Lampl[7], E. Lancon[136], U. Landgraf[48], M.P.J. Landon[75], V.S. Lang[58a], C. Lange[42], A.J. Lankford[163], F. Lanni[25], K. Lantzsch[175], S. Laplace[78], C. Lapoire[21], J.F. Laporte[136], T. Lari[89a], A. Larner[118], M. Lassnig[30], P. Laurelli[47], V. Lavorini[37a,37b], W. Lavrijsen[15], P. Laycock[73], O. Le Dortz[78], E. Le Guirriec[83], E. Le Menedeu[12], T. LeCompte[6], F. Ledroit-Guillon[55], H. Lee[105], J.S.H. Lee[116], S.C. Lee[151], L. Lee[176], M. Lefebvre[169], M. Legendre[136], F. Legger[98], C. Leggett[15], M. Lehmacher[21], G. Lehmann Miotto[30], M.A.L. Leite[24d], R. Leitner[126], D. Lellouch[172], B. Lemmer[54], V. Lendermann[58a], K.J.C. Leney[145b], T. Lenz[105], G. Lenzen[175], B. Lenzi[30], K. Leonhardt[44], S. Leontsinis[10], F. Lepold[58a], C. Leroy[93], J-R. Lessard[169], C.G. Lester[28], C.M. Lester[120], J. Levêque[5], D. Levin[87], L.J. Levinson[172], A. Lewis[118], G.H. Lewis[108], A.M. Leyko[21], M. Leyton[16], B. Li[83], H. Li[148], H.L. Li[31], S. Li[33b,t], X. Li[87], Z. Liang[118,u], H. Liao[34], B. Liberti[133a], P. Lichard[30], M. Lichtnecker[98], K. Lie[165], W. Liebig[14], C. Limbach[21], A. Limosani[86], M. Limper[62], S.C. Lin[151,v], F. Linde[105], J.T. Linnemann[88], E. Lipeles[120], A. Lipniacka[14], T.M. Liss[165], D. Lissauer[25], A. Lister[49], A.M. Litke[137], C. Liu[29], D. Liu[151], H. Liu[87], J.B. Liu[87], L. Liu[87], M. Liu[33b], Y. Liu[33b], M. Livan[119a,119b], S.S.A. Livermore[118], A. Lleres[55], J. Llorente Merino[80], S.L. Lloyd[75], E. Lobodzinska[42], P. Loch[7], W.S. Lockman[137], T. Loddenkoetter[21], F.K. Loebinger[82], A. Loginov[176], C.W. Loh[168], T. Lohse[16], K. Lohwasser[48], M. Lokajicek[125], V.P. Lombardo[5], R.E. Long[71], L. Lopes[124a], D. Lopez Mateos[57], J. Lorenz[98], N. Lorenzo Martinez[115], M. Losada[162], P. Loscutoff[15], F. Lo Sterzo[132a,132b], M.J. Losty[159a,*], X. Lou[41], A. Lounis[115], K.F. Loureiro[162], J. Love[6], P.A. Love[71], A.J. Lowe[143,e], F. Lu[33a], H.J. Lubatti[138], C. Luci[132a,132b], A. Lucotte[55], A. Ludwig[44], D. Ludwig[42], I. Ludwig[48], J. Ludwig[48], F. Luehring[60], G. Luijckx[105], W. Lukas[61], L. Luminari[132a], E. Lund[117], B. Lund-Jensen[147], B. Lundberg[79], J. Lundberg[146a,146b], O. Lundberg[146a,146b], J. Lundquist[36], M. Lungwitz[81], D. Lynn[25], E. Lytken[79], H. Ma[25], L.L. Ma[173], G. Maccarrone[47], A. Macchiolo[99], B. Maček[74], J. Machado Miguens[124a], R. Mackeprang[36], R.J. Madaras[15], H.J. Maddocks[71], W.F. Mader[44], R. Maenner[58c], T. Maeno[25], P. Mättig[175], S. Mättig[81], L. Magnoni[163], E. Magradze[54], K. Mahboubi[48], J. Mahlstedt[105], S. Mahmoud[73], G. Mahout[18], C. Maiani[136], C. Maidantchik[24a], A. Maio[124a,b], S. Majewski[25], Y. Makida[65], N. Makovec[115], P. Mal[136], B. Malaescu[30], Pa. Malecki[39], P. Malecki[39], V.P. Maleev[121], F. Malek[55], U. Mallik[62], D. Malon[6], C. Malone[143], S. Maltezos[10], V. Malyshev[107], S. Malyukov[30], R. Mameghani[98], J. Mamuzic[13b], A. Manabe[65], L. Mandelli[89a], I. Mandić[74], R. Mandrysch[16], J. Maneira[124a], A. Manfredini[99], P.S. Mangeard[88], L. Manhaes de Andrade Filho[24b], J.A. Manjarres Ramos[136], A. Mann[54], P.M. Manning[137], A. Manousakis-Katsikakis[9], B. Mansoulie[136], A. Mapelli[30], L. Mapelli[30], L. March[167], J.F. Marchand[29], F. Marchese[133a,133b], G. Marchiori[78], M. Marcisovsky[125], C.P. Marino[169], F. Marroquim[24a], Z. Marshall[30], F.K. Martens[158], L.F. Marti[17], S. Marti-Garcia[167], B. Martin[30], B. Martin[88], J.P. Martin[93], T.A. Martin[18], V.J. Martin[46], B. Martin dit Latour[49], S. Martin-Haugh[149], M. Martinez[12], V. Martinez Outschoorn[57], A.C. Martyniuk[169], M. Marx[82], F. Marzano[132a], A. Marzin[111], L. Masetti[81], T. Mashimo[155], R. Mashinistov[94], J. Masik[82], A.L. Maslennikov[107], I. Massa[20a,20b], G. Massaro[105], N. Massol[5], P. Mastrandrea[148], A. Mastroberardino[37a,37b], T. Masubuchi[155], P. Matricon[115], H. Matsunaga[155], T. Matsushita[66], C. Mattravers[118,c], J. Maurer[83], S.J. Maxfield[73], D.A. Maximov[107,f], A. Mayne[139], R. Mazini[151], M. Mazur[21], L. Mazzaferro[133a,133b], M. Mazzanti[89a], J. Mc Donald[85], S.P. Mc Kee[87], A. McCarn[165], R.L. McCarthy[148], T.G. McCarthy[29], N.A. McCubbin[129], K.W. McFarlane[56,*], J.A. Mcfayden[139], G. Mchedlidze[51b], T. Mclaughlan[18], S.J. McMahon[129], R.A. McPherson[169,k], A. Meade[84], J. Mechnich[105], M. Mechtel[175], M. Medinnis[42], R. Meera-Lebbai[111], T. Meguro[116], S. Mehlhase[36], A. Mehta[73], K. Meier[58a], B. Meirose[79], C. Melachrinos[31], B.R. Mellado Garcia[173], F. Meloni[89a,89b], L. Mendoza Navas[162], Z. Meng[151,w], A. Mengarelli[20a,20b], S. Menke[99], E. Meoni[161], K.M. Mercurio[57], P. Mermod[49], L. Merola[102a,102b], C. Meroni[89a], F.S. Merritt[31], H. Merritt[109], A. Messina[30,x], J. Metcalfe[25], A.S. Mete[163], C. Meyer[81], C. Meyer[31], J-P. Meyer[136], J. Meyer[174], J. Meyer[54], T.C. Meyer[30], S. Michal[30], L. Micu[26a], R.P. Middleton[129], S. Migas[73], L. Mijović[136], G. Mikenberg[172], M. Mikestikova[125], M. Mikuž[74], D.W. Miller[31], R.J. Miller[88], W.J. Mills[168], C. Mills[57], A. Milov[172], D.A. Milstead[146a,146b], D. Milstein[172], A.A. Minaenko[128], M. Miñano Moya[167], I.A. Minashvili[64], A.I. Mincer[108], B. Mindur[38], M. Mineev[64], Y. Ming[173], L.M. Mir[12],

G. Mirabelli[132a], J. Mitrevski[137], V.A. Mitsou[167], S. Mitsui[65], P.S. Miyagawa[139], J.U. Mjörnmark[79], T. Moa[146a,146b], V. Moeller[28], K. Mönig[42], N. Möser[21], S. Mohapatra[148], W. Mohr[48], R. Moles-Valls[167], A. Molfetas[30], J. Monk[77], E. Monnier[83], J. Montejo Berlingen[12], F. Monticelli[70], S. Monzani[20a,20b], R.W. Moore[3], G.F. Moorhead[86], C. Mora Herrera[49], A. Moraes[53], N. Morange[136], J. Morel[54], G. Morello[37a,37b], D. Moreno[81], M. Moreno Llácer[167], P. Morettini[50a], M. Morgenstern[44], M. Morii[57], A.K. Morley[30], G. Mornacchi[30], J.D. Morris[75], L. Morvaj[101], H.G. Moser[99], M. Mosidze[51b], J. Moss[109], R. Mount[143], E. Mountricha[10,y], S.V. Mouraviev[94,*], E.J.W. Moyse[84], F. Mueller[58a], J. Mueller[123], K. Mueller[21], T.A. Müller[98], T. Mueller[81], D. Muenstermann[30], Y. Munwes[153], W.J. Murray[129], I. Mussche[105], E. Musto[102a,102b], A.G. Myagkov[128], M. Myska[125], O. Nackenhorst[54], J. Nadal[12], K. Nagai[160], R. Nagai[157], K. Nagano[65], A. Nagarkar[109], Y. Nagasaka[59], M. Nagel[99], A.M. Nairz[30], Y. Nakahama[30], K. Nakamura[155], T. Nakamura[155], I. Nakano[110], G. Nanava[21], A. Napier[161], R. Narayan[58b], M. Nash[77,c], T. Nattermann[21], T. Naumann[42], G. Navarro[162], H.A. Neal[87], P.Yu. Nechaeva[94], T.J. Neep[82], A. Negri[119a,119b], G. Negri[30], M. Negrini[20a], S. Nektarijevic[49], A. Nelson[163], T.K. Nelson[143], S. Nemecek[125], P. Nemethy[108], A.A. Nepomuceno[24a], M. Nessi[30,z], M.S. Neubauer[165], M. Neumann[175], A. Neusiedl[81], R.M. Neves[108], P. Nevski[25], F.M. Newcomer[120], P.R. Newman[18], V. Nguyen Thi Hong[136], R.B. Nickerson[118], R. Nicolaidou[136], B. Nicquevert[30], F. Niedercorn[115], J. Nielsen[137], N. Nikiforou[35], A. Nikiforov[16], V. Nikolaenko[128], I. Nikolic-Audit[78], K. Nikolics[49], K. Nikolopoulos[18], H. Nilsen[48], P. Nilsson[8], Y. Ninomiya[155], A. Nisati[132a], R. Nisius[99], T. Nobe[157], L. Nodulman[6], M. Nomachi[116], I. Nomidis[154], S. Norberg[111], M. Nordberg[30], P.R. Norton[129], J. Novakova[126], M. Nozaki[65], L. Nozka[113], I.M. Nugent[159a], A.-E. Nuncio-Quiroz[21], G. Nunes Hanninger[86], T. Nunnemann[98], E. Nurse[77], B.J. O'Brien[46], D.C. O'Neil[142], V. O'Shea[53], L.B. Oakes[98], F.G. Oakham[29,d], H. Oberlack[99], J. Ocariz[78], A. Ochi[66], S. Oda[69], S. Odaka[65], J. Odier[83], H. Ogren[60], A. Oh[82], S.H. Oh[45], C.C. Ohm[30], T. Ohshima[101], W. Okamura[116], H. Okawa[25], Y. Okumura[31], T. Okuyama[155], A. Olariu[26a], A.G. Olchevski[64], S.A. Olivares Pino[32a], M. Oliveira[124a,h], D. Oliveira Damazio[25], E. Oliver Garcia[167], D. Olivito[120], A. Olszewski[39], J. Olszowska[39], A. Onofre[124a,aa], P.U.E. Onyisi[31], C.J. Oram[159a], M.J. Oreglia[31], Y. Oren[153], D. Orestano[134a,134b], N. Orlando[72a,72b], I. Orlov[107], C. Oropeza Barrera[53], R.S. Orr[158], B. Osculati[50a,50b], R. Ospanov[120], C. Osuna[12], G. Otero y Garzon[27], J.P. Ottersbach[105], M. Ouchrif[135d], E.A. Ouellette[169], F. Ould-Saada[117], A. Ouraou[136], Q. Ouyang[33a], A. Ovcharova[15], M. Owen[82], S. Owen[139], V.E. Ozcan[19a], N. Ozturk[8], A. Pacheco Pages[12], C. Padilla Aranda[12], S. Pagan Griso[15], E. Paganis[139], C. Pahl[99], F. Paige[25], P. Pais[84], K. Pajchel[117], G. Palacino[159b], C.P. Paleari[7], S. Palestini[30], D. Pallin[34], A. Palma[124a], J.D. Palmer[18], Y.B. Pan[173], E. Panagiotopoulou[10], J.G. Panduro Vazquez[76], P. Pani[105], N. Panikashvili[87], S. Panitkin[25], D. Pantea[26a], A. Papadelis[146a], Th.D. Papadopoulou[10], A. Paramonov[6], D. Paredes Hernandez[34], W. Park[25,ab], M.A. Parker[28], F. Parodi[50a,50b], J.A. Parsons[35], U. Parzefall[48], S. Pashapour[54], E. Pasqualucci[132a], S. Passaggio[50a], A. Passeri[134a], F. Pastore[134a,134b,*], Fr. Pastore[76], G. Pásztor[49,ac], S. Pataraia[175], N. Patel[150], J.R. Pater[82], S. Patricelli[102a,102b], T. Pauly[30], M. Pecsy[144a], S. Pedraza Lopez[167], M.I. Pedraza Morales[173], S.V. Peleganchuk[107], D. Pelikan[166], H. Peng[33b], B. Penning[31], A. Penson[35], J. Penwell[60], M. Perantoni[24a], K. Perez[35,ad], T. Perez Cavalcanti[42], E. Perez Codina[159a], M.T. Pérez García-Estañ[167], V. Perez Reale[35], L. Perini[89a,89b], H. Pernegger[30], R. Perrino[72a], P. Perrodo[5], V.D. Peshekhonov[64], K. Peters[30], B.A. Petersen[30], J. Petersen[30], T.C. Petersen[36], E. Petit[5], A. Petridis[154], C. Petridou[154], E. Petrolo[132a], F. Petrucci[134a,134b], D. Petschull[42], M. Petteni[142], R. Pezoa[32b], A. Phan[86], P.W. Phillips[129], G. Piacquadio[30], A. Picazio[49], E. Piccaro[75], M. Piccinini[20a,20b], S.M. Piec[42], R. Piegaia[27], D.T. Pignotti[109], J.E. Pilcher[31], A.D. Pilkington[82], J. Pina[124a,b], M. Pinamonti[164a,164c], A. Pinder[118], J.L. Pinfold[3], B. Pinto[124a], C. Pizio[89a,89b], M. Plamondon[169], M.-A. Pleier[25], E. Plotnikova[64], A. Poblaguev[25], S. Poddar[58a], F. Podlyski[34], L. Poggioli[115], D. Pohl[21], M. Pohl[49], G. Polesello[119a], A. Policicchio[37a,37b], A. Polini[20a], J. Poll[75], V. Polychronakos[25], D. Pomeroy[23], K. Pommès[30], L. Pontecorvo[132a], B.G. Pope[88], G.A. Popeneciu[26a], D.S. Popovic[13a], A. Poppleton[30], X. Portell Bueso[30], G.E. Pospelov[99], S. Pospisil[127], I.N. Potrap[99], C.J. Potter[149], C.T. Potter[114], G. Poulard[30], J. Poveda[60], V. Pozdnyakov[64], R. Prabhu[77], P. Pralavorio[83], A. Pranko[15], S. Prasad[30], R. Pravahan[25], S. Prell[63], K. Pretzl[17], D. Price[60], J. Price[73], L.E. Price[6], D. Prieur[123], M. Primavera[72a], K. Prokofiev[108], F. Prokoshin[32b], S. Protopopescu[25], J. Proudfoot[6], X. Prudent[44], M. Przybycien[38], H. Przysiezniak[5], S. Psoroulas[21], E. Ptacek[114], E. Pueschel[84], J. Purdham[87], M. Purohit[25,ab], P. Puzo[115], Y. Pylypchenko[62], J. Qian[87], A. Quadt[54], D.R. Quarrie[15], W.B. Quayle[173], F. Quinonez[32a], M. Raas[104], V. Radeka[25], V. Radescu[42], P. Radloff[114], T. Rador[19a], F. Ragusa[89a,89b], G. Rahal[178], A.M. Rahimi[109], D. Rahm[25], S. Rajagopalan[25], M. Rammensee[48], M. Rammes[141], A.S. Randle-Conde[40], K. Randrianarivony[29], F. Rauscher[98], T.C. Rave[48], M. Raymond[30], A.L. Read[117], D.M. Rebuzzi[119a,119b], A. Redelbach[174], G. Redlinger[25], R. Reece[120], K. Reeves[41], E. Reinherz-Aronis[153], A. Reinsch[114], I. Reisinger[43], C. Rembser[30], Z.L. Ren[151], A. Renaud[115], M. Rescigno[132a], S. Resconi[89a], B. Resende[136], P. Reznicek[98], R. Rezvani[158], R. Richter[99], E. Richter-Was[5,ae], M. Ridel[78], M. Rijpstra[105], M. Rijssenbeek[148], A. Rimoldi[119a,119b], L. Rinaldi[20a], R.R. Rios[40], I. Riu[12], G. Rivoltella[89a,89b], F. Rizatdinova[112], E. Rizvi[75], S.H. Robertson[85,k], A. Robichaud-Veronneau[118], D. Robinson[28], J.E.M. Robinson[82], A. Robson[53], J.G. Rocha de Lima[106], C. Roda[122a,122b], D. Roda Dos Santos[30], A. Roe[54], S. Roe[30], O. Røhne[117], S. Rolli[161], A. Romaniouk[96], M. Romano[20a,20b], G. Romeo[27], E. Romero Adam[167], N. Rompotis[138], L. Roos[78], E. Ros[167], S. Rosati[132a], K. Rosbach[49], A. Rose[149], M. Rose[76], G.A. Rosenbaum[158], E.I. Rosenberg[63], P.L. Rosendahl[14], O. Rosenthal[141], L. Rosselet[49], V. Rossetti[12], E. Rossi[132a,132b], L.P. Rossi[50a],

M. Rotaru[26a], I. Roth[172], J. Rothberg[138], D. Rousseau[115], C.R. Royon[136], A. Rozanov[83], Y. Rozen[152], X. Ruan[33a,af], F. Rubbo[12], I. Rubinskiy[42], N. Ruckstuhl[105], V.I. Rud[97], C. Rudolph[44], G. Rudolph[61], F. Rühr[7], A. Ruiz-Martinez[63], L. Rumyantsev[64], Z. Rurikova[48], N.A. Rusakovich[64], A. Ruschke[98], J.P. Rutherfoord[7], P. Ruzicka[125], Y.F. Ryabov[121], M. Rybar[126], G. Rybkin[115], N.C. Ryder[118], A.F. Saavedra[150], I. Sadeh[153], H.F-W. Sadrozinski[137], R. Sadykov[64], F. Safai Tehrani[132a], H. Sakamoto[155], G. Salamanna[75], A. Salamon[133a], M. Saleem[111], D. Salek[30], D. Salihagic[99], A. Salnikov[143], J. Salt[167], B.M. Salvachua Ferrando[6], D. Salvatore[37a,37b], F. Salvatore[149], A. Salvucci[104], A. Salzburger[30], D. Sampsonidis[154], B.H. Samset[117], A. Sanchez[102a,102b], V. Sanchez Martinez[167], H. Sandaker[14], H.G. Sander[81], M.P. Sanders[98], M. Sandhoff[175], T. Sandoval[28], C. Sandoval[162], R. Sandstroem[99], D.P.C. Sankey[129], A. Sansoni[47], C. Santamarina Rios[85], C. Santoni[34], R. Santonico[133a,133b], H. Santos[124a], J.G. Saraiva[124a], T. Sarangi[173], E. Sarkisyan-Grinbaum[8], F. Sarri[122a,122b], G. Sartisohn[175], O. Sasaki[65], Y. Sasaki[155], N. Sasao[67], I. Satsounkevitch[90], G. Sauvage[5,*], E. Sauvan[5], J.B. Sauvan[115], P. Savard[158,d], V. Savinov[123], D.O. Savu[30], L. Sawyer[25,m], D.H. Saxon[53], J. Saxon[120], C. Sbarra[20a], A. Sbrizzi[20a,20b], D.A. Scannicchio[163], M. Scarcella[150], J. Schaarschmidt[115], P. Schacht[99], D. Schaefer[120], U. Schäfer[81], A. Schaelicke[46], S. Schaepe[21], S. Schaetzel[58b], A.C. Schaffer[115], D. Schaile[98], R.D. Schamberger[148], A.G. Schamov[107], V. Scharf[58a], V.A. Schegelsky[121], D. Scheirich[87], M. Schernau[163], M.I. Scherzer[35], C. Schiavi[50a,50b], J. Schieck[98], M. Schioppa[37a,37b], S. Schlenker[30], E. Schmidt[48], K. Schmieden[21], C. Schmitt[81], S. Schmitt[58b], M. Schmitz[21], B. Schneider[17], U. Schnoor[44], L. Schoeffel[136], A. Schoening[58b], A.L.S. Schorlemmer[54], M. Schott[30], D. Schouten[159a], J. Schovancova[125], M. Schram[85], C. Schroeder[81], N. Schroer[58c], M.J. Schultens[21], J. Schultes[175], H.-C. Schultz-Coulon[58a], H. Schulz[16], M. Schumacher[48], B.A. Schumm[137], Ph. Schune[136], C. Schwanenberger[82], A. Schwartzman[143], Ph. Schwegler[99], Ph. Schwemling[78], R. Schwienhorst[88], R. Schwierz[44], J. Schwindling[136], T. Schwindt[21], M. Schwoerer[5], G. Sciolla[23], W.G. Scott[129], J. Searcy[114], G. Sedov[42], E. Sedykh[121], S.C. Seidel[103], A. Seiden[137], F. Seifert[44], J.M. Seixas[24a], G. Sekhniaidze[102a], S.J. Sekula[40], K.E. Selbach[46], D.M. Seliverstov[121], B. Sellden[146a], G. Sellers[73], M. Seman[144b], N. Semprini-Cesari[20a,20b], C. Serfon[98], L. Serin[115], L. Serkin[54], R. Seuster[159a], H. Severini[111], A. Sfyrla[30], E. Shabalina[54], M. Shamim[114], L.Y. Shan[33a], J.T. Shank[22], Q.T. Shao[86], M. Shapiro[15], P.B. Shatalov[95], K. Shaw[164a,164c], D. Sherman[176], P. Sherwood[77], S. Shimizu[101], M. Shimojima[100], T. Shin[56], M. Shiyakova[64], A. Shmeleva[94], M.J. Shochet[31], D. Short[118], S. Shrestha[63], E. Shulga[96], M.A. Shupe[7], P. Sicho[125], A. Sidoti[132a], F. Siegert[48], Dj. Sijacki[13a], O. Silbert[172], J. Silva[124a], Y. Silver[153], D. Silverstein[143], S.B. Silverstein[146a], V. Simak[127], O. Simard[136], Lj. Simic[13a], S. Simion[115], E. Simioni[81], B. Simmons[77], R. Simoniello[89a,89b], M. Simonyan[36], P. Sinervo[158], N.B. Sinev[114], V. Sipica[141], G. Siragusa[174], A. Sircar[25], A.N. Sisakyan[64,*], S.Yu. Sivoklokov[97], J. Sjölin[146a,146b], T.B. Sjursen[14], L.A. Skinnari[15], H.P. Skottowe[57], K. Skovpen[107], P. Skubic[111], M. Slater[18], T. Slavicek[127], K. Sliwa[161], V. Smakhtin[172], B.H. Smart[46], L. Smestad[117], S.Yu. Smirnov[96], Y. Smirnov[96], L.N. Smirnova[97], O. Smirnova[79], B.C. Smith[57], D. Smith[143], K.M. Smith[53], M. Smizanska[71], K. Smolek[127], A.A. Snesarev[94], S.W. Snow[82], J. Snow[111], S. Snyder[25], R. Sobie[169,k], J. Sodomka[127], A. Soffer[153], C.A. Solans[167], M. Solar[127], J. Solc[127], E.Yu. Soldatov[96], U. Soldevila[167], E. Solfaroli Camillocci[132a,132b], A.A. Solodkov[128], O.V. Solovyanov[128], V. Solovyev[121], N. Soni[1], V. Sopko[127], B. Sopko[127], M. Sosebee[8], R. Soualah[164a,164c], A. Soukharev[107], S. Spagnolo[72a,72b], F. Spanò[76], R. Spighi[20a], G. Spigo[30], R. Spiwoks[30], M. Spousta[126,ag], T. Spreitzer[158], B. Spurlock[8], R.D. St. Denis[53], J. Stahlman[120], R. Stamen[58a], E. Stanecka[39], R.W. Stanek[6], C. Stanescu[134a], M. Stanescu-Bellu[42], M.M. Stanitzki[42], S. Stapnes[117], E.A. Starchenko[128], J. Stark[55], P. Staroba[125], P. Starovoitov[42], R. Staszewski[39], A. Staude[98], P. Stavina[144a,*], G. Steele[53], P. Steinbach[44], P. Steinberg[25], I. Stekl[127], B. Stelzer[142], H.J. Stelzer[88], O. Stelzer-Chilton[159a], H. Stenzel[52], S. Stern[99], G.A. Stewart[30], J.A. Stillings[21], M.C. Stockton[85], K. Stoerig[48], G. Stoicea[26a], S. Stonjek[99], P. Strachota[126], A.R. Stradling[8], A. Straessner[44], J. Strandberg[147], S. Strandberg[146a,146b], A. Strandlie[117], M. Strang[109], E. Strauss[143], M. Strauss[111], P. Strizenec[144b], R. Ströhmer[174], D.M. Strom[114], J.A. Strong[76,*], R. Stroynowski[40], B. Stugu[14], I. Stumer[25,*], J. Stupak[148], P. Sturm[175], N.A. Styles[42], D.A. Soh[151,u], D. Su[143], HS. Subramania[3], R. Subramaniam[25], A. Succurro[12], Y. Sugaya[116], C. Suhr[106], M. Suk[126], V.V. Sulin[94], S. Sultansoy[4d], T. Sumida[67], X. Sun[55], J.E. Sundermann[48], K. Suruliz[139], G. Susinno[37a,37b], M.R. Sutton[149], Y. Suzuki[65], Y. Suzuki[66], M. Svatos[125], S. Swedish[168], I. Sykora[144a], T. Sykora[126], J. Sánchez[167], D. Ta[105], K. Tackmann[42], A. Taffard[163], R. Tafirout[159a], N. Taiblum[153], Y. Takahashi[101], H. Takai[25], R. Takashima[68], H. Takeda[66], T. Takeshita[140], Y. Takubo[65], M. Talby[83], A. Talyshev[107,f], M.C. Tamsett[25], K.G. Tan[86], J. Tanaka[155], R. Tanaka[115], S. Tanaka[131], S. Tanaka[65], A.J. Tanasijczuk[142], K. Tani[66], N. Tannoury[83], S. Tapprogge[81], D. Tardif[158], S. Tarem[152], F. Tarrade[29], G.F. Tartarelli[89a], P. Tas[126], M. Tasevsky[125], E. Tassi[37a,37b], M. Tatarkhanov[15], Y. Tayalati[135d], C. Taylor[77], F.E. Taylor[92], G.N. Taylor[86], W. Taylor[159b], M. Teinturier[115], F.A. Teischinger[30], M. Teixeira Dias Castanheira[75], P. Teixeira-Dias[76], K.K. Temming[48], H. Ten Kate[30], P.K. Teng[151], S. Terada[65], K. Terashi[155], J. Terron[80], M. Testa[47], R.J. Teuscher[158,k], J. Therhaag[21], T. Theveneaux-Pelzer[78], S. Thoma[48], J.P. Thomas[18], E.N. Thompson[35], P.D. Thompson[18], P.D. Thompson[158], A.S. Thompson[53], L.A. Thomsen[36], E. Thomson[120], M. Thomson[28], W.M. Thong[86], R.P. Thun[87], F. Tian[35], M.J. Tibbetts[15], T. Tic[125], V.O. Tikhomirov[94], Y.A. Tikhonov[107,f], S. Timoshenko[96], E. Tiouchichine[83], P. Tipton[176], S. Tisserant[83], T. Todorov[5], S. Todorova-Nova[161], B. Toggerson[163], J. Tojo[69], S. Tokár[144a],

K. Tokushuku[65], K. Tollefson[88], M. Tomoto[101], L. Tompkins[31], K. Toms[103], A. Tonoyan[14], C. Topfel[17], N.D. Topilin[64], I. Torchiani[30], E. Torrence[114], H. Torres[78], E. Torró Pastor[167], J. Toth[83,ac], F. Touchard[83], D.R. Tovey[139], T. Trefzger[174], L. Tremblet[30], A. Tricoli[30], I.M. Trigger[159a], S. Trincaz-Duvoid[78], M.F. Tripiana[70], N. Triplett[25], W. Trischuk[158], B. Trocmé[55], C. Troncon[89a], M. Trottier-McDonald[142], P. True[88], M. Trzebinski[39], A. Trzupek[39], C. Tsarouchas[30], J.C-L. Tseng[118], M. Tsiakiris[105], P.V. Tsiareshka[90], D. Tsionou[5,ah], G. Tsipolitis[10], S. Tsiskaridze[12], V. Tsiskaridze[48], E.G. Tskhadadze[51a], I.I. Tsukerman[95], V. Tsulaia[15], J.-W. Tsung[21], S. Tsuno[65], D. Tsybychev[148], A. Tua[139], A. Tudorache[26a], V. Tudorache[26a], J.M. Tuggle[31], M. Turala[39], D. Turecek[127], I. Turk Cakir[4e], E. Turlay[105], R. Turra[89a,89b], P.M. Tuts[35], A. Tykhonov[74], M. Tylmad[146a,146b], M. Tyndel[129], G. Tzanakos[9], K. Uchida[21], I. Ueda[155], R. Ueno[29], M. Ugland[14], M. Uhlenbrock[21], M. Uhrmacher[54], F. Ukegawa[160], G. Unal[30], A. Undrus[25], G. Unel[163], Y. Unno[65], D. Urbaniec[35], P. Urquijo[21], G. Usai[8], M. Uslenghi[119a,119b], L. Vacavant[83], V. Vacek[127], B. Vachon[85], S. Vahsen[15], J. Valenta[125], S. Valentinetti[20a,20b], A. Valero[167], S. Valkar[126], E. Valladolid Gallego[167], S. Vallecorsa[152], J.A. Valls Ferrer[167], R. Van Berg[120], P.C. Van Der Deijl[105], R. van der Geer[105], H. van der Graaf[105], R. Van Der Leeuw[105], E. van der Poel[105], D. van der Ster[30], N. van Eldik[30], P. van Gemmeren[6], I. van Vulpen[105], M. Vanadia[99], W. Vandelli[30], A. Vaniachine[6], P. Vankov[42], F. Vannucci[78], R. Vari[132a], E.W. Varnes[7], T. Varol[84], D. Varouchas[15], A. Vartapetian[8], K.E. Varvell[150], V.I. Vassilakopoulos[56], F. Vazeille[34], T. Vazquez Schroeder[54], G. Vegni[89a,89b], J.J. Veillet[115], F. Veloso[124a], R. Veness[30], S. Veneziano[132a], A. Ventura[72a,72b], D. Ventura[84], M. Venturi[48], N. Venturi[158], V. Vercesi[119a], M. Verducci[138], W. Verkerke[105], J.C. Vermeulen[105], A. Vest[44], M.C. Vetterli[142,d], I. Vichou[165], T. Vickey[145b,ai], O.E. Vickey Boeriu[145b], G.H.A. Viehhauser[118], S. Viel[168], M. Villa[20a,20b], M. Villaplana Perez[167], E. Vilucchi[47], M.G. Vincter[29], E. Vinek[30], V.B. Vinogradov[64], M. Virchaux[136,*], J. Virzi[15], O. Vitells[172], M. Viti[42], I. Vivarelli[48], F. Vives Vaque[3], S. Vlachos[10], D. Vladoiu[98], M. Vlasak[127], A. Vogel[21], P. Vokac[127], G. Volpi[47], M. Volpi[86], G. Volpini[89a], H. von der Schmitt[99], H. von Radziewski[48], E. von Toerne[21], V. Vorobel[126], V. Vorwerk[12], M. Vos[167], R. Voss[30], T.T. Voss[175], J.H. Vossebeld[73], N. Vranjes[136], M. Vranjes Milosavljevic[105], V. Vrba[125], M. Vreeswijk[105], T. Vu Anh[48], R. Vuillermet[30], I. Vukotic[31], W. Wagner[175], P. Wagner[120], H. Wahlen[175], S. Wahrmund[44], J. Wakabayashi[101], S. Walch[87], J. Walder[71], R. Walker[98], W. Walkowiak[141], R. Wall[176], P. Waller[73], B. Walsh[176], C. Wang[45], H. Wang[173], H. Wang[33b,aj], J. Wang[151], J. Wang[55], R. Wang[103], S.M. Wang[151], T. Wang[21], A. Warburton[85], C.P. Ward[28], D.R. Wardrope[77], M. Warsinsky[48], A. Washbrook[46], C. Wasicki[42], I. Watanabe[66], P.M. Watkins[18], A.T. Watson[18], I.J. Watson[150], M.F. Watson[18], G. Watts[138], S. Watts[82], A.T. Waugh[150], B.M. Waugh[77], M.S. Weber[17], P. Weber[54], J.S. Webster[31], A.R. Weidberg[118], P. Weigell[99], J. Weingarten[54], C. Weiser[48], P.S. Wells[30], T. Wenaus[25], D. Wendland[16], Z. Weng[151,u], T. Wengler[30], S. Wenig[30], N. Wermes[21], M. Werner[48], P. Werner[30], M. Werth[163], M. Wessels[58a], J. Wetter[161], C. Weydert[55], K. Whalen[29], A. White[8], M.J. White[86], S. White[122a,122b], S.R. Whitehead[118], D. Whiteson[163], D. Whittington[60], F. Wicek[115], D. Wicke[175], F.J. Wickens[129], W. Wiedenmann[173], M. Wielers[129], P. Wienemann[21], C. Wiglesworth[75], L.A.M. Wiik-Fuchs[21], P.A. Wijeratne[77], A. Wildauer[99], M.A. Wildt[42,r], I. Wilhelm[126], H.G. Wilkens[30], J.Z. Will[98], E. Williams[35], H.H. Williams[120], W. Willis[35], S. Willocq[84], J.A. Wilson[18], M.G. Wilson[143], A. Wilson[87], I. Wingerter-Seez[5], S. Winkelmann[48], F. Winklmeier[30], M. Wittgen[143], S.J. Wollstadt[81], M.W. Wolter[39], H. Wolters[124a,h], W.C. Wong[41], G. Wooden[87], B.K. Wosiek[39], J. Wotschack[30], M.J. Woudstra[82], K.W. Wozniak[39], K. Wraight[53], M. Wright[53], B. Wrona[73], S.L. Wu[173], X. Wu[49], Y. Wu[33b,ak], E. Wulf[35], B.M. Wynne[46], S. Xella[36], M. Xiao[136], S. Xie[48], C. Xu[33b,y], D. Xu[139], B. Yabsley[150], S. Yacoob[145a,al], M. Yamada[65], H. Yamaguchi[155], A. Yamamoto[65], K. Yamamoto[63], S. Yamamoto[155], T. Yamamura[155], T. Yamanaka[155], T. Yamazaki[155], Y. Yamazaki[66], Z. Yan[22], H. Yang[87], U.K. Yang[82], Y. Yang[109], Z. Yang[146a,146b], S. Yanush[91], L. Yao[33a], Y. Yao[15], Y. Yasu[65], G.V. Ybeles Smit[130], J. Ye[40], S. Ye[25], M. Yilmaz[4c], R. Yoosoofmiya[123], K. Yorita[171], R. Yoshida[6], K. Yoshihara[155], C. Young[143], C.J. Young[118], S. Youssef[22], D. Yu[25], J. Yu[8], J. Yu[112], L. Yuan[66], A. Yurkewicz[106], M. Byszewski[30], B. Zabinski[39], R. Zaidan[62], A.M. Zaitsev[128], Z. Zajacova[30], L. Zanello[132a,132b], D. Zanzi[99], A. Zaytsev[25], C. Zeitnitz[175], M. Zeman[125], A. Zemla[39], C. Zendler[21], O. Zenin[128], T. Ženiš[144a], Z. Zinonos[122a,122b], S. Zenz[15], D. Zerwas[115], G. Zevi della Porta[57], D. Zhang[33b,aj], H. Zhang[88], J. Zhang[6], X. Zhang[33d], Z. Zhang[115], L. Zhao[108], Z. Zhao[33b], A. Zhemchugov[64], J. Zhong[118], B. Zhou[87], N. Zhou[163], Y. Zhou[151], C.G. Zhu[33d], H. Zhu[42], J. Zhu[87], Y. Zhu[33b], X. Zhuang[98], V. Zhuravlov[99], A. Zibell[98], D. Zieminska[60], N.I. Zimin[64], R. Zimmermann[21], S. Zimmermann[21], S. Zimmermann[48], M. Ziolkowski[141], R. Zitoun[5], L. Živković[35], V.V. Zmouchko[128,*], G. Zobernig[173], A. Zoccoli[20a,20b], M. zur Nedden[16], V. Zutshi[106], L. Zwalinski[30]

[1]School of Chemistry and Physics, University of Adelaide, Adelaide, Australia

[2]Physics Department, SUNY Albany, Albany NY, United States of America

[3]Department of Physics, University of Alberta, Edmonton AB, Canada

[4(a)]Department of Physics, Ankara University, Ankara; [(b)]Department of Physics, Dumlupinar University, Kutahya; [(c)]Department of Physics, Gazi University, Ankara; [(d)]Division of Physics, TOBB University of Economics and Technology, Ankara; [(e)]Turkish Atomic Energy Authority, Ankara, Turkey

[5]LAPP, CNRS/IN2P3 and Université de Savoie, Annecy-le-Vieux, France

[6]High Energy Physics Division, Argonne National Laboratory, Argonne IL, United States of America
[7]Department of Physics, University of Arizona, Tucson AZ, United States of America
[8]Department of Physics, The University of Texas at Arlington, Arlington TX, United States of America
[9]Physics Department, University of Athens, Athens, Greece
[10]Physics Department, National Technical University of Athens, Zografou, Greece
[11]Institute of Physics, Azerbaijan Academy of Sciences, Baku, Azerbaijan
[12]Institut de Física d'Altes Energies and Departament de Física de la Universitat Autònoma de Barcelona and ICREA, Barcelona, Spain
[13(a)]Institute of Physics, University of Belgrade, Belgrade; [(b)]Vinca Institute of Nuclear Sciences, University of Belgrade, Belgrade, Serbia
[14]Department for Physics and Technology, University of Bergen, Bergen, Norway
[15]Physics Division, Lawrence Berkeley National Laboratory and University of California, Berkeley CA, United States of America
[16]Department of Physics, Humboldt University, Berlin, Germany
[17]Albert Einstein Center for Fundamental Physics and Laboratory for High Energy Physics, University of Bern, Bern, Switzerland
[18]School of Physics and Astronomy, University of Birmingham, Birmingham, United Kingdom
[19(a)]Department of Physics, Bogazici University, Istanbul; [(b)]Division of Physics, Dogus University, Istanbul; [(c)]Department of Physics Engineering, Gaziantep University, Gaziantep; [(d)]Department of Physics, Istanbul Technical University, Istanbul, Turkey
[20(a)]INFN Sezione di Bologna; [(b)]Dipartimento di Fisica, Università di Bologna, Bologna, Italy
[21]Physikalisches Institut, University of Bonn, Bonn, Germany
[22]Department of Physics, Boston University, Boston MA, United States of America
[23]Department of Physics, Brandeis University, Waltham MA, United States of America
[24(a)]Universidade Federal do Rio De Janeiro COPPE/EE/IF, Rio de Janeiro; [(b)]Federal University of Juiz de Fora (UFJF), Juiz de Fora; [(c)]Federal University of Sao Joao del Rei (UFSJ), Sao Joao del Rei; [(d)]Instituto de Fisica, Universidade de Sao Paulo, Sao Paulo, Brazil
[25]Physics Department, Brookhaven National Laboratory, Upton NY, United States of America
[26(a)]National Institute of Physics and Nuclear Engineering, Bucharest; [(b)]University Politehnica Bucharest, Bucharest; [(c)]West University in Timisoara, Timisoara, Romania
[27]Departamento de Física, Universidad de Buenos Aires, Buenos Aires, Argentina
[28]Cavendish Laboratory, University of Cambridge, Cambridge, United Kingdom
[29]Department of Physics, Carleton University, Ottawa ON, Canada
[30]CERN, Geneva, Switzerland
[31]Enrico Fermi Institute, University of Chicago, Chicago IL, United States of America
[32(a)]Departamento de Física, Pontificia Universidad Católica de Chile, Santiago; [(b)]Departamento de Física, Universidad Técnica Federico Santa María, Valparaíso, Chile
[33(a)]Institute of High Energy Physics, Chinese Academy of Sciences, Beijing; [(b)]Department of Modern Physics, University of Science and Technology of China, Anhui; [(c)]Department of Physics, Nanjing University, Jiangsu; [(d)]School of Physics, Shandong University, Shandong, China
[34]Laboratoire de Physique Corpusculaire, Clermont Université and Université Blaise Pascal and CNRS/IN2P3, Clermont-Ferrand, France
[35]Nevis Laboratory, Columbia University, Irvington NY, United States of America
[36]Niels Bohr Institute, University of Copenhagen, Kobenhavn, Denmark
[37(a)]INFN Gruppo Collegato di Cosenza; [(b)]Dipartimento di Fisica, Università della Calabria, Arcavata di Rende, Italy
[38]AGH University of Science and Technology, Faculty of Physics and Applied Computer Science, Krakow, Poland
[39]The Henryk Niewodniczanski Institute of Nuclear Physics, Polish Academy of Sciences, Krakow, Poland
[40]Physics Department, Southern Methodist University, Dallas TX, United States of America
[41]Physics Department, University of Texas at Dallas, Richardson TX, United States of America
[42]DESY, Hamburg and Zeuthen, Germany
[43]Institut für Experimentelle Physik IV, Technische Universität Dortmund, Dortmund, Germany
[44]Institut für Kern- und Teilchenphysik, Technical University Dresden, Dresden, Germany
[45]Department of Physics, Duke University, Durham NC, United States of America

[46]SUPA - School of Physics and Astronomy, University of Edinburgh, Edinburgh, United Kingdom
[47]INFN Laboratori Nazionali di Frascati, Frascati, Italy
[48]Fakultät für Mathematik und Physik, Albert-Ludwigs-Universität, Freiburg, Germany
[49]Section de Physique, Université de Genève, Geneva, Switzerland
[50(a)]INFN Sezione di Genova; [(b)]Dipartimento di Fisica, Università di Genova, Genova, Italy
[51(a)]E. Andronikashvili Institute of Physics, Iv. Javakhishvili Tbilisi State University, Tbilisi; [(b)]High Energy Physics Institute, Tbilisi State University, Tbilisi, Georgia
[52]II Physikalisches Institut, Justus-Liebig-Universität Giessen, Giessen, Germany
[53]SUPA - School of Physics and Astronomy, University of Glasgow, Glasgow, United Kingdom
[54]II Physikalisches Institut, Georg-August-Universität, Göttingen, Germany
[55]Laboratoire de Physique Subatomique et de Cosmologie, Université Joseph Fourier and CNRS/IN2P3 and Institut National Polytechnique de Grenoble, Grenoble, France
[56]Department of Physics, Hampton University, Hampton VA, United States of America
[57]Laboratory for Particle Physics and Cosmology, Harvard University, Cambridge MA, United States of America
[58(a)]Kirchhoff-Institut für Physik, Ruprecht-Karls-Universität Heidelberg, Heidelberg; [(b)]Physikalisches Institut, Ruprecht-Karls-Universität Heidelberg, Heidelberg; [(c)]ZITI Institut für technische Informatik, Ruprecht-Karls-Universität Heidelberg, Mannheim, Germany
[59]Faculty of Applied Information Science, Hiroshima Institute of Technology, Hiroshima, Japan
[60]Department of Physics, Indiana University, Bloomington IN, United States of America
[61]Institut für Astro- und Teilchenphysik, Leopold-Franzens-Universität, Innsbruck, Austria
[62]University of Iowa, Iowa City IA, United States of America
[63]Department of Physics and Astronomy, Iowa State University, Ames IA, United States of America
[64]Joint Institute for Nuclear Research, JINR Dubna, Dubna, Russia
[65]KEK, High Energy Accelerator Research Organization, Tsukuba, Japan
[66]Graduate School of Science, Kobe University, Kobe, Japan
[67]Faculty of Science, Kyoto University, Kyoto, Japan
[68]Kyoto University of Education, Kyoto, Japan
[69]Department of Physics, Kyushu University, Fukuoka, Japan
[70]Instituto de Física La Plata, Universidad Nacional de La Plata and CONICET, La Plata, Argentina
[71]Physics Department, Lancaster University, Lancaster, United Kingdom
[72(a)]INFN Sezione di Lecce; [(b)]Dipartimento di Matematica e Fisica, Università del Salento, Lecce, Italy
[73]Oliver Lodge Laboratory, University of Liverpool, Liverpool, United Kingdom
[74]Department of Physics, Jožef Stefan Institute and University of Ljubljana, Ljubljana, Slovenia
[75]School of Physics and Astronomy, Queen Mary University of London, London, United Kingdom
[76]Department of Physics, Royal Holloway University of London, Surrey, United Kingdom
[77]Department of Physics and Astronomy, University College London, London, United Kingdom
[78]Laboratoire de Physique Nucléaire et de Hautes Energies, UPMC and Université Paris-Diderot and CNRS/IN2P3, Paris, France
[79]Fysiska institutionen, Lunds universitet, Lund, Sweden
[80]Departamento de Fisica Teorica C-15, Universidad Autonoma de Madrid, Madrid, Spain
[81]Institut für Physik, Universität Mainz, Mainz, Germany
[82]School of Physics and Astronomy, University of Manchester, Manchester, United Kingdom
[83]CPPM, Aix-Marseille Université and CNRS/IN2P3, Marseille, France
[84]Department of Physics, University of Massachusetts, Amherst MA, United States of America
[85]Department of Physics, McGill University, Montreal QC, Canada
[86]School of Physics, University of Melbourne, Victoria, Australia
[87]Department of Physics, The University of Michigan, Ann Arbor MI, United States of America
[88]Department of Physics and Astronomy, Michigan State University, East Lansing MI, United States of America
[89(a)]INFN Sezione di Milano; [(b)]Dipartimento di Fisica, Università di Milano, Milano, Italy
[90]B.I. Stepanov Institute of Physics, National Academy of Sciences of Belarus, Minsk, Republic of Belarus
[91]National Scientific and Educational Centre for Particle and High Energy Physics, Minsk, Republic of Belarus
[92]Department of Physics, Massachusetts Institute of Technology, Cambridge MA, United States of America
[93]Group of Particle Physics, University of Montreal, Montreal QC, Canada

[94]P.N. Lebedev Institute of Physics, Academy of Sciences, Moscow, Russia
[95]Institute for Theoretical and Experimental Physics (ITEP), Moscow, Russia
[96]Moscow Engineering and Physics Institute (MEPhI), Moscow, Russia
[97]Skobeltsyn Institute of Nuclear Physics, Lomonosov Moscow State University, Moscow, Russia
[98]Fakultät für Physik, Ludwig-Maximilians-Universität München, München, Germany
[99]Max-Planck-Institut für Physik (Werner-Heisenberg-Institut), München, Germany
[100]Nagasaki Institute of Applied Science, Nagasaki, Japan
[101]Graduate School of Science and Kobayashi-Maskawa Institute, Nagoya University, Nagoya, Japan
[102(a)]INFN Sezione di Napoli; [(b)]Dipartimento di Scienze Fisiche, Università di Napoli, Napoli, Italy
[103]Department of Physics and Astronomy, University of New Mexico, Albuquerque NM, United States of America
[104]Institute for Mathematics, Astrophysics and Particle Physics, Radboud University Nijmegen/Nikhef, Nijmegen, Netherlands
[105]Nikhef National Institute for Subatomic Physics and University of Amsterdam, Amsterdam, Netherlands
[106]Department of Physics, Northern Illinois University, DeKalb IL, United States of America
[107]Budker Institute of Nuclear Physics, SB RAS, Novosibirsk, Russia
[108]Department of Physics, New York University, New York NY, United States of America
[109]Ohio State University, Columbus OH, United States of America
[110]Faculty of Science, Okayama University, Okayama, Japan
[111]Homer L. Dodge Department of Physics and Astronomy, University of Oklahoma, Norman OK, United States of America
[112]Department of Physics, Oklahoma State University, Stillwater OK, United States of America
[113]Palacký University, RCPTM, Olomouc, Czech Republic
[114]Center for High Energy Physics, University of Oregon, Eugene OR, United States of America
[115]LAL, Université Paris-Sud and CNRS/IN2P3, Orsay, France
[116]Graduate School of Science, Osaka University, Osaka, Japan
[117]Department of Physics, University of Oslo, Oslo, Norway
[118]Department of Physics, Oxford University, Oxford, United Kingdom
[119(a)]INFN Sezione di Pavia; [(b)]Dipartimento di Fisica, Università di Pavia, Pavia, Italy
[120]Department of Physics, University of Pennsylvania, Philadelphia PA, United States of America
[121]Petersburg Nuclear Physics Institute, Gatchina, Russia
[122(a)]INFN Sezione di Pisa; [(b)]Dipartimento di Fisica E. Fermi, Università di Pisa, Pisa, Italy
[123]Department of Physics and Astronomy, University of Pittsburgh, Pittsburgh PA, United States of America
[124(a)]Laboratorio de Instrumentacao e Fisica Experimental de Particulas - LIP, Lisboa, Portugal; [(b)]Departamento de Fisica Teorica y del Cosmos and CAFPE, Universidad de Granada, Granada, Spain
[125]Institute of Physics, Academy of Sciences of the Czech Republic, Praha, Czech Republic
[126]Faculty of Mathematics and Physics, Charles University in Prague, Praha, Czech Republic
[127]Czech Technical University in Prague, Praha, Czech Republic
[128]State Research Center Institute for High Energy Physics, Protvino, Russia
[129]Particle Physics Department, Rutherford Appleton Laboratory, Didcot, United Kingdom
[130]Physics Department, University of Regina, Regina SK, Canada
[131]Ritsumeikan University, Kusatsu, Shiga, Japan
[132(a)]INFN Sezione di Roma I; [(b)]Dipartimento di Fisica, Università La Sapienza, Roma, Italy
[133(a)]INFN Sezione di Roma Tor Vergata; [(b)]Dipartimento di Fisica, Università di Roma Tor Vergata, Roma, Italy
[134(a)]INFN Sezione di Roma Tre; [(b)]Dipartimento di Fisica, Università Roma Tre, Roma, Italy
[135(a)]Faculté des Sciences Ain Chock, Réseau Universitaire de Physique des Hautes Energies - Université Hassan II, Casablanca; [(b)]Centre National de l'Energie des Sciences Techniques Nucleaires, Rabat; [(c)]Faculté des Sciences Semlalia, Université Cadi Ayyad, LPHEA, Marrakech; [(d)]Faculté des Sciences, Université Mohamed Premier and LPTPM, Oujda; [(e)]Faculté des sciences, Université Mohammed V-Agdal, Rabat, Morocco
[136]DSM/IRFU (Institut de Recherches sur les Lois Fondamentales de l'Univers), CEA Saclay (Commissariat a l'Energie Atomique), Gif-sur-Yvette, France
[137]Santa Cruz Institute for Particle Physics, University of California Santa Cruz, Santa Cruz CA, United States of America
[138]Department of Physics, University of Washington, Seattle WA, United States of America
[139]Department of Physics and Astronomy, University of Sheffield, Sheffield, United Kingdom

[140]Department of Physics, Shinshu University, Nagano, Japan
[141]Fachbereich Physik, Universität Siegen, Siegen, Germany
[142]Department of Physics, Simon Fraser University, Burnaby BC, Canada
[143]SLAC National Accelerator Laboratory, Stanford CA, United States of America
[144(a)]Faculty of Mathematics, Physics & Informatics, Comenius University, Bratislava; [(b)]Department of Subnuclear Physics, Institute of Experimental Physics of the Slovak Academy of Sciences, Kosice, Slovak Republic
[145(a)]Department of Physics, University of Johannesburg, Johannesburg; [(b)]School of Physics, University of the Witwatersrand, Johannesburg, South Africa
[146(a)]Department of Physics, Stockholm University; [(b)]The Oskar Klein Centre, Stockholm, Sweden
[147]Physics Department, Royal Institute of Technology, Stockholm, Sweden
[148]Departments of Physics & Astronomy and Chemistry, Stony Brook University, Stony Brook NY, United States of America
[149]Department of Physics and Astronomy, University of Sussex, Brighton, United Kingdom
[150]School of Physics, University of Sydney, Sydney, Australia
[151]Institute of Physics, Academia Sinica, Taipei, Taiwan
[152]Department of Physics, Technion: Israel Institute of Technology, Haifa, Israel
[153]Raymond and Beverly Sackler School of Physics and Astronomy, Tel Aviv University, Tel Aviv, Israel
[154]Department of Physics, Aristotle University of Thessaloniki, Thessaloniki, Greece
[155]International Center for Elementary Particle Physics and Department of Physics, The University of Tokyo, Tokyo, Japan
[156]Graduate School of Science and Technology, Tokyo Metropolitan University, Tokyo, Japan
[157]Department of Physics, Tokyo Institute of Technology, Tokyo, Japan
[158]Department of Physics, University of Toronto, Toronto ON, Canada
[159(a)]TRIUMF, Vancouver BC; [(b)]Department of Physics and Astronomy, York University, Toronto ON, Canada
[160]Faculty of Pure and Applied Sciences, University of Tsukuba, Tsukuba, Japan
[161]Department of Physics and Astronomy, Tufts University, Medford MA, United States of America
[162]Centro de Investigaciones, Universidad Antonio Narino, Bogota, Colombia
[163]Department of Physics and Astronomy, University of California Irvine, Irvine CA, United States of America
[164(a)]INFN Gruppo Collegato di Udine, Udine; [(b)]ICTP, Trieste; [(c)]Dipartimento di Chimica, Fisica e Ambiente, Università di Udine, Udine, Italy
[165]Department of Physics, University of Illinois, Urbana IL, United States of America
[166]Department of Physics and Astronomy, University of Uppsala, Uppsala, Sweden
[167]Instituto de Física Corpuscular (IFIC) and Departamento de Física Atómica, Molecular y Nuclear and Departamento de Ingeniería Electrónica and Instituto de Microelectrónica de Barcelona (IMB-CNM), University of Valencia and CSIC, Valencia, Spain
[168]Department of Physics, University of British Columbia, Vancouver BC, Canada
[169]Department of Physics and Astronomy, University of Victoria, Victoria BC, Canada
[170]Department of Physics, University of Warwick, Coventry, United Kingdom
[171]Waseda University, Tokyo, Japan
[172]Department of Particle Physics, The Weizmann Institute of Science, Rehovot, Israel
[173]Department of Physics, University of Wisconsin, Madison WI, United States of America
[174]Fakultät für Physik und Astronomie, Julius-Maximilians-Universität, Würzburg, Germany
[175]Fachbereich C Physik, Bergische Universität Wuppertal, Wuppertal, Germany
[176]Department of Physics, Yale University, New Haven CT, United States of America
[177]Yerevan Physics Institute, Yerevan, Armenia
[178]Centre de Calcul de l'Institut National de Physique Nucléaire et de Physique des Particules (IN2P3), Villeurbanne, France
[a]Also at Laboratorio de Instrumentacao e Fisica Experimental de Particulas - LIP, Lisboa, Portugal
[b]Also at Faculdade de Ciencias and CFNUL, Universidade de Lisboa, Lisboa, Portugal
[c]Also at Particle Physics Department, Rutherford Appleton Laboratory, Didcot, United Kingdom
[d]Also at TRIUMF, Vancouver BC, Canada
[e]Also at Department of Physics, California State University, Fresno CA, United States of America
[f]Also at Novosibirsk State University, Novosibirsk, Russia
[g]Also at Fermilab, Batavia IL, United States of America

[h] Also at Department of Physics, University of Coimbra, Coimbra, Portugal
[i] Also at Department of Physics, UASLP, San Luis Potosi, Mexico
[j] Also at Università di Napoli Parthenope, Napoli, Italy
[k] Also at Institute of Particle Physics (IPP), Canada
[l] Also at Department of Physics, Middle East Technical University, Ankara, Turkey
[m] Also at Louisiana Tech University, Ruston LA, United States of America
[n] Also at Dep Fisica and CEFITEC of Faculdade de Ciencias e Tecnologia, Universidade Nova de Lisboa, Caparica, Portugal
[o] Also at Department of Physics and Astronomy, University College London, London, United Kingdom
[p] Also at Department of Physics, University of Cape Town, Cape Town, South Africa
[q] Also at Institute of Physics, Azerbaijan Academy of Sciences, Baku, Azerbaijan
[r] Also at Institut für Experimentalphysik, Universität Hamburg, Hamburg, Germany
[s] Also at Manhattan College, New York NY, United States of America
[t] Also at CPPM, Aix-Marseille Université and CNRS/IN2P3, Marseille, France
[u] Also at School of Physics and Engineering, Sun Yat-sen University, Guanzhou, China
[v] Also at Academia Sinica Grid Computing, Institute of Physics, Academia Sinica, Taipei, Taiwan
[w] Also at School of Physics, Shandong University, Shandong, China
[x] Also at Dipartimento di Fisica, Università La Sapienza, Roma, Italy
[y] Also at DSM/IRFU (Institut de Recherches sur les Lois Fondamentales de l'Univers), CEA Saclay (Commissariat a l'Energie Atomique), Gif-sur-Yvette, France
[z] Also at Section de Physique, Université de Genève, Geneva, Switzerland
[aa] Also at Departamento de Fisica, Universidade de Minho, Braga, Portugal
[ab] Also at Department of Physics and Astronomy, University of South Carolina, Columbia SC, United States of America
[ac] Also at Institute for Particle and Nuclear Physics, Wigner Research Centre for Physics, Budapest, Hungary
[ad] Also at California Institute of Technology, Pasadena CA, United States of America
[ae] Also at Institute of Physics, Jagiellonian University, Krakow, Poland
[af] Also at LAL, Université Paris-Sud and CNRS/IN2P3, Orsay, France
[ag] Also at Nevis Laboratory, Columbia University, Irvington NY, United States of America
[ah] Also at Department of Physics and Astronomy, University of Sheffield, Sheffield, United Kingdom
[ai] Also at Department of Physics, Oxford University, Oxford, United Kingdom
[aj] Also at Institute of Physics, Academia Sinica, Taipei, Taiwan
[ak] Also at Department of Physics, The University of Michigan, Ann Arbor MI, United States of America
[al] Also at Discipline of Physics, University of KwaZulu-Natal, Durban, South Africa
[*] Deceased